

Development of a Reference Database for Particle Induced Gamma Ray Emission (PIGE) Spectroscopy



DEVELOPMENT OF
A REFERENCE DATABASE
FOR PARTICLE INDUCED GAMMA RAY
EMISSION (PIGE) SPECTROSCOPY

The following States are Members of the International Atomic Energy Agency:

| | | |
|-------------------------------------|-------------------------------------|--|
| AFGHANISTAN | GEORGIA | OMAN |
| ALBANIA | GERMANY | PAKISTAN |
| ALGERIA | GHANA | PALAU |
| ANGOLA | GREECE | PANAMA |
| ANTIGUA AND BARBUDA | GUATEMALA | PAPUA NEW GUINEA |
| ARGENTINA | GUYANA | PARAGUAY |
| ARMENIA | HAITI | PERU |
| AUSTRALIA | HOLY SEE | PHILIPPINES |
| AUSTRIA | HONDURAS | POLAND |
| AZERBAIJAN | HUNGARY | PORTUGAL |
| BAHAMAS | ICELAND | QATAR |
| BAHRAIN | INDIA | REPUBLIC OF MOLDOVA |
| BANGLADESH | INDONESIA | ROMANIA |
| BARBADOS | IRAN, ISLAMIC REPUBLIC OF | RUSSIAN FEDERATION |
| BELARUS | IRAQ | RWANDA |
| BELGIUM | IRELAND | SAN MARINO |
| BELIZE | ISRAEL | SAUDI ARABIA |
| BENIN | ITALY | SENEGAL |
| BOLIVIA, PLURINATIONAL STATE OF | JAMAICA | SERBIA |
| BOSNIA AND HERZEGOVINA | JAPAN | SEYCHELLES |
| BOTSWANA | JORDAN | SIERRA LEONE |
| BRAZIL | KAZAKHSTAN | SINGAPORE |
| BRUNEI DARUSSALAM | KENYA | SLOVAKIA |
| BULGARIA | KOREA, REPUBLIC OF | SLOVENIA |
| BURKINA FASO | KUWAIT | SOUTH AFRICA |
| BURUNDI | KYRGYZSTAN | SPAIN |
| CAMBODIA | LAO PEOPLE'S DEMOCRATIC REPUBLIC | SRI LANKA |
| CAMEROON | LATVIA | SUDAN |
| CANADA | LEBANON | SWAZILAND |
| CENTRAL AFRICAN REPUBLIC | LESOTHO | SWEDEN |
| CHAD | LIBERIA | SWITZERLAND |
| CHILE | LIBYA | SYRIAN ARAB REPUBLIC |
| CHINA | LIECHTENSTEIN | TAJIKISTAN |
| COLOMBIA | LITHUANIA | THAILAND |
| CONGO | LUXEMBOURG | THE FORMER YUGOSLAV REPUBLIC OF MACEDONIA |
| COSTA RICA | MADAGASCAR | TOGO |
| CÔTE D'IVOIRE | MALAWI | TRINIDAD AND TOBAGO |
| CROATIA | MALAYSIA | TUNISIA |
| CUBA | MALI | TURKEY |
| CYPRUS | MALTA | TURKMENISTAN |
| CZECH REPUBLIC | MARSHALL ISLANDS | UGANDA |
| DEMOCRATIC REPUBLIC OF THE CONGO | MAURITANIA | UKRAINE |
| DENMARK | MAURITIUS | UNITED ARAB EMIRATES |
| DJIBOUTI | MEXICO | UNITED KINGDOM OF GREAT BRITAIN AND NORTHERN IRELAND |
| DOMINICA | MONACO | UNITED REPUBLIC OF TANZANIA |
| DOMINICAN REPUBLIC | MONGOLIA | UNITED STATES OF AMERICA |
| ECUADOR | MONTENEGRO | URUGUAY |
| EGYPT | MOROCCO | UZBEKISTAN |
| EL SALVADOR | MOZAMBIQUE | VANUATU |
| ERITREA | MYANMAR | VENEZUELA, BOLIVARIAN REPUBLIC OF |
| ESTONIA | NAMIBIA | VIET NAM |
| ETHIOPIA | NEPAL | YEMEN |
| FIJI | NETHERLANDS | ZAMBIA |
| FINLAND | NEW ZEALAND | ZIMBABWE |
| FRANCE | NICARAGUA | |
| GABON | NIGER | |
| | NIGERIA | |
| | NORWAY | |

The Agency's Statute was approved on 23 October 1956 by the Conference on the Statute of the IAEA held at United Nations Headquarters, New York; it entered into force on 29 July 1957. The Headquarters of the Agency are situated in Vienna. Its principal objective is "to accelerate and enlarge the contribution of atomic energy to peace, health and prosperity throughout the world".

IAEA-TECDOC-1822

DEVELOPMENT OF
A REFERENCE DATABASE
FOR PARTICLE INDUCED GAMMA RAY
EMISSION (PIGE) SPECTROSCOPY

INTERNATIONAL ATOMIC ENERGY AGENCY
VIENNA, 2017

COPYRIGHT NOTICE

All IAEA scientific and technical publications are protected by the terms of the Universal Copyright Convention as adopted in 1952 (Berne) and as revised in 1972 (Paris). The copyright has since been extended by the World Intellectual Property Organization (Geneva) to include electronic and virtual intellectual property. Permission to use whole or parts of texts contained in IAEA publications in printed or electronic form must be obtained and is usually subject to royalty agreements. Proposals for non-commercial reproductions and translations are welcomed and considered on a case-by-case basis. Enquiries should be addressed to the IAEA Publishing Section at:

Marketing and Sales Unit, Publishing Section
International Atomic Energy Agency
Vienna International Centre
PO Box 100
1400 Vienna, Austria
fax: +43 1 2600 29302
tel.: +43 1 2600 22417
email: sales.publications@iaea.org
<http://www.iaea.org/books>

For further information on this publication, please contact:

Nuclear Data Section
International Atomic Energy Agency
Vienna International Centre
PO Box 100
1400 Vienna, Austria
Email: Official.Mail@iaea.org

© IAEA, 2017
Printed by the IAEA in Austria
September 2017

IAEA Library Cataloguing in Publication Data

Names: International Atomic Energy Agency.
Title: Development of a reference database for particle induced gamma ray emission (PIGE) spectroscopy / International Atomic Energy Agency.
Description: Vienna : International Atomic Energy Agency, 2017. | Series: IAEA TECDOC series, ISSN 1011-4289 ; no. 1822 | Includes bibliographical references.
Identifiers: IAEAL 17-01109 | ISBN 978-92-0-106317-5 (paperback : alk. paper)
Subjects: LCSH: Nuclear reactions. | Ion bombardment. | Cross sections (Nuclear physics). | Gamma ray spectrometry.

FOREWORD

Providing nuclear data for use in ion beam analysis (IBA) has been a significant part of the IAEA mission to provide its Member States with reliable nuclear data for energy and non-energy applications. The modern analytical techniques that make use of ion beams are used in a broad range of applications, including microelectronics, cultural heritage studies, forensics, biology and materials sciences. These techniques are also employed in the development of fusion technologies to study and test structural materials.

In response to the growing need for a systematic and traceable compilation of nuclear reaction data for IBA purposes, the IAEA held a coordinated research project (CRP) from 2005 to 2010, entitled Development of a Reference Database for Ion Beam Analysis. The CRP produced the Ion Beam Analysis Nuclear Data Library (IBANDL), which has since served the IBA community by making readily available all existing and published experimental data on charged particle elastic scattering and nuclear reaction cross-sections.

However, the goal of making IBANDL a comprehensive database was not fully reached, since cross-section data for nuclear reactions that produce gamma rays were not taken into consideration. At that time, particle induced gamma ray emission (PIGE) spectroscopy, a powerful analytical technique that employs ion beams, had not been developed to its full potential, mainly owing to the lack of consistent and reliable cross-section data.

Given these circumstances, the IAEA initiated a second CRP, entitled Development of a Reference Database for Particle-Induced Gamma-ray Emission (PIGE) Spectroscopy. The project produced new measurements, to resolve existing discrepancies and to fill in the gaps in existing data. It also determined the accuracy and precision limits of the PIGE analysis technique and set the groundwork for the full development of the standardless PIGE by making available a PIGE simulation computer program. IBANDL now contains the majority of the existing experimental cross-section data for IBA and, going forward, will require only regular updates in the form of routine maintenance.

The IAEA wishes to thank the participants of the CRP for their contributions both to the extension of IBANDL for PIGE analysis and to the present publication. The IAEA is grateful to M. Stanley (United States of America), who contributed significantly to the preparation of the publication. The IAEA officer responsible for this publication was P. Dimitriou of the Division of Physical and Chemical Sciences.

EDITORIAL NOTE

This publication has been prepared from the original material as submitted by the contributors and has not been edited by the editorial staff of the IAEA. The views expressed remain the responsibility of the contributors and do not necessarily represent the views of the IAEA or its Member States.

Neither the IAEA nor its Member States assume any responsibility for consequences which may arise from the use of this publication. This publication does not address questions of responsibility, legal or otherwise, for acts or omissions on the part of any person.

The use of particular designations of countries or territories does not imply any judgement by the publisher, the IAEA, as to the legal status of such countries or territories, of their authorities and institutions or of the delimitation of their boundaries.

The mention of names of specific companies or products (whether or not indicated as registered) does not imply any intention to infringe proprietary rights, nor should it be construed as an endorsement or recommendation on the part of the IAEA.

The IAEA has no responsibility for the persistence or accuracy of URLs for external or third party Internet web sites referred to in this publication and does not guarantee that any content on such web sites is, or will remain, accurate or appropriate.

CONTENTS

| | | |
|------|--|----|
| 1. | INTRODUCTION..... | 1 |
| 1.1. | BACKGROUND | 1 |
| 1.2. | OBJECTIVE..... | 2 |
| 1.3. | SCOPE | 2 |
| | 1.3.1. Compilation of existing data..... | 2 |
| | 1.3.2. New measurements..... | 2 |
| | 1.3.3. Co-ordinated Measurements | 3 |
| | 1.3.4. Evaluations of PIGE cross-sections | 3 |
| | 1.3.5. PIGE Analysis Code..... | 3 |
| | 1.3.6. Updated IBANDL | 3 |
| 1.4. | STRUCTURE..... | 5 |
| | REFERENCES TO SECTION 1..... | 6 |
| 2. | PIGE CONCEPTS AND IMPLEMENTATION | 7 |
| 2.1. | PIGE BULK ANALYSIS | 7 |
| | 2.1.1. PIGE bulk analysis | 7 |
| | 2.1.2. Production and acquisition of gamma-ray spectra | 7 |
| | 2.1.3. Determination of isotopic/elemental concentrations | 13 |
| | 2.1.4. The standard-based method | 14 |
| | 2.1.5. The standardless method..... | 14 |
| 2.2. | PIGE DEPTH PROFILING WITH NUCLEAR RESONANCES..... | 16 |
| 2.3. | A TYPICAL MINIMAL PIGE FACILITY | 20 |
| | 2.3.1. Particle accelerator | 21 |
| | 2.3.2. Charge collection and measuring system | 22 |
| | 2.3.3. Gamma-ray detector..... | 23 |
| | 2.3.4. Example of a minimal PIGE set-up..... | 25 |
| | 2.3.5. Example of an in-vacuum multi detector system..... | 25 |
| 2.4. | EXAMPLES OF APPLICATIONS IN NA BULK ANALYSIS..... | 26 |
| | 2.4.1. Identification of lapis-lazuli in paint layers | 26 |
| | 2.4.2. Quantification of Na in ancient glasses | 28 |
| 2.5. | HYDROGEN DEPTH PROFILING | 29 |
| | REFERENCES TO SECTION 2..... | 33 |
| 3. | METHODOLOGY OF CROSS-SECTION MEASUREMENTS..... | 37 |
| 3.1. | ENERGY CALIBRATION OF THE ACCELERATOR | 37 |
| | 3.1.1. Narrow resonances | 37 |
| | 3.1.2. Neutron producing threshold reactions | 38 |
| | 3.1.3. Elastic scattering | 39 |
| 3.2. | EFFICIENCY CALIBRATION OF THE DETECTOR..... | 39 |
| 3.3. | TARGET PREPARATION..... | 40 |
| 3.4. | CHARGE COLLECTION | 41 |
| 3.5. | CROSS-SECTION DETERMINATION..... | 42 |
| 3.6. | INTERLABORATORY EXERCISE: MEASUREMENT OF THE CROSS-SECTION OF THE $^{27}\text{Al}(\text{P},\text{P}^{\prime})^{27}\text{Al}$ REACTION | 43 |
| | 3.6.1. Implementation | 43 |
| | 3.6.2. Experiment..... | 45 |
| | 3.6.3. Results and discussion..... | 50 |

| | |
|--|-----|
| REFERENCES TO SECTION 3..... | 57 |
| 4. MEASUREMENTS OF PARTICLE-INDUCED GAMMA-RAY EMISSION (PIGE) CROSS-SECTIONS..... | 61 |
| 4.1. LITHIUM..... | 62 |
| 4.1.1. Gamma-ray production cross-sections of lithium from proton- induced nuclear reactions | 62 |
| 4.1.2. Gamma-ray production cross-sections of lithium from deuteron- induced nuclear reactions | 72 |
| 4.2. BERYLLIUM..... | 75 |
| 4.2.1. Gamma-ray production cross-sections of beryllium from proton- induced nuclear reactions | 75 |
| 4.2.2. Gamma-ray production cross-sections of beryllium from deuteron-induced nuclear reactions..... | 77 |
| 4.2.3. Gamma-ray production cross-sections of beryllium from alpha- induced nuclear reactions | 79 |
| 4.3. BORON..... | 79 |
| 4.3.1. Gamma-ray production cross-sections of boron from proton- induced nuclear reactions | 79 |
| 4.3.2. Gamma-ray production cross-sections of boron from deuteron- induced nuclear reactions | 94 |
| 4.4. CARBON | 95 |
| 4.4.1. Gamma-ray production cross-sections of carbon from proton- induced nuclear reactions | 95 |
| 4.4.2. Gamma-ray production cross-sections of carbon from deuteron- induced nuclear reactions | 99 |
| 4.5. NITROGEN..... | 103 |
| 4.5.1. Gamma-ray production cross-sections of nitrogen from proton- induced nuclear reactions | 103 |
| 4.5.2. Gamma-ray production cross-sections of nitrogen from deuteron- induced nuclear reactions | 109 |
| 4.6. FLUORINE | 117 |
| 4.6.1. Gamma-ray production cross-sections of fluorine from proton- induced nuclear reactions | 117 |
| 4.6.2. Thick target yields..... | 128 |
| 4.7. SODIUM..... | 132 |
| 4.7.1. Gamma-ray production cross-sections of sodium from proton- induced nuclear reactions | 132 |
| 4.7.2. Thick target yields..... | 142 |
| 4.8. MAGNESIUM | 144 |
| 4.8.1. Gamma-ray production cross-sections of magnesium from proton- induced nuclear reactions | 144 |
| 4.8.2. Thick target yields..... | 150 |
| 4.9. ALUMINUM..... | 154 |
| 4.9.1. Gamma-ray production cross-sections of aluminum from proton- induced nuclear reactions | 154 |
| 4.9.2. Thick target yields..... | 164 |
| 4.10. SILICON..... | 171 |
| 4.10.1. Gamma-ray production cross-sections of silicon from proton- induced nuclear reactions..... | 171 |
| 4.10.2. Thick target yields..... | 176 |

| | |
|---|-----|
| 4.10.3. Gamma-ray production cross-sections of silicon from deuteron-induced nuclear reactions | 178 |
| 4.11. PHOSPHORUS | 182 |
| 4.11.1. Gamma-ray production cross-sections of phosphorus from proton-induced nuclear reactions | 182 |
| 4.11.2. Thick target yields | 185 |
| 4.12. SULPHUR..... | 186 |
| 4.12.1. Gamma-ray production cross-sections of sulphur from proton-induced nuclear reactions | 186 |
| 4.12.2. Gamma-ray production cross-sections of sulphur from deuteron-induced nuclear reactions | 191 |
| 4.13. TITANIUM..... | 191 |
| 4.13.1. Gamma-ray production cross-sections of titanium from proton-induced nuclear reactions | 191 |
| 4.14. CHROMIUM..... | 196 |
| 4.14.1. Gamma-ray production cross-sections of chromium from proton-induced nuclear reactions | 196 |
| REFERENCES TO SECTION 4..... | 199 |
| 5. THE EMITTED RADIATION YIELD ANALYSIS (ERYA) CODE FOR PIGE ANALYSIS..... | 207 |
| 5.1. INTRODUCTION | 207 |
| 5.2. ERYA..... | 207 |
| 5.2.1. ERYA-bulk | 207 |
| 5.2.2. ERYA-profiling..... | 213 |
| 5.3. USER FEEDBACK AND FUTURE DEVELOPMENTS | 220 |
| REFERENCES TO SECTION 5..... | 221 |
| 6. CONCLUSIONS..... | 222 |
| APPENDIX..... | 224 |
| LIST OF CONTRIBUTORS TO DRAFTING AND REVIEW..... | 231 |

1. INTRODUCTION

1.1. BACKGROUND

Ion beam analysis (IBA) is an important group of analytical techniques that is widely used in applications ranging from analysis of fission reactor material to biomedicine, environment, cultural heritage, and more recently, fusion reactor technologies. The technique uses energetic ion beams to probe the surface of materials in order to determine composition. All IBA methods are non-destructive, highly sensitive and allow the detection of elements in depths ranging up to several hundreds of micrometers.

Among the various existing types of IBA techniques, Particle-Induced Gamma-ray Emission (PIGE) spectroscopy, based on gamma-producing nuclear reactions, is one of the most powerful. The PIGE technique involves measuring the energy spectra of the prompt gamma-rays that are emitted as a result of accelerated charged particles hitting the target matter. Based on these measurements, the composition and structural details of the surface region of the target matter can be determined. This technique has been used regularly since the early 1960's, when it was discovered that it has the potential for performing depth profiling of the surface region of materials with better resolution than other IBA techniques. This unique characteristic of PIGE has proven particularly useful in the development of hydrogen depth profiling: a technique which is now widely used.

As with all IBA methods, including Rutherford backscattering (RBS), elastic backscattering (EBS) and nuclear reactions analysis (NRA), PIGE relies largely on the availability of differential cross-section data. Our poor knowledge of cross-sections for nuclear reactions using charged particles accelerated to only a few megaelectron-volts of energy has significantly hindered progress in the implementation of IBA techniques in general. To address the IBA data needs, a Coordinated Research Project (CRP) on the Development of a Reference Database for Ion Beam Analysis from 2005 to 2010 was initiated [1.1]. Over the course of these five years, the CRP produced a comprehensive and reliable database of cross-section data and evaluated cross-sections that are primarily relevant for eEBS and NRA techniques. The experimental cross-section data are available on the Ion Beam Analysis Nuclear Data Library (IBANDL) [1.2] and the evaluated cross-sections are available through the online calculator SigmaCalc [1.3].

Although the CRP from 2005 to 2010 met the data needs for EBS and NRA techniques, the data sets available for PIGE remained minimal. There existed a considerable amount of published data on PIGE within the nuclear physics literature, but no current and comprehensive compilation dedicated to IBA purposes. Furthermore, although some PIGE cross-section data had already been uploaded to IBANDL by members of the IBA community, a preliminary survey of the data revealed numerous discrepancies. It was deemed necessary to resolve these discrepancies and add more data sets to those already available, to allow the unfolding of the advantages of the PIGE technique without having to resort to using known 'standards' and further enhance the implementation of 'standardless' PIGE.

In response, a consultant's meeting to assess the situation and propose actions for improving the quality and availability of nuclear cross-section PIGE data was organized. The meeting was held in 2010 [1.4] and resulted in the recommendation of a CRP.

1.2. OBJECTIVE

The IAEA CRP on ‘Development of a Reference Database for Particle-Induced Gamma-ray Emission (PIGE) spectroscopy was subsequently established in 2011 with the overall objective of producing updated and reliable nuclear data for PIGE analysis and making these data freely available to the user community.

1.3. SCOPE

To achieve the overall objective of the CRP, the following areas of work with corresponding deliverables and reports were defined:

1.3.1. Compilation of existing data

- 1) Exhaustive survey of the existing literature to find all the data regarding nuclear reactions with the nuclides deemed the most important for studies using the PIGE technique, i.e., Li, B, Be, ^{12}C , N, F, Na, Mg, Al, Si, P, Cl, S, Ti and Cr.
- 2) Identify discrepancies between measurements and which measurements were missing or needed to be repeated.
- 3) Compilation of retrieved data in IBANDL.
- 4) Deliverables: (i) List of compiled data complete with references and (ii) Updated IBANDL.

1.3.2. New measurements

- 1) New measurements of differential cross-sections and thick target yields of gamma-ray producing reactions listed in Table A.1 of the Appendix at different angles in order to obtain angular distributions of the emitted gamma-rays to establish the isotropy or anisotropy of the reactions studied.
- 2) Deliverables: (i) cross-sections and thick-target yields data files, (ii) Updated IBANDL, (iii) Publications of new measurements in peer-reviewed scientific journals, (iv) Reporting of progress in Research Coordination Meeting (RCM) reports and scientific journals [1.5-1.8].

1.3.3. Co-ordinated Measurements

Perform an inter-laboratory exercise to calibrate equipment and co-ordinate measurements:

- 1) Measurement of the excitation function of the $^{27}\text{Al}(p,p\gamma_{1-0})^{27}\text{Al}$ reaction, which is known to emit a gamma-ray with an energy (E_γ) of 844 keV, at incident energies ranging from 2.5 to 3 MeV at intervals of 10 keV. Since the cross-section of this reaction is known to be isotropic due to spin considerations, the angles of measurements do not matter.
- 2) Measurements of thick target yields using the same targets that are routinely employed for accelerator energy calibration. The aim was to reproduce the resonance of the $^{27}\text{Al}(p,\gamma)^{28}\text{Si}$ reaction at the proton energy of 0.991 MeV by measuring the 1.779 MeV gamma-ray that this reaction is known to produce.

1.3.4. Evaluations of PIGE cross-sections

Evaluation of PIGE cross-sections using the same methodology that was applied to the evaluation of the charged-particle cross-sections in SigmaCalc [1.3].

Deliverables: (i) Evaluated data files for the following reactions $^{27}\text{Al}(p,p'\gamma)^{27}\text{Al}$, $^{23}\text{Na}(p,p'\gamma)^{23}\text{Na}$ and $^{52}\text{Cr}(p,\gamma)^{53}\text{Mn}$ in IBANDL, (ii) Report of evaluation [1.9, 1.10].

1.3.5. PIGE Analysis Code

Development of a PIGE analysis code to calculate all the integral quantities needed in PIGE analyses of bulk samples and also in depth profiling. In particular, the code must be able to calculate the material composition in the case of bulk analysis and the layer composition in the case of depth profiling by using the differential cross-section data and stopping power ranges that are available in the corresponding databases.

Deliverable: PIGE analysis code (ERYA) available on the web including a detailed manual [1.11].

1.4. IBANDL

The final end-product of the CRP is an updated and complete IBANDL. All the new cross-section data and thick target yields compiled and measured during the course of the CRP have been made available in IBANDL. The number of published articles containing PIGE data found during the CRP (2011–2015) on the nuclides listed earlier in is illustrated in Fig. 1.1, while the distribution of new measurements over the nuclides is shown in Fig. 1.2.

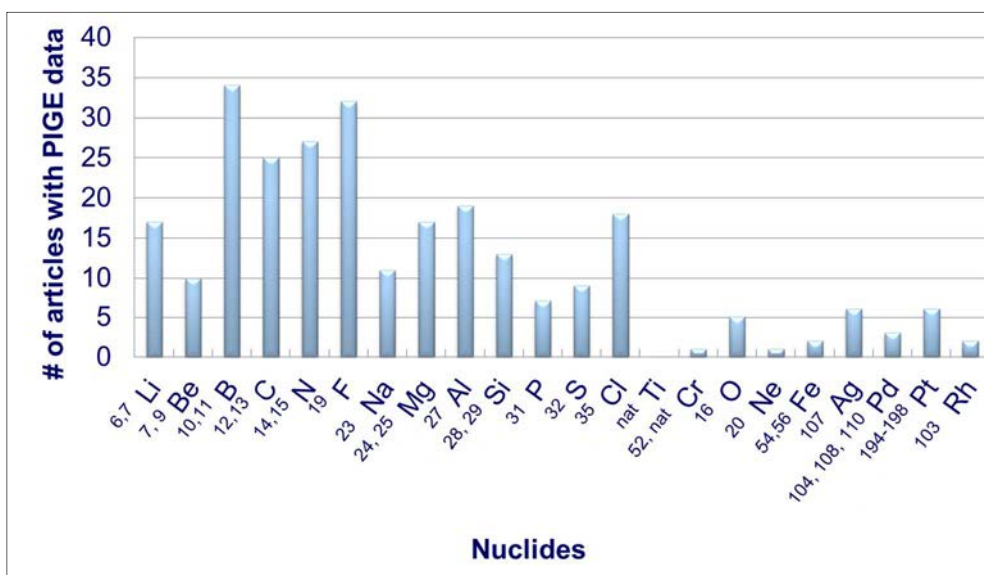


FIG. 1.1. Number of articles with published PIGE data for particular nuclides that were found during the first step of the CRP (2011–2015). All data are available in IBANDL.

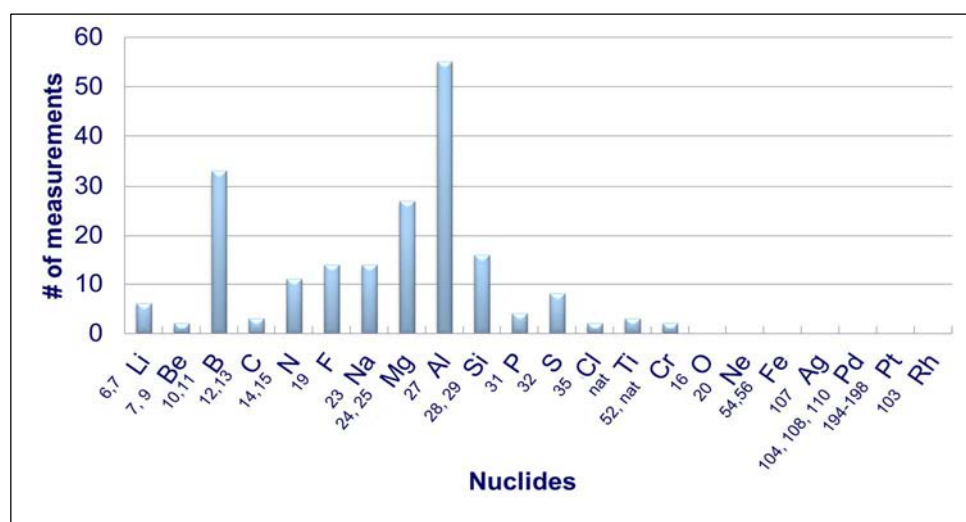


FIG. 1.2. Number of measurements for various nuclides performed during the CRP (2011–2015). All measurements are available in IBANDL

The tremendous expansion of PIGE data sets included in IBANDL is illustrated in Fig. 1.3. Although the majority of the expansion of data occurred during the CRP, some data sets continued to be uploaded to IBANDL continuing through 2016. To date over 600 PIGE data sets have been uploaded.

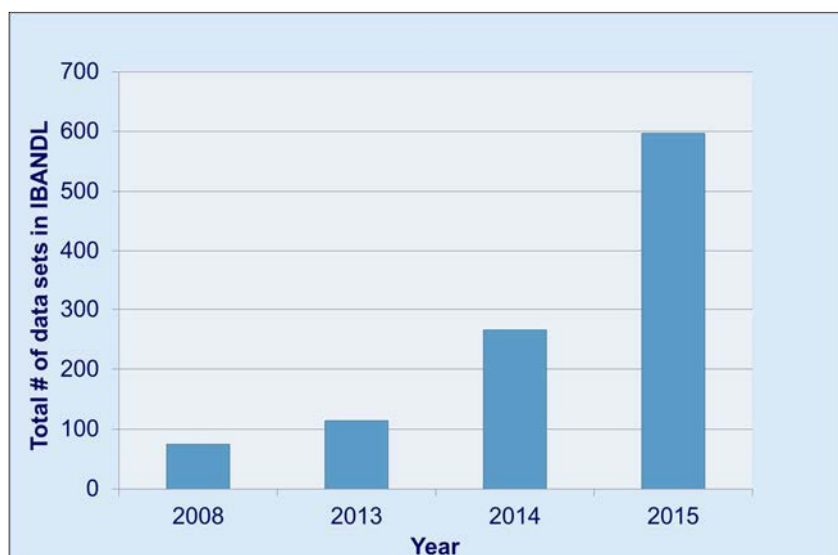


FIG. 1.3. Total number of PIGE data sets in IBANDL before the CRP (2008) in comparison to each consecutive year during the course of the CRP (2013–2015).

In the past decade, the concerted efforts made within the two CRPs, has led to a huge increase of EBS, NRA and PIGE data sets in IBANDL which is illustrated in Fig. 1.4. IBANDL is currently the only online database dedicated to experimental nuclear cross-section data for IBA applications that is comprehensive and continuously up-to-date.

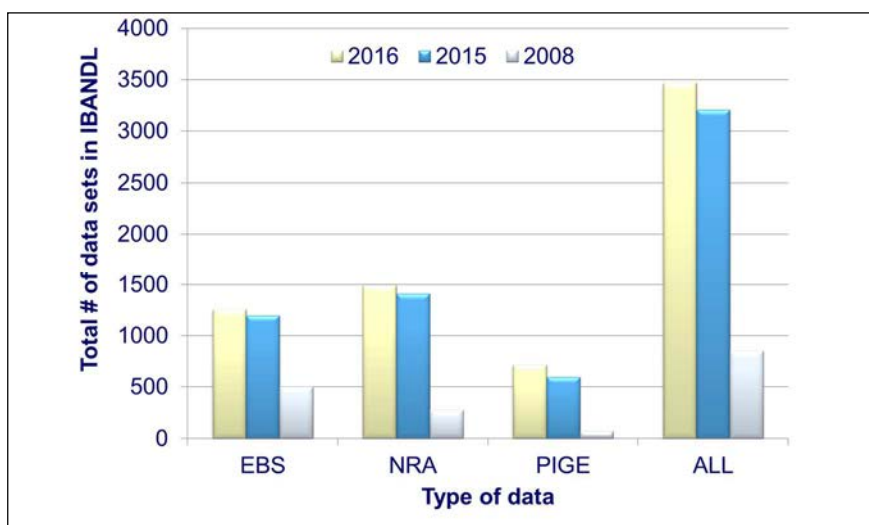


FIG. 1.4. Total number of EBS, NRA and PIGE data sets in the IBANDL database before either CRP (2008) compared to the end of both CRPs (2015) and currently (2016).

1.5. STRUCTURE

Section 2 of the report provides an overview of the concepts and implementation of the PIGE analysis technique, while Section 3 outlines the methodology applied in cross-section and thick-target yield measurements. The data measured during the CRP are presented and assessed in Section 4, and the PIGE analysis code (ERYA) is described in Section 5. Some conclusions are given in Section 6.

REFERENCES TO SECTION 1

- [1.1] INTERNATIONAL ATOMIC ENERGY AGENCY, Development of a Reference Database for Ion Beam Analysis, IAEA-TECDOC-1780, IAEA, Vienna (2015).
- [1.2] Ion Beam Analysis Nuclear Data Library (IBANDL), <http://www-nds.iaea.org/ibandl/>
- [1.3] SigmaCalc Online Calculator, <http://sigmacalc.iate.obninsk.ru/>
- [1.4] ABRIOLA, D., PEDRO DE JESUS, A., Assessment of Nuclear Data Needs for Particle Induced Gamma Ray Emission (PIGE) (Proc. Consultants' Mtg. Vienna, 2010), INDC(NDS)--0568, IAEA, Vienna (2010).
- [1.5] ABRIOLA, D., PEDRO DE JESUS, A., Development of a Reference Database for Particle-induced Gamma Ray Emission (PIGE) Spectroscopy (Proc. 1st Res. Coordination mtg. Vienna, 2011), INDC(NDS)-0589, IAEA, Vienna (2011).
- [1.6] ABRIOLA, D., DIMITRIOU, P., PEDRO DE JESUS, A., Development of a Reference Database for Particle-induced Gamma Ray Emission (PIGE) Spectroscopy (Proc. 2nd Res. Coordination mtg. Vienna, 2012), INDC(NDS)-0625, IAEA, Vienna (2012).
- [1.7] DIMITRIOU, P., PEDRO DE JESUS, A., Development of a Reference Database for Particle-induced Gamma Ray Emission (PIGE) Spectroscopy (Proc. 3rd Res. Coordination mtg. Vienna, 2014), INDC(NDS)-0664, IAEA, Vienna (2014).
- [1.8] DIMITRIOU, P., BECKER, H.-W., BOGDANOVIĆ-RADOVIĆ, I., CHIARI, M., GONCHAROV, A., JESUS, A.P., KAKUEE, O., KISS, A.Z., LAGOYANNIS, A., RÄISÄNEN, J., STRIVAY, D., ZUCCHIATTI, A., Development of a reference database for particle-induced gamma-ray emission spectroscopy, Nucl. Instrum. Methods Phys. Res. B **317** (2016) 33–36.
- [1.9] DIMITRIOU, P. (Ed.), Developments in the Ion Beam Analysis Nuclear Data Library (IBANDL), INDC(NDS)-0660, IAEA, Vienna (2014).
- [1.10] GURBICH, A.F., Evaluation of cross-sections for particle induced gamma-ray emission (PIGE) spectroscopy, Nucl. Instrum. Methods Phys. Res. B **331** (2014) 31–33.
- [1.11] FONSECA, M., JESUS, A.P., LUÍS, H., MATEUS, R., CRUZ, J., GASQUES, L., GALAVIZ, D., RIBEIRO, J.P., PIGE analysis of magnesium and beryllium, Nucl. Instrum. Methods Phys. Res. B **268** 11–12 (2010) 1806–1808.
- [1.12] VICKRIDGE, I.C., Proposed ASCII Format for Communication of Reaction Cross-sections in the IBA Community, DSIR Physical Sciences Report 33, Geological and Nuclear Sciences Ltd, Lower Hutt, (2004).
- [1.13] MAYER, M., SIMNRA: Computer simulation of RBS, ERDA and NRA, Max-Planck-Institut für Plasmaphysik, Garching, <http://home.mpcdf.mpg.de/~mam/>
- [1.14] BARRADAS, N.P., JEYNES, C., Advanced physics and algorithms in the IBA DataFurnace, Nucl. Instrum. Methods Phys. Res. B **266** 8 (2008) 1875–1879.
- [1.15] NDF - General purpose code for data analysis of Ion Beam Analysis Data, http://www.itn.pt/facilities/lfi/ndf/uk_lfi_ndf.htm

2. PIGE CONCEPTS AND IMPLEMENTATION

2.1. PIGE BULK ANALYSIS

The implementation of the PIGE technique began in the 1960s when NaI (TI) detectors were still used [2.1–2.4]. However, the full multi-elemental analytical potential of the technique was only revealed in the 1970s by taking advantage of the high resolution of Ge(HP) detectors [2.5, 2.6]. In 1980, Borderie *et al.* [2.5] introduced the methodology for homogeneous thick samples, i.e. PIGE bulk analysis. Boni *et al.* adapted that methodology for thin target analysis and measured several cross-sections of gamma-emitting reactions [2.7–2.9]. Other efforts to measure and compile useful information, such as cross-sections and thick target yields followed [2.10–2.16]. In the last decade, a standardless methodology for bulk analysis, based on the integration of the pertinent nuclear reaction along the depth of the sample, was developed [2.17–2.22]. Although deuterons have been explored as analyzing beams, most of the work done so far is based on protons.

2.1.1. PIGE bulk analysis

When protons of a few MeV bombard a sample, for some light elements, such as Li, Be, B, F, Na, Mg, Al, the cross-sections of a gamma-producing reaction, such as $(p,\alpha\gamma)$ or $(p,p'\gamma)$ reach the hundreds of millibarns and, consequently, a high yield of characteristic gamma-rays are produced, which may be used to detect and quantify the corresponding isotopes (elements). Since the referred elements are generally not detectable, or can only be quantified with a large degree of uncertainty by PIXE (Particle-Induced X-Ray Emission), PIGE can be used as a complementary analytical technique. The PIXE technique in this case is based on the specific details of the experimental set-up and the employed X-ray detector, which includes variable such as in-vacuum or external-beam set-up, detector entrance window thickness and material. In the following subsections, the basic procedure for a typical PIGE bulk analysis is discussed.

2.1.2. Production and acquisition of gamma-ray spectra

Instrumentation for PIGE measurements is, in principle, very similar to the one used for PIXE, with the exception of the radiation detector, which must have a full energy peak intrinsic efficiency that is suited for detecting radiation in the range above 100 keV. In comparison, X-rays are in the range of a few to tens of keV. Therefore, the following experimental conditions must be met:

- (a) Accelerator (1–3 MV terminal voltage) — which together with the associated electromagnetic beam transport system must assure a very good definition of energy (a resolution of 1 keV or less);
- (b) Reaction chamber — with a 10^{-6} mbar or better vacuum produced by, preferably, free-oil pumps, in order to avoid the deposition of carbon films on the sample. PIGE bulk analysis can also be easily and proficiently performed in external beam or ambient pressure set-ups, which reduces the risk to the samples in terms of charging, heating and carbon build-up effects;

- (c) Beam charge collection system — with implemented conditions to avoid the loss of secondary electrons sputtered from the target, if analysis is done in vacuum, and to measure the correct value of the beam charge;
- (d) Target holder — with multi-target capacity and degrees of freedom that allow changing between the samples and the ability to tilt them with respect to the incoming beam direction, if necessary;
- (e) Gamma-ray detector — for multi-elemental analysis, HPGe or Ge(Li) detectors with a few keV energy resolution must be used. For standard free analysis, this detector must be calibrated in efficiency by radioactive sources certified in activity and/or by Monte-Carlo simulations (codes Geant, Penelope).

More details about a typical set-up are given in Section 2.3.

The definition of the beam energy is complete only after performing a thorough accelerator energy calibration. For very stable Cockroft and Walton type accelerators, the high voltage terminal values may be calibrated. Another choice is the calibration of the magnetic fields of the analyzing magnets, measured by Nuclear Magnetic Resonance (NMR) probes. In either case, nuclear reaction resonances provide the beam energy values. Several resonances have been employed for this purpose. In Appendix 19 of the Handbook of Modern Ion Beam Materials Analysis, a description of calibration methods and a table of resonances can be found [2.23]. More alternatives are described in Section 3.2.

Care should be taken when using resonance energies from the literature. For strong, isolated resonances like the one for $^{27}\text{Al}(p,\gamma)^{28}\text{Si}$ at 991.6 keV, the proton energy value corresponding to half-the-height of a thick (compared to the width of the resonance) target yield curve gives the correct value of the resonance energy. For other resonances, thin target resonances may be preferable, but one should note that the experimental maximum of the resonance may deviate from the tabulated resonance energy, E_R , due to the target thickness. Where ΔE is the target thickness and Γ is the natural width of the resonance: for $\Delta E \ll \Gamma$, the maximum corresponds to E_R ; for $\Delta E \gg \Gamma$ the maximum corresponds to $E_R + \Delta E/2$; for other intermediate situations, intermediate values between E_R and $E_R + \Delta E/2$ are used.

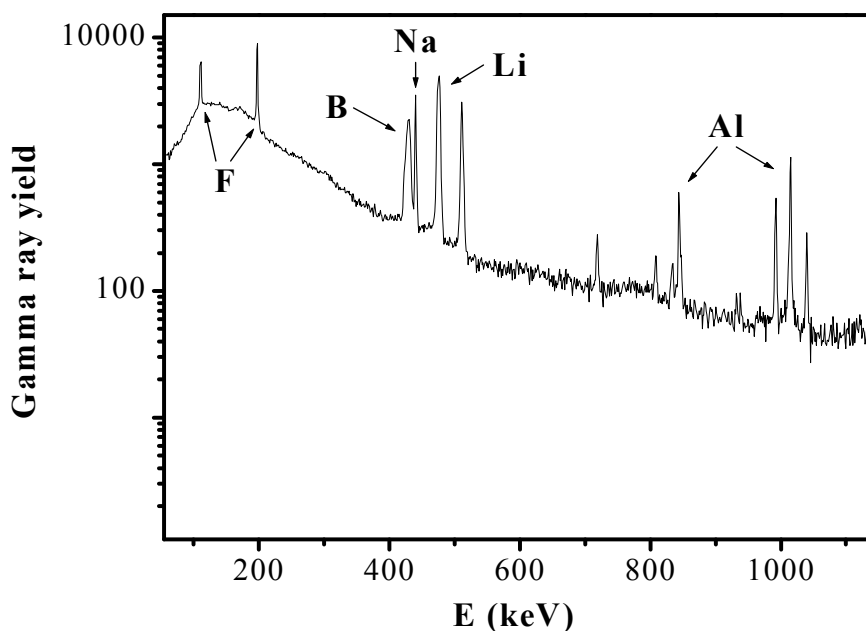


FIG. 2.1. Gamma-ray spectrum from a mineral sample containing fluorine, boron, sodium, lithium and aluminium. It is represented in logarithmic scale to enhance the continuum background from Compton interactions of the radiation with the detector.

Table 2.1 summarizes some of the gamma-ray lines which may be used for PIGE analysis, for different light isotopes (mass $A < 40$). These may be easily separated by high resolution detection as illustrated in Fig. 2.1. It can also be observed that these lines are sitting on a continuum produced by Compton interactions in the detector. Although some of the background originates from environmental and cosmic radiation, most of it is due to prompt gamma radiation from the beam bombarding the target or from the interaction of the beam with collimators or other parts of the measurement set-up. Hence, the continuum background is mostly dependent on the composition of the target and also on the specific experimental set-up. This implies that it is not possible to define general sensitivity limits [2.24]. For example, the $^{19}\text{F}(p,\alpha\gamma)^{16}\text{O}$ reaction, which has the highest cross-section of all nuclear reactions, produces high-energy gamma-rays ($\sim 6\text{--}7$ MeV), which contribute to the continuum Compton background. The presence of fluorine in a sample is thus a factor that limits the sensitivity of the detection of the other elements. The best sensitivity values that can be attained are of the order of $\mu\text{g/g}$ for fluorine, lithium and sodium at energies equal to or higher than 2.4 Me

TABLE 2.1. PIGE REACTIONS ON LIGHT NUCLEI AND CORRESPONDING GAMMA-RAY ENERGIES

| E_γ (keV) | Reaction | Isotopic abundance (%) |
|------------------|---|------------------------|
| 429* | ${}^7\text{Li}(p, n\gamma){}^7\text{Be}$ | 93 |
| 478 | ${}^7\text{Li}(p, p\gamma){}^7\text{Li}$ | |
| 429* | ${}^{10}\text{B}(p, \alpha\gamma){}^7\text{Be}$ | 19 |
| 718 | ${}^{10}\text{B}(p, p\gamma){}^{10}\text{B}$ | |
| 2125 | ${}^{11}\text{B}(p, p\gamma){}^{11}\text{B}$ | 81 |
| 110 | ${}^{19}\text{F}(p, p\gamma){}^{19}\text{F}$ | 100 |
| 197 | ${}^{19}\text{F}(p, p\gamma){}^{19}\text{F}$ | |
| 1236 | ${}^{19}\text{F}(p, p\gamma){}^{19}\text{F}$ | |
| 1349 | ${}^{19}\text{F}(p, p\gamma){}^{19}\text{F}$ | |
| 1357 | ${}^{19}\text{F}(p, p\gamma){}^{19}\text{F}$ | |
| 1459 | ${}^{19}\text{F}(p, p\gamma){}^{19}\text{F}$ | |
| 6129 | ${}^{19}\text{F}(p, \alpha\gamma){}^{16}\text{O}$ | |
| 390 | ${}^{25}\text{Mg}(p, p\gamma){}^{25}\text{Mg}$ | 10.1 |
| 417 | ${}^{25}\text{Mg}(p, \gamma){}^{26}\text{Al}$ | |
| 452 | ${}^{24}\text{Mg}(p, \gamma){}^{25}\text{Al}$ | 78.7 |
| 585 | ${}^{25}\text{Mg}(p, p\gamma){}^{25}\text{Mg}$ | |
| 844* | ${}^{26}\text{Mg}(p, \gamma){}^{27}\text{Al}$ | 11.3 |
| 975 | ${}^{25}\text{Mg}(p, p\gamma){}^{25}\text{Mg}$ | |
| 990 | ${}^{25}\text{Mg}(p, p\gamma){}^{25}\text{Mg}$ | |
| 1014* | ${}^{26}\text{Mg}(p, \gamma){}^{27}\text{Al}$ | |
| 1369* | ${}^{24}\text{Mg}(p, p\gamma){}^{24}\text{Mg}$ | |

TABLE 2.1. PIGE REACTIONS ON LIGHT NUCLEI AND CORRESPONDING GAMMA-RAY ENERGIES (cont.)

| E_γ (keV) | Reaction | Isotopic abundance (%) |
|------------------|---|------------------------|
| 1380 | $^{25}\text{Mg}(p,p\gamma)^{25}\text{Mg}$ | |
| 1612 | $^{25}\text{Mg}(p,p\gamma)^{25}\text{Mg}$ | |
| 1809 | $^{26}\text{Mg}(p,p\gamma)^{26}\text{Mg}$ | |
| 1965 | $^{25}\text{Mg}(p,p\gamma)^{25}\text{Mg}$ | |
| 390 | $^{25}\text{Mg}(p,p\gamma)^{25}\text{Mg}$ | 10.1 |
| 171 | $^{27}\text{Al}(p, p\gamma)^{27}\text{Al}$ | |
| 844* | $^{27}\text{Al}(p, p\gamma)^{27}\text{Al}$ | |
| 1014* | $^{27}\text{Al}(p, p\gamma)^{27}\text{Al}$ | 100 |
| 1369* | $^{27}\text{Al}(p, \alpha\gamma)^{24}\text{Mg}$ | |
| 1720 | $^{27}\text{Al}(p, p\gamma)^{27}\text{Al}$ | |
| 1779 | $^{27}\text{Al}(p, \gamma)^{28}\text{Si}$ | |
| 2211 | $^{27}\text{Al}(p, p\gamma)^{27}\text{Al}$ | |
| 2734 | $^{27}\text{Al}(p, p\gamma)^{27}\text{Al}$ | |
| 2839 | $^{27}\text{Al}(p, \gamma)^{28}\text{Si}$ | |
| 755 | $^{29}\text{Si}(p, p\gamma)^{29}\text{Si}$ | 4.71 |
| 1266* | $^{30}\text{Si}(p, \gamma)^{31}\text{P}$ | 3.12 |
| 1273 | $^{29}\text{Si}(p, p\gamma)^{29}\text{Si}$ | |
| 1779* | $^{28}\text{Si}(p, p\gamma)^{28}\text{Si}$ | 92.2 |
| 2028 | $^{29}\text{Si}(p, p\gamma)^{29}\text{Si}$ | |
| 440 | $^{23}\text{Na}(p,p\gamma)^{23}\text{Na}$ | 100 |
| 1369 | $^{23}\text{Na}(p, \gamma)^{24}\text{Mg}$ | |
| 1634 | $^{23}\text{Na}(p, \alpha\gamma)^{20}\text{Ne}$ | |
| 1636 | $^{23}\text{Na}(p,p\gamma)^{23}\text{Na}$ | |
| 1951 | $^{23}\text{Na}(p,p\gamma)^{23}\text{Na}$ | |

TABLE 2.1. PIGE REACTIONS ON LIGHT NUCLEI AND CORRESPONDING GAMMA-RAY ENERGIES (cont.)

| E_γ (keV) | Reaction | Isotopic abundance (%) |
|------------------|--|------------------------|
| 2391 | $^{23}\text{Na}(p,p\gamma)^{23}\text{Na}$ | |
| 440 | $^{23}\text{Na}(p,p\gamma)^{23}\text{Na}$ | 100 |
| 1369 | $^{23}\text{Na}(p,\gamma)^{24}\text{Mg}$ | |
| 1634 | $^{23}\text{Na}(p,\alpha\gamma)^{20}\text{Ne}$ | |
| 1636 | $^{23}\text{Na}(p,p\gamma)^{23}\text{Na}$ | |
| 1951 | $^{23}\text{Na}(p,p\gamma)^{23}\text{Na}$ | |
| 2391 | $^{23}\text{Na}(p,p\gamma)^{23}\text{Na}$ | |
| 440 | $^{23}\text{Na}(p,p\gamma)^{23}\text{Na}$ | 100 |
| 1266* | $^{31}\text{P}(p,p\gamma)^{31}\text{P}$ | 100 |
| 1779* | $^{31}\text{P}(p,\alpha\gamma)^{28}\text{Si}$ | |
| 2230 | $^{31}\text{P}(p,\gamma)^{32}\text{S}$ | |
| 2233 | $^{31}\text{P}(p,p\gamma)^{31}\text{P}$ | |
| 1266* | $^{31}\text{P}(p,p\gamma)^{31}\text{P}$ | 100 |
| 1779* | $^{31}\text{P}(p,\alpha\gamma)^{28}\text{Si}$ | |
| 2230 | $^{31}\text{P}(p,\gamma)^{32}\text{S}$ | |
| 2233 | $^{30}\text{Si}(p,\gamma)^{31}\text{P}$ | |
| 2235 | $^{30}\text{Si}(p,p\gamma)^{30}\text{Si}$ | |

* γ -rays emitted by more than one reaction

2.1.3. Determination of isotopic/elemental concentrations

For a thin target, where the cross-sections and stopping-power can be assumed to be constant, the yield of gamma-rays with energy E_γ , detected at a given ion beam energy E depends on the number of bombarding ions Q/e (Q being the collected charge and e the charge state of the ion beam), the number of nuclei of the relevant isotope per surface unit N_{iA} , the relevant nuclear reaction cross-section σ (which may be dependent on the detection angle) and the detection absolute efficiency ε_{abs} . For an isotropic gamma-line the yield may be written as:

$$Y(E) = \varepsilon_{abs}(E_\gamma) \cdot \left(\frac{Q}{e}\right) \cdot \sigma(E) \cdot N_{iA} = \varepsilon_{abs}(E_\gamma) \cdot \left(\frac{Q}{e}\right) \cdot \sigma(E) \cdot N_i \cdot \Delta x \quad (2.1)$$

where N_i is the number of nuclei of the relevant isotope per volume unit and Δx is the target linear thickness.

For a thick target, where by definition the thickness is greater than the range of the bombarding ions, the above equation still applies, but for each thin layer that is parallel to the target surface (for normal incidence), as is illustrated in Fig. 2.2.

For each layer of linear thickness dx or mass thickness (mass per surface unit) $d\Gamma$, a similar equation may be written in terms of the relevant element mass fraction f_m :

$$dY(E) = \varepsilon_{abs}(E_\gamma) \cdot \left(\frac{Q}{e}\right) \cdot \sigma(E) \cdot f_m \cdot f_i \cdot N_{av} \cdot A^{-1} \cdot d\Gamma \quad (2.2)$$

where f_i is the isotopic abundance, N_{av} is the Avogadro number and A is the atomic mass of the relevant element.

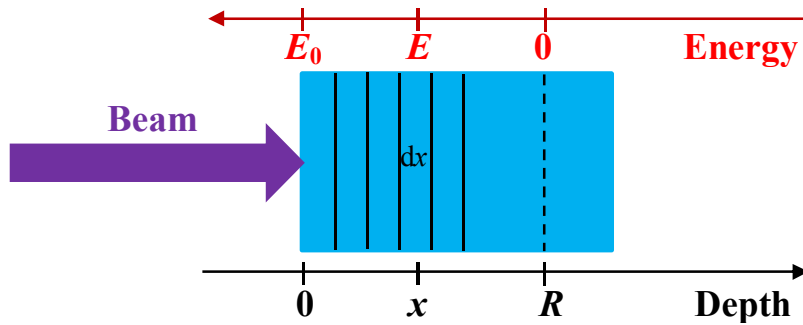


FIG. 2.2. Division of a thick target in layers and relation between depth and energy dimensions.

The thick-target yield is the result of integrating the above equation over the range of the incident ions in the target, R :

$$Y(E) = \varepsilon_{abs}(E_\gamma) \cdot \left(\frac{Q}{e}\right) \cdot f_m \cdot f_i \cdot N_{av} \cdot A^{-1} \cdot \int_0^R \sigma(\Gamma) d\Gamma \quad (2.3)$$

or

$$Y(E) = \varepsilon_{\text{abs}}(E_\gamma) \cdot \left(\frac{Q}{e} \right) \cdot f_m \cdot f_i \cdot N_{\text{av}} \cdot A^{-1} \cdot \int_0^{E_0} \sigma(E) / S_m(E) dE , \quad (2.4)$$

where E_0 is the incident energy of the beam and $S_m(E)$ represents the mass stopping power expressed in energy per areal mass units, which describes the influence of the sample composition over the incident beam. This is a similar expression to the one used for PIXE, except for the presence of the isotopic abundance term, which is needed only for PIGE, and the absence of the term for the transmission of radiation through the target, which is only needed for PIXE. The self-absorption effect for gamma-rays produced by proton bombardment of a thick-target sample is indeed negligible.

There are currently two approaches used to determine the mass fractions of the elements in a sample: the standard-based method and the standardless method.

2.1.4. The standard-based method

If one assumes that, in a first approximation, the stopping power is not energy dependent, the integration in Eq. 2.4 is performed over the cross-section only and is therefore independent of the target composition. This first approximation has been used for PIGE analysis based on comparison with a standard sample. When irradiating the sample and a standard under the same experimental conditions, the ratio of the mass fraction f_m between an individual light element in sample i and a standard st is given by:

$$\frac{f_m^i}{f_m^{st}} = \frac{S_m^i(E_{1/2})}{S_m^{st}(E_{1/2})} \cdot \frac{Y^i}{Y^{st}} , \quad (2.5)$$

where S_m and Y are the corresponding mass stopping powers and yields of detected gamma-rays and $E_{1/2}$ is the beam energy for which the gamma-ray yield is half of the one obtained at incident beam energy. A similar expression is valid for atomic fractions, if atomic stopping powers (in energy per areal atomic density) are used.

This standard-based method has some drawbacks:

- (i) It depends on the availability of standards, which should be as similar in composition to the samples as possible (see below);
- (ii) The exact major compositions of the standard and the sample must be known, in order to calculate the stopping powers with low uncertainty;
- (iii) The half energy $E_{1/2}$ must be known. If the major compositions of the sample and standard are not similar, $E_{1/2}$ for the sample is not equal to $E_{1/2}$ for the standard. Thick-target yields obtained before and during this CRP, now available in IBANDL, may be helpful.

2.1.5. The standardless method

In order to avoid standards, one may use Eq. 2.4 and perform the calculations. Similar to PIXE, the integral in Eq. 2.4 can be calculated. It is, in principle, easier than for PIXE, because the radiation transmission for PIGE in the sample is constant and equal to one (it is a self-absorption free technique), but for many years it seemed to be more difficult, due to the cross-section function (or excitation function).

For PIXE, the cross-section is a smooth function of the beam energy and it may be determined from theoretical calculations (e.g. Energy-Loss Coulomb-Repulsion Perturbed-Stationary State Relativistic Theory (CPSSR) for inner shell ionization) or from polynomial fits to experimental data. For PIGE, the nuclear reaction excitation functions may have several thin and broad resonances, which hinder this analytical approach. However, if cross-sections are available in numerical form, with resonances defined in detail, the energy steps used for the cross-section measurements may be used to define the layers that are necessary for the subdivision of the target in thin layers and, furthermore, the integral may be calculated as a sum of terms corresponding to these layers (Fig. 2.2):

$$\int_0^{E_0} \sigma(E)/\varepsilon(E) dE = \sum_k \left[(I/S_{mk}) \cdot \int_{E_k}^{E_{k+1}} \sigma(E) dE \right] = \sum_k \left[(I/S_{mk}) \cdot \sigma(E_{k,k+1}) \cdot (E_{k+1} - E_k) \right], \quad (2.6)$$

where the cross-section for each layer k is the mean between σ_k and σ_{k+1} , i.e. the measured cross-sections at energies E_k and E_{k+1} . As the integrated cross-section rises quickly with the proton energy, it is not necessary to go down to zero energy, but only to the minimum energy used for the cross-section measurement, E_{\min} .

When performing PIGE analysis using the standardless method based on Eq. 2.4, with the integral calculated by Eq. 2.6, one has to be aware of the value of the E_{\min} in order to choose a beam energy E_0 for which the yield is much larger than Y_{\min} . If this is not possible, Y_{\min} cannot be neglected and should be measured for the sample to be analysed and added up to the calculated yield. When choosing the incident energy, it is important to avoid the resonances. The choice of bombarding energy between resonances reduces the effect in the final results of the uncertainty and/or deviations of the ion beam energy.

The propagation of the uncertainties of the cross-section values, the absolute value of the collected charge, the detector efficiency and the stopping powers leads to an uncertainty of the determined mass fractions which may be larger than 20%. However, this may be reduced if calibrations are performed (as is typically done for standardless PIXE). The calibration consists of the following procedure.

For each light element to be analysed, a comparison is made between the measured gamma-ray yield and the calculated gamma-ray yield for either (i) a pellet made of a pure inorganic compound that contains the element to be analysed or (ii) a standard reference sample. The ratio of the experimental to calculated yield is then used as an external calibration factor (or correction factor) in future analyses of the given element, provided the same experimental conditions (e.g. ion beam, detector type and detector geometry) are used and also that the same excitation function is used in the calculations. In order to confirm the stability of the experimental conditions (mainly of the charge measurement), one might use a lithium or a boron standard sample (the cross-sections related to ${}^7\text{Li}(p,p'\gamma){}^7\text{Li}$ and ${}^{10}\text{B}(p,p'\gamma){}^{10}\text{B}$ reactions are smooth) and measure its yield before each analytical running time. Repeatability and reproductibility tests should be performed to estimate the uncertainties to be assigned to the analytical procedure. By applying a careful calibration procedure in conjunction with a good knowledge of the major elements' composition of the samples to be analysed, the uncertainties may be lowered down to 5–7%, which is currently the average uncertainty of the stopping powers. In other words, the analytical procedure is dominated by the uncertainties of the stopping powers.

This method is also valid for semi-thick targets, meaning targets inducing a proton energy loss that is not negligible, but with a thickness smaller than the range of protons in the target. In this case, instead of extending the sum in Eq. 2.6 to E_{\min} , one sums down to E_f , the energy with which protons emerge from the target. For a thin target of mass thickness equal to $\Delta\Gamma$, an expression equivalent to Eq. 2.4 applies:

$$Y(E_0) = \varepsilon_{abs}(E_\gamma) \cdot \left(\frac{Q}{e} \right) \cdot \sigma(E_0) \cdot f_m \cdot f_i \cdot N_{av} \cdot A^{-1} \cdot \Delta\Gamma, \quad (2.7)$$

where E_0 is the incident proton energy.

When dealing with semi-thick or thin samples, attention must be paid to the position of the sample with respect to the beam. The angle θ , which is subtended by the normal both to the sample surface and to the beam, will increase the sample thickness by $1/\cos\theta$ (in comparison with the normal position). The uncertainty in this angle will propagate into the uncertainty of the final mass fraction results.

A code that is developed to calculate the mass fraction from the experimental yields may also include a fitting procedure to optimize the sample composition (major and minor elements/isotopes) by modifying the first guess introduced by the user. This can be done simultaneously for all light elements present in the sample (see Section 5 for more details about the ERYA code).

Hence, the standardless method, where standard samples are not required for routine analysis, also has the possibility to adjust and improve the major composition of the sample, which is often not completely known.

This method may also be applied to multi-layered samples. If the element to be analysed is only present in one layer, E_0 is simply replaced by the proton energy at the entrance of that layer. However, if the element is present in more than one layer, the information obtained from the code corresponds to the averaged concentration.

2.2. PIGE DEPTH PROFILING WITH NUCLEAR RESONANCES

As described above in Section 2.1, for the analysis of bulk PIGE measurements, the number of emitted gamma-rays is proportional to the integral of the cross-section from zero to the incident beam energy (Eq. 2.4). In cases where layers are to be investigated, this integral has to be calculated from the energy given by the energy loss at the end of the layer up to the energy of the beam at the entrance of the layer. Since the emitted gamma-ray carries no information about the depth from which it originated from, the method is not depth sensitive. However, since the cross-section for the reaction might vary strongly with incident energy, the sensitivity to the reaction for a given isotope can also vary with depth. By exploiting the energy dependence of the cross-section, it is possible to obtain moderate depth information when a sample is investigated with different beam energies [2.25]. A more refined method, called depth profiling, is described in the following.

Depth profiling with resonances in particle-induced gamma-ray emitting reactions makes use of those resonances in the reaction cross-section where the cross-section is significantly stronger than in the (non-resonant) region above and below the resonance energy. In almost all cases of PIGE depth profiling, the incident beam is a proton beam, but for the depth

profiling of hydrogen, heavier beams such as ^{15}N , ^{18}O or ^{19}F beams are used in the inverse kinematics. In an ideal case, a resonance should be very strong and narrow, so that the contributions to the reaction are limited to a narrow energy region.

Depth profiling is performed by measuring the gamma-yield of the reaction as a function of the beam energy. When starting with energies near the resonance energy, the concentration of an isotope is probed only at the surface of the sample, since the beam loses energy while penetrating into the sample due to the electronic stopping and therefore the corresponding cross-section lies in the region of low cross-section beyond the resonance. By increasing the beam energy sequentially above the resonance energy, the beam energy will reach the resonance energy at a certain depth, after losing energy due to electronic stopping. In visual terms, the resonance window, i.e. the window of energy where the crossing of the ion beam through the sample is most sensitive to the nuclear reaction is ‘shifted’ to different depths in the sample. Thus a depth profile is obtained by scanning a given energy range with the accelerator and measuring the gamma-yield at each energy. The principle is illustrated in Fig. 2.3 for the case of the $^1\text{H}(^{15}\text{N},\alpha\gamma)^{12}\text{C}$ reaction with a well-known resonance at 6.4 MeV. These measurements are more time consuming than a simple PIGE measurement at one beam energy.

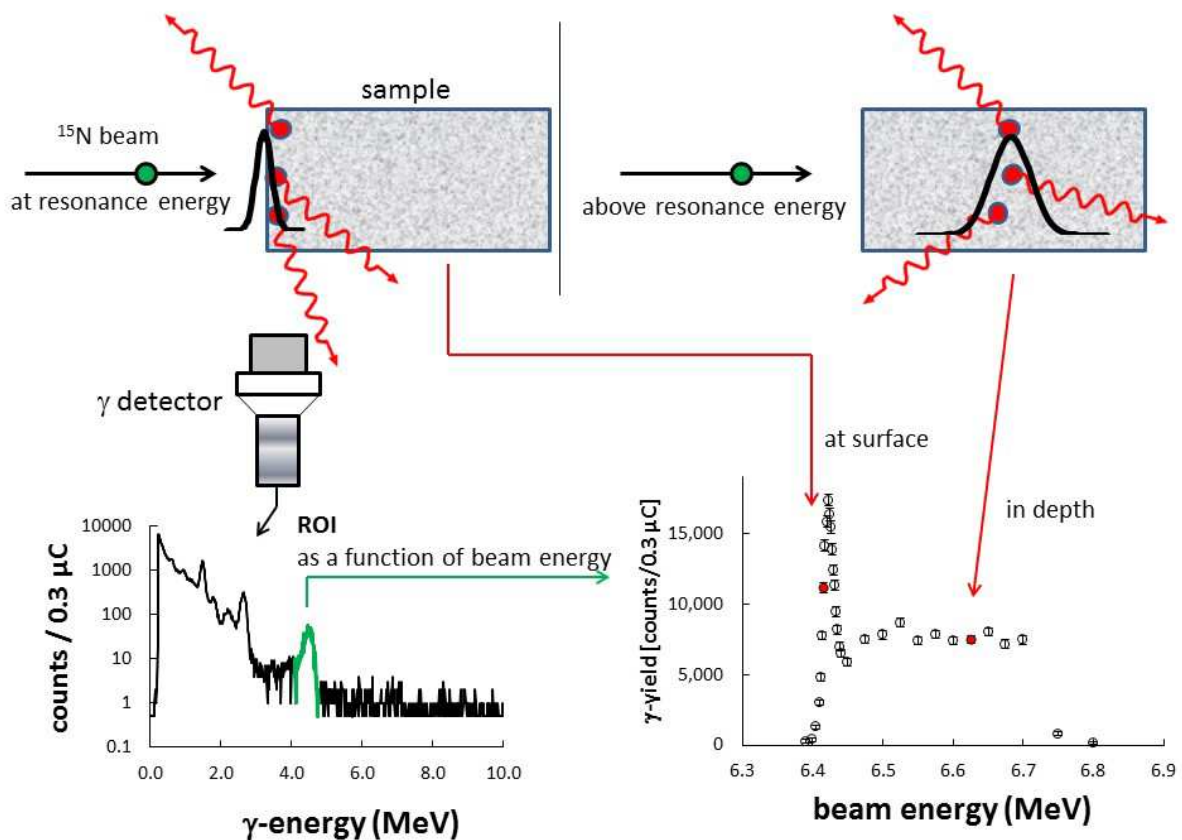


FIG. 2.3. Principle of depth profiling. Reproduced courtesy of Springer [2.44].

In the following, the basic principles of the analysis of depth profiles are outlined. More details and special cases are discussed in [2.23].

In order to convert the gamma-yield measured at a given energy into a concentration, the integral of the cross-section over the resonance needs to be calculated. This integral is essentially equal to the product of the width of the resonance and the cross-section at the maximum. The energy dependence of a resonance cross-section is given by the Breit-Wigner formula (in units of area such as barn):

$$\sigma_{ab}(E) = \frac{\pi \cdot \omega \cdot \lambda^2 \cdot \Gamma_a \Gamma_b}{(E - E_R)^2 + \frac{\Gamma^2}{4}}, \quad (2.8)$$

where a and b denote the incoming and outgoing reaction channels, E_R is the resonance energy, ω is a statistical factor calculated from the spins of the involved nuclear states, Γ_a and Γ_b are the partial widths, Γ is the total width of the resonance and λ is the De-Broglie wavelength of the incoming particle. A resonance can be characterized, apart from the resonance energy, by either the maximal cross-section at the resonance energy E_R or the total width Γ or the resonance strength S , which is defined (in units of energy) as:

$$S = (2J + 1) \frac{\Gamma_a \Gamma_b}{\Gamma}, \quad (2.9)$$

where J is the spin of the resonance state. The quantity S is the only way possible to quantify a resonance in cases where the resonance width is too small for a direct cross-section measurement. S is, in these cases, determined from an integral measurement over the resonance, which corresponds to a step function in a yield curve. For details see [2.23].

The method of converting the measured yield into a concentration profile is dependent on the resonance width, the energy resolution of the beam and the energy straggling of the beam and involves the integration of these parameters over the energy. This can be done by analysis codes such as the ERYA code (see Section 5). For cases where the resonance is very narrow, the beam energy is spread out and the straggling is negligible, the ratio R of the probed atoms to the total number of atoms in the sample at a beam energy E can be calculated as:

$$R(E) = Y(E) \cdot \frac{1}{S \cdot \eta \cdot \Delta\Omega} \cdot \varepsilon, \quad (2.10)$$

where $Y(E)$ is the gamma-yield, i.e. the number of γ -rays per incident beam ion, measured in a detector, η and $\Delta\Omega$ are the efficiency and the solid angle of the detector, respectively, and ε is the stopping cross-section of the beam ions in the sample at the resonance energy. When the emitted gamma-radiation is not isotropic but rather has an angular distribution, this must also be taken into account.

The depth information is obtained from the difference between the resonance energy and the beam energy at which the gamma-yield is measured, i.e. it is given as an energy loss. The energy loss can be simply converted to atoms/cm² or to nm (if the density of the sample is known) by using the stopping power of the beam in the sample; therefore, the sample bulk composition must be known or measured.

The depth resolution of the method does not depend on the detector resolution, but is primarily defined by the width of the resonance and can be, in theory, in the nm range or

below. In practice, however, other effects such as the beam energy resolution or the Doppler broadening, which is caused by the thermal motion of the target atoms, can limit the resolution that is attainable in an experiment.

The energy resolution of low-energy accelerators is typically in the range of 100 eV to 1 keV. To exploit the full potential of narrow resonance depth profiling, even better beam resolutions are required [2.26].

The Doppler broadening can be calculated by:

$$\Delta E_D = 4 \sqrt{\frac{\ln 2MEk_B T}{m}}, \quad (2.11)$$

where E is the energy of the beam, k_B the Boltzmann constant, T the temperature, M the mass of the beam ion and m the mass of the sample atom.

In addition, for measurements made deeper within a sample, the energy resolution can deteriorate due to the energy straggling of the beam. This can be estimated by:

$$\Delta E_S = 1.2 \cdot \sqrt{Z_1^2 Z_2 N}, \quad (2.12)$$

where the straggling ΔE_S is given in keV, the depth at which a concentration is measured, N is given in 10^{18} atoms/cm², Z_1 is the atomic number of the projectile and Z_2 is the atomic number of the sample atoms.

The beam energy distribution, the Doppler broadening and the straggling can all be assumed to be Gaussian and can therefore be added quadratically. The resonance width has to be added numerically since the shape of a resonance is a Lorentzian curve. The total experimental energy resolution ΔE_{exp} can be converted to depth resolution ΔX by:

$$\Delta X = \frac{\Delta E_{\text{exp}}}{\varepsilon}, \quad (2.13)$$

where ε is the stopping power of the beam in the sample. Resonances suitable for depth profiling can be found for light nuclei in the mass region up to phosphorus at low beam energies (below 3 MeV); in fact, almost all light elements have at least one isotope with a low energy resonance suitable for depth profiling. One prominent example is the 0.43 MeV resonance of the $^{15}\text{N}(p,\alpha\gamma)^{12}\text{C}$ reaction, which can be used to detect nitrogen in a sample and which is often used in inverse kinematics to probe hydrogen with an ^{15}N beam. A comprehensive list of resonances used for depth profiling in material science can be found in [2.23], where either the cross-sections at maximum and the width or the resonance strength are tabulated. The energy of the emitted γ -ray is also given in these tables.

Since nuclear reactions can have several resonances, it is to the advantage of the user, when planning a depth profiling analysis, to find a case where only one resonance contributes to a depth profile. This is illustrated for the $^{27}\text{Al}(p,\gamma)^{28}\text{Si}$ reaction in Fig. 2.4. Similar data for other reactions can be found in Section 4 or in the IBANDL data base. For profiling aluminium, the resonance at 0.992 MeV is the strongest and has a small width. Therefore, it is preferred for better sensitivity and depth resolution.

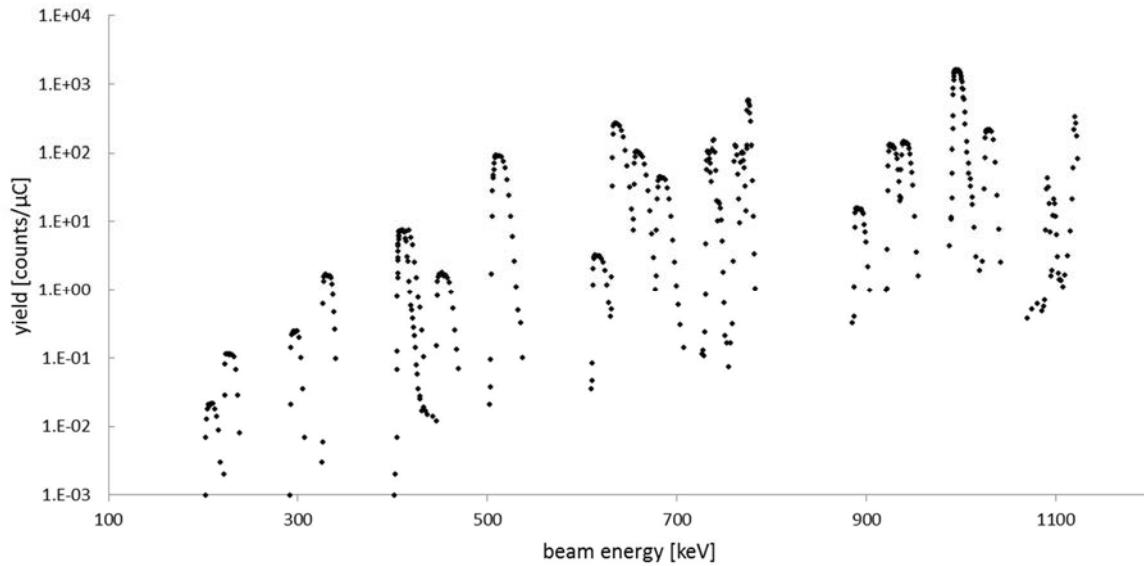


FIG. 2.4. Yield curve of the $^{27}\text{Al}(p,\gamma)^{28}\text{Si}$ reaction as a function of beam energy [2.27].

The next resonance at higher energies lies at $E = 1.002$ MeV (seen in Fig. 2.4 as a shoulder of the 0.992 MeV resonance only), fairly close to the 0.992 MeV resonance, which limits the energy scan for the 0.992 MeV resonance to a range of 10 keV. This would correspond, for example, in Si to a depth of around 250 nm.

The next resonance below the 0.992 MeV is at 0.937 MeV. If the layer under investigation is so thick that a proton beam would lose more than the difference of 55 keV (for silicon that would correspond to 1.4 μm), then this resonance would influence the depth profile. If the layer is infinitely thick, all lower resonances lying below 0.992 MeV would contribute to the depth profiling. The deconvolution of a depth profile that is influenced by more than one resonance is, in theory, possible, for example by employing the ERYA code, but at the cost of accuracy. In such cases, it is often better to choose a resonance at low energy. Resonances at low energies are generally favourable because the background is usually lower and the higher stopping power leads to a better depth resolution.

2.3. A TYPICAL MINIMAL PIGE FACILITY

In this section, practical instrumental aspects that need to be addressed in the analytical application of PIGE, but which are also essential, with different constraints, for the measurement of gamma-ray production cross-sections are presented.

The most common case is for a thick sample to be analysed by proton induced gamma-ray emission. The mass fraction of the element to be analysed f_m (Eq. 2.2) depends on the gamma-production cross-section and the material stopping power, both normally tabulated as a function of energy. It also depends on experimental and instrumental quantities, which include the beam energy (determined by the accelerator beam), the collected charge (also determined by the accelerator beam), the detector absolute efficiency (determined by the available detector) and the photon yield of the reaction channel used for detecting the analyte (also determined by the available detector). Therefore, to perform a PIGE analysis, the essential set-up would include:

- (a) A particle accelerator;
- (b) A charge collection and measuring system;
- (c) A gamma-ray detector (and associated electronics and data acquisition system).

Considering that a PIGE analysis facility may be required to analyze several samples in a row, maintaining the background level as low as possible throughout these measurements is essential. Therefore, it is highly recommended to expand the above-mentioned minimal system by adding two more components:

- (i) A beam defining system free of light elements (e.g. Al) that might create background gamma-radiation (full energy or Compton), associated with a reaction chamber in vacuum. Such a system, ideal for cross-section measurements, is quite convenient if small, non-volatile, temperature resistant samples have to be analysed;
- (ii) A remotely controlled sample holder.

Items a), b), and c) are elaborated in the following sub-sections.

2.3.1. Particle accelerator

Electrostatic accelerators are the type of accelerators generally adopted in IBA. The reader is referred to the IAEA Accelerator knowledge portal (<https://nucleus.iaea.org/sites/accelerators/Pages/default.aspx>) and the database included therein for an overview of the characteristics of worldwide electrostatic (mostly) research accelerators, in regard to the accelerator type/technology (Table 2.2) and the maximum terminal voltage (Fig. 2.5).

TABLE 2.2. STATISTICS OF ACCELERATOR TYPES AND ACCELERATION TECHNOLOGY

| Accelerator type | Accelerator technology | | | | | | | |
|------------------|------------------------|-----------|--------------|-------------|------------|----|----|-------|
| | Pelletron | Tandetron | Van de Graaf | EN-FN-MP-UD | Dynamitron | MP | EN | Other |
| Single ended | 3 | | 31 | 2 | 8 | | | 6 |
| Tandem | 47 | 5 | 10 | 28 | 35 | 1 | 2 | 19 |
| Other | | | | | | | | 3 |

*data from IAEA accelerator knowledge portal

Excluding accelerators with low terminal voltage ($T_V < 200$ kV), which are used in industrial fabrication, and high terminal voltage machines ($T_V > 6000$ kV), which are used mainly in fundamental nuclear physics, all accelerators with a middle-range terminal voltage (200 kV $< T_V < 6000$ kV) can be and are used for IBA. For resonance depth profiling in particular, the range of terminal voltage between 200 and 500 keV is relevant.

To a large extent, they also fulfill the requirements of a PIGE analysis. A reliable energy control system, e.g. the Generating VoltMeter (see Section 3.1) and a lower limit for the energy of protons around 200–500 keV are needed if the experimental set-up is dedicated to the measurement of PIGE cross-sections and high resolution PIGE depth profiling (see Section 2.2). Beam currents up to a few hundred nA can suit the large majority of specific

PIGE requirements and are easily achieved with standard ion sources, e.g. duoplasmatron and sputtering ion sources.

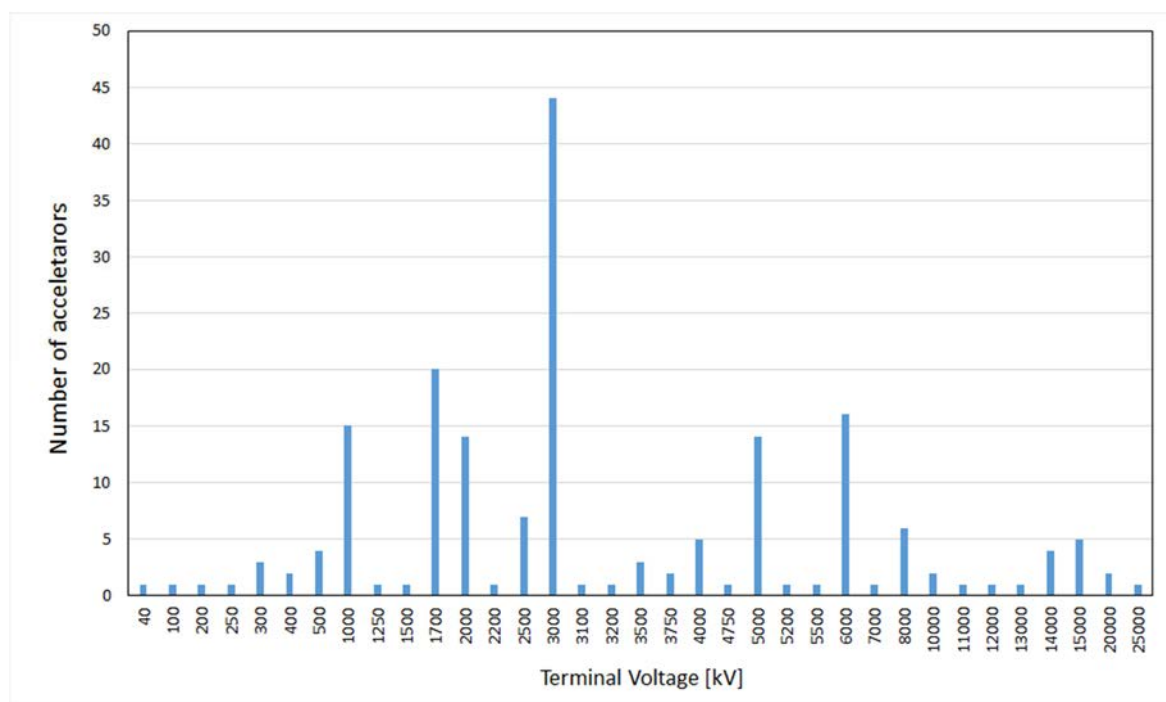


FIG. 2.5. The maximum terminal voltage featured by the accelerators listed in the IAEA accelerator knowledge portal (data on January 2016).

2.3.2. Charge collection and measuring system

In PIGE analysis, the proton energy will be almost always below 5 MeV and the current will be limited to a few hundred nA for a power around 1 W to be dissipated. Such beam currents can be easily measured, in vacuum, by simple insertion devices, such as (i) a transmission Faraday cup (TFC), which intercepts the beam partially and periodically, before or after the sample, and (ii) a Faraday cup (FC) that intercepts the beam continuously after the sample [2.28]. The current can be integrated from both devices by a current digitizer (there are many commercial models) that can give a pulse with a lower limit of 0.1 nC, which guarantees, in theory, a precise measure of the collected charge. Besides the problem connected to the emission of secondary electrons from the target (see Section 3.4), there are problems connected with the device itself. The first is that the FC, in PIGE set-ups and, in general IBA set-ups, is located close to the sample, which often forms a unit with the sample holder, and is generally not shielded. This may create a gamma-ray background that affects the detector response. Light materials, like carbon, must be avoided and preference given to high Z metals. The second and more important problem is produced by the emission of secondary electrons from the FC after the proton impact. The secondary electron energy is a few ten eV and the flux is proportional to the cosine of the emission angle with respect to the surface normal. Their escape increases the positive current in the circuit and generates a systematic overestimation of the charge. Secondary emission is reduced by assuring that the cup shape features a diameter as small as possible compared to the length of the FC and is efficiently suppressed by introducing a ring in front of the FC, which is maintained at a negative

potential of a few hundred volts, to push the electron back to the FC surface. The same suppressor can be put in action in the case of a beam profile monitor (BPM).

In external beams a relative charge monitor can be envisaged. It is a commonly-used device that is preferred over a beam chopper (see Section 3.4) because of its mechanical simplicity, which takes advantage of the in-beam stability of the Si_3N_4 membranes that are nowadays widely used as exit windows. For each energy, the number of X-rays emitted by Si in the membrane, and collected by a fixed Si(Li) or Silicon Drift Detector (SDD) dedicated detector, is in constant proportion with the charge that has been transmitted through it and delivered to the sample. In the case of a standard-based method, the relative charge monitor, given by the X-ray counts, assures the comparison with the standard. For a standardless analysis, the system must be carefully calibrated, energy by energy, against known collected charges, which is not easy for a system in air.

2.3.3. Gamma-ray detector

Both the error (statistical + fit) on the gamma-yield, as well as the PIGE analysis minimum detection limit (MDL) are lower when the yield is higher and the background (from peaks overlap or competing reactions, or from Compton interactions of higher energy radiation with the detector) is lower in the energy region (normally the Full Width at Half Maximum) covered by the gamma-ray peak used to detect the analyte. This puts some minimum requirements on the efficiency and energy resolution of gamma-ray detectors and on the experimental set-up.

Taking into consideration the elements from lithium to phosphorus and the reactions listed in Table 2.1, it is expected that characteristic gamma-rays below or around 2 MeV will be detected, with a difference between nearest neighbouring lines from 2 to 343 keV. Background peaks come from the ^{232}Th series (^{208}Tl , ^{212}Pb , ^{212}Bi , ^{224}Ra , ^{228}Ac), the ^{238}U series (^{214}Pb , ^{214}Bi , ^{226}Ra) and ^{40}K . The most intense peaks that are expected inside an accelerator vault are from ^{208}Tl (510.7 and 583.2 keV), ^{212}Pb (238.6 keV), ^{214}Pb (295.2 keV), ^{214}Bi (609.3 and 1120.3 keV), ^{228}Ac (911.2 and 968.9 keV) and ^{40}K (1460.8 keV). High volume Ge detectors can provide a resolution at FWHM of 1.2–1.5 keV at $E_\gamma = 59$ keV and of 2–3 keV at $E_\gamma = 1332$ keV, which is sufficient to separate all the expected PIGE peaks below 1636 keV from each other and from the background peaks, with the exception of the 585 keV line from ^{25}Mg and the 1459 keV line from ^{19}F .

Modern, fast scintillator detectors, like the LaBr_3 , give a FWHM energy resolution roughly between 7% at 60 keV and 2% at 1460 keV, which means an absolute value between 8.4 keV at 60 keV and 58 keV at 1460 keV. The performance is acceptable for energies below about 800 keV, where the self-activity of LaBr_3 is not interfering. Self-activity comes from the naturally occurring ^{138}La that decays to ^{138}Ba by emitting a gamma-ray of 1436 keV (66.4%) or to ^{138}Ce by emitting a gamma-ray of 789 keV (66.4%). Since they are compact and light, the handling of these detectors is quite easy in comparison to a Ge detector with its liquid nitrogen dewar.

The yield of a gamma-ray at energy E_γ depends on the absolute efficiency of the detector ϵ_{abs} [2.29]. Assuming a point-like gamma-ray source, the detector absolute efficiency ϵ_{abs} is defined as the ratio between the gamma detected, at their full energy E_γ , and the gamma emitted in the whole solid angle in the same time, i.e.:

$$\varepsilon_{abs} = \frac{N_{Det}(T)}{N_{TOT}(T)} = \frac{1}{4\pi} \iint \Delta\theta\Delta\varphi\varepsilon(E_\gamma, \theta, \varphi) \sin\theta d\theta d\varphi, \quad (2.14)$$

where $\varepsilon(E_\gamma, \theta, \varphi)$ is the detector efficiency in its more general form, i.e. as a function of the photon flight direction (θ, φ) and energy E_γ . Absolute efficiency increases when the solid angle covered by the detector is wider but also when the detector entrance window is thinner. The absolute efficiency is measured (see methodological details in Section 3.2) with the use of calibrated sources. The most often-used combination includes ^{133}Ba , ^{152}Eu , ^{137}Cs , ^{60}Co , which results in a relevant number of sufficiently intense, well-spaced peaks, from 53.1622 keV (^{133}Ba) to 1408.013 keV (^{152}Eu), that covers both the low energy region, where the effect of the entrance window may strongly reduce ε_{abs} , and the high one.

The absolute efficiency of a $5\text{cm} \times 5\text{cm}$ LaBr_3 detector is not much lower than that of a $6\text{cm} \times 6\text{cm}$ Ge (see Fig. 2.6). However the MDL, usually defined as the analyte quantity that gives a number of counts corresponding to $\sqrt{N_{BKG}}$, where N_{BKG} is the number of background counts below the gamma-ray peak, is reduced in a Ge detector, given its superior energy resolution. This makes Ge detectors an excellent choice for cross-section measurements or application of PIGE for materials characterization.

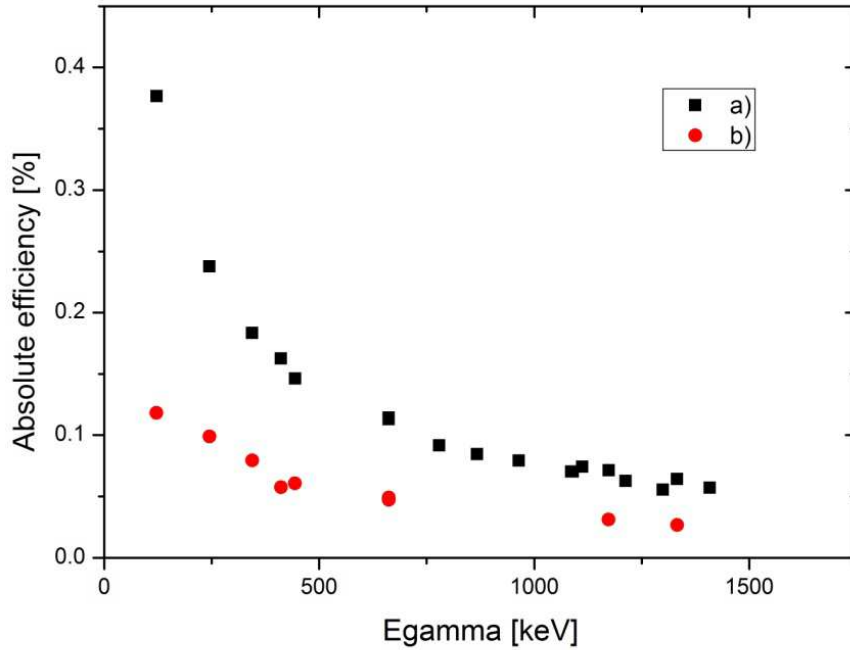


FIG. 2.6. The absolute efficiency, as a function of gamma energy, of: a) a $6\text{cm} \times 6\text{cm}$ REGe detector and b) a $5\text{cm} \times 5\text{cm}$ LaBr_3 scintillator at the same distance from the gamma-ray source.

The achievement of best detector performance requires some attention. For increasing the integral yield/charge ratio, which helps lowering MDL's or shortening measure time, the solid angle may be increased by moving the detector towards the target. When deciding on the final distance from the target, a compromise must be reached between solid angle, increased count rate, pile-up distortion and possible increase in background due to the electromagnetic cascade, which originates from gamma-rays generated outside the target. A different solution consists in using a multi-detector system that will detect photons under the sum of the solid angles for single detectors. Although it is an expensive solution, if the investment has already

been made, e.g. to measure in shorter times angular distributions, and the gamma-emission from the examined reaction is expected to be quite isotropic, the effort spent in combining the individual spectra may be compensated by the increased overall detection efficiency.

2.3.4. Example of a minimal PIGE set-up

A minimal PIGE set-up is shown in Fig. 2.7. A general purpose external micro-beam line, already provided with a PIXE and RBS detector system, as well as with a relative charge monitor that is based on the X-ray emission from the Si_3N_4 exit window, has been implemented with a LaBr_3 scintillator for the analysis, in air, of samples that cannot stand vacuum conditions, e.g. large objects (see Section 2.4.1). The addition of a detector for PIGE, that does not require cooling and is small and light, simplifies the operation and produces an efficient set-up for measuring characteristic gamma-rays that are below about 800 keV and measurements that can be performed with a standard-based method or, as a second choice, can be semi-quantitative, given the difficulty of a monitor calibration.

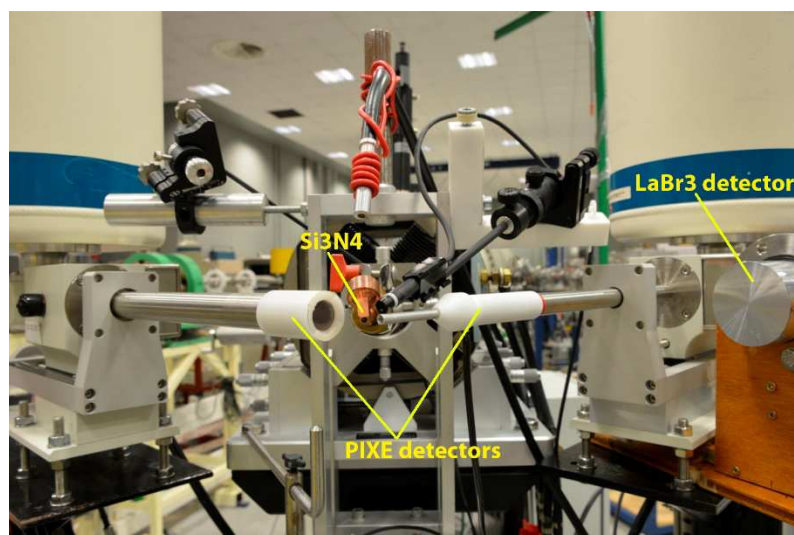


FIG. 2.7. The external microbeam set-up at CMAM-UAM of Madrid, Spain implemented with a LaBr_3 detector.

2.3.5. Example of an in-vacuum multi detector system

PIGE analysis and, even more so, the measurement of cross-sections may require a more elaborated experimental set-up, e.g. the one shown in Fig. 2.8. In this case, the PIGE reaction is produced inside a vacuum chamber, equipped with three high purity Ge detectors for gamma-rays as well as a large surface $\text{Si}(\text{Li})$ detector and a fast SDD detector for X-rays. Such a system has the capability of measuring differential PIGE cross-sections at three angles simultaneously, allowing the determination of angular distribution asymmetries and the production of more precise total cross-sections. On the analytic side, the fact that this set-up, like the previous in-air one, features both gamma-ray and X-ray detectors is of great advantage for fully determining the target composition, over a large Z range, by combining PIGE and PIXE data. It can only be used for samples, however, that can stand the vacuum without degrading.

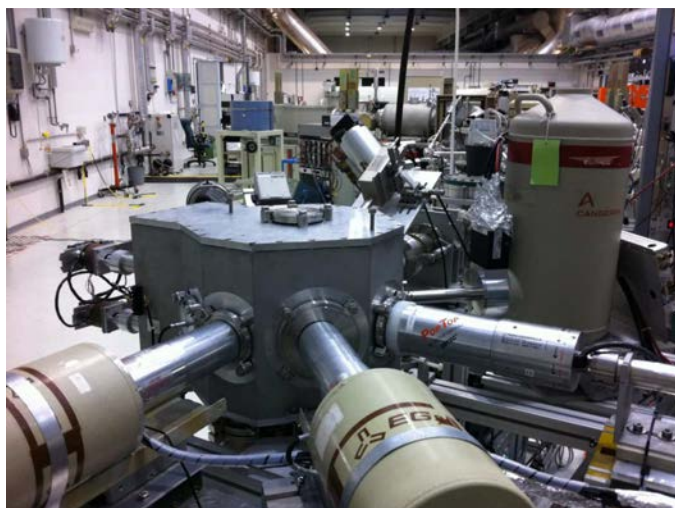


FIG. 2.8. The PIGE set-up at LABEC-INFN in Florence, Italy with the three germanium detectors in the forefront.

In summary, implementing a PIGE experimental station is relatively simple and can be done at a reasonable cost. A high resolution detector, such as an ultrapure germanium detector, will be able to solve the large majority of analytic problems, given that it has the efficiency and energy resolution necessary to univocally identify the light elements against other elements in the sample or the background signals. The best use of PIGE will certainly be in combination with PIXE, due to the fact that these two techniques are commensurate for the analysis of elements such as Na, Mg, Al and Si and that PIGE can be further extended to low Z in order to cover the lighter elements.

2.4. EXAMPLES OF APPLICATIONS IN NA BULK ANALYSIS

2.4.1. Identification of lapis-lazuli in paint layers

Lapis-lazuli is a blue pigment that has been used since the Middle Ages in different kinds of painting techniques. It is obtained from a semi-precious stone that is mainly composed of lazurite ($3\text{Na}_2\text{O}\cdot 3\text{Al}_2\text{O}_3\cdot 6\text{SiO}_2\cdot 2\text{Na}_2\text{S}$), but that also contains small amounts of calcite (CaCO_3) and pyrite (FeS_2) in variable quantities. It was considered to be a very precious and expensive pigment; therefore, it was used, in particular, for religious-themed art, where it emphasized the symbolic value of the work. In canvas and wood paintings, the pigment can be regularly found mixed with lead white ($2\text{PbCO}_3\cdot \text{Pb}(\text{OH})_2$) to produce a paler shade.

Although PIXE is a useful analytical technique to distinguish different pigments [2.30, 2.31], the effectiveness of the technique is severely limited by different factors in cases where lapis-lazuli is mixed with lead white. First, the presence of large quantities of lead results in a strong self-absorption of the low energy X-rays emitted by the light elements (Na, Al and Si) characteristic of this pigment within the paint layer itself. In addition, Al and Si cannot be considered a unique fingerprint for lapis-lazuli, since they are found in many other pigments that are often added to the paint layer to modify the chromatic shade. Furthermore, the presence of the protective layer of varnish, which is made from organic materials and placed with varying thickness on wood and canvas paintings, further reduces the detection sensitivity for these light elements. Finally, the highest Z element of lazurite (S), which is less affected by absorption problems, is difficult to identify in the presence of a large amount of lead, due

to the overlap of Pb M lines with the S K α line. A deconvolution of the K line of S from the M lines of Pb is practically impossible, even with the good energy resolution of SDD detectors.

To solve this problem, PIGE was used to identify lapis-lazuli in pigment layers by detecting the 441 keV gamma-ray from the $^{23}\text{Na}(p,p'\gamma)^{23}\text{Na}$ reaction [2.32]. This is shown in the following example from the study of the ‘‘Madonna dei fusi’’ (ex-Redford version, 1501, private collection), which is a famous painting by Leonardo da Vinci (Fig. 2.9).

Measurements were performed at the KN3000 Van de Graaff accelerator of INFN in Florence, using a proton beam extracted into atmosphere, which had 2.7 MeV of energy on the target, with a 1 mm diameter size and intensity ranging from some tens of pA to 0.1 nA, in order to avoid any risk of damage. Two Si(Li) detectors were used to detect X-rays for PIXE, while a planar Ge detector was used for PIGE (23 mm thickness, 700 eV FWHM energy resolution at 122 keV, placed at about 135° to the beam direction and covering a solid angle of about 0.5 sr).

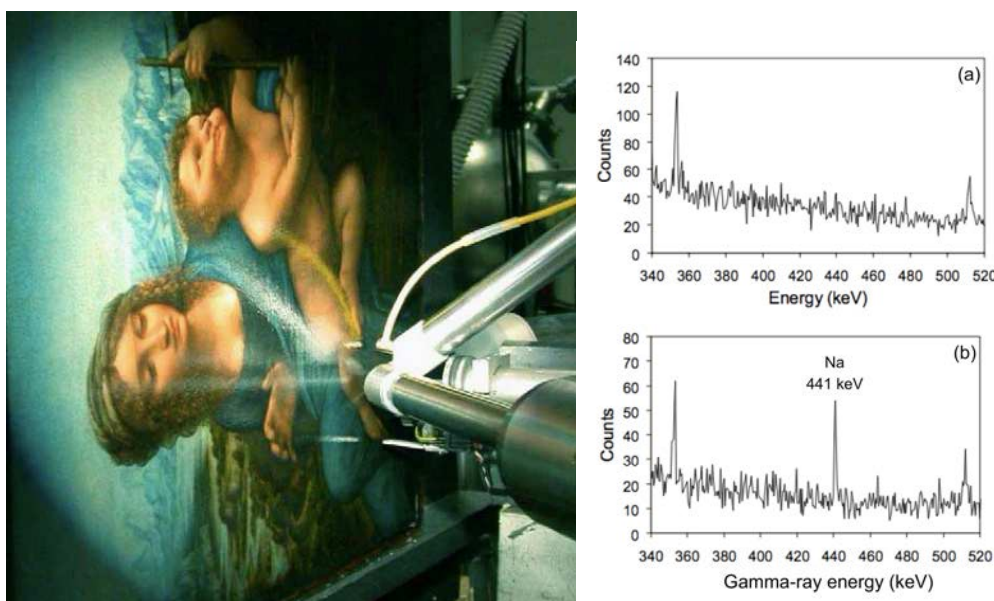


FIG. 2.9. On the left, the ‘‘Madonna dei fusi’’ painting from Leonardo da Vinci during PIXE–PIGE measurements. On the right, PIGE spectra obtained irradiating two blue areas in: (a) a restored area; (b) an original area. The presence of lapis-lazuli pigment in the original paint layer is evidenced by the 441 keV γ -ray peak from the $^{23}\text{Na}(p,p'\gamma)^{23}\text{Na}$ reaction [2.33].

PIXE spectra obtained from some of the blue areas revealed the presence of zinc white (ZnO) and cobalt blue (CoO·Al₂O₃), which only came into use at the beginning of the 19th century. It was thus possible, using these PIXE measurements, to identify many areas that had undergone restoration (mainly in the mantle of the Virgin).

In the original blue areas, which are characterized by a large amount of Pb and were clearly associated with lead white, none of the elements characterizing a blue pigment were detected by PIXE; not even Cu from azurite (copper carbonate, Cu₃(CO₃)₂(OH)₂), the most probable period-compatible alternative blue pigment. Therefore, if conclusions were based on PIXE measurements alone, the use of lapis-lazuli for these blue zones could only be indirectly

suggested. PIGE measurements, however, positively revealed the presence of lapis-lazuli through the detection of the 441 keV gamma-rays from the $^{23}\text{Na}(p,p'\gamma)^{23}\text{Na}$ reaction shown in Fig. 2.9b.

2.4.2. Quantification of Na in ancient glasses

It is well known that a typical effect of ancient glass ageing [2.34] is surface alteration due to a water-inflicted corrosion processes. A surface decrease (leaching) in alkali ion concentration, due to exchange between H^+ from water and Na^+ or K^+ in glass, is caused by humidity from the environment. Therefore, a layer of hydrate silicates is formed in the altered surface, which is depleted in Na, K or Ca elements and enriched in hydrogen. The extent of the weathering process depends on time and on burial/exposure conditions, with leached layers extending up to some tens of μm [2.35, 2.36].

Detection and quantification of Na in ancient glasses can be crucial, for instance to distinguish the *natron* glass of the Roman times (with high Na_2O and low K_2O and MgO content) from later ones like plant ash glass, which have been used since the Middle Ages (with low Na_2O and high K_2O content) [2.37, 2.38]. However, the presence of Na in the bulk may be completely hidden to a PIXE analysis, since the altered layers present at the surface may strongly absorb the X-rays from the lightest elements and thus heavily affect the characterization of the bulk material.

To address problems of this kind, a combined use of PIXE and PIGE is particularly effective [2.25, 2.39–2.43], since it exploits the $^{23}\text{Na}(p,p'\gamma)^{23}\text{Na}$ reaction that produces the 441 keV gamma-ray for Na determination. PIXE information on Na is limited to the first few microns from the surface due to strong self-absorption effects (Na X-ray energy is 1.04 keV), while the integrated yield of gamma-rays refers to a much larger depth, since gamma-rays are detected with no attenuation regardless of the depth from where they originate. It is thus possible to immediately qualitatively distinguish between surface and bulk composition.

An example from the PIXE-PIGE measurement of an area of a blue coloured *tessera* from the famous Roman complex of Villa Adriana (Tivoli) [2.40] is shown in Fig. 2.10. The examined area displays three different kinds of surfaces with different characterizations: a brighter colour (region 1), a more opaque area (region 2) and a white, clearly altered area (not shown in Fig. 2.10). The measurements were carried out at the 3 MV Tandatron of INFN in Florence at the external microprobe set-up, using a proton beam of 2.9 MeV energy on target extracted into atmosphere through a 100 nm Si_3N_4 window, with 100 μm size and about 1 nA intensity. The beam was scanned over an area of $2 \times 2 \text{ mm}^2$ and larger areas were analysed by combining beam scans on adjacent zones obtained by mechanical target displacement. Two detectors were employed for PIXE, a SDD and a Si(Li), which provided altogether a good efficiency from Na X-rays to those of the highest-Z elements, while a HPGe detector was used for PIGE (n-type, 25% efficiency, placed 6 cm from target at 0°).

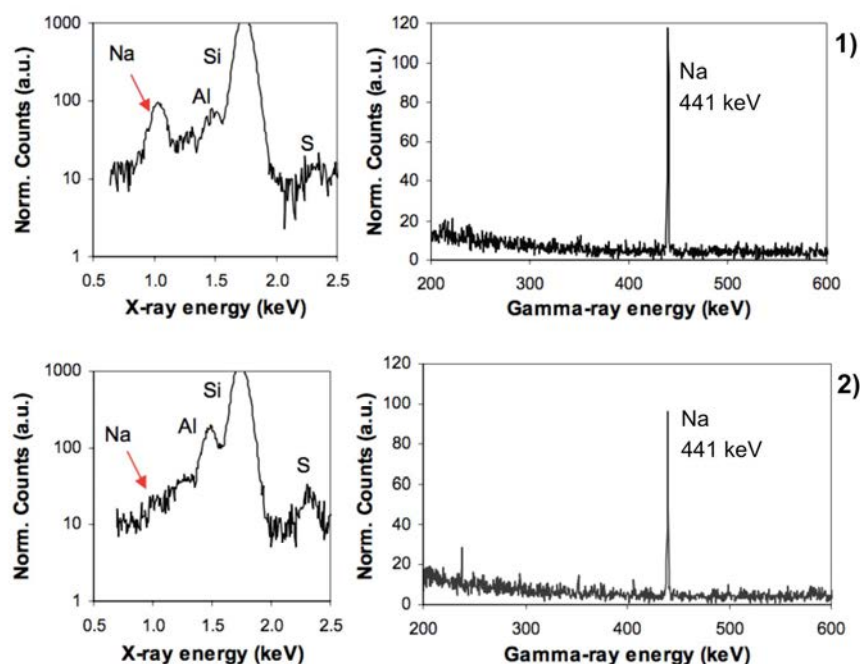


FIG. 2.10. X-ray (left) and γ -ray spectra (right) referring to two of the three different regions of a blue glass tesserae. Only the energy ranges around the Na peaks are displayed [2.33].

The differences between PIXE and PIGE spectra observed in Fig. 2.10 can be explained by the presence of surface alterations leading to Na-depleted layers. Both X-rays and gamma-rays are clearly detected in region 1. In region 2, Na X-rays are not detected; however, there is no appreciable difference in the gamma-ray yields of the two regions. This indicates that the opaque area has a Na-depleted layer that is very thin. Since Na X-rays are not totally undetected, the depletion layer in region 2 cannot be larger than a few microns. Therefore, the fraction of missing gamma-ray yield due to proton energy loss in the thin Na-depleted surface layer is not relevant. A quantitative evaluation of Na content from PIGE spectra from region 2 alone would therefore provide a reasonable lower limit, but quantification through PIXE would be largely incorrect.

In the specific example, the Na_2O content derived from PIGE analysis using the standard-based method, as described in Section 2.1 above, was around 15%. This allows the unambiguous identification of the Roman origin of the studied glass tesserae, since, in the literature, there is evidence that the composition of natron glasses during Roman times was almost constant, with a Na_2O concentration between 16% and 18%.

2.5. HYDROGEN DEPTH PROFILING

Hydrogen depth profiling by using a narrow resonance in a particle-induced gamma-ray emission reaction is of importance because it offers a straightforward, easy-to-quantify and depth-sensitive method for the investigation of hydrogen in materials, which cannot be achieved with most other analytical techniques. The difference between this method and the other PIGE measurement methods is that the beam that is employed is not a proton beam but rather a heavier beam such as ^{15}N , and the target is the lighter hydrogen atom ^1H . Therefore, the proton-induced gamma-ray emitting reaction is used in inverse kinematics. The method works also with ^{18}O or ^{19}F ions as projectile beams, but the resonance in $^1\text{H}(^{15}\text{N},\alpha\gamma)^{12}\text{C}$ at 6.4

MeV has favourable features regarding sensitivity and depth resolution (see Section 2.2 for details) and is most frequently used for hydrogen depth profiling. With this reaction, depth resolutions of a few nm and sensitivities down to the ppm range have been achieved [2.44]. Recent reviews of the method can be found in [2.45] and [2.46].

The principle of this method has already been described in Section 2.2 above. However, having the heavy beam particle is an advantage since the background from other components of samples is negligible and the emitted gamma-ray of 4.4 MeV from the reaction is well separated from room background. Therefore, an optimum resolution of the gamma-detector is not needed, i.e. NaI(Tl) or BGO detectors can be used, which offer a high gamma-ray efficiency and, consequently, a higher sensitivity. Because of the high gamma-ray efficiency, smaller beam currents can be used, which is preferred given that beam-induced changes in the sample and in the hydrogen depth profile can be quite large when using a ^{15}N beam compared to a proton beam.

There are several laboratories equipped with a dedicated set-up for hydrogen depth profiling. They are either optimized with regard to sample handling, maintenance and costs enabling a high rate of processing samples, or high sensitivity. Figure 2.11 shows a set-up dedicated to the detection of low hydrogen concentrations, as used at the University of Bochum (RUB). The sample holder assembly is mounted on the end of a pipe, which can be surrounded by a 12×12 inch NaI(Tl) detector in 4π geometry, to gain a detection efficiency for the 4.4 MeV gamma-ray of almost 50 %.

Figure 12 gives an example of a depth profile for a multilayer sample, as used in research for future hydrogen storage materials that are loaded with a high hydrogen concentration. The layer structure has been determined by RBS and is sketched at the bottom. There is a surface peak of hydrogen, which is observed for almost all samples handled within the laboratory environment. In the region of the titanium layer that is partially oxidized, the hydrogen concentration increases as the oxygen content decreases.



FIG. 2.11. Set-up for hydrogen depth profiling. Reproduced courtesy of Springer [2.45].

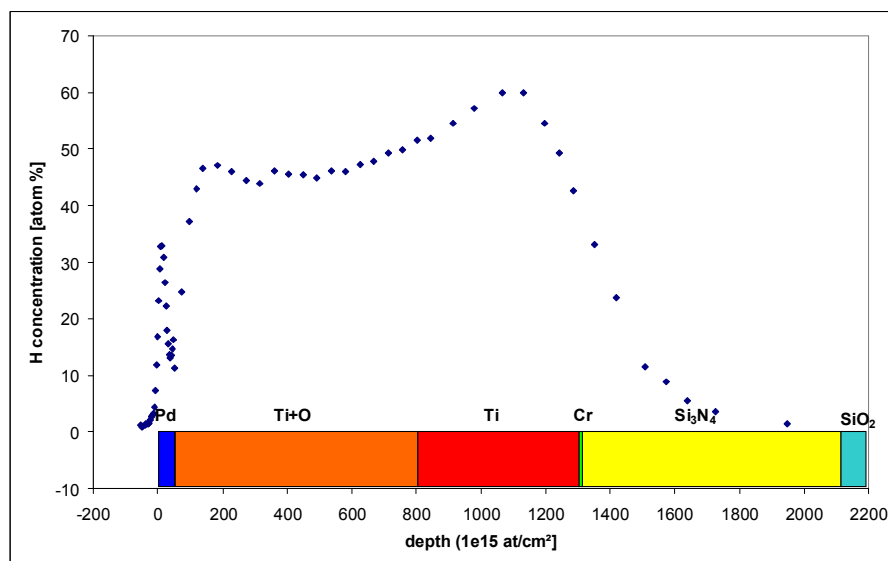


FIG. 2.12. Hydrogen depth profile of a multilayer system. The layer structure is indicated at the bottom.

Hydrogen can alter the properties of materials drastically, even at low concentrations. An example is hydrogen in olivine, which is the most abundant mineral in the earth's crust. In this instance, hydrogen concentrations in the ppm range have a strong influence on mechanical properties such as the plastic flow in geological conditions. For such applications, there have been significant efforts to improve the sensitivity of the method into the ppm range.

When hydrogen concentrations below 100 ppm have to be measured, special conditions have to be fulfilled. One is that the constructive elements of the set-up, such as collimators, which are hit by the beam, have to have low hydrogen contaminations and have to be mounted as far from the detector as possible. Another condition is that the surface of the sample has to be free of hydrogen, which is usually easily adsorbed onto almost any sample surface. When a low hydrogen concentration in the depth of a material is measured, the beam has to hit the sample at an energy above the resonance energy (see Section 2.2). The cross-section for the reaction at the surface is several (almost five) orders of magnitude lower than at the peak of the resonance. However, if the hydrogen concentration of a surface layer is five orders of magnitude higher than in the bulk, the number of γ -rays from the surface is equal to contributions of the bulk. It should be noted that this problem arises even if the surface layer is only a few atomic layers thick.

Therefore, a UHV sample chamber that can produce a vacuum better than 10^{-8} mbar and options to clean sample surfaces in-situ are mandatory for a facility intending to do low concentration hydrogen depth profiling analysis. In the set-up of Fig. 11, for example, surface cleaning can be accomplished by heating the sample via electron bombardment with an ion sputter gun. Details can be found in [2.47].

REFERENCES TO SECTION 2

- [2.1] SIPPEL, R.F., GLOVER, E.D., Sedimentary rock analysis by charged particle bombardment, *Nucl. Instrum. Methods* **9** (1960) 37–48.
- [2.2] PIERCE, T.B., PECK, P.F., HENRY, W.M., Determination of carbon in steels by measurement of the prompt γ -radiation emitted during proton bombardment, *Nature* **204** (1964) 571.
- [2.3] PIERCE, T.B., PECK, P.F., HENRY, W.M., The rapid determination of carbon in steels by measurement of the prompt radiation emitted during deuteron bombardment, *Analyst* **90** (1965) 339.
- [2.4] PIERCE, T.B., PECK, P.F., CUFF, D.R.A., Application of inelastic proton scattering to the rapid determination of silicon in steels, *Anal. Chim. Acta* **39** (1967) 433.
- [2.5] BORDERIE, B., BARRANDON, J.N., New analytical developments in prompt gamma-ray spectrometry with low-energy tritons and alpha particles, *Nucl. Instrum. Methods* **156** (1978) 438.
- [2.6] BORDERIE, B., Present possibilities for bulk analysis in prompt gamma-ray spectrometry with charged projectiles, *Nucl. Instrum. Methods* **175** (1980) 465.
- [2.7] BONI, C., CEREDA, E., BRAGA MARCAZZAN, G.M., DE TOMASI, V., Prompt gamma emission excitation functions for PIGE analysis, *Nucl. Instrum. Methods Phys. Res. B* **35** (1988) 80.
- [2.8] BONI, C., CARUSO, E., CEREDA, E., BRAGA MARCAZZAN, G.M., and REDAELLI, P., A PIXE-PIGE system for the quantitative elemental analysis of thin samples, *Nucl. Instrum. Methods Phys. Res. B* **40/41** (1989) 620.
- [2.9] BONI, C., CARUSO, E., CEREDA, E., BRAGA MARCAZZAN, G.M., REDAELLI, P., Simultaneous PIXE-PIGE analysis of thin and thick samples, *Nucl. Instrum. Methods Phys. Res. B* **49** (1990) 106.
- [2.10] ANTTILA, A., HÄNNINEN, R., RÄISÄNEN, J., Proton-induced thick-target gamma-ray yields for the elemental analysis of the $Z = 3-9, 11-21$ elements, *J. Radioanalytical Chemistry* **62** (1981) 293.
- [2.11] RÄISÄNEN, J., HÄNNINEN, R., Heavy element ($Z > 30$) thick-target gamma-ray yields induced by 1.7 and 2.4 MeV protons, *Nucl. Instrum. Methods* **205** (1983) 259.
- [2.12] LAPPALAINEN, R., ANTTILA, A., RÄISÄNEN, J., Absolute α -induced thick-target gamma-ray yields for the elemental analysis of light elements, *Nucl. Instrum. Methods* **212** (1983) 441.
- [2.13] KISS, Á.Z., KOLTAY, E., NYAKÓ, B., SOMORJAI, E., ANTTILA, A., RÄISÄNEN, J., Measurements of relative thick target yields for PIGE analysis on light elements in the proton energy interval 2.4–4.2 MeV, *J. Radioanalytical Nucl. Chemistry* **89** (1985) 123.
- [2.14] RÄISÄNEN, J., WITTING, T., KEINONEN, J., Absolute thick-target γ -ray yields for elemental analysis by 7 and 9 MeV protons, *Nucl. Instrum. Methods Phys. Res. B* **28** (1987) 199.
- [2.15] KISS, A. Z., I. BIRON, T. CALLIGARO, J SALOMON, Thick target yields of deuteron induced gamma-ray emission from light elements, *Nucl. Instrum. Methods Phys. Res. B* **85** (1994) 118.
- [2.16] ELEKES, Z., KISS, A.Z., BIRON, I., CALLIGARO, T., SALOMON, J., Thick target γ -ray yields for light elements measured in the deuteron energy interval of 0.7–3.4 MeV, *Nucl. Instrum. Methods Phys. Res. B* **168** (2001) 305
- [2.17] MATEUS, R., JESUS, A.P., BRAZINHA, B., CRUZ, J., PINTO, J.V., RIBEIRO, J.P., Proton-induced γ -ray analysis of lithium in thick samples, *Nucl. Instrum. Methods Phys. Res. B* **190** (2002) 117

- [2.18] MATEUS, R., JESUS, A.P., RIBEIRO, J.P., Quantitative analysis of light elements in thick samples by PIGE, Nucl. Instrum. Methods Phys. Res. B **219–220** (2004) 519.
- [2.19] MATEUS, R., JESUS, A.P., RIBEIRO, J.P., A code for quantitative analysis of light elements in thick samples by PIGE, Nucl. Instrum. Methods Phys. Res. B **229** (2005) 302.
- [2.20] CACIOLLI, A., CHIARI, M., CLIMENT-FONT, A., FERNÁNDEZ-JIMÉNEZ, M. T., GARCÍA-LÓPEZ, G., *et al.*, Measurements of γ -ray emission induced by protons on fluorine and lithium, Nucl. Instrum. Methods Phys. Res. B **249** (2006) 98.
- [2.21] CACIOLLI, A., CALZOLAI, G., CHIARI, M., CLIMENT-FONT, A., GARCIA, G., *et al.*, Proton elastic scattering and proton induced γ -ray emission cross-sections on Na from 2 to 5 MeV, Nucl. Instrum. Methods Phys. Res. B **266** (2008) 1392.
- [2.22] CALZOLAI, G., CHIARI, M., LUCARELLI, F., NAVA, S., PORTARENA, S., Proton induced γ -ray emission yields for the analysis of light elements in aerosol samples in an external beam set-up, Nucl. Instrum. Methods Phys. Res. **268** (2010) 1540.
- [2.23] WANG, Y, NASTASI, M. (Eds), Handbook of Modern Ion Beam Materials Analysis, 2nd edn, Materials Research Society, Pennsylvania (2009).
- [2.24] MATEUS, R. A., JESUS, P., FONSECA, M., LUÍS, H., RIBEIRO, J.P., The sensitivity of the PIGE analytical technique, Nucl. Instrum. Methods Phys. Res. B **264** (2007) 340.
- [2.25] CLIMENT-FONT, A., MUNOZ-MARTIN, A., YNSA, M.D., ZUCCHIATTI, A., quantification of sodium in ancient Roman glasses with ion beam analysis, Nucl. Instrum. Methods Phys. Res. B **266** (2008) 640.
- [2.26] SCHULTE, W.H., EBBING, H., BECKER, H.W., BERHEIDE, M., BUSCHMANN, M., *et al.*, High resolution depth profiling in near-surface regions of solids by narrow nuclear reaction resonances below 0.5 MeV with low energy spread proton beams, Vacuum **44** (1993) 185.
- [2.27] HARISSOPULOS, S., CHRONIDOU, C., SPYROU, K., PARADELLIS, T., ROLFS, C., *et al.*, The $^{27}\text{Al}(p,\gamma)^{28}\text{Si}$ reaction: direct capture cross-section and resonance strengths at $E_p = 0.2\text{--}1.12$ MeV, Eur. Phys. J. A **9** (2000) 479.
- [2.28] A. WU CHAO, A., TIGNER, M. (Eds), Handbook of accelerator Physics and Engineering, World Scientific (2002), pp. 556–559.
- [2.29] ZUCCHIATTI, A., CORVISIERO, P., PIGE: a useful technique for the study of innovative energy related materials. Technical note on the measurement of gamma-ray production cross-sections, Energy Procedia **41** (2013) 110–118.
- [2.30] MANDÓ, P.A., FEDI, M.E., GRASSI, N., MIGLIORI, A., Differential PIXE for investigating the layer structure of paintings, Nucl. Instrum. Methods Phys. Res. B **239** (2005) 71.
- [2.31] GRASSI, N., BONANNI, P., MAZZOTTA, C., MIGLIORI, A., MANDÓ, P.A., PIXE analysis of a painting by Giorgio Vasari, X-Ray Spectrom. **38** (2009) 301.
- [2.32] GRASSI, N., MIGLIORI, A., MANDO, P.A., CALVO DEL CASTILLO, H., Identification of lapis-lazuli pigments in paint layers by PIGE measurements, Nucl. Instrum. Methods Phys. Res. B **219–220** (2004) 48.
- [2.33] CHIARI, M., *private communication*.
- [2.34] DAL BIANCO, B., BERTONCELLO, R., MILANESE, L., BARISON, S., Glasses on the seabed: surface study of chemical corrosion in sunken Roman glasses, J. Non-Cryst. Solids **343** (2004) 91.
- [2.35] WEBER, G., STRIVAY, D., MARTINOT, L., GARNIR, H.P., Use of PIXE– PIGE under variable incident angle for ancient glass corrosion measurements, Original Nucl. Instrum. Methods Phys. Res. B **189** (2002) 350.

- [2.36] GRATUZE, B., BARRANDON, J.N., DULIN, L., AL ISA, K., Ancient glassy materials analyses: a new bulk nondestructive method based on fast neutron activation analysis with a cyclotron, *Nucl. Instrum. Methods Phys. Res. B* **71** (1992) 70.
- [2.37] SAYRE, E.V., SMITH, R.W., Compositional categories of ancient glass, *Science* **133** (1961) 1824.
- [2.38] HENDERSON, J., *The Science and Archaeology of Materials*, Routledge, London and New York (2000).
- [2.39] GÓMEZ-TUBÍO, B., ONTALBA SALAMANCA, M.A., ORTEGA-FELIU, I., RESPALDIZA, M.A., AMORES CARREDANO, F., GONZÁLEZ-ACUÑA, D., PIXE-PIGE analysis of late Roman glass fragments, *Nucl. Instrum. Methods Phys. Res. B* **249** (2006) 616.
- [2.40] GRASSI, N., GIUNTINI, L., MANDÒ, P.A., MASSI, M., Advantages of scanning-mode ion beam analysis for the study of Cultural Heritage, *Nucl. Instrum. Methods Phys. Res. B* **256** (2007) 712.
- [2.41] ŠMIT, Z., JEZERŠEK, D., KNIFIC, T., ISTENIC, J., PIXE-PIGE analysis of Carolingian period glass from Slovenia, *Nucl. Instrum. Methods Phys. Res. B* **267** (2009) 121.
- [2.42] ŠMIT, Z., TARTARI, F., STAMATI, F., VEVECKA PRIFTAJ, A., ISTENIC, J., Analysis of Roman glass from Albania by PIXE-PIGE method, *Nucl. Instrum. Methods Phys. Res. B* **96** (2013) 7.
- [2.43] ŠMIT, Z., MILAVEC, T., FAJFAR, H., REHREN, LANKTON, J.W., GRATUZE, B., Analysis of glass from the post-Roman settlement Tonovcov grad (Slovenia) by PIXE-PIGE and LA-ICP-MS, *Nucl. Instrum. Methods Phys. Res. B* **311** (2013) 53.
- [2.44] ENDISCH, D., STURM, H., RAUCH, F., Nuclear reaction analysis of hydrogen at levels below 10 at.ppm, *Nucl. Instrum. Methods Phys. Res. B* **84** (1994) 380.
- [2.45] FRITZSCHE, H., HUOT, J., FRUCHART, D. (Eds), *Neutron Scattering and Other Nuclear Techniques for Hydrogen in Materials*, Springer (2016).
- [2.46] WILDE, M., FUKUTANI, K., Hydrogen detection near surfaces and shallow interfaces with resonant nuclear reaction analysis, *Surf. Sci. Rep.* **69** (2014) 196.
- [2.47] TRAEGER, F., KAUER, M., WÖLL, CH., ROGALLA, D., BECKER, H.W., Analysis of surface, subsurface, and bulk hydrogen in ZnO using nuclear reaction analysis, *Phys. Rev. B* **84** (2011) 075462.

3. METHODOLOGY OF CROSS-SECTION MEASUREMENTS

Accurate differential cross-section determination is dependent on the accuracy of recordings and measurements performed in the laboratory. These measurements depend on a number of parameters, which will be described in Sections 3.1–3.4, including (i) energy calibration of the accelerator, (ii) efficiency calibration of the detector, (iii) target preparation and (iv) charge collection. Since these parameters all directly affect the cross-section calculations, it is of paramount importance that they are all undertaken with great care for accuracy and precision so as to minimize error and discrepancy. Further details on the methodology in determining cross-sections are discussed in Section 3.5.

3.1. ENERGY CALIBRATION OF THE ACCELERATOR

Since the correct recording of the precise energy at which the reaction has occurred is vital to the accurate determination of differential cross-sections, especially when narrow resonances are involved, an energy calibration of the accelerator is performed before any measurements are made. It is also advisable to confirm results by performing a second energy calibration after all of the measurements have been made. There are several possible calibration methods proposed in the literature, three of which are described below in more detail. There are also several ways of measuring the energy of the accelerator during the experiment [3.1]. The most common method is by measuring the voltage in the terminal of the accelerator using a Generating VoltMeter (GVM). Another possibility is by measuring the magnetic field of a bending magnet with the aid of an NMR probe.

3.1.1. Narrow resonances

One of the most accurate and widely used methods of calibration employs gamma-ray reactions that exhibit well-studied, strong, narrow resonances [3.1, 3.2]. Most of these resonances are produced when a proton incident beam is used. A list of commonly used resonances can be found in Table 3.1. The beam is directed onto a target containing the appropriate element. It is considered good practice to choose a thick, polished, mono-elementary target, but a composite one could be used as long as the composition was known. The emitted gamma-rays are recorded by a detector, such as a HPGe or NaI detector, placed at a fixed angle with respect to the beam axis.

TABLE 3.1. COMMON RESONANCES USED FOR ENERGY CALIBRATION

| Reaction | Resonance energy (keV) | Width (keV) | Gamma-ray emitted (keV) | Reference |
|--|------------------------|-------------|-------------------------|-----------|
| $^{27}\text{Al}(p,\gamma)^{28}\text{Si}$ | 991.9 | 0.1 | 1779 | [3.3] |
| $^{13}\text{C}(p,\gamma)^{14}\text{N}$ | 1746.9 | 0.075 | 2730 | [3.4] |
| $^{32}\text{S}(p,p'\gamma)^{32}\text{S}$ | 3379 | 1.2 | 2230 | [3.5] |
| $^{14}\text{N}(p,p'\gamma)^{14}\text{N}$ | 5937 | 17 | 2313 | [3.2] |

The calibration procedure is as follows: (i) the accelerator terminal is set at a voltage, or the magnet is set at an NMR value, corresponding to an energy lying well below the resonance. After accumulating a certain amount of integrated beam charge, (ii) the gamma-rays emitted by the reaction are recorded. Then (iii) the voltage of the terminal is increased and the procedure is repeated, making sure to keep the same beam charge. As the beam energy

approaches the resonance energy, (iv) the number of gamma-rays that are emitted increases as the tail of the resonance enters the surface of the target. Further increment of the energy leads to further increment of the production of the gamma-rays as a larger part of the resonance contributes to it, until (v) a plateau is reached. This plateau indicates that the resonance has fully entered the target and no further increment of gamma-rays is expected. (vi) The experimental data is fitted using a sigmoidal function and the NMR value that corresponds to the resonance energy is given by sigma. An example of the resulting graph (yield vs terminal voltage (NMR value)) is presented in Fig. 3.1.

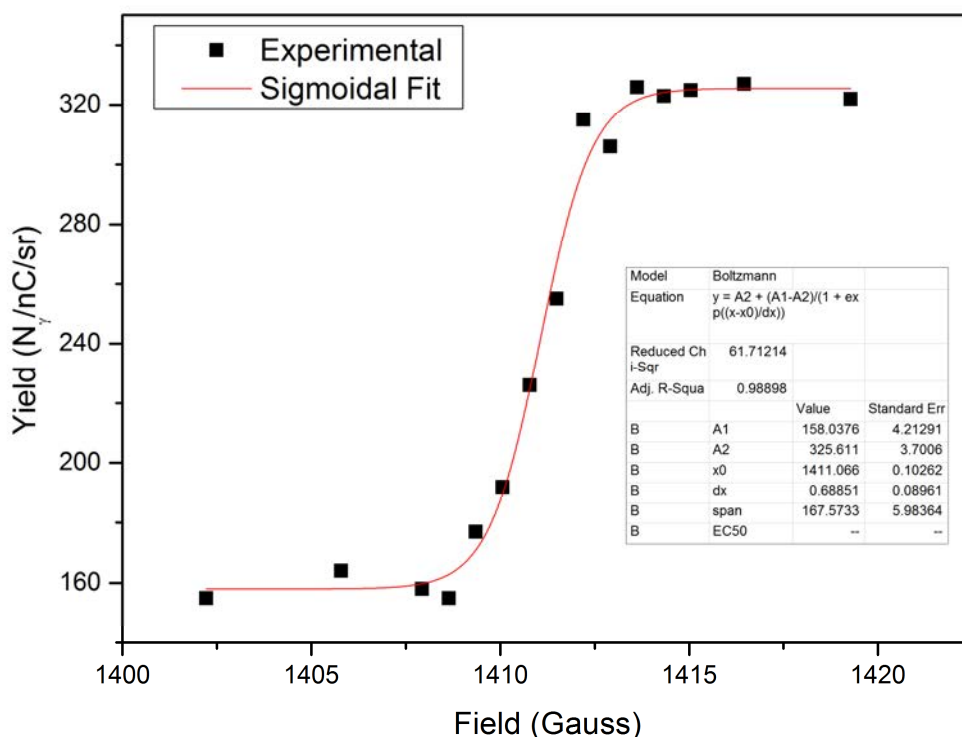


FIG. 3.1. Yield of gamma-rays as a function of terminal voltage (NMR value) as performed for the $^{27}\text{Al}(p,\gamma)^{28}\text{Si}$ resonance from Table 3.1 above. Experimental data points are fitted with a sigmoidal function.

(vii) Steps i–vi are repeated with another resonance of another isotope. (viii) Finally, the terminal voltages (NMR values) are plotted against the resonance energies and the data is fitted with a linear equation. This linear equation represents the accelerator’s calibration.

3.1.2. Neutron producing threshold reactions

A second method of calibrating the energy of the accelerator is based on neutron producing threshold reactions [3.6–3.8]. The underlying principle is that when the energy of the beam is lower than the threshold, no reaction occurs and no neutrons are produced. Once again, a thick target containing the neutron producing element is needed. A neutron counter, such as BF_3 , is used for the detection of neutrons. The terminal voltage of the accelerator is set to a lower starting value than the threshold for the reaction and the produced neutrons are counted. Since the energy is lower than the threshold, any neutrons that exist originate mainly from other sources such as reactions of other elements, the building materials of the chamber or the

collimators. Since the cross-sections of secondary reactions increase with voltage, it can be deduced that the number of emitted neutrons increases linearly with the increase of voltage. When the threshold energy is reached, the production of neutrons increases rapidly, but the relationship remains linear. On a graph of the resulting data, the point at which the line changes slope corresponds to the threshold energy, which is then related with the terminal voltage and consequently used to calibrate the accelerator. The main advantage of this method is that it can be used with a deuteron or a proton incident beam.

3.1.3. Elastic scattering

A third calibration method makes use of the elastic scattering of the ion beam [3.9, 3.10]. While this method can be used with any beam, it yields better results with a light ion beam. It is less accurate, however, than the two above mentioned methods. The elastic scattering method is based on the fact that ions produced by a two-body reaction are backscattered with a well-defined energy due to kinematics. An ion beam is focused on a polished target and the backscattered ions are detected with the aid of a Silicon Surface Barrier (SSB) or Silicon PIN diode detector. Prior to the experiment, the detector should be calibrated using a point source. The energy of the detected ions is then inserted into a set of equations describing two-body kinematics, and the initial energy of the beam is calculated, which in turn corresponds to the terminal voltage set. The whole procedure can then be repeated with different beam energies, producing more points between the terminal voltage and the accelerator's energy. While this method has the advantage of being able to produce an infinite number of such points, its accuracy is restricted by the resolution of the particle detector, which is usually around 15 keV, and also by the roughness of the target used.

3.2. EFFICIENCY CALIBRATION OF THE DETECTOR

The term efficiency, as it is used in Eq. 3.1, refers to the absolute efficiency of the detector and not the intrinsic efficiency. When calculated with the procedure described below, it also takes into account the solid angle covered by the detector.

Although efficiency calibration is a common procedure, it requires attention to detail in order to produce accurate results. Depending on the energy of the gamma-ray, (i) a suitable point source is placed as close as possible to the position of the actual target. The positioning of the target is crucial since the solid angle must be taken into account as well as the attenuation of the gamma-rays due to the materials between the source and the detector. The latter effect is more important when low energy gamma-rays are concerned. (ii) The accumulated spectrum is analysed and each gamma-ray peak area is corrected for the dead time of the measurement, which should be kept as low as possible. (iii) The efficiency for each of the gamma-rays emitted is calculated using:

$$\varepsilon = \frac{N_{\gamma}}{\Delta t \cdot R \cdot I}, \quad (3.1)$$

where N_{γ} represents the number of detected gamma-rays, R is the activity of the source, Δt is the time duration of the measurement and I is the branching ratio of the detected gamma-ray.

Next, (iv) efficiency ε is plotted against the energy of the gamma-ray and fitted with a suitable function, taking into account the corresponding errors. There are a variety of functions that have been proposed for fitting the experimental data [3.11, 3.12]. Finally, (v) the efficiency

for the given gamma-ray is calculated from the fitted function. Special care must be taken for the calculation of the error of the detector's efficiency at that energy. A common mistake is to calculate the error by a quadratic summation of the errors of the fitting parameters, which is mathematically incorrect since the fitting parameters are not independent variables, and also leads to an overestimation of the error. Instead, the error must be estimated by calculating the 66% confidence band of the fitted function. It is worthwhile noting that while the various proposed functions give approximately the same value for the efficiency in a region well-defined by nearby gamma-rays, their confidence bands may deviate significantly. For this reason, best practice is to use a source that emits gamma-rays close in energy to the one under study.

If gamma-rays are recorded that are more energetic than the ones emitted by the source, there are several possible methods for dealing with them. The simplest and least accurate method is by extrapolating the fitted function obtained by a source with low gamma-rays. Because of the intrinsic uncertainty that enters every extrapolation procedure, this method should be avoided. A second more complicated but far more accurate method employs the gamma-rays emitted by well-studied reactions, including well-known resonant reactions [3.13]. If the cross-section or the strength of the resonance is known with great accuracy, the efficiency of the detector can be deduced by solving the inverse problem. A third method, which is widely used, is to simulate the detector's efficiency by means of a simulation package such as GEANT [3.14–3.17], or PENELOPE [3.18, 3.19]. After building the geometry of the detector, the simulation should be checked against a low-energy gamma-ray source before being used for the calculation of the efficiency at higher energies. The main advantage of this method is that once the simulation is made for a specific detector, it can be used again for future experiments using the same detector as long as the geometry of the experiment does not change, or as long as the simulation is adjusted accordingly.

3.3. TARGET PREPARATION

The main requirement for all cross-section measurements is a thin target of known composition. There are multiple ways of producing such a target, depending mainly on the pure element or compound to be produced. The produced target may be self-supported or deposited onto a thick backing. The backing should not emit additional gamma-rays. For this reason, backings such as Ta, Cu or even Au with high purity are commonly used. A good practice is to check the gamma-rays emitted from the backing before using it. This check can also be performed at any point during the experiment by flipping the target so that the beam faces the backing.

If the target can be obtained prefabricated from a commercial company, this is the recommended option due to the guaranteed purity of the target. Independent measurements to confirm the nominal thickness, however, should still be performed.

If the target cannot be obtained from a commercial company, it can be prepared in the lab using specialized equipment such as evaporators. The simplest method uses thermal evaporation to prepare targets of compounds with low evaporation points. The compound is placed into a metal boat (Ta, Mo or W) inside a vacuum chamber. Current flows through the boat heating the compound, which eventually evaporates. The vapour rises to deposit onto a thick backing placed at some distance above the crucible boat. A second method uses an electron gun evaporator within a vacuum chamber. A filament is heated to produce electrons, under high vacuum, which are guided with the aid of magnets onto the compound. The

electrons sputter the atoms in the compound, which then deposit onto an appropriate backing that has been placed inside the chamber. The third method, in the case of metallic targets, involves rolling a foil several times until it reaches the desired thickness.

When performing any of the three mentioned manufacturing methods, there are a few key considerations and precautions: (i) if the target is a poor thermal conductor, the heat produced as a result of the beam hitting the target could change either the stoichiometry or the initial thickness of the target. If excess heat occurs, it is advisable to use a low beam current and duplicate some measurements in order to determine if any thermal damage has occurred. If needed, the target should be cooled, however proper consideration should be taken when deciding how to cool the target so the target is not damaged further and so that the integration of the beam charge is not altered. (ii) There are different methods of measuring the beam charge. In direct methods, the target must be a conductor so that no discharges will occur during the experiment. Indirect methods detect backscattered particles and require that a thin metal film of a heavy element, such as Au or Ag, be deposited onto the actual target. Further discussion of this topic can be found in Section 3.4.

After a target is manufactured in the lab, it must be characterized. This can be achieved using other ion beam analysis techniques such as RBS, NRA or Elastic Recoil Detection Analysis (ERDA). The characterization is crucial not only because the thickness directly affects the cross-section but also in order to discover any possible impurities in the target.

3.4. CHARGE COLLECTION

There are direct and indirect ways of measuring the charge [3.20]. The easiest direct way, if the incident beam loses all of its energy within the target, is by electrically connecting the target to a sensitive current integrator. If the target is thin enough, the beam may pass through it, at which point it must be halted and collected in a Faraday cup. Although it seems a straightforward and easy method, several potential sources of uncertainty and error must be taken into consideration. The most important source of uncertainty in direct collection is the production of secondary electrons. As the beam impinges on the target, it emits electrons that, when allowed to escape the target, produce a 'fake' positive charge, with the amount of electrons produced dependent on the nature of the target. The same effect can be produced if electrons escape from the collimator and reach the target, which reduces the beam charge on the target. A common way of resolving the problem is to apply a positive voltage on the target and on the collimators so as to suppress the production of electrons. This suppression voltage (typically $\sim +300$ V), when used in conjunction with a Faraday cup surrounding the target, is sufficient for a reliable charge collection. The setup must be checked, however, before each experiment in order to ensure proper function.

A widely-used way of indirectly measuring the charge is by simultaneously detecting both the gamma-rays and the beam particles scattered at backward angles. A SSB detector placed in a backward angle between 150° and 170° detects the elastically backscattered ions coming from a thin metallic film evaporated on the target. If the thickness of the film and the solid angle covered by the SSB detector are known, the number of incident ions can be calculated with the Rutherford formula. A heavy element for the film will ensure the validity of Rutherford's scattering law.

Besides the common method, other more elaborate indirect methods have been proposed. One example of a different method is the use of a beam chopper, which is a device that interacts

with the beam in predefined time intervals and can directly and indirectly measure the beam current.

3.5. CROSS-SECTION DETERMINATION

The differential cross-section is calculated using the following formula:

$$\left(\frac{d\sigma}{d\Omega}\right)(E, \theta) = \frac{N_\gamma(E, \theta)}{\xi \cdot N_p \cdot \varepsilon_{\alpha\gamma}(E_\gamma)}, \quad (3.2)$$

where $N_\gamma(E, \theta)$ is the number of detected gamma-rays, ξ is the thickness of the target in atoms/cm², N_p is the number of incident particles and $\varepsilon_{\alpha\gamma}(E_\gamma)$ is the absolute efficiency of the detector. Since the methods of determining quantities for most of the variables in Eq. 3.2 have already been discussed in Section 2, only the method of determining N_γ is elaborated on here.

Depending on the multi-polarity of the gamma-ray, the emission can be anisotropic, which requires the measurement of the cross-section at more than one angle, or isotropic. If there is a possibility of an angular dependence, the angle should be defined with the best possible accuracy acquired by placing the detector as far away from the target as possible. On the other hand, a large distance dramatically reduces the counting rate of the experiment. To maximize both counting rate and accuracy, a middle ground should be found. Once the distance has been set, cross-sections can be measured either by simultaneously using multiple detectors placed at different angles or by using one detector and making a new measurement at each angle.

After setting up the detector and associated electronics, a test run should be performed to study the gamma-rays coming from the background, either natural or from the interaction of the beam with the building materials of the beamline. If there are no outside gamma-rays emitted in the vicinity, the target can be placed in the chamber. If the target is backed, a test run must be performed with the beam directed on the backing material to ensure that no overlapping gamma-rays are emitted. It is recommended that the measurement be repeated at a higher energy beam, since a reaction channel that was closed at a low energy may open at a higher one.

Before starting the actual experiment, the energy step of the beam must be carefully selected. This decision is based mainly on three factors: (i) the ripple of the accelerator, (ii) the thickness of the target and (iii) the shape of the cross-section. While the first two can be taken into account before starting the experiment, the third can only be determined during the experiment, and then adjusted as needed, i.e. if sharp resonances exist in the cross-section. One way of predicting any potential resonance energies is by studying the level scheme of the compound nucleus, if it is available. During the experiment, the intensity of the incident beam should be kept as low as possible so as not to damage the target or produce pile-up effects on the detection system.

After recording the spectra, an appropriate integration or fitting computer code should be used. In cases where a strong background exists, more than one computer code should be used, at least for some measurements, so as to avoid any systematic errors in the integration procedure. The measured cross-section can then be determined using Eq. 3.2. Finally, the energy of the measured cross-section must be corrected using the accelerator's calibration and the beam's energy loss within the target.

3.6. INTERLABORATORY EXERCISE: MEASUREMENT OF THE CROSS-SECTION OF THE $^{27}\text{Al}(p,p't)^{27}\text{Al}$ REACTION

After surveying the scientific literature for publications containing previous measurements of cross-sections for PIGE spectroscopy, it was discovered that large discrepancies exist between cross-sections of the same reaction measured by different authors in different laboratories. In response, a concerted and coordinated effort was made to assess the experimental constraints and difficulties associated with measurements of $(p,p'\gamma)$ reactions.

An interlaboratory exercise was organized to measure the differential cross-section of the $^{27}\text{Al}(p,p'\gamma)^{27}\text{Al}$ reaction that produces the 844 keV gamma-ray. The emission of this gamma-ray is isotropic due to the spin of the initial state which is $J_i = 1/2$. The measurements were made at energies ranging from 2.5 MeV to 3 MeV with a 10 keV energy step. Additionally, thick target yields were measured for the $^{27}\text{Al}(p,\gamma)^{28}\text{Si}$ reaction at energies between 0.98 and 1.1 MeV with the energy step small enough to reproduce the 991.9 keV resonance, using the 1.779 MeV gamma-ray line (see Table 3.1).

3.6.1. Implementation

The methodology used in the interlaboratory exercise follows the steps detailed in Sections 3.1–3.5. Each step of the measurement, including energy calibration, target preparation, charge collection and efficiency determination, was discussed beforehand and guidelines were agreed upon in order to minimize variance and uncertainty from different set-ups. Unavoidable uncertainties associated with each step were estimated and collected for comparisons into Table 3.4 for differential cross-sections and Table 3.5 for thick target yields. In the following sections, each step of the interlaboratory exercise is presented and the results are discussed.

Efficiency (ϵ): In order to minimize discrepancies related to the determination of gamma-ray detector absolute efficiency $\epsilon_{a\gamma}$, it was decided to use the branching ratios of calibration source gamma-ray lines, as reported in a recent IAEA compilation [3.21], and fit the experimental results by the following equation:

$$\epsilon_{a\gamma}(E_\gamma) = a + \frac{b}{E_\gamma} + \frac{c}{E_\gamma^2} + \frac{d}{E_\gamma^3}, \quad (3.3)$$

where E_γ is the energy of the gamma-ray line, and a, b, c, and d are fitting parameters.

Targets: For differential cross-section measurements, thin self-supporting Al films or thin films of Al over thin self-supporting Ag (or Au) films were used. For thick target yield measurements, freshly polished Al foils or freshly evaporated thick films of Al were used. In this instance, ‘thin target’ means that the proton energy loss in the target, i.e. the energy thickness of the target, is much smaller than the natural widths of the resonances to be measured.

Cross-sections: Different approaches were used by the different laboratories in relation to differential cross-section measurement and determination.

One approach is based on Eq. 3.2 for the differential cross-section at incident proton energy E . Due to the isotropy of the emitted gamma radiation, the equation can be simplified to the following:

$$\frac{d\sigma}{d\Omega}(E) = \frac{A_\gamma(E)}{4\pi \cdot N_p \cdot N_{Al} \cdot \varepsilon_{a\gamma}}, \quad (3.4)$$

where $A_\gamma(E)$ is the peak area of the detected gamma-rays, N_p and N_{Al} are the number of incident projectiles and the number of Al atoms per surface unit (target thickness ξ) respectively, and $\varepsilon_{a\gamma}$ is the absolute efficiency of the gamma-ray detector. To use this equation, the composition of the target (usually determined by an independent RBS measurement) and the absolute value of the collected charge related to each gamma-ray spectrum must be known.

Since the above mentioned values are often difficult to accurately obtain, the following approach is often used, which is based on simultaneously measuring the elastic scattering of the projectiles from a heavy component of the target (which could be either a self-supporting film or a very thin evaporated film). Using Eq. 3.4 and the yield of projectiles scattered from the heavy element (H) in the target (Eq. 3.5), one can deduce Eq. 3.6, which is used for the determination of the differential cross-section:

$$A_{sp}(E, \beta) = \sigma_{R,H}(E, \beta) \cdot N_p \cdot N_H \cdot \Omega_p \cdot \varepsilon_{ip}, \quad (3.5)$$

$$\frac{d\sigma}{d\Omega}(E) = \frac{A_\gamma(E) \cdot \sigma_{R,H}(E, \beta) \cdot \Omega_p \cdot \varepsilon_{ip}}{4\pi \cdot r \cdot A_{sp}(E, \beta) \cdot \varepsilon_{ip\gamma}}. \quad (3.6)$$

In the above equations, $A_{sp}(E)$ is the peak area of the detected projectiles scattered from the heavy element (H) at an angle β with respect to the beam direction, at a beam energy E . $\sigma_{R,H}(E, \beta)$ is the Rutherford cross-section at energy E and scattering angle β . Ω_p is the solid angle of the particle detector, with ε_{ip} representing the intrinsic efficiency (typically equal to 1 for protons in the considered energy range). r is the ratio of the number of Al atoms to the number of atoms of the heavy element.

When using the normalization procedure of Eq. 3.6, the underlying assumption is that the elastic scattering cross-sections for heavy elements at the energies applied are purely Rutherford. In this method, the uncertainty related to the determination of the absolute value of the collected charge, which could be very large [3.20], can be avoided by using the Rutherford cross-section for heavy elements, which is precisely and accurately described. Another advantage of this method is that the thickness of the target is not required: only elemental ratios need to be known. Since the elemental ratios of the compound can be determined with a higher degree of accuracy, the uncertainty of the calculation is further minimized. The cross-section determination using Eq. 3.6 may be done for each measured energy point or for just one (plus a few for cross-checking), with the rest of the measurement points normalized to this point. This implies relying upon the reproducibility of relative charge measurements, with corresponding uncertainty usually much smaller than the one affecting the absolute value of the collected charge.

A third approach is based on the transformation of Eq. 3.4 into Eq. 3.7:

$$\frac{d\sigma}{d\Omega}(E) = \frac{A_\gamma(E) \cdot S_{AA}}{4\pi \cdot N_p \cdot \Delta_E \cdot \varepsilon_{a\gamma}}, \quad (3.7)$$

where Δ_E is the energy thickness of the target and S_{AA} is the stopping cross-section in units of energy by atoms per area squared. The target energy thickness may be measured by RBS or determined from the experimental width of a resonance with very small natural width, e.g. the one at 991.9 keV in the $^{27}\text{Al}(p,\gamma)^{28}\text{Si}$ reaction. In this approach, care must be taken when determining S_{AA} with due consideration of the possible oxidation of the aluminium film. In this particular interlaboratory exercise, some of the laboratories followed the approach related to Eq. 3.4, while others determined their cross-sections by Eq. 3.6 or Eq. 3.7.

For thick target measurements, the gamma-ray yield $Y_\gamma(E)$ as a function of proton beam energy E can be calculated using the following formula:

$$Y_\gamma(E) = \frac{A_\gamma(E)}{\varepsilon_{a\gamma} \cdot Q \cdot f_i \cdot f_m \cdot N_{Av} \cdot A^{-1}}, \quad (3.8)$$

where Q is the integrated proton beam current, f_i is the abundance of the isotope producing the gamma-radiation, f_m is the mass fraction of the analysed element, N_{Av} is the Avogadro number and A is the atomic mass of the element. Since pure Al targets were used, both f_i and f_m are equal to 1 in this case.

3.6.2. Experiment

The experimental conditions employed in each laboratory are described in full in Section 4. The essential experimental details related particularly to this interlaboratory exercise are summarized in Table 3.2 and Table 3.3.

TABLE 3.2. EXPERIMENTAL DETAILS FOR EACH OF THE PARTICIPATING LABORATORIES (Five out of ten laboratories)

| | NCSR "Demokritos" | CTN/ IST | KIPT | NSTRI | RBI |
|--|--|--|---|--|--|
| Terminal voltage | X | X | X | X | X |
| Magnetic field | X | | | | |
| Calibration points and methods | 992 keV, $^{27}\text{Al}(p, \gamma)^{28}\text{Si}$ Peak position in RBS spectra | 992 keV, $^{27}\text{Al}(p, \gamma)^{28}\text{Si}$ 672, 872 and 1371 keV, $^{19}\text{F}(p, \alpha\gamma)^{16}\text{O}$ 1645 and 1931 keV, $^{23}\text{Na}(p, p'\gamma)^{23}\text{Na}$ 2400, 2914 and 3660 keV, $^{24}\text{Mg}(p, p'\gamma)^{24}\text{Mg}$ | 992 keV, $^{27}\text{Al}(p, \gamma)^{28}\text{Si}$ Peak position in gamma-ray spectra (direct capture) | 992 keV, $^{27}\text{Al}(p, \gamma)^{28}\text{Si}$ 1880 keV threshold, $^7\text{Li}(p, n)^7\text{Be}$ | 992 keV, $^{27}\text{Al}(p, \gamma)^{28}\text{Si}$ 1880 keV threshold, $^7\text{Li}(p, n)^7\text{Be}$ |
| Calibration of projectile energy | | | | | |
| Type | HPGe | HPGe | DGDK 80B | HPGe | HPGe |
| Active Volume | | | ~80 cm ³ | 213 cm ³ | 108 cm ³ |
| Distance to target | 15 cm | 50 mm | 50 mm | 51.9 mm | 66 mm |
| Angle to beam direction | 90° | 130° | 90° | 90° | 135° |
| Detector parameters | | | | | |
| Absolute efficiency at 844 keV | 1.5×10^{-3} | 3.2×10^{-3} | 21×10^{-3} | 11.9×10^{-3} | 3.0×10^{-3} |
| Absolute efficiency at 1779 keV | — | 2.1×10^{-3} | 9.1×10^{-3} | 5.7×10^{-3} | 1.4×10^{-3} |
| Material and thickness | Pure Al (equivalent thickness 3 keV for 992 keV protons) | 28 $\mu\text{g}/\text{cm}^2$ Al on 100 $\mu\text{g}/\text{cm}^2$ Ag | — | 26 $\mu\text{g}/\text{cm}^2$ Al on 129 $\mu\text{g}/\text{cm}^2$ Ag | 55 $\mu\text{g}/\text{cm}^2$ Al on 6.3 μm Mylar, 3.5 $\mu\text{g}/\text{cm}^2$ Au top layer |
| Target for differential cross-section measurements | | | | | |
| Thickness determined by | Gamma-ray resonance | RBS with alphas | — | RBS with alphas | RBS with alphas |

TABLE 3.2. EXPERIMENTAL DETAILS FOR EACH OF THE PARTICIPATING LABORATORIES (Five out of ten laboratories) (cont.)

| | NCSR “Demokritos” | CTN/ IST | KIPT | NSTRI | RBI |
|--|-------------------------------------|-------------------------------------|-------------------------------------|------------------------------|---|
| Material and thickness | — | Thick Al foil | Thick Al foil | — | — |
| Target for thick target gamma-ray yield measurements | Target and chamber as a Faraday cup | Target and chamber as a Faraday cup | Target and chamber as a Faraday cup | Faraday cup after the target | Target and Faraday cup after target, suppressor around target |
| Normalization procedure | Eq. 3.6 | Eq. 3.7 | | Eq. 3.7 | Eq. 3.7 |

TABLE 3.3. EXPERIMENTAL DETAILS FOR EACH OF THE PARTICIPATING LABORATORIES (other five laboratories)

| | ATOMKI | RUB | CMAM-UAM | Helsinki | LABEC- INFN |
|--|---|--|---|---|--|
| Terminal voltage | | | X | | X |
| Magnetic field | X | X | | X | |
| Calibration points and methods | 992 keV, $^{27}\text{Al}(p, \gamma)^{28}\text{Si}$ | 342 keV, $^{19}\text{F}(p, \alpha \gamma)^{16}\text{O}$ 992 keV, $^{27}\text{Al}(p, \gamma)^{28}\text{Si}$ 1666 keV, $^4\text{He}(^{11}\text{B}, \gamma)^{15}\text{N} (*)$ 5663 keV, $^4\text{He}(^{14}\text{N}, \gamma)^{18}\text{F} (*)$ (*): inverse kinematics with gas target | 992 keV, $^{27}\text{Al}(p, \gamma)^{28}\text{Si}$ Non resonant particle emitting nuclear reaction and RBS according to INDC(NDS)-0589 p. 30 | 3903, 3996 and 5937 keV, $^{14}\text{N}(p, p' \gamma)^{14}\text{N}$ | 992 keV, $^{27}\text{Al}(p, \gamma)^{28}\text{Si}$ 1683 keV, $^{27}\text{Al}(p, p' \gamma)^{27}\text{Al}$ 2876 keV, $^{27}\text{Al}(p, p)^{27}\text{Al}$ 3470 keV, $^{16}\text{O}(p, p)^{16}\text{O}$ |
| Calibration of projectile energy | | | | | |
| Type | HPGe | HPGe | Reverse Ge | Electrode Ge | Coaxial Ge |
| Active Volume | 170 cm ³ | 110 % rel. to $4'' \times 4''$ NaI(Tl) | 178 cm ³ | 38% rel. to $4'' \times 4''$ NaI(Tl) | 235 cm ³ |
| Distance to target | 95 mm | 135 mm | 210.6 mm | 20 mm | 205 mm |
| Angle to beam direction | 55° | 90° | 135° | 55° | 90° |
| Absolute efficiency at 844 keV | 3.6×10^{-3} | 3.2×10^{-3} | 0.9×10^{-3} | 3.1×10^{-3} | 1.2×10^{-3} |
| Absolute efficiency at 1779 keV | 1.9×10^{-3} | 2.1×10^{-3} | 0.6×10^{-3} | 1.5×10^{-3} | 0.8×10^{-3} |
| Target for differential cross-section measurements | 39 $\mu\text{g}/\text{cm}^2$ Al on 33 $\mu\text{g}/\text{cm}^2$ C | Pure Al (equivalent thickness 6.9 keV for 992 keV protons) | 22 $\mu\text{g}/\text{cm}^2$ Al on 39 $\mu\text{g}/\text{cm}^2$ Ag | 203 $\mu\text{g}/\text{cm}^2$ Al | 29 $\mu\text{g}/\text{cm}^2$ Al on 102 $\mu\text{g}/\text{cm}^2$ Ag |
| Thickness determined by | RBS with alphas | Gamma-ray resonance | RBS with Li | ERDA | RBS with alphas; PIXE with protons |

TABLE 3.3. EXPERIMENTAL DETAILS FOR EACH OF THE PARTICIPATING LABORATORIES (other five laboratories) (cont.)

| | ATOMKI | RUB | CMAM-UAM | Helsinki | LABEC-INFN |
|-------------------------|-------------------------------------|--|-------------------------------------|--------------------------|---|
| Material and thickness | — | Pure Al (equivalent thickness 6.9 keV for 992 keV protons) | — | — | Thick Al foil |
| Charge collection | Target and chamber as a Faraday cup | Polarized target | Target and chamber as a Faraday cup | Faraday cup after target | Target and Faraday cup after the target |
| Normalization procedure | Eq. 3.4 | Eq. 3.4 | Eq. 3.6 | Eq. 3.4 | Eq. 3.7 |

3.6.3. Results and discussion

3.6.3.1. Differential cross-section measurements

The results of the differential cross-sections obtained from the reaction $^{27}\text{Al}(p,p'\gamma)^{27}\text{Al}$, $E_\gamma = 844$ keV by the nine laboratories that participated in this interlaboratory exercise (ATOMKI [3.22], University of Bochum [3.23], CMAM-UAM [3.24], University of Helsinki [3.25], LABEC-INFN [3.26], NCSR “Demokritos” [3.27], CTN/IST [3.28], NSTRI [3.29] and RBI [3.30]) are displayed in the first rows of Table 3.2 and Table 3.3 under the row heading ‘Calibration of projectile energy’. The estimated uncertainty budget for the measurement parameters that contribute to the absolute differential cross-section values, for each laboratory, is reported in Table 3.4. The large discrepancies in cross-section values and proton energy calibration, which are the results of the uncertainties present within each experimental set-up, are illustrated in panel II of Fig. 3.2. These discrepancies introduce another degree of difficulty to the accurate assessment of cross-section values. Two main reasons why the resonance points from different laboratories are not directly comparable are (i) the large energy steps that were used, leading to poorly-defined resonances, and (ii) energy calibration discrepancies, which led to different laboratories measuring different energy points.

To assist in the assessment of the experimental values, an evaluated cross-section was produced [3.31]. As part of the evaluation process, a theoretical gamma-ray production cross-section for the $^{27}\text{Al}(p,p'\gamma)^{27}\text{Al}$ reaction was obtained from the calculation of the inelastic (p,p') cross-section in the framework of the R-matrix theory [3.32]. According to [3.31], in the energy range under consideration proton inelastic scattering by Al leaves the residual nucleus mainly in the first excited state ($J^\pi = 1/2^+$, $E_x = 844$ keV), with ~3% contribution from the transition from the second excited state ($J^\pi = 3/2^+$, $E_x = 1015$ keV). Both the cross-sections for the $^{27}\text{Al}(p,p_1)^{27}\text{Al}$ and $^{27}\text{Al}(p,p_2)^{27}\text{Al}$ reactions were calculated and the contribution from the second excited state could be taken into account. The initial data for the resonance parameters that were required for the R-matrix calculations were taken from [3.33]. Comparisons were then made between the theoretical cross-sections and all the experimental data from the interlaboratory exercise, taking into account the uncertainty budget. Based on this analysis, an evaluated cross-section was produced, which represents the best estimation for the actual cross-section value. This evaluated cross-section is illustrated as a solid line in Figs. 3.2 and 3.3.

TABLE 3.4. ESTIMATED UNCERTAINTY BUDGET FOR MEASUREMENT PARAMETERS THAT CONTRIBUTE TO THE ABSOLUTE DIFFERENTIAL CROSS-SECTION VALUES GENERATED BY EACH OF THE LABORATORIES (ERROR: 1 STANDARD DEVIATION)

| Parameters | Uncertainty | | | | | | | | |
|---|-------------|--------|--------------|----------|----------------|----------------------|---------|--------|--------|
| | ATOMKI | RUB | CMAM- UAM | Helsinki | LABEC- INFN | NCSR “Demokritos” | CTN/IST | NSTRI | RBI |
| γ -ray peak area (A_γ) ^a | 1.0% | 1.0–4% | 1% | 1.5–3% | 1.0–3% | 1–3% | 1.0–3% | 1.0% | 1.0–4% |
| p+ heavy element (H) elastic peak area (A_{sp}) | | | | 1.0% | | | 1.0% | 1.0% | < 1% |
| p+ heavy element (H) Rutherford cross-section ($\sigma_{R,H}$) ^b | | | | 1.0% | | | 1.0% | 1.0% | 1.0% |
| Al-to-heavy element (H) atomic ratio (r) | | | 3% | | | | 3% | 4% | 2.0% |
| Al atomic density (N_{Al}) | 3% | | 5% | 3% | | | | | |
| energy thickness of the target (Δ_E) | | 1.5% | | | | 2% | | | |
| stopping power (S_{AA}) | | 4% | | | | 4% | | | |
| number of incident protons (N_p) | 3% | 10% | 1–2% | 3% | | 5% | | | |
| particle detector solid angle (Ω_p) | | | | | 2.4% | | 2.5% | 2.8% | 2.0% |
| absolute γ -ray efficiency (ϵ_{crf}) | 4% | 10% | 4% | 8% | 6% | 5% | 6% | 7% | 7% |
| proton beam energy (E) | 0.1% | 0.1% | 0.1% | 0.1% | 0.1% | 0.1% | 0.1% | < 0.1% | 0.1% |

^a When two values are indicated, the first refers to resonant and the second to off-resonance energy points, respectively.

^b Uncertainty originates in the proton beam energy in the heavy element layer in the target and in the particle detector scattering angle.

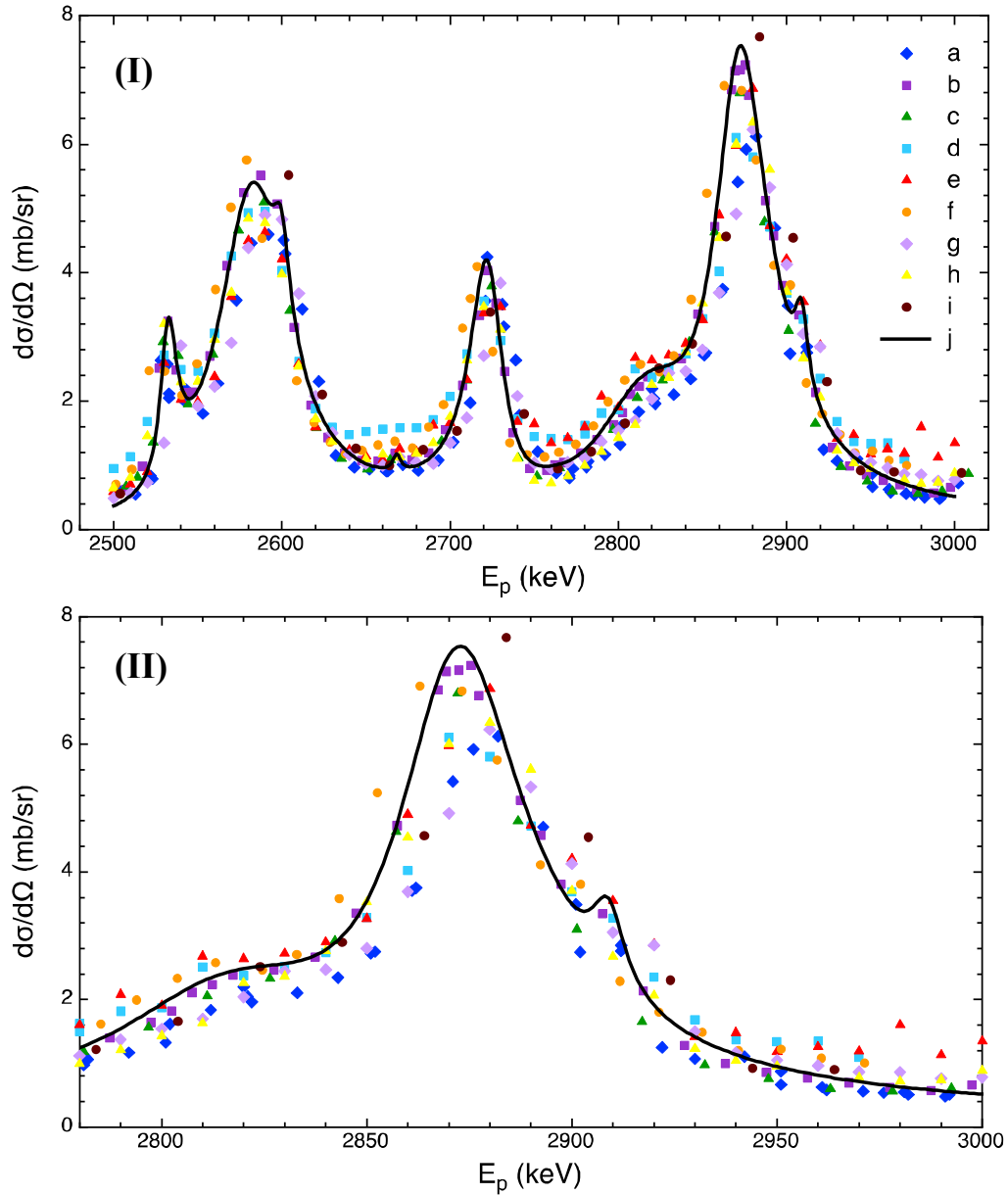


FIG. 3.2. Panel I displays differential gamma-ray production cross-sections of the 844 keV gamma-ray of the $^{27}\text{Al}(p,p'\gamma)^{27}\text{Al}$ reaction as a function of proton energy, deduced from work of each of the nine laboratories participating in this exercise: a) [3.22], b) [3.26], c) [[3.30], d) [3.25], e) [3.24], f) [3.28], g) [3.23], h) [3.29] and i) [3.27]. The solid line (j) [3.31]) corresponds to the evaluated cross-section. Panel II is a close up view of panel I. Within the resonance (peak) region, the large deviations in proton energy between the different datasets are more noticeable.

The energy scales of the different laboratories were then adjusted with respect to the evaluated cross-section, by adding or subtracting amounts up to 8 keV, but less than $3\text{-}\sigma$ of the assessed uncertainty on the calibrated proton beam energy. Using the same energy adjustment for the entire energy interval allows a better comparison of the excitation curves, as shown in Fig. 3.3.I. The discrepancies between measurements made at different laboratories are most apparent in the resonance regions, as shown in Fig. 3.2.II. Evident in Fig 3.3.II, which is a close up of Fig. 3.3.I, is that data outside the resonance region more closely agree and, furthermore, most of the measurements agree within the quoted total uncertainties (10–12%), which stem from the measurement parameters (Table 3.4).

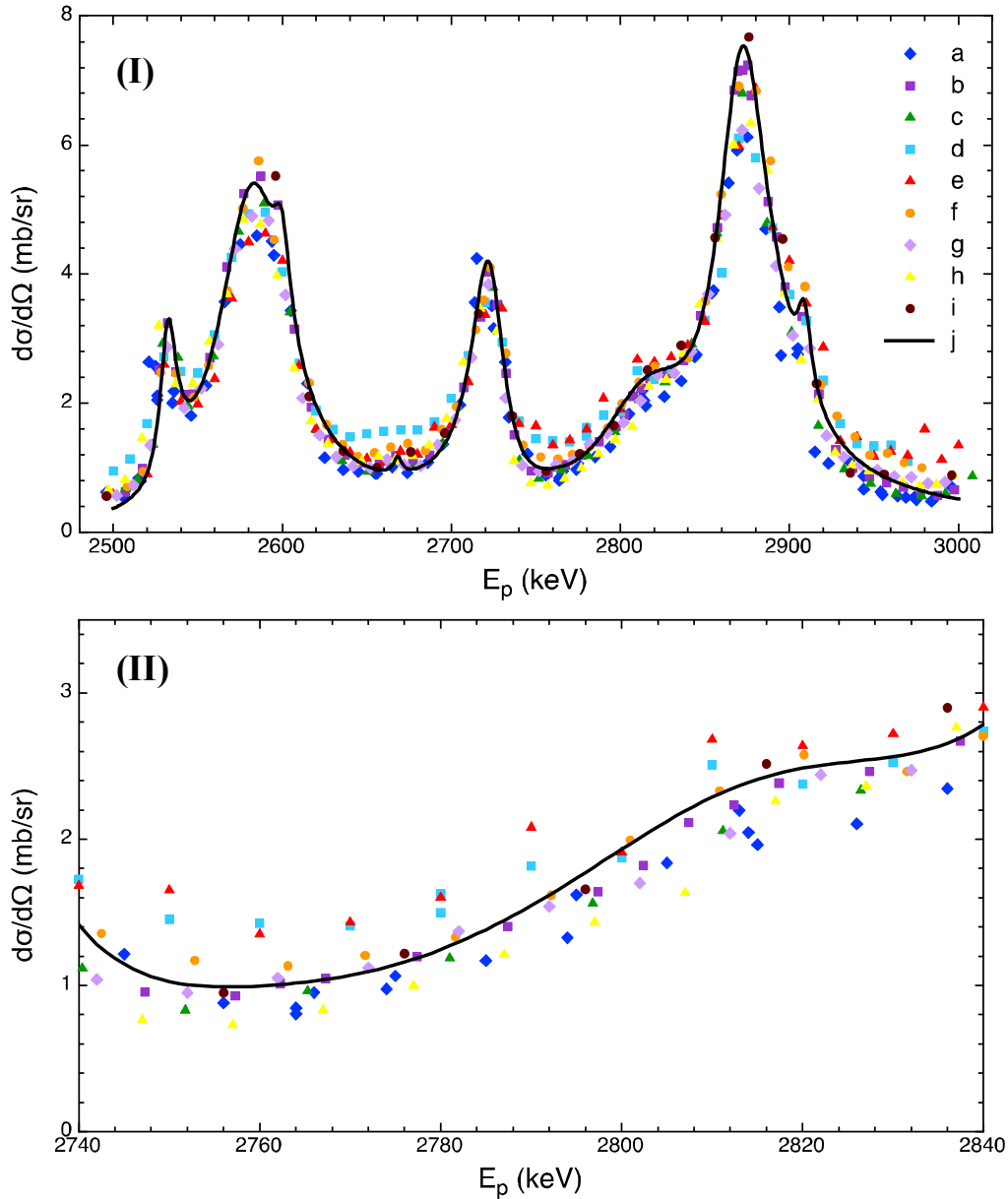


FIG. 3.3. Panel I displays differential gamma-ray production cross-sections of the 844 keV gamma-ray of the $^{27}\text{Al}(p,p'\gamma)^{27}\text{Al}$ reaction as a function of proton energy, after the application of a correction, which is based on the evaluated cross-section, to the energy scales reported by the different laboratories: a) [3.22], b) [3.26], c) [3.30], d) [3.25], e) [3.24], f) [3.28], g) [3.23], h) [3.29] and i) [3.27]. The solid line corresponds to the evaluated data: j) [3.31]. In panel II, which is a close up of panel I, it is shown that, outside of the narrow resonance regions, most of the measurements agree within the quoted total uncertainties (10–12%).

After evaluating the approach used by each laboratory, it can be concluded that the results obtained through methods that were not directly dependent on the absolute value of the collected charge are in slightly better agreement and have discrepancies closer to the quoted uncertainties.

Figure 3.2.II shows in larger detail the discrepancies in projectile energy calibration, raising questions concerning the cause of such large deviations. One of the difficulties with calibrating, particularly for energies higher than 2 MeV, is that there are few narrow resonances to rely on. Table 3.2 and Table 3.3 list the resonances that have been employed for

projectile energy calibration. Since there is a lack of consistency of the energy values of those resonances in the literature, this may be one cause of the discrepancies in projectile energy calibration.

As an example, in the CTN/IST laboratory, proton energy calibration was first performed using the high energy resonances of the $^{24}\text{Mg}(p,p'\gamma)^{24}\text{Mg}$ reaction, which were measured earlier by Boni *et al.* [3.34]. The calibration was later repeated with the resonance for $^{16}\text{O}(p,p)^{16}\text{O}$ at 3470 keV. The fit using the ^{16}O resonance instead of the ^{24}Mg resonances that have energies higher than 2 MeV, leads to a slope that implies a better energy scale agreement between the measured data points of the CTN/IST laboratory and the evaluated cross-section. Support for the discrepancies of the ^{24}Mg resonance energies in comparison with the ^{25}Al resonance energies can be found in recent literature. The energies quoted in the paper of Boni *et al.* are in close agreement with excited states of ^{25}Al taken from the compilation of Endt and van der Leun [3.35]. However recent experimental work [3.36] assigns higher energy values to excited states of ^{25}Al above 5 MeV, the region of the 2914 and 3660 keV resonances.

Regarding the cross-section values, discrepancies higher than 3 times the quoted uncertainties (7–12% at 1σ level) may only be explained by systematic deviations in the assessment of the target elemental ratios and/or of either (a) the particle detector solid angle, if the approach based on Eq. 3.6 is followed, or of (b) the charge and target thickness, if the approach based on Eq. 3.4 or 3.7 is applied. Although background and multiple scattering may give a more than negligible contribution to the particle spectra, such spectra are simple to deal with if the following conditions are met: (i) scattered protons originating near the chamber walls and components do not reach the particle detector and (ii) the heavy element (i.e Ag or Au) peak within the scattered proton spectra is completely separated from other peaks, allowing easy quantification. Moreover, a non-negligible background peak around 844 keV due to interaction of the proton beam with aluminium, stainless steel (847 keV gamma-ray line from the $^{56}\text{Fe}(p,p'\gamma)^{56}\text{Fe}$ reaction) or other materials containing Al or Fe, even at trace levels, found either along the beamline or in the scattering chamber (collimators, beam stopper, Faraday cup) could contribute to the production of higher cross-section values in the off-resonance regions. Integration of all the resonances over the total target thickness smooths and broadens the resonance shape so that the measured cross-section values appear lower, especially in thick targets.

3.6.3.2. Thick target yield measurements

In determining the yield of the gamma-ray with energy $E_\gamma = 1779$ keV from the 991.9 keV resonance of the $^{27}\text{Al}(p,\gamma)^{28}\text{Si}$ reaction, several thick or semi-thick target measurements were made (University of Bochum [3.23], LABEC-INFN [3.37], CTN/IST [3.28] and KIPT [3.38]). The estimated uncertainty budget associated with the measured absolute thick target gamma-ray yields is reported in Table 3.5.

TABLE 3.5. ESTIMATED UNCERTAINTY BUDGET FOR THE MEASURED THICK TARGET GAMMA-RAY YIELDS PERFORMED IN DIFFERENT LABORATORIES (ERROR: ONE STANDARD DEVIATION)

| Quantity | Uncertainty | | | |
|-------------------------------------|-------------|-------------|----------|------|
| | RUB | LABEC- INFN | CTN/ IST | KIPT |
| γ -ray peak area | 3% | 5–8% | 4% | — |
| charge integration (absolute value) | 10% | 5% | 8% | — |
| absolute γ -ray efficiency | 10% | 6% | 5% | — |
| proton beam energy | 0.1% | 0.1% | 0.1% | 0.1% |

In Fig. 3.4, a thick target measurement is shown, whereas in Fig. 3.5 a semi-thick one is displayed. Here, ‘semi-thick’ does not mean ‘thin’, as defined earlier, but rather that the target has a thickness smaller than the proton beam energy range. The smooth line is a generated fit to the data based on the integral of a Breit-Wigner resonance shape with a constant background term, which takes into account the contribution to the integrated yield of resonances at lower energy:

$$Y_{\gamma}(E) = a \cdot \arctan \left[2 \cdot \frac{(E-b)}{c} + \frac{\pi}{2} \right] + d \quad . \quad (3.9)$$

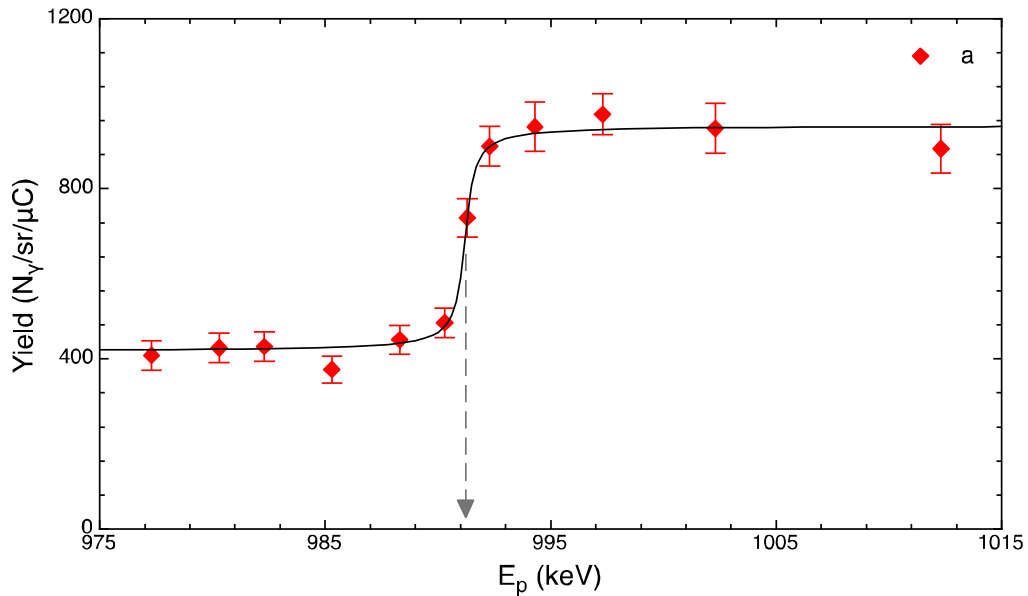


FIG. 3.4. Thick target gamma-ray yield of the 1779 keV gamma-ray from the $^{27}\text{Al}(p,\gamma)^{28}\text{Si}$ reaction as a function of proton energy, around the 991.9 keV resonance. Function deduced from the experimental data of a) [3.37]. Only statistical errors are shown. The arrow indicates the measured resonance energy.

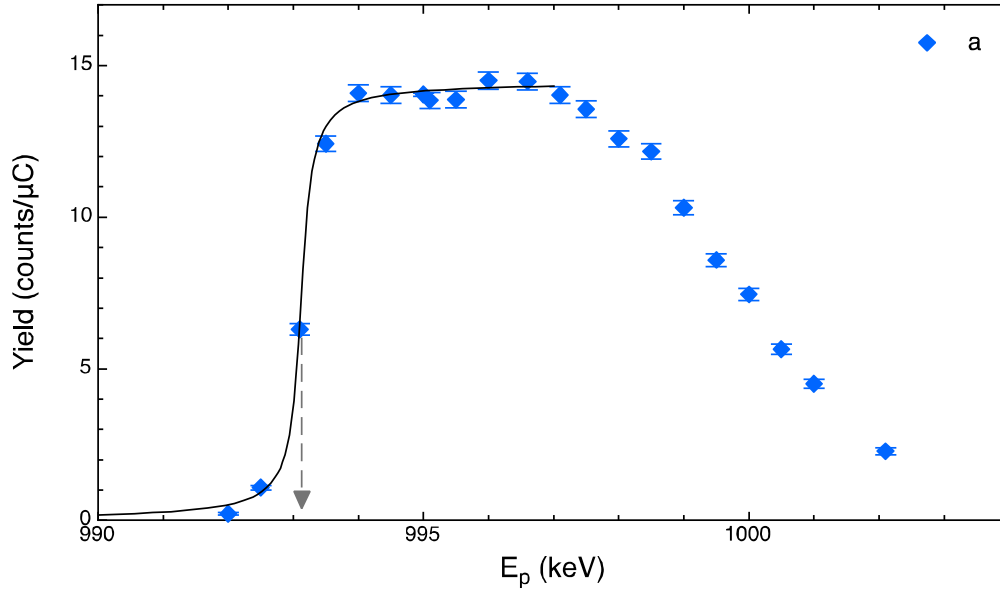


FIG. 3.5. Semi-thick target gamma-ray yield of the 1779 keV gamma-ray from the $^{27}\text{Al}(p,\gamma)^{28}\text{Si}$ reaction as a function of proton energy, around the 991.9 keV resonance, as deduced from the experimental data of a) [3.23]. Only statistical errors are shown. The arrow indicates the measured resonance energy.

Without taking into account information on the energy resolution, i.e. assuming a fresh polished smooth surface or a freshly evaporated Al film, the maximum yield for a thick target $Y_{\max}(\infty)$ (corresponding to $a - \pi$ with a obtained from the fitting function of Eq. 3.9) divided by the number of incident particles and the absolute efficiency, should be constant at the same detection angle (the yield is weakly dependent on the detection angle [3.13]) and given by [3.39]:

$$\frac{Y_{\max}(\infty)}{N_p \epsilon_{a\gamma}} = \frac{\lambda^2}{2} \omega \gamma \frac{M+m}{M} \frac{1}{S_{AA}} \quad (3.10)$$

where λ is the centre-of-mass de Broglie wavelength of the projectile, $\omega \gamma$ is the resonance strength, m and M are the masses of the projectile and target, respectively. The mass ratio corrects for the energy term of the stopping cross-section, which is measured or calculated in the laboratory coordinate system. The yields given in Table 3.6 correspond to the first term of Eq. 3.10 divided by 4π . Correction factors were applied to obtain the thick target yields from semi-thick target yields.

TABLE 3.6. YIELDS FOR RELEVANT PARAMETERS RELATED TO THE MEASUREMENT OF THE 991.9 keV RESONANCE OF THE $^{27}\text{Al}(p,\gamma)^{28}\text{Si}$ REACTION

| Parameters | RUB | LABEC- INFN | CTN/ IST | KIPT |
|---|--------------|--------------|----------------|--------------|
| Maximum yield ($N\gamma/\mu\text{C}/\text{sr}$) | 617 ± 90 | 550 ± 55 | $610 \pm 60^*$ | 600 ± 50 |
| Resonance energy (keV) | 993 ± 1 | 991 ± 1 | 992 ± 1 | 991 ± 1 |
| Energy spread (keV) | 1 | 2 | 2 | 4 |

The maximum yield for CTN/ IST was originally measured to be $618 \text{ N}_\gamma/\mu\text{C}/\text{sr}$ at an angle of 130° , but was multiplied by an angular distribution correction factor [3.13] so that the value could be applied to a 90° angle in order to compare it with the values from the other labs. The results are in agreement with each other within 10% uncertainty, and the weighted average and its associated error give $\omega\gamma = 2.01 \pm 0.11 \text{ eV}$, which is in agreement within the quoted uncertainty with the reference value of $1.93 \pm 0.13 \text{ eV}$ [3.22].

3.6.3.3. Conclusions

The goal for the interlaboratory exercise was to assess and evaluate different methods for the experimental determination of cross-sections and thick target yields of gamma-ray producing nuclear reactions in order to understand the large discrepancies that exist among cross-section data and to determine methods to minimize the discrepancies. Common methodology and conditions were established at the beginning and two simple cases were chosen: one using a thin Al target and one using a thick Al target. Results indicate that one of the major sources of uncertainty is the accelerator energy calibration. Relative differences among laboratories were greater than 10 keV. This may be caused by the lack of consistency in the existing data on resonance energies used for accelerator energy calibration in the energy region between 2 and 4 MeV. In regards to the differential cross-section measurements, the results obtained from laboratories that used a method not directly dependent on the absolute value of the collected charge were found to be in slightly better agreement, with discrepancies closer to the quoted uncertainties.

REFERENCES TO SECTION 3

- [3.1] WANG, Y, NASTASI, M. (Eds), Handbook of Modern Ion Beam Materials Analysis, 2nd edn, Materials Research Society, Pennsylvania (2009) p. 147.
- [3.2] RÄISÄNEN, J., TIKKANEN, P.O., Calibration of accelerator proton energy by the $^{14}\text{N}(p,p'\gamma)^{14}\text{N}$ reaction resonances, Nucl. Instrum. Methods Phys. Res. A **723** (2013) 5.
- [3.3] HARISSOPULOS, S., CHRONIDOU, C., SPYROU, K., PARADELLIS, T., ROLFS, C., SCHULTE, W.H., BECKER, H.W., The $^{27}\text{Al}(p,\gamma)^{28}\text{Si}$ reaction: direct capture cross-section and resonance strengths at $E_p = 0.2\text{--}1.12 \text{ MeV}$, Eur. Phys. J. A **9** (2000) 479.
- [3.4] MARION, J.B., HAGEDORN, F.B., 1.75 MeV resonance in $\text{C}^{13}(p, \gamma)\text{N}^{14}$, Phys. Rev. **104** (1956) 1028.
- [3.5] RAO, P., KUMAR, S., VIKRAMKUMAR, S., RAJU, V.S., Measurement of differential cross-sections and widths of resonances in $^{32}\text{S}(p,p'\gamma)^{32}\text{S}$ reaction in the 3.0 – 4.0 MeV region, Nucl. Instrum. Methods Phys. Res. B **269** (2011) 2557.
- [3.6] FREEMAN, J.M., (p,n) threshold measurements for accelerator calibration and the problem of Q-value deductions, Nucl. Instrum. Methods **134** (1976) 153.
- [3.7] SHAMU, R.E., BERNSTEIN, E.M., PARROTT, M.J., Accelerator energy calibration using the $^{12}\text{C}(\alpha,n_0)^{15}\text{O}$ threshold, Nucl. Instrum. Methods **114** 3 (1974) 605.
- [3.8] OVERLEY, J.C., PARKER, P.D., BROMLEY, D.A., The energy calibration of tandem accelerators, Nucl. Instrum. Methods **68** (1969) 61.
- [3.9] FERRERO, A.M.J., GARCIA, A., GIL, S., ETCHEGOYEN, A., DI TADA, M., PACHECO, A.J., ABRIOLA, D., DIGREGORIO, D.E., ELGUE, M., ETCHEGOYEN, M.C., FERNÁNDEZ NIELLO, J.O., MACCHIAVELLI, A.O.,

- TESTONI, J.E., Improved beam-energy calibration technique for heavy-ion accelerators, Nucl. Instrum. Methods Phys. Res. B **42** 3 (1998) 389.
- [3.10] SANTRA, S., MAHATA, K., SINGH, P., FERNANDES, C.V., HEMALATHA, M., KAILAS, S., Beam energy calibration for the folded tandem ion accelerator, Nucl. Instrum. Methods Phys. Res. A **496** (2003) 44.
- [3.11] DEBERTIN, K., HELMER, R.G., Gamma and X-Ray Spectrometry with Semiconductor Detectors, North Holland, Oxford (1988).
- [3.12] KISS, Z., FAZEKAS, B., OSTOR, J., REVAY, ZS., BELGYA, T., MOLNAR, G.L., KOLTAY, L., Comparison of efficiency functions for Ge gamma-ray detectors in a wide energy range, Nucl. Instrum. Methods Phys. Res. A **418** (1998) 374.
- [3.13] ANTTILA, A., KEINONEN, J., HAUTALA, M., FORSBLOM, I., Use of the $^{27}\text{Al}(p, y)^{28}\text{Si}$, $E_p = 992$ keV resonance as a gamma-ray intensity standard, Nucl. Instrum. Methods **147** (1977) 501.
- [3.14] KARAMANIS, D., LACOSTE, V., ANDRIAMONJE, S., BARREAU, G., PETIT, M., Experimental and simulated efficiency of a HPGe detector with point-like and extended sources, Nucl. Instrum. Methods Phys. Res. A **487** (2002) 477.
- [3.15] ANIL KUMAR, G., MAZUMDAR, I., GOTHE, D.A., Experimental measurements and GEANT4 simulations for a comparative study of efficiencies of $\text{LaBr}_3:\text{Ce}$, $\text{NaI}(\text{Tl})$, and BaF_2 , Nucl. Instrum. Methods Phys. Res. A **610** (2009) 522.
- [3.16] AGOSTINELLI, S., ALLISON, J., AMAKO, K., APOSTOLAKIS, J., ARAUJO, H., *et al.*, Geant4—a simulation toolkit, Nucl. Instrum. Methods Phys. Res. A **506** (2003) 250.
- [3.17] ALLISON, J., AMAKO, K., APOSTOLAKIS, J., ARAUJO, H., ARCE DUBOIS, P., *et al.*, Geant4 developments and applications, IEEE Trans. Nucl. Sci. **53** (2006) 270.
- [3.18] PEYRES, V., GARCÍA-TORANO, E., Efficiency calibration of an extended-range Ge detector by a detailed Monte Carlo simulation, Nucl. Instrum. Methods Phys. Res. A **580** (2007) 296.
- [3.19] JURADO VARGAS, M., GUERRA, A.L., Application of PENELOPE code to the efficiency calibration of coaxial germanium detectors (Proc. 15th Int. Conf. Radionuclide Metrology and its Applications Oxford, 2005), Applied Radiation and Isotopes **64** 10–11 (2006) 1319.
- [3.20] WANG, Y, NASTASI, M. (Eds), Handbook of Modern Ion Beam Materials Analysis, 2nd edn, Materials Research Society, Pennsylvania (2009) p. 347.
- [3.21] INTERNATIONAL ATOMIC ENERGY AGENCY, “Recommended decay data, high energy gamma ray standards and angular correlation coefficients”, Update of X Ray and Gamma Ray Decay Data Standards for Detector Calibration and Other Applications, Vol. 1, IAEA, Vienna (2007).
- [3.22] CSEDREKI, L., *et al.*, unpublished data, available in IBANDL [<https://www-nds.iaea.org/exfor/ibandl.htm>].
- [3.23] BECKER, H.-W., unpublished data.
- [3.24] ZUCCHIATTI, A., *et al.*, unpublished data.
- [3.25] RAISANEN, J., unpublished data, available in [<https://www-nds.iaea.org/exfor/ibandl.htm>].
- [3.26] CHIARI, M., MELON, B., SALVESTRINI, L., FONSECA, M., ALVES, E., JESUS, A.P., Measurement of proton induced γ -ray emission cross-sections on Al from 2.5 to 4.1 MeV, Nucl. Instrum. Methods Phys. Res. B **332** (2014) 355.
- [3.27] LAGOYANNIS, A., *et al.*, unpublished data.
- [3.28] JESUS, A.P., *et al.*, unpublished data, available in IBANDL [<https://www-nds.iaea.org/exfor/ibandl.htm>]

- [3.29] JOKAR, A., KAKUEE, O., LAMEHI-RACHTI, M., SHARIFZADEH, N., FATHOLLAHI, V., Differential cross-section measurements of $^{27}\text{Al}(p,p'\gamma)^{27}\text{Al}$ and $^{27}\text{Al}(p,\alpha)^{24}\text{Mg}$ reactions in the energy range of 1.6–3.0 MeV, Nucl. Instrum. Methods Phys. Res. B **362** (2015) 138.
- [3.30] ZAMBONI, I., *et al.*, unpublished data, available in IBANDL [<https://www-nds.iaea.org/exfor/ibandl.htm>].
- [3.31] GURBICH, A.F., SigmaCalc recent development and present status of the evaluated cross-sections for IBA, Nucl. Instrum. Methods Phys. Res. B **371** (2015) 27.
- [3.32] LANE, A.M., THOMAS, R.G., R-matrix theory of nuclear reactions, Rev. Mod. Phys. **30** (1958) 257.
- [3.33] NELSON, R.O., BILPUCH, E.G., WESTERFELDT, C.R., MICHELL, G.E., Proton resonances in ^{28}Si from $E_x = 13.4$ to 14.5 MeV, Phys. Rev. C **30** (1984) 755.
- [3.34] BONI, C., CEREDA, E., BRAGA MARCAZZAN, G.M., DE TOMASI, V., Prompt gamma emission excitation functions for PIGE analysis, Nucl. Instrum. Methods Phys. Res. B **35** (1988) 80.
- [3.35] ENDT, P.M., VAN DÈR LEUN, C., Energy levels of $A = 21$ –44 nuclei (V), Nucl. Phys. A **214** (1973) 1.
- [3.36] PITTMAN, S.T., BARDAYAN, D.W., BLACKMON, J.C., KOZUB, R.L., SMITH, M.S., Analysis of ^{25}Al energy levels observed in the $^{28}\text{Si}(p,\alpha)^{25}\text{Al}$ reaction, Phys. Rev. C **80** (2009) 038801.
- [3.37] CHIARI, M., unpublished data, available in IBANDL [<https://www-nds.iaea.org/exfor/ibandl.htm>].
- [3.38] GONCHAROV, A., *et al.*, unpublished data.
- [3.39] ROLFS, C.E., AND RODNEY, W.S., Cauldrons in the Cosmos: Nuclear Astrophysics, University of Chicago Press, USA (1988).

4. MEASUREMENTS OF PARTICLE-INDUCED GAMMA-RAY EMISSION (PIGE) CROSS-SECTIONS

One of the most important goals of the CRP was to improve the existing experimental cross-section database for Particle Induced Gamma-ray Emission (PIGE) by performing new cross-section measurements. Measurements were especially important in cases where no data existed or where unresolved discrepancies between measured data needed clarification. At the beginning of the CRP, it was important to unify the approaches used by participants from different laboratories in order to minimize potential discrepancies and errors in cross-section measurements. The methodology, described in detail in Section 3, was adopted by all CRP participants and an effort was made to provide, apart from the absolute values of the cross-sections, a well documented uncertainty budget that considered all the known factors (for details see Section 3) including: the counting statistics of peak areas, thickness of the target, current integration, γ -ray detector absolute efficiency, detector solid angle and dead time. When possible, thin targets were selected to avoid problems related with cross-sections calculated from thick target yields. The accelerator energy was calibrated using well known resonant reactions, such as $^{27}\text{Al}(p,\gamma)^{28}\text{Si}$ at 992 keV, $^{19}\text{F}(p,\alpha\gamma)^{16}\text{O}$ at 872 keV and neutron threshold reactions such as $^7\text{Li}(p,n)^7\text{Be}$ at 1880.6 keV. Uncertainties in the detector angular settings were minimized to a negligible value. When possible, normalization to a Rutherford cross-section was done in order to remove uncertainties due to dead time, improper charge collection and solid angle. The energy step for cross-section measurements was adjusted according to the complexity of the excitation function in order to record all the necessary details.

In the rest of Section 4, all measurements that were completed within the framework of the CRP are explained in detail. All energies, angles and cross-sections are given in the laboratory system. Performed measurements are organized according to the target element. New measurements were compared with the data already existing in the literature, and a critical assessment of all data was performed. Where possible, recommendations concerning which data sets to use are stated. Obtained excitation functions are given in graphical form. Tabulated values were uploaded onto IBANDL (<http://www-nds.iaea.org/ibandl/>). Measured cross-sections are presented in units (mb/sr). When the angular distribution of the emitted γ -ray is isotropic, the units (/sr) reflect the solid angle of the detector. When the angular distribution is anisotropic, the angles of detection are explicitly mentioned in the graphs. Most of the data were published in scientific journals and a complete set of references is given at the end of Section 4.

The laboratories that participated in the CRP measurements:

- Centro de Micro Análisis de Materiales, Universidad Autónoma de Madrid, (CMAM-UAM), Madrid
- University of Helsinki (Helsinki), Helsinki
- Institute for Nuclear Research, Hungarian Academy of Sciences (ATOMKI), Debrecen
- Kharkov Institute of Physics and Technology (KIPT), Kharkov
- Campus Tecnológico Nuclear/Institut Superior Técnico (CTN/IST), Lisbon
- LABEC – Istituto nazionale di Fisica Nucleare (LABEC-INFN), Florence

- National Centre for Scientific Research “Demokritos” (NCSR “Demokritos”), Athens
- Nuclear Science and Technology Research Institute (NSTRI), Tehran
- Ruđer Bošković Institute (RBI), Zagreb
- Ruhr Universität Bochum (RUB), Bochum

4.1. LITHIUM

4.1.1. Gamma-ray production cross-sections of lithium from proton-induced nuclear reactions

Previous thick-target yield measurements on natural lithium [4.1–4.3] determined that there are two γ -rays that have a large enough yield for analytical purposes: the 429 keV γ -ray from the ${}^7\text{Li}(p,n\gamma_{1-0}){}^7\text{Be}$ reaction and the 478 keV γ -ray from the ${}^7\text{Li}(p,p\gamma_{1-0}){}^7\text{Li}$ reaction. Both γ -rays are expected to have an exactly isotropic angular distribution. The (p, γ) radiative capture reactions of both lithium isotopes (${}^6\text{Li}$, 7.5% abundance, and ${}^7\text{Li}$, 92.5% abundance) have just astrophysical significance.

4.1.1.1. ${}^7\text{Li}(p,n\gamma_{1-0}){}^7\text{Be}$: 429 keV γ -ray

Apart from the data already included in the IBANDL compilation, only the paper from Rio *et al.* [4.4] presents emission yields (Fig. 1d from [4.4]) of the 429 keV γ -ray from the ${}^7\text{Li}(p,n\gamma_{1-0}){}^7\text{Be}$ reaction for proton energies from 1 to 3 MeV. However, since the units used in the paper (counts per μC) are arbitrary, the data are of limited practical use for the PIGE technique. Table 4.1 reports the only two cross-section data sets found in the literature and Table 4.2 reports the only two thick-target yield data sets.

TABLE 4.1. DATA IN THE LITERATURE FOR THE DIFFERENTIAL GAMMA-RAY PRODUCTION CROSS-SECTIONS OF 429 keV ${}^7\text{Li}(p,n\gamma_{1-0}){}^7\text{Be}$

| Reference | Data source | Angle | E_p (MeV) | Target | Quoted uncertainties | Data presentation |
|-----------|-------------|-------|-------------|---|-------------------------------------|--------------------|
| [4.5] | IBANDL | 90° | 2.2–3.8 | 1000 Å LiF evaporated on Nuclepore filters | 15% | Tabular (R33 file) |
| [4.6] | IBANDL | 135° | 3.0–5.5 | 50 $\mu\text{g}/\text{cm}^2$ LiF on 30 mg/cm^2 C, coated with 20 $\mu\text{g}/\text{cm}^2$ Au | 1–20% statistical, 13.5% systematic | Tabular (R33 file) |

TABLE 4.2. DATA IN THE LITERATURE FOR THE THICK-TARGET YIELD OF 429 keV ${}^7\text{Li}(p,n\gamma_{1-0}){}^7\text{Be}$

| Reference | Data source | Angle | E_p (MeV) | Target | Quoted uncertainties | Data presentation |
|-----------|-------------|------------|-------------|---|---------------------------------|--------------------|
| [4.2] | IBANDL | 55° | 3.1–4.2 | Pellet of Li chemical compound | — | Tabular (R33 file) |
| [4.3] | IBANDL | 55° | 7.0–9.0 | Pellet of Li powdered chemical compound, 1 mm thick | 2–5% statistical, 7% systematic | Tabular (R33 file) |

Figure 4.1 portrays the cross-sections listed in Table 4.1. The proton energy and the differential cross-sections are given in the laboratory frame of reference, with energy units in keV and cross-section units in mb/sr.

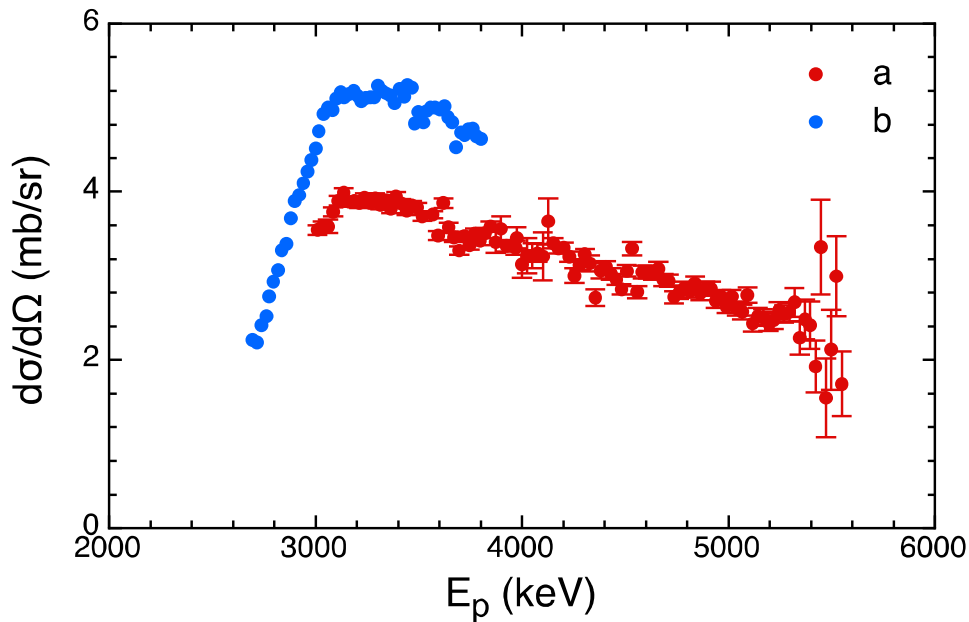


FIG. 4.1. Differential γ -ray production cross-sections of the 429 keV ${}^7\text{Li}(p,n\gamma_{1-0}){}^7\text{Be}$ resonance as a function of proton energy, deduced from the works of a) [4.6] and b) [4.5]. Only statistical errors are shown.

The two cross-section data sets in Fig. 4.1 agree in shape, but data from Boni *et al.* [4.5] are about 30–35% higher than data from Caciolli *et al.* [4.6]. The quoted total uncertainties for the two data sets are 15% and 13.5% respectively. To solve this discrepancy and determine a recommended cross-section data set, a comparison with thick target yields was necessary.

The thick target yields listed in Table 4.2 are portrayed in Fig. 4.2. The proton energy and the thick target yields are given in the laboratory frame of reference, with energy units in keV and gamma-ray yield units in number of emitted gamma-rays per sr and per μC .

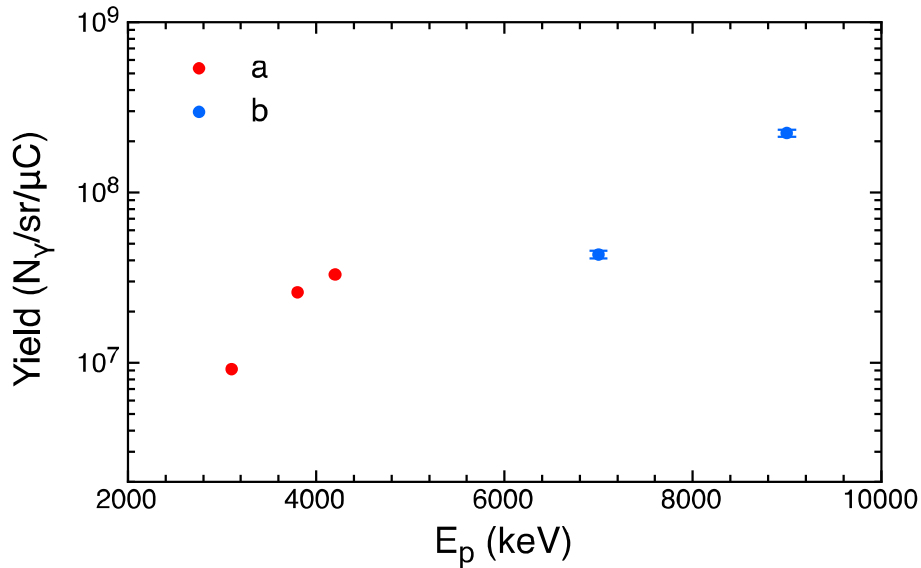


FIG. 4.2. Gamma-ray yield of the 429 keV ${}^7\text{Li}(p,n\gamma_{1-0}){}^7\text{Be}$ resonance as a function of proton energy, deduced from the works of a) [4.2] and b) [4.3]. Only statistical errors are shown.

(a) Assessment and recommended data

The measured thick target gamma-ray yields from Kiss *et al.* [4.2] indicate a proton energy range comparable to those used in the works from Boni *et al.* [4.5] and Caciolli *et al.* [4.6], in particular the values at 3.1 and 3.8 MeV proton energy. These values were compared with the corresponding calculated thick target yields obtained from integrating the gamma-ray producing cross sections measured by Boni *et al.* and Caciolli *et al.* between 3.1 and 3.8 MeV proton energy and making sure to take the proton energy loss into account. As reported in Table 4.3, it was found that the calculated values from Boni *et al.* are 12% higher than the experimental thick-target yield, whereas the calculated values from Caciolli *et al.* are 18% lower. The quoted uncertainties were calculated considering the quoted total uncertainties in the differential cross-section and the uncertainty in the stopping power for protons (4.2% [4.7]). The calculated yields are in reasonable agreement with the thick target yield, within the quoted uncertainties, which enabled a recommended cross-section data set for the 429 keV γ -ray from the ${}^7\text{Li}(p,n\gamma_{1-0}){}^7\text{Be}$ reaction in the range from 2 to 5 MeV proton energy to be obtained. This was completed by multiplying the data from Caciolli *et al.* by 1.18 and the data from Boni *et al.* by 0.89. Additional thick target yield measurements should be carried out in the future to confirm this result.

TABLE 4.3. COMPARISON BETWEEN EXPERIMENTAL THICK TARGET YIELD AND THE INTEGRATED DIFFERENTIAL CROSS-SECTIONS OF 429 keV ${}^7\text{Li}(p,n\gamma_{1-0}){}^7\text{Li}$

| Energy interval | Thick target yield [4.2] | Calculated yield [4.6] | Calculated yield [4.5] |
|-----------------|--------------------------|-------------------------------|-------------------------------|
| 3.8–3.1 MeV | 1.68×10^7 | $(1.42 \pm 0.22) \times 10^7$ | $(1.88 \pm 0.29) \times 10^7$ |

* γ -ray yields are expressed in units of $N_\gamma/\text{sr}/\mu\text{C}$

4.1.1.2. ${}^7\text{Li}(p,p\gamma_{1-0}){}^7\text{Li}$: 478 keV γ -ray

Apart from the data already included in the IBANDL and EXFOR [4.8] compilations, other papers within the literature present cross-section data in arbitrary or relative units, which makes them of limited practical use for the PIGE technique. In particular, the paper from Rio *et al.* [4.4] presents the emission yields of the 478 keV γ -ray for proton energies from 1 to 3 MeV (Fig. 1c in [4.4]), expressed as counts per μC , whereas the paper from Newson *et al.* [4.9] presents the relative yield of the same reaction for energies up to the threshold energy (Fig. 3 in [4.9]).

(a) New measurements

The Lisbon group measured both the differential cross-section and the thick-target yield of the ${}^7\text{Li}(p,p\gamma_{1-0}){}^7\text{Li}$ reaction that emits a 478 keV γ -ray. The experiments were carried out at the 3.0 MV Tandatron accelerator of CTN/IST, using a reaction chamber that is electrically insulated from the beam line and that works together with the target holder and beam stopper as one Faraday cup for beam charge collection. The proton beam energy was calibrated with an accuracy of 0.1 % by using the 1645 keV and 1930.7 keV resonances of the ${}^{23}\text{Na}(p,p'\gamma){}^{23}\text{Na}$ reaction and the 3470 keV resonance of the ${}^{16}\text{O}(p,p){}^{16}\text{O}$ reaction. Gamma-rays were detected by a HPGe detector with 45% nominal efficiency located at 130° with respect to the incident beam direction and at a distance of 55.5 mm from the target, subtending an angle from 100 to 160° .

Measurements of the differential cross-section [4.10] were performed at proton energies from 2.15 to 4.07 MeV, with energy steps ranging from 2 to 20 keV. The target consisted of a thin film of LiF deposited over a thin self-supporting film of Ag. As the stoichiometry of the target was impossible to measure, the absolute differential cross-section was obtained by normalization to previously measured results for energies lower than 2350 keV [4.11]. The measured cross-section is given as the total cross-section on the basis of the isotropicity of the 478 keV γ -ray emission. The quoted uncertainties are 2% statistical and 7% systematic.

The measurements of the thick target yields [4.10, 4.12] were performed at proton energies in the range of 1.6 to 4.0 MeV, with proton beam currents to the order of 20 nA. The target was a pressed pellet made of LiF powder mixed thoroughly with silver powder, yielding an isotopic ${}^7\text{Li}$ fraction of 3.7%. For this experiment, the absolute efficiency of the HPGe detector, as a function of the γ -ray energy, was obtained by measuring the yields of γ -rays produced by radioactive sources (${}^{133}\text{Ba}$ and ${}^{152}\text{Eu}$), calibrated in activity, as well as by Monte Carlo simulations using GEANT and PENELOPE. The combined uncertainty for the measurement of the thick target γ -ray yield is 13.5% and can be broken down into the following components: 1% γ -ray peak area, 6% γ -ray detector absolute efficiency, 10% absolute value of the collected charge, 5% ${}^7\text{Li}$ fraction and 5% stopping power correction.

(b) Data in the literature and assessment

Table 4.4 lists the cross-section data sets found in the literature and the new cross-section data measured in the framework of the CRP [4.10]. Table 4.5 reports the thick-target yield data sets.

TABLE 4.4. DATA IN THE LITERATURE FOR THE DIFFERENTIAL CROSS-SECTIONS OF 478 keV ${}^7\text{Li}(p,p\gamma_{1-0}){}^7\text{Li}$

| Reference | Data source | Angle | E_p (MeV) | Target | Quoted uncertainties | Data presentation |
|-----------|-------------|-------|-------------|--|------------------------------------|---------------------------------|
| [4.13] | EXFOR | 90° | 0.9–1.4 | Li evaporated on Be foil | 20% | Tabular ^a |
| [4.14] | EXFOR | — | 1.7–6.0 | 0.2 mg/cm ² metallic Li evaporated on Ta backing | 10% | Tabular ^a |
| [4.15] | IBANDL | — | 3.0–8.0 | 1 mg/cm ² metallic Li evaporated on 1 mm Mylar backing | 2%–6% | Tabular (R33 file) |
| [4.5] | IBANDL | 90° | 2.2–3.8 | 1000 Å LiF evaporated on Nuclepore filters | 15% | Tabular (R33 file) |
| [4.11] | IBANDL | 135° | 0.6–2.5 | 51 µg/cm ² LiF on 34 µg/cm ² Cu, on 15 µg/cm ² C | 10% | Tabular ^a (R33 file) |
| [4.16] | IBANDL | — | 1.0–1.8 | Thin isotopically enriched ${}^7\text{Li}$ (99.9%) layer evaporated on a Ta disc | 10% | Tabular ^a (R33 file) |
| [4.6] | IBANDL | 135° | 3.0–5.5 | 50 µg/cm ² LiF on 30 µg/cm ² C, coated with 20 µg/cm ² Au | 1–9% statistical, 13.5% systematic | Tabular (R33 file) |
| [4.10] | IBANDL | 130° | 2.1–4.1 | Thin LiF film on a thin Ag film | 2% statistical, 7% systematic | Tabular ^a (R33 file) |

^a cross-section values are given as total (in mbarn)

TABLE 4.5. DATA IN THE LITERATURE FOR THE THICK TARGET YIELD OF 478 keV ${}^7\text{Li}(p,\gamma){}_6^7\text{Li}$

| Reference | Data source | Angle | E_p (MeV) | Target | Quoted uncertainties | Data presentation |
|--------------|-------------|-------|-------------|---|----------------------------------|--------------------|
| [4.1] | IBANDL | 55° | 1.0–2.4 | Li powdered compound pressed into pill, 1 mm thick | — | Tabular (R33 file) |
| [4.2] | IBANDL | 55° | 2.4–4.2 | Pellet of Li chemical compound | — | Tabular (R33 file) |
| [4.3] | IBANDL | 55° | 7.0–9.0 | Pellet of Li powdered chemical compound, 1 mm thick | 2–5% statistical, 7% systematic | Tabular (R33 file) |
| [4.17] | IBANDL | 90° | 1.0–4.1 | Pellets of Li compound (< 10%) mixed with powder graphite and cellulose | — | Tabular (R33 file) |
| [4.10, 4.12] | IBANDL | 130° | 1.6–4.0 | Pellet of LiF mixed with Ag | 1% statistical, 13.5% systematic | Tabular (R33 file) |

Figure 4.3 illustrates the cross-sections that are listed in Table 4.4. The proton energy and the differential cross-sections are given in the laboratory frame of reference, with energy units in keV and cross-section units in mbarn/sr. The values from [4.10], [4.11], [4.13], [4.14] and [4.16] are given in IBANDL as total cross-section: for the comparison shown in Fig. 4.3, the isotropic angular distribution of the emitted γ -ray has been taken into account by scaling the cross-sections down by 4π .

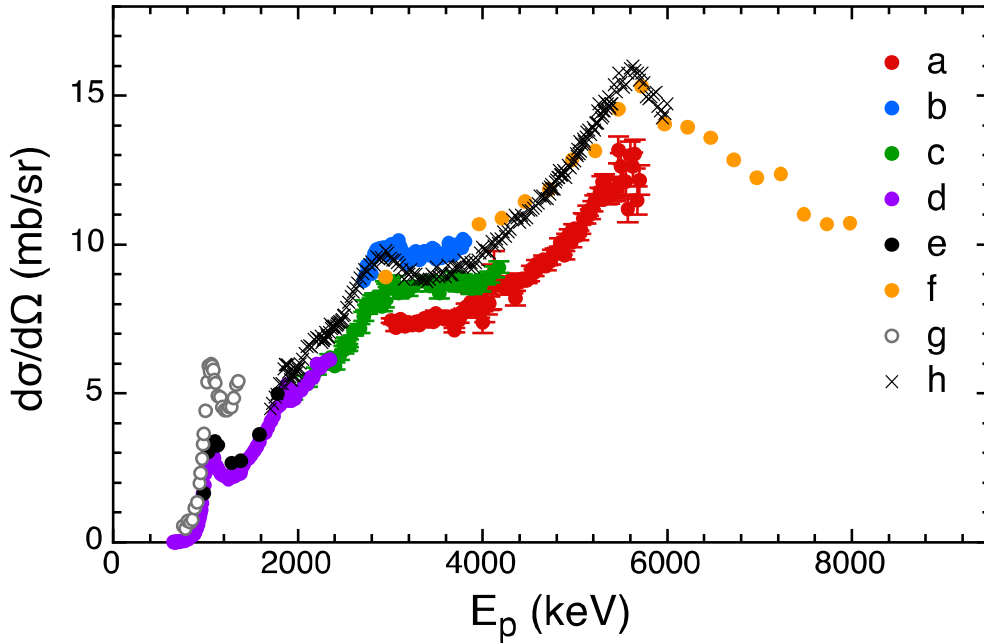


FIG. 4.3. Differential gamma-ray production cross-sections of the 478 keV ${}^7\text{Li}(p, p\gamma_{1-0}){}^7\text{Li}$ resonance as a function of proton energy deduced from the works of a) [4.6], b) [4.5], c) [4.10], d) [4.11], e) [4.16], f) [4.15], g) [4.13] and h) [4.14]. Only statistical errors are shown.

In general there is an overall agreement in shapes between the different data sets. In the proton energy region below 2 MeV, data from Brown *et al.* [4.13] are two times higher than those from Mateus *et al.* [4.11], whereas data from Aslam *et al.* [4.16] are about 17–18% higher than those from Mateus *et al.* Both the quoted uncertainties are 10%, but appear shifted in energy around 30 keV.

In the high proton energy region, above 2 MeV, data from Fonseca *et al.* [4.10] are in obvious agreement with those from Mateus *et al.*, having been normalized to the latter. Cross-section values from Boni *et al.* [4.5] are about 12% higher than those from Fonseca *et al.* while those from Cacioli *et al.* [4.6] are about 10–15% lower. Data from Presser and Bass [4.14] are about 5–10% higher than data from Fonseca *et al.* It should be noted that the bump in the cross-section around 2.9 MeV proton energy and evident in the data from Presser and Bassi, is not visible in the other data, except, partially, in those from Boni *et al.* Although scarce, the data from Guzhovskij *et al.* [4.15] are in reasonable agreement with those from Presser and Bass. Considering that the quoted uncertainties for the different cross-section data sets are around 10–15%, the observed systematic discrepancies between the different data are within the errors.

Figure 4.4 illustrates the thick target yields listed in Table 4.5. The proton energy and the thick target yields are given in the laboratory frame of reference, with energy units in keV and gamma-ray yield units in number of emitted gamma-rays per sr and per μC .

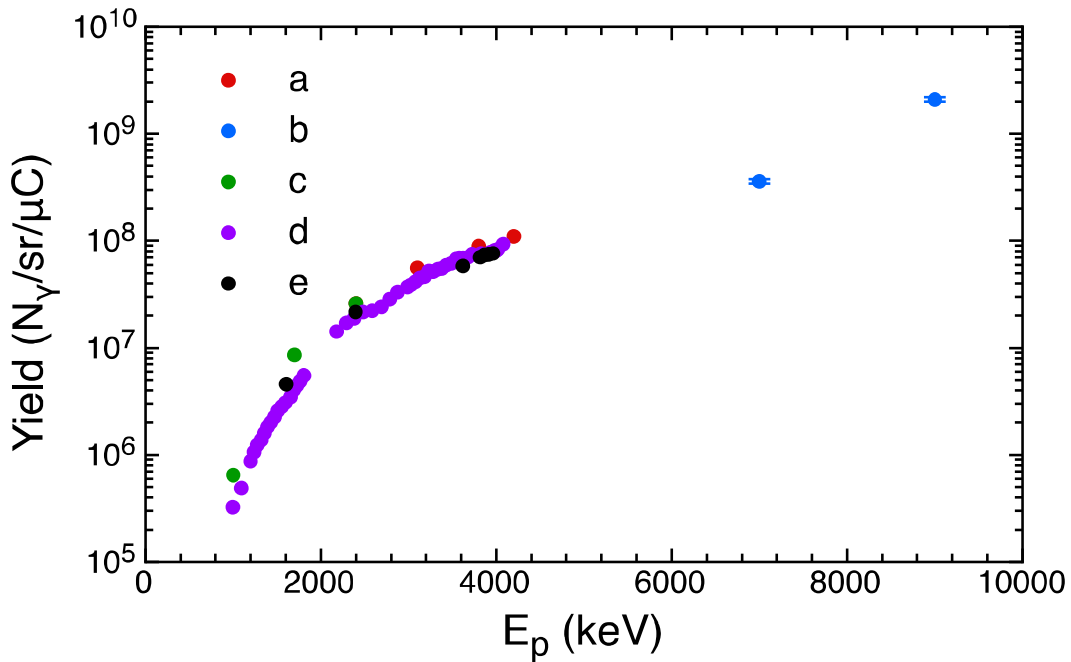


FIG. 4.4. Gamma-ray yield of the 478 keV ${}^7\text{Li}(p,\gamma_{1-0}){}^7\text{Li}$ resonance as a function of proton energy, deduced from the works of a) [4.2], b) [4.3], c) [4.1], d) [4.17] and e) [4.10, 4.12]. Only statistical errors are shown.

Note that the thick target γ -ray yields from Kiss *et al.* [4.2] are normalized to the yields from Antilla *et al.* [4.1] at 2.4 MeV proton energy. Gamma-ray yields from Savidou *et al.* [4.17] are 20% to 50% lower than those from Kiss *et al.* and Antilla *et al.*, with the larger differences appearing in the low proton energy region (below 2.4 MeV). Gamma-ray yields from Jesus *et al.* [4.10, 4.12] are slightly lower (from 5% to 15%) than those from Savidou *et al.*, but still in agreement within the quoted uncertainties in the high proton energy range (above 3.6 MeV). However, the difference increases 15% for the data at 2.4 MeV and 50% for the data at 1.6 MeV. These results indicate that the overall shapes of the three thick-target γ -ray yields obtained from the measurements of Kiss and Antilla, Savidou and Jesus are different.

The measured thick-target γ -ray yields from [4.1], [4.2], [4.10, 4.12] and [4.17], refer to a proton energy range from 4.2 to 1.0 MeV, which is comparable to the one used in several works on cross-section measurements. These yields were compared with corresponding calculated thick-target yields obtained by integrating the γ -ray producing cross-sections measured by Fonseca *et al.*, Caciolli *et al.*, Presser and Bass, Boni *et al.*, Mateus *et al.* and Aslam *et al.*, taking the proton energy loss into account and using the following proton energy integration intervals: 4.2–3.8 MeV, 3.8–3.1 MeV, 3.1–2.4 MeV, 2.4–1.7 MeV and 1.7–1.0 MeV. Given the measured data points, the thick-target yields from Jesus *et al.* will be considered only for comparison within the integration interval 2.4–1.7 MeV. Gamma-ray yields from Räsänen *et al.* [4.3] refer to proton energies that are higher than those used for measuring the differential gamma-ray production cross-sections of the 478 keV γ -ray. Therefore they could not be used for the validation.

As shown in Table 4.6, it was found that, for proton energies above 3 MeV, the calculated yield values from Fonseca *et al.* [4.10] and from Presser and Bass [4.14] are in good agreement with the measured thick target yields and well within the quoted uncertainties. The uncertainties are calculated considering the quoted total uncertainties in the differential cross-section and the uncertainty in the stopping power for protons (4.2% [4.7]). Calculated values based on the values from Boni *et al.* [4.5] are higher than measured γ -yields and values from Caciolli *et al.* [4.6] are lower than the measured γ -yields.

In the energy interval between 2.4 and 1.7 MeV, the calculated γ -ray yield from the only existing data set, i.e. Presser and Bass, is in agreement with the experimental thick target yields from Savidou *et al.* [4.17], Jesus *et al.* [4.10, 4.12] and Antilla *et al.* [4.1], within the quoted uncertainties. It must be noted that, given the measured data points, the thick-target yield from the data of Jesus *et al.* refers to a larger energy range (1.6–2.4 MeV) and therefore overestimates the yield. However, the difference is less than 10%. Below 1.7 MeV there is a factor of 2 between the thick target yields from Savidou *et al.* and Antilla *et al.*, while the calculated yields using the cross-section values of Mateus *et al.* [4.11] and Aslam *et al.* [4.16] lie just in between.

It is recommended that additional thick target yield measurements be carried out, in particular for proton energies below 3 MeV, to solve the aforementioned discrepancies.

The data included in this detailed analysis had a cut-off date of December 2016. Since then, there have been additional publications of new data from CMAM [4.10]. These data were not included in our assessment; however they are available in IBANDL.

TABLE 4.6. COMPARISON BETWEEN EXPERIMENTAL THICK-TARGET YIELDS AND THE INTEGRATED DIFFERENTIAL CROSS-SECTIONS OF 478 keV ${}^7\text{Li}(p,p\gamma)({}^7\text{Li})$

| Energy interval (MeV) | Thick target yield [4.2] | Thick target yield [4.17] | Thick target yield [4.10, 4.12] | Thick target yield [4.1] | Calculated yield [4.10] | Calculated yield [4.6] | Calculated yield [4.14] | Calculated yield [4.5] | Calculated yield [4.11] | Calculated yield [4.16] |
|-----------------------|--------------------------|---------------------------|---------------------------------|--------------------------|-------------------------------|-------------------------------|-------------------------------|-------------------------------|-------------------------------|-------------------------------|
| 4.2-3.8 | 2.10×10^7 | — | — | — | $(1.97 \pm 0.16) \times 10^7$ | $(1.99 \pm 0.28) \times 10^7$ | $(2.34 \pm 0.25) \times 10^7$ | — | — | — |
| 3.8-3.1 | 3.30×10^7 | 3.25×10^7 | — | — | $(3.34 \pm 0.27) \times 10^7$ | $(2.80 \pm 0.23) \times 10^7$ | $(3.40 \pm 0.37) \times 10^7$ | $(3.64 \pm 0.57) \times 10^7$ | — | — |
| 3.1-2.4 | 3.00×10^7 | 2.43×10^7 | — | — | $(2.39 \pm 0.19) \times 10^7$ | — | $(2.82 \pm 0.30) \times 10^7$ | — | — | — |
| 2.4-1.7 | — | 1.45×10^7 | $(1.71 \pm 0.23) \times 10^7$ | 1.74×10^7 | — | — | $(1.58 \pm 0.17) \times 10^7$ | — | — | — |
| 1.7-1.0 | — | 3.93×10^6 | — | 7.95×10^6 | — | — | — | — | $(5.46 \pm 0.59) \times 10^6$ | $(6.51 \pm 0.70) \times 10^6$ |

* γ -ray yields are expressed in units of $N_\gamma/\text{sr}/\mu\text{C}$

4.1.2. Gamma-ray production cross-sections of lithium from deuteron-induced nuclear reactions

Thick target measurements [4.18] determined that, in the case of lithium, only two γ -rays from the ${}^6\text{Li}$ isotope are excited by deuterons with energy less than 2 MeV. These are the 429 keV γ -ray from the ${}^6\text{Li}(d,n\gamma_{1-0}){}^7\text{Be}$ reaction and the 478 keV γ -ray from the ${}^6\text{Li}(d,p\gamma_{1-0}){}^7\text{Li}$ reaction. Both γ -rays have exactly isotropic angular distribution. There are no γ -rays originating from the more abundant ${}^7\text{Li}$ isotope; the ${}^7\text{Li}(d,p\gamma_{1-0}){}^8\text{Li}$ reaction, which emits a γ -ray of 981 keV has a negative Q-value of -192 keV and the threshold for the transition from the first excited level is 1.51 MeV, which means that the yield of the γ -ray is very low for deuterons with energy less than 2 MeV.

4.1.2.1. ${}^6\text{Li}(d,n\gamma_{1-0}){}^7\text{Be}$: 429 keV γ -ray

Table 4.7 lists the only thick-target yield data set that was found for this reaction.

TABLE 4.7. DATA IN THE LITERATURE FOR THE THICK-TARGET YIELD OF 429 keV ${}^6\text{Li}(d,n\gamma_{1-0}){}^7\text{Be}$

| Reference | Data source | Angle | E_d (MeV) | Target | Quoted uncertainties | Data presentation |
|-----------|-------------|-------|-------------|--------------------------------|--------------------------------------|--------------------|
| [4.18] | IBANDL | 135° | 0.7–1.9 | LiSO ₄ thick sample | 7–15% statistical 5% systematical | Tabular (R33 file) |

Figure 4.5 illustrates the thick target yield listed in Table 4.7. The deuteron energy and the thick-target yield are given in the laboratory frame of reference, with energy units in keV and gamma-ray yield units in number of emitted gamma-rays per sr and per μC .

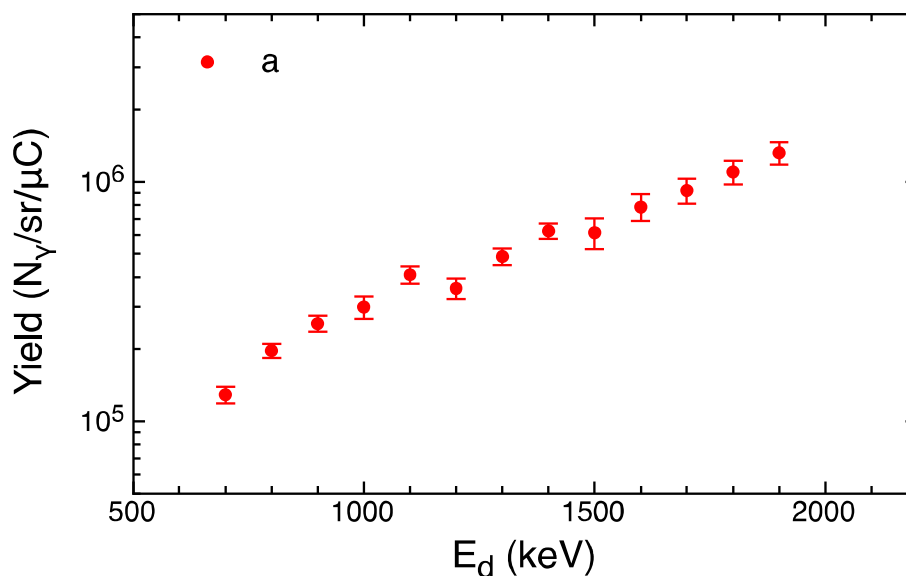


FIG. 4.5. Gamma-ray yield of the 429 keV ${}^6\text{Li}(d,n\gamma_{1-0}){}^7\text{Be}$ resonance as a function of deuteron energy deduced from the work of a) [4.18]. Only statistical errors are shown.

4.1.2.2. ${}^6\text{Li}(d,p\gamma_{1-0}){}^7\text{Li}$: 478 keV γ -ray

After an investigation of the literature, it was found that the only cross-section data was from Sziki *et al.* [4.19] and had already been uploaded to IBANDL. Another data set, from Guzhovskij *et al.* [4.15], is available in the EXFOR database [4.8]. However, it refers to high deuteron energies from 3 to 11 MeV, which means that these cross-sections are of limited practical use for the PIGE technique.

Table 4.8 reports the cross-section data found in the literature and Table 4.9 reports the thick-target yield data found in the literature.

TABLE 4.8. DATA IN THE LITERATURE FOR THE DIFFERENTIAL CROSS-SECTIONS OF 478 keV ${}^6\text{Li}(d,p\gamma_{1-0}){}^7\text{Li}$

| Reference | Data source | Angle | E_d (MeV) | Target | Quoted uncertainties | Data presentation |
|-----------|-------------|-------|-------------|---|-------------------------------------|--------------------|
| [4.19] | IBANDL | 60° | 0.8–2.0 | LiF and LiBO ₂ layer onto Ta substrate | 1–7% statistical 5% systematical | Tabular (R33 file) |

TABLE 4.9. DATA IN THE LITERATURE FOR THE THICK-TARGET YIELD OF 478 keV ${}^6\text{Li}(d,p\gamma_{1-0}){}^7\text{Li}$

| Reference | Data source | Angle | E_d (MeV) | Target | Quoted uncertainties | Data presentation |
|-----------|-------------|-------|-------------|--------------------------------|-------------------------------------|--------------------|
| [4.18] | IBANDL | 135° | 0.8–2.0 | LiSO ₄ thick sample | 2–8% statistical 5% systematical | Tabular (R33 file) |

Figure 4.6 presents the cross-section listed in Table 4.8. The deuteron energy and the differential cross-sections are given in the laboratory frame of reference, with energy units in keV and cross-section units in mb/sr.

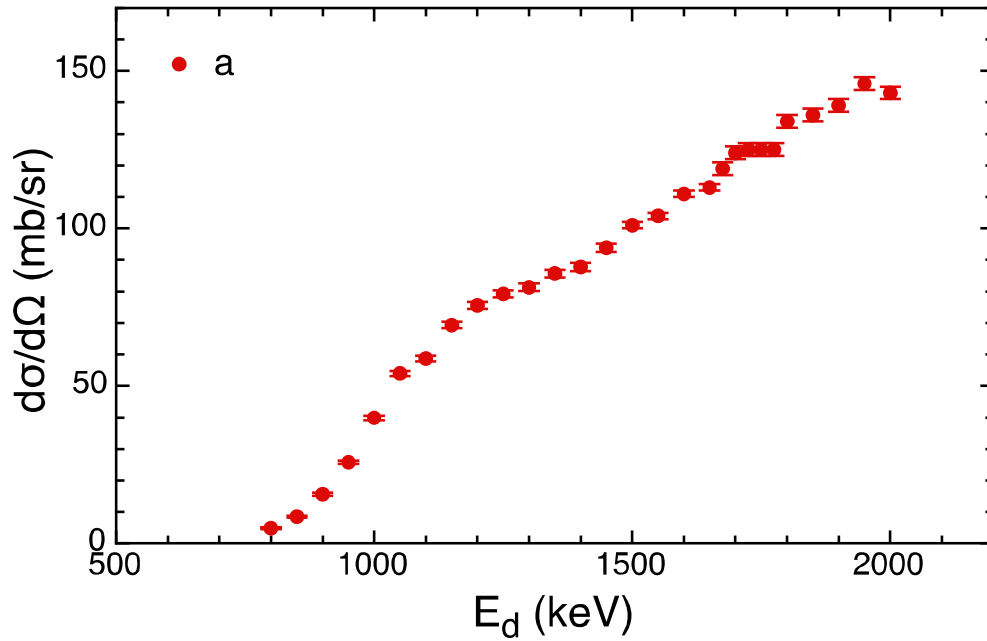


FIG. 4.6. Differential γ -ray production cross-sections of the 478 keV ${}^6\text{Li}(d,p\gamma_{1-0}){}^7\text{Li}$ resonance as a function of deuteron energy deduced from the works of a) [4.19]. Only statistical errors are shown.

Figure 4.7 presents the thick-target yield listed in Table 4.9. The deuteron energy and the thick-target yield are given in the laboratory frame of reference, with energy units in keV and γ -ray yield units in number of emitted γ -rays per sr and per μC .

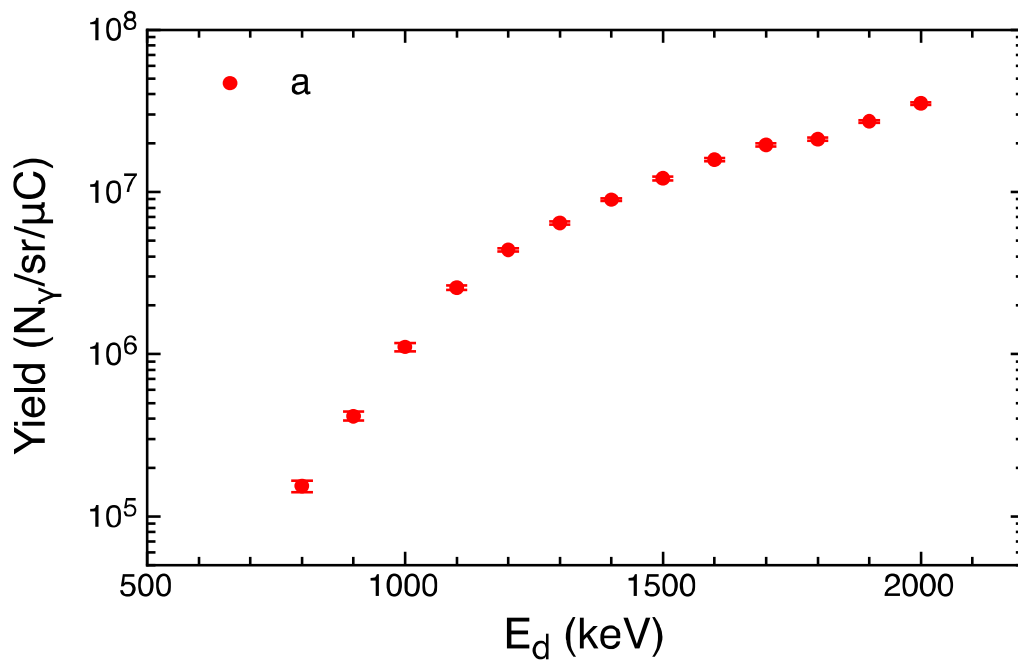


FIG. 4.7. Gamma-ray thick-target yield of the 478 keV ${}^6\text{Li}(d,p\gamma_{1-0}){}^7\text{Li}$ resonance as a function of deuteron energy deduced from the works of a) [4.18]. Only statistical errors are shown.

(c) Assessment and recommended data

Since the measured thick target γ -ray yields from Elekes *et al.* [4.18] refer to the same deuteron energy range used in the work from Sziki *et al.* [4.19], they were compared with corresponding calculated thick-target yields obtained by integrating from 1.0 to 2.0 MeV deuteron energy over the γ -ray producing cross-sections measured by Sziki *et al.*, taking the proton energy loss into account. As shown in Table 4.10, it was found that the calculated values from Sziki *et al.* are in good agreement with the thick-target yield from Elekes *et al.*, within the quoted uncertainties. For the calculated yield, the quoted uncertainties were obtained by considering the quoted total uncertainties in the differential cross-section and the uncertainty in the stopping power for deuterons (assumed conservatively to be 5%). Based on these results, the cross-section data set from Sziki *et al.* for the 478 keV γ -ray from the ${}^6\text{Li}(d,p\gamma_{1-0}){}^7\text{Li}$ reaction in the range from 1 to 2 MeV deuteron energy can be recommended.

TABLE 4.10. COMPARISON BETWEEN EXPERIMENTAL THICK-TARGET YIELD AND THE INTEGRATED DIFFERENTIAL CROSS-SECTIONS OF 478 keV ${}^6\text{Li}(d,p\gamma_{1-0}){}^7\text{Li}$

| Energy interval | Thick target yield [4.18] | Calculated yield [4.19] |
|-----------------|-------------------------------|-------------------------------|
| 2.0–1.0 MeV | $(3.40 \pm 0.25) \times 10^7$ | $(3.02 \pm 0.21) \times 10^7$ |

* γ -ray yields are expressed in units of $\text{N}_\gamma/\text{sr}/\text{mC}$.

4.2. BERYLLIUM

Beryllium can be detected in PIGE measurements of reactions induced by proton, deuteron and alpha particles. The γ -ray emission by heavy ion beams such as carbon, nitrogen or oxygen at energies between 22 and 33 MeV have been reported by Seppälä *et al.* [4.20], but are at present beyond the scope of this report and the IBANDL data base. The deuteron and alpha induced reactions are favorable, because they have a higher sensitivity than the proton-induced reactions, however at the cost of a neutron background. The proton and deuteron induced reactions are often used because they enable the simultaneous determination of other light elements. It should be noted that particle spectroscopy is sometimes favored over the PIGE technique for the detection of Be because the detectors are less sensitive to neutrons and some depth information can be obtained.

4.2.1. Gamma-ray production cross-sections of beryllium from proton-induced nuclear reactions

4.2.1.1. ${}^9\text{Be}(p,\gamma){}^{10}\text{B}$

The ${}^9\text{Be}(p,\gamma){}^{10}\text{B}$ reaction has a limited sensitivity for the detection of beryllium [4.21] due to a low cross-section. The cross-section has been studied for astrophysical purposes in the energy range of 70 keV to 1.8 MeV by Zahnnow *et al.* [4.22] and is displayed in Fig. 4.8 together with earlier data [4.23].

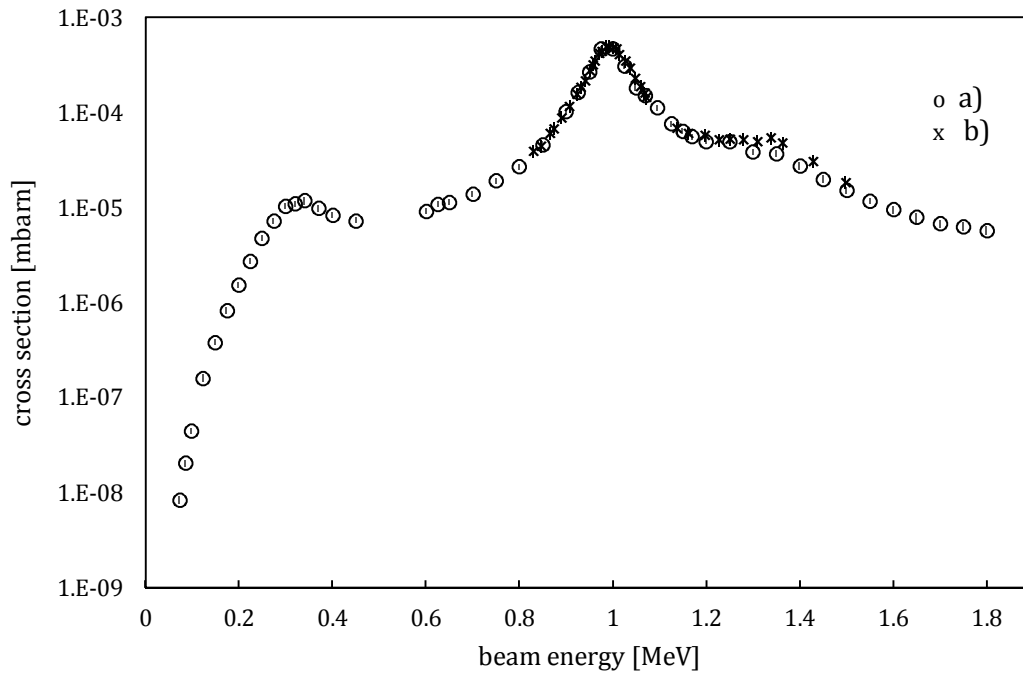


FIG. 4.8. Cross-section of the ${}^9\text{Be}(p,\gamma){}^{10}\text{B}$ reaction as a function of beam energy, deduced from the works of a) [4.22] and b) [4.23]. Data of a narrow resonance at $E_p = 1.087$ have been omitted.

The data from Zahnow *et al.* have been measured with a 4π NaI(Tl) summing crystal that analyzes the summing peak with energies between 6.5 and 8.3 MeV. The authors quote an error for the absolute cross-section of 7%, which is caused mainly by the uncertainty of the detector efficiency.

During the course of the CRP, thick-target yields were measured [4.24] in the beam energy range between 200 keV and 1.6 MeV, to analyze the 718 keV γ -line from the first excited state in ${}^{10}\text{B}$. These measurements were compared to thick-target yields calculated with the ERYA code (see Section 5) by an integration of the data from Zahnow *et al.* (shown in Fig. 4.8). The authors also measured cross-sections for the 718 keV transition at selected energies and renormalized the excitation curve of Zahnow *et al.* to these results. The agreement between the calculated values and the measured thick-target yields is better than 10%, indicating that the relative cross-section data in Fig. 4.8 are correct within this error.

4.2.1.2. ${}^9\text{Be}(p,\alpha\gamma){}^6\text{Li}$

The γ -yield of thick targets has been measured by Meyerhof *et al.* [4.25] and later, in studies dedicated to material analysis, by Anttila *et al.* [4.1] and Kiss *et al.* [4.2] for different γ -lines at several beam energies. The results of the latter two are summarized in Table 4.11. (Table 1 in [4.2]). The 3562 keV line from the ${}^9\text{Be}(p,\alpha\gamma){}^6\text{Li}$ reaction becomes the dominant contribution for increasing beam energies, leading to better sensitivity. This has been used, for example, to measure beryllium concentrations in PIXE/PIGE studies of emeralds with an external proton beam of 3.0 MeV [4.26] and 2.4 MeV [4.27].

TABLE 4.11. THICK TARGET YIELDS FROM 3562 keV γ -RAY OF ${}^9\text{Be}(p,\alpha\gamma){}^6\text{Li}$ AND ${}^9\text{Be}(p,\gamma){}^{10}\text{B}$ (ALL OTHER RESONANCES).

| E_γ (keV) | Yield [$N_\gamma/(\mu\text{C} \cdot \text{sr})$] | | | | | |
|------------------|--|-------------------|-------------------|-------------------|-------------------|-------------------|
| | [4.1] | | | [4.2] | | |
| | 1.0 MeV | 1.7 MeV | 2.4 MeV | 3.1 MeV | 3.8 MeV | 4.2 MeV |
| 415 | 0.4×10^3 | 0.6×10^3 | 0.6×10^3 | — | — | — |
| 718 | 1.2×10^3 | 3.5×10^3 | 5.3×10^3 | — | — | — |
| 1022 | 0.4×10^3 | 0.8×10^3 | 1.3×10^3 | — | — | — |
| 3562 | — | 0.1×10^3 | 2.5×10^4 | 2.5×10^6 | 5.1×10^6 | 6.2×10^6 |
| 7477 | 3.3×10^3 | 3.0×10^3 | — | — | — | — |

The data from Table 4.11 have been measured at a detection angle of 55° . No detailed error discussion is given but the authors estimate that the main error is probably due to the uncertainties in the stopping power.

4.2.2. Gamma-ray production cross-sections of beryllium from deuteron-induced nuclear reactions

4.2.2.1. ${}^9\text{Be}(d,n\gamma){}^{10}\text{B}$

Among the deuteron induced reactions, the ${}^9\text{Be}(d,n\gamma){}^{10}\text{B}$ reaction is the only γ -ray emitting one with potential for material analysis. It has the drawback of a relatively high neutron flux, which is disadvantageous for Germanium detectors and can cause serious deterioration of the detector properties. Nevertheless it has a high sensitivity for the beryllium detection comparable to the α -induced reaction (see below).

The first excited state in ${}^{10}\text{B}$ has spin value $1+$, and therefore the emitted γ -ray is expected to have anisotropic angular distribution. The cross-section for this γ -line 718 keV has been measured with thin targets in the energy range 600–2 MeV under a detection angle of 60° by Sziki *et al.* [4.19]. The data are presented in Fig. 4.9. The error bars in the figure represent the error in the number of target atoms ($< 1\%$), the charge accumulation ($< 0.3\%$), the detector efficiency (3 %) and the stopping power (3%).

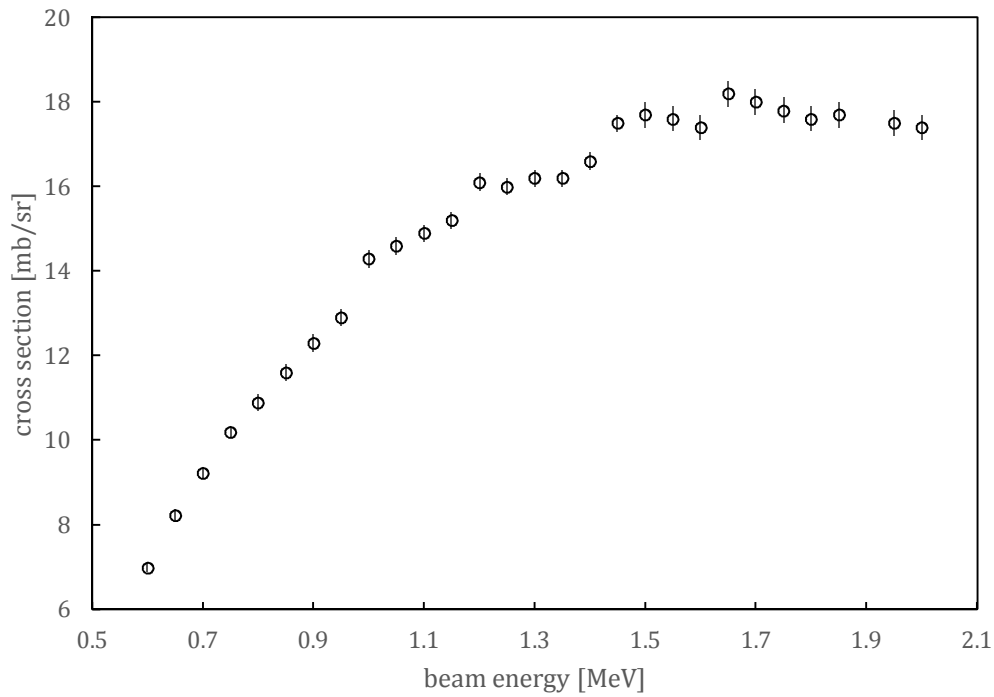


FIG. 4.9. Cross-section of the 718 keV ${}^9\text{Be}(d,n\gamma){}^{10}\text{B}$ resonance at 60° as a function of beam energy in MeV, deduced from the work of [4.19].

Perdikakis *et al.* [4.21] have measured thick target yields for beam energies between 600 keV and 2.1 MeV and also for the 718 keV line, but with a detection angle of 90° . For the beam energy of 1.5 MeV, they report 1.1×10^7 gammas/ $(\mu\text{C}\cdot\text{sr})$. The energy dependence is displayed in Fig. 4.10.

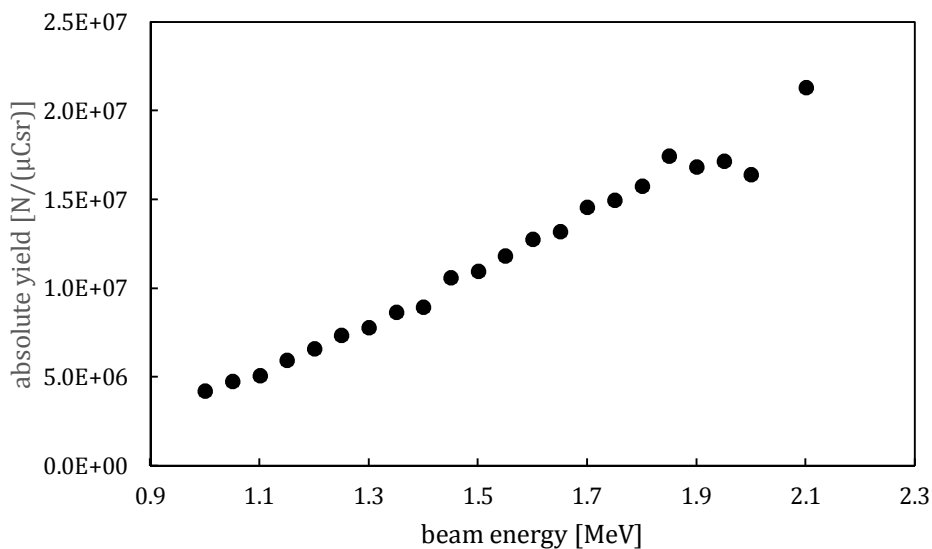


FIG. 4.10. Thick target absolute yield for the 718 keV ${}^9\text{Be}(d,n\gamma){}^{10}\text{B}$ resonance at 90° as a function of beam energy in MeV, as deduced from the work of [4.21].

The angular distribution of the 718 keV line was investigated at the beam energy of 1.85 MeV at angles of 90°, 75° and 60° and found to be isotropic within 15%. In this pioneering work, the reaction was used to analyze Be in soil, asphalt and concrete, with sensitivities below 100 ppm.

4.2.3. Gamma-ray production cross-sections of beryllium from alpha-induced nuclear reactions

4.2.3.1. ${}^9\text{Be}(\alpha, n\gamma){}^{12}\text{C}$

The gamma emission of the α -induced reaction on beryllium is for analysis purposes similar to the case of the deuteron-induced reaction in that it is also hampered by the high neutron flux and therefore not often used. The deuteron-induced reaction, however, has the advantage of being sensitive to other light elements. Nevertheless, the alpha-induced reaction has some importance for the analysis of fusion devices [4.28] and can be used for analysis with accelerator beams as well. Borderie *et al* [4.29] explored the analytical potential by estimating the sensitivity for Be in Nb with a beam energy of 3.5 MeV, but did not report cross-sections or thick-target yields. The sensitivity was estimated to be 0.5 ppm. Later, Lappalainen *et al.* [4.30] measured the thick-target yield at 2.4 MeV to be 1.6×10^6 gammas/($\mu\text{C}\cdot\text{sr}$) at a detection angle of 55° and deduced a detection limit in volcanic stone of 0.45 ppm. Future measurements at various beam energies are recommended.

It should be noted that thick-target yields for beam energies between 5.6 and 10 MeV have been measured by Heaton *et al.* [4.31]. These measurements are needed for the calculation of the background of ultralow-background experiments, but such high beam energies may not be useful for material analysis.

4.3. BORON

4.3.1. Gamma-ray production cross-sections of boron from proton-induced nuclear reactions

Boron is the fifth lightest element, consisting of two isotopes: ${}^{11}\text{B}$ (80.1%) and ${}^{10}\text{B}$ (19.9%). Its low Z makes detection almost impossible with the PIXE technique and it can only be quantified by other IBA techniques (EBS, NRA, etc.) when present in suitable matrices. PIGE has been proven to be a reliable and widely used method for its detection and quantification. The most commonly used reactions in PIGE are ${}^{10}\text{B}(\text{p}, \alpha\gamma_{1-0}){}^7\text{Be}$, ${}^{10}\text{B}(\text{p}, \text{p}'\gamma_{1-0}){}^{10}\text{B}$ and ${}^{11}\text{B}(\text{p}, \text{p}'\gamma_{1-0}){}^{11}\text{B}$, which emit the 429, 718 and 2125 keV gamma-rays, respectively. Despite the fact that they have been used for over two decades [4.5, 4.32, 4.33], the available cross-section data contains large discrepancies, with differences that in some cases reach up to a factor of 5. In the framework of the present CRP, a new set of measurements was considered necessary in order to untangle these differences.

4.3.1.1. ${}^{10}\text{B}(\text{p}, \alpha\gamma_{1-0}){}^7\text{Be}$: 429 keV γ -ray

(a) New measurements

The 429 keV γ -ray is emitted from the de-excitation of the first excited level of ${}^7\text{Be}$, populated through the ${}^{10}\text{B}(\text{p}, \alpha\gamma){}^7\text{Be}$ reaction. The angular distribution of this γ -ray is expected to be isotropic since the spin of the first excited state of ${}^7\text{Be}$ is $-1/2$. A recent measurement of the differential cross-section of the ${}^{10}\text{B}(\text{p}, \alpha\gamma_{1-0}){}^7\text{Be}$ reaction was performed by Lagoyannis *et*

al. [4.34] for eight angles and for the proton energy range between 2.0 to 5.0 MeV with a variable step of 20 to 40 keV. The measurement was performed at the 5.5 MV Tandem Accelerator installed at the Institute of Nuclear and Particle Physics, NCSR “Demokritos”. The energy calibration of the accelerator was performed using the narrow resonances of $^{27}\text{Al}(p,\gamma)^{28}\text{Si}$ and $^{13}\text{C}(p,\gamma)^{14}\text{N}$ at $E_p = 991.9$ and 1746.9 keV, respectively. Two thin-targets were used throughout the experiment: an enriched ^{10}B and a natural ^{10}B . Both targets were produced by electron gun evaporation onto tantalum backings and were characterized by simultaneously implementing the EBS and NRA techniques. The targets were placed at the center of a cylindrical chamber, which also acted as a Faraday cup. The beam charge was collected using a current integrator while a suppression voltage of + 300 volts was applied onto a tantalum collimator placed ~ 1 meter before the chamber. The produced γ -rays were detected using four HPGe detectors placed at initial angles of 0° , 55° , 90° and 165° with respect to the beam direction, and at a distance of ~ 25 cm from the target. After each energy step, the detectors were rotated by 15° to a set of four new angles, i.e. 15° , 40° , 105° and 150° . The energy and efficiency calibration of the HPGe detectors were performed using a calibrated point source of ^{152}Eu [4.34].

The statistical error derived from the integration of the accumulated spectrum peaks did not exceed 5%, but the overall systematic error, which takes into account the uncertainties from (i) beam charge collection, (ii) efficiency calibration and (iii) target thickness was estimated at 8%. The uncertainty budget can be found in Table 4.12.

TABLE 4.12. UNCERTAINTY BUDGET FOR THE DIFFERENTIAL CROSS- SECTIONS OF 429 keV γ -RAY OF $^{10}\text{B}(p,\alpha\gamma)^7\text{Be}$ [4.34]

| Quantity | Uncertainty |
|-----------------------|-------------|
| Peak Integration | 3–5% |
| Beam charge | 3.5 % |
| Target thickness | 7% |
| Detector’s efficiency | 3% |

The measured differential cross-sections with respect to the proton beam energy are presented in Fig. 4.11.

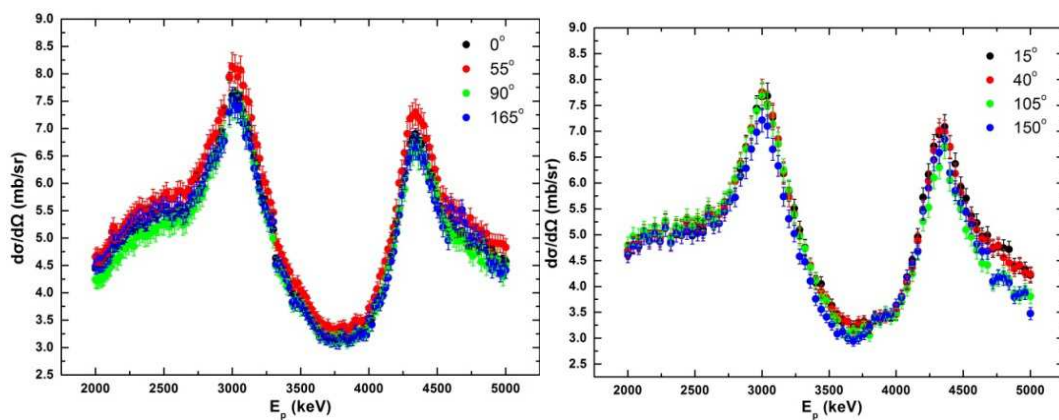


FIG. 4.11. Differential cross-sections of the 429 keV $^{10}\text{B}(p,\alpha\gamma)^7\text{Be}$ resonance as a function of proton energy, deduced from the work of [4.34]. Gamma-rays detected from eight different angles with respect to the beam direction.

In addition to the differential cross-section measurements, new thick-target yields were measured by Chiari *et al.* [4.35]. Three HPGe detectors were placed at 0° , 45° and 90° with respect to the beam axis and were calibrated using two point sources; ^{152}Eu and ^{226}Ra . The proton beam ranged from 2.5 to 4.1 MeV in steps of 150 keV. The accelerator was calibrated using the resonances at 991.86 keV, 1683.57 and 3470 keV from the $^{27}\text{Al}(p,\gamma)^{28}\text{Si}$, $^{27}\text{Al}(p,p'\gamma)^{27}\text{Al}$ and $^{16}\text{O}(p,p)^{16}\text{O}$ reactions, respectively. A voltage of + 300 V was applied to the target in order to suppress secondary electrons emission. The uncertainty budget of the experiment is summarized in Table 4.13 and the results are shown in Fig. 4.12.

TABLE 4.13. UNCERTAINTY BUDGET FOR THE THICK-TARGET YIELDS FOR 429 keV γ -RAY OF $^{10}\text{B}(p,\alpha\gamma)^7\text{Be}$ [4.35]

| Quantity | Uncertainty |
|--------------------------------|-------------|
| Peak Area | 1–2% |
| Beam charge | 4 % |
| Sample Composition | 2 % |
| Stopping power | 4% |
| Detector's absolute efficiency | 6% |

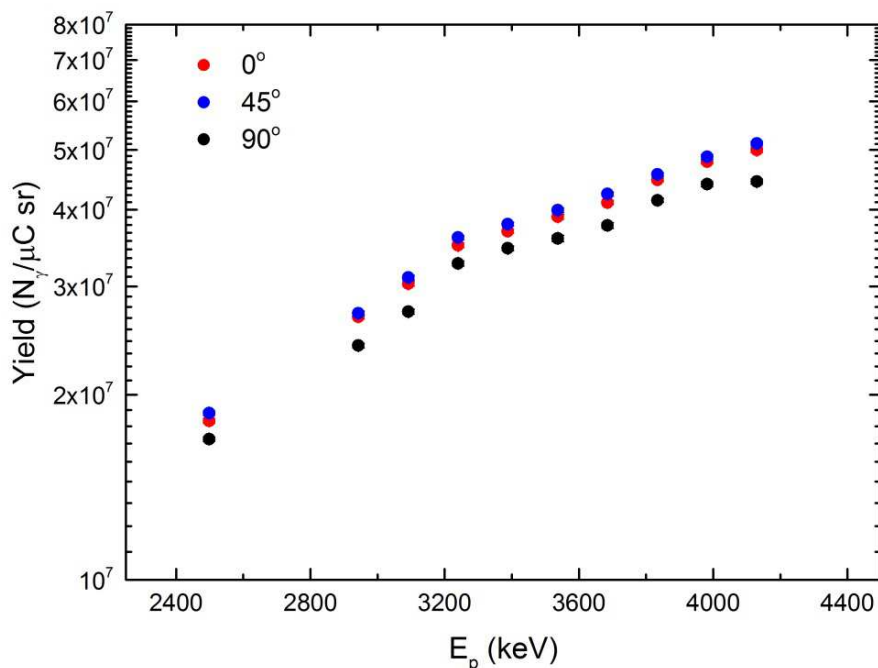


FIG. 4.12. Thick target yields of the 429 keV $^{10}\text{B}(p,\alpha\gamma)^7\text{Be}$ resonance as a function of proton energy, deduced from the work of [4.35]. Gamma-rays detected at angles of 0° , 45° and 90° with respect to the beam axis.

(b) Data in the literature and assessment

In Fig. 4.13, a compilation of the existing cross-section data are presented along with the new data from Lagoyannis *et al.* [4.34] at 55° .

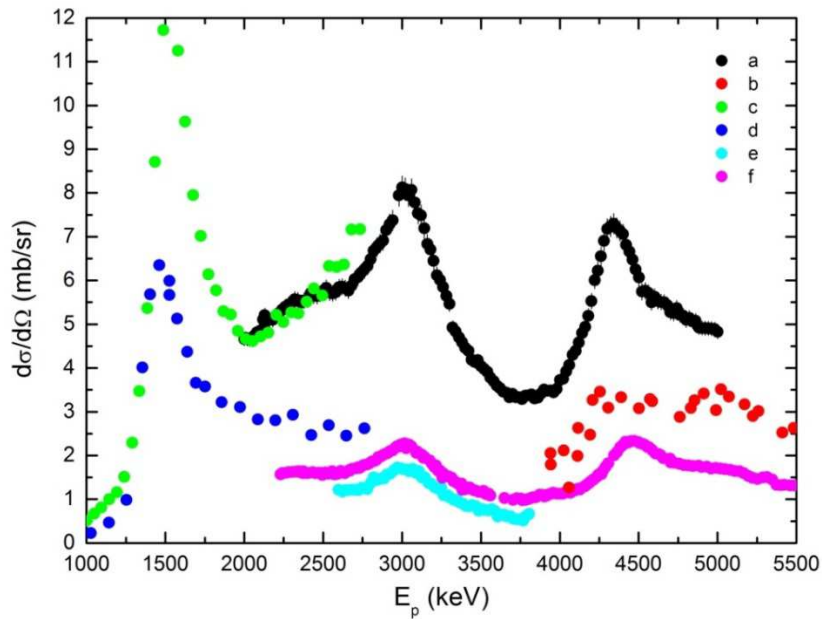


FIG. 4.13. Comparison of the available differential cross-sections of the 429 keV $^{10}\text{B}(p,\alpha\gamma)^7\text{Be}$ resonance as a function of proton energy. Data from the works of (a) [4.34] at 55° , (b) [4.32], (c) [4.33] at 90° , (d) [4.36] at 0° , (e) [4.5] at 90° , and (f) [4.37] at 55° .

The data reveals huge discrepancies between the existing datasets and confirms the need for new measurements, both of which issues were addressed within the framework of this CRP. The differential cross-sections of the $^{10}\text{B}(p,\alpha\gamma_{1-0})^7\text{Be}$ reaction were measured by Ophel *et al.* [4.37] using a $7.6\text{ cm} \times 7.6\text{ cm}$ sodium iodide crystal placed at 55° for the proton energy range between 2.4 MeV and 7.2 MeV. The target was composed of a layer of enriched 99.8% ^{10}B with a thickness of $675\text{ }\mu\text{g}/\text{cm}^2$ supported by a tantalum backing. The old data are approximately 3.5 times lower than the new measurements, a factor which cannot be explained by the 20% uncertainty given by the authors. However, the authors state that in the derivation of the cross-section data, they used the nominal thickness of the target as was provided by the manufacturer and that no additional measurement was performed. Comparison of the data also reveals a slight energy shift of $\sim 70\text{ keV}$ above $E_p = 4.2\text{ MeV}$.

The measurements from Boni *et al.* [4.5] are lower by a factor of ~ 5 compared with the new data, but there is a high level of agreement with respect to the excitation function. The detection setup consisted of a HPGe detector placed at 90° and the proton energy range covered was between 2.2 and 3.8 MeV with a 20 keV step. The target used was composed of a thin (600 Å) layer of natural boron evaporated onto a Nulcepore filter. The systematic uncertainty, as stated by the authors, is 15%, which cannot explain the existing differences.

Segel *et al.* [4.32] used a thin enriched 96% metallic ^{10}B target, which was evaporated onto a carbon foil. The produced gamma-rays were detected by two large NaI detectors placed perpendicularly to the beam axis and were operated together and separately. The authors report a rather high dead time (50%) during the measurement: a fact which could explain the disagreement between the reported cross-sections and those of Lagoyannis *et al.* [4.34].

There is no clear reason for the disagreement between the new data and those of Hunt *et al.* [4.36] since an uncertainty budget is not provided by the authors. For the experiment, they

used a $4'' \times 4''$ NaI(Th) detector placed at 0° and a set of thin ($10\text{--}100 \mu\text{g}/\text{cm}^2$) enriched (99%) ^{10}B targets evaporated onto copper or tantalum backings.

Finally, there is very good agreement between the new data and the data from Day *et al.* [4.33], for the proton energy range between 2.0 and 2.5 MeV. Above 2.5 MeV, Day *et al.* claim that there is an overestimation of the reported cross-sections coming from the overlapping of the 429 keV and 718 keV peaks due to the poor resolution of the NaI detector used.

Further assessment of the cross-section data was done by comparing the integrated cross-section data with previously reported thick-target yields in Fig. 4.14. Anttila *et al.* [4.1] measured thick-target yields in two proton energies: 1.7 and 2.4 MeV. Additional data for higher proton energies are provided by Kiss *et al.* [4.2]. However, the data of Kiss are not absolute measurements but are normalized to those of Anttila *et al.* at 2.4 MeV. An independent measurement by Savidou *et al.* [4.17] was also included in the comparison, as was the data of Chiari *et al.* [4.35]. Since Chiari *et al.* measured isotopic thick-target yields, the data had to be normalized to the elemental in order for accurate comparisons to be made with the data from Antilla, Savidou and Kiss. The integrated cross-section data were normalized to the closest thick-target yield, with the exception of the data from Lagoyannis *et al.* [4.34], for which a normalization factor was not used. The comparison indicates that there is close agreement between most of the thick-target data and the data of Day *et al.* and Lagoyannis *et al.*

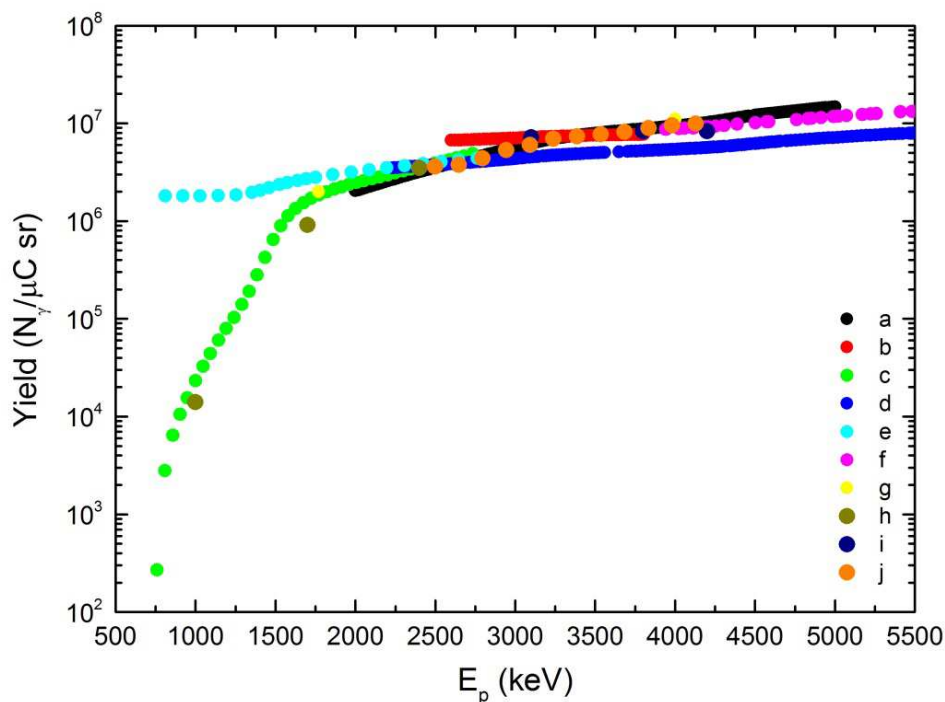


FIG. 4.14. Comparison of the thick-target yields of the 429 keV $^{10}\text{B}(p,\alpha)^7\text{Be}$ resonance as a function of proton energy. Gamma-rays were detected at 0° and were normalized to elemental yields. Deduced from the works of (a) [4.34], (b) [4.5], (c) [4.33], (d) [4.37], (e) [4.36], (f) [4.32], (g) [4.17], (h) [4.1], (i) [4.2] and (j) [4.35].

(c) Recommended data

For the proton energy range between 0.94 and 2.0 MeV, the dataset of Day *et al.* [4.33] is recommended, since it is in close agreement with the thick-target yield measurements. Moreover, Mateus *et al.* [4.38] have applied these data and successfully reproduced the concentration of boron in various thick samples. For the energy range above 2.0 MeV, the data of Lagoyannis *et al.* [4.34] are recommended, since they agree with those of Day *et al.* in the common energy range and reproduce the measured thick-target yields by Chiari [4.35], Kiss [4.2] and Savidou [4.17].

4.3.1.2. $^{10}\text{B}(p,p\gamma_{1-0})^{10}\text{B}$: 718 keV γ -ray

(a) New measurements

The 718 keV γ -ray is the result of the de-excitation from the first excited state of ^{10}B , which is populated through the $^{10}\text{B}(p,p'\gamma)^{10}\text{B}$ reaction. The angular distribution of this γ -line is expected to be anisotropic due to the spin 1+ value of the ^{10}B first excited state. While a number of previous datasets exist in the literature [4.32, 4.33, 4.36, 4.37], there are disagreements between them, just like there are for the 429 keV γ -ray. A new measurement was performed by Lagoyannis *et al.* [4.34] in order to sort out these differences. The experimental setup used was the same as in the case of the $^{10}\text{B}(p,\alpha\gamma)^7\text{Be}$ reaction and all the experimental details can be found in the section labeled $^{10}\text{B}(p,\alpha\gamma)^7\text{Be}$: 429 keV γ -ray. The differential cross-sections for all eight angles are presented in Fig. 4.15.

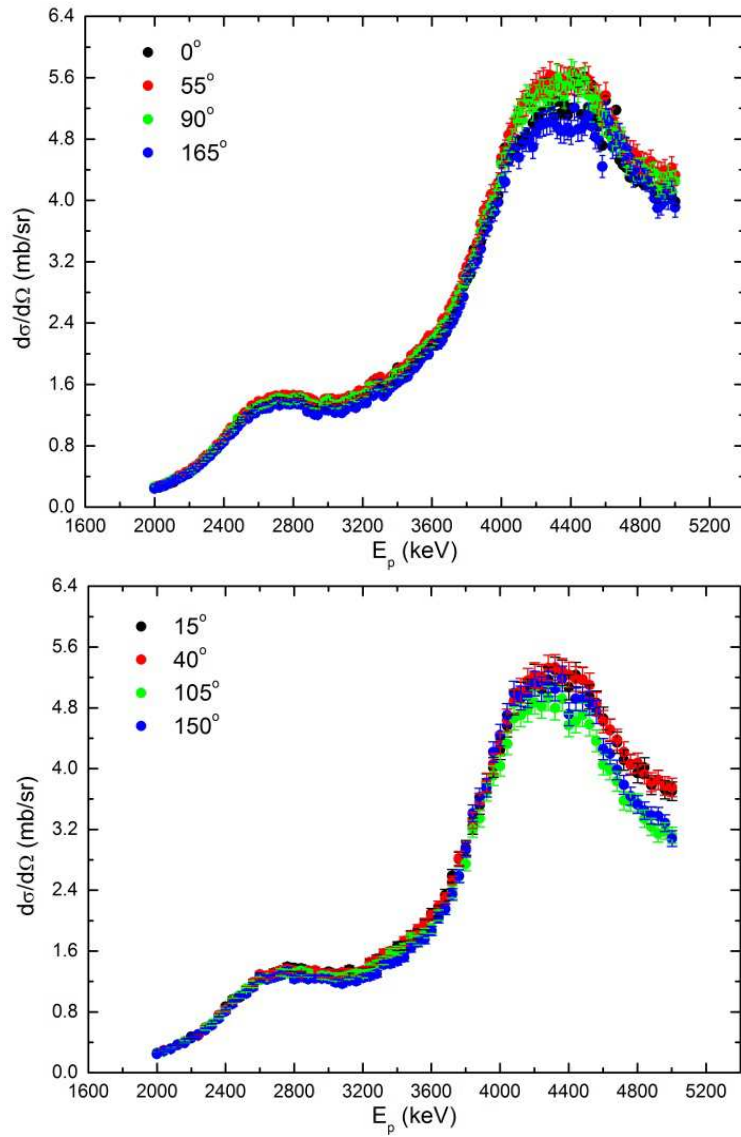


FIG. 4.15. Differential cross-sections of the 718 keV $^{10}\text{B}(p,p'\gamma)^{10}\text{B}$ resonance as a function of proton energy, deduced from the work of [4.34]. Measurements taken at eight different angles with respect to the beam axis, as noted in the legend within each panel.

As in the case of the 429 keV γ -ray, Chiari *et al.* [4.35] measured thick-target yields for three angles. The experimental setup is the same as that described in the section labeled $^{10}\text{B}(p,\alpha\gamma)^7\text{Be}$: 429 keV γ -ray and results are presented in Fig. 4.16.

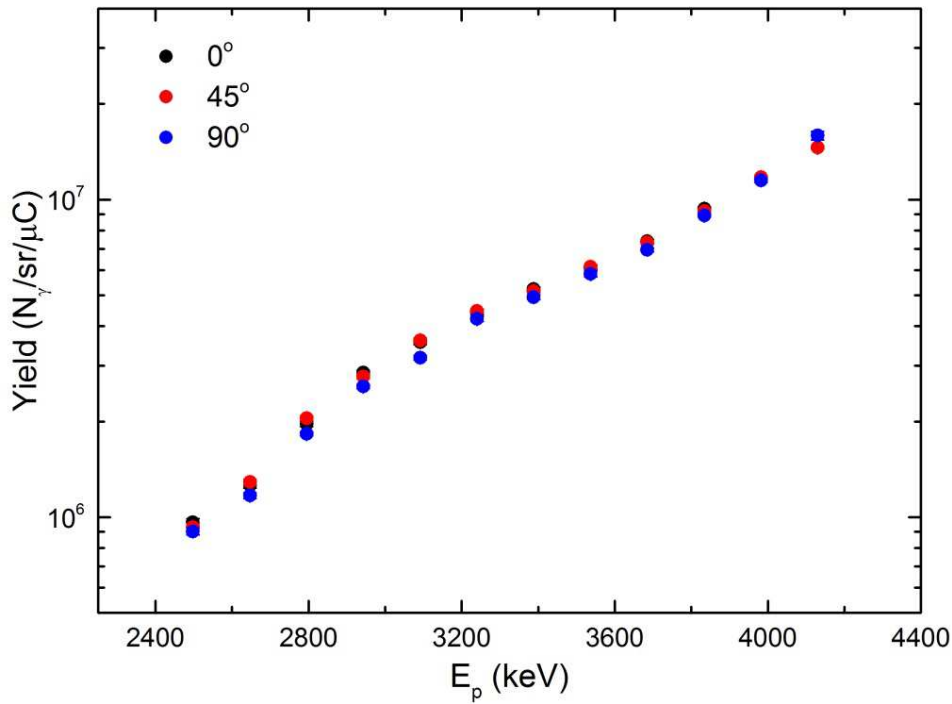


FIG. 4.16. Thick target yields of the 718 keV $^{10}\text{B}(p,p'\gamma)^{10}\text{B}$ resonance as a function of proton energy, deduced from the work of [4.35]. Gamma-ray yield was detected at 0° , 45° and 90° with respect to the beam axis.

(b) Data in the literature and assessment

Thick-target yields for the $^{10}\text{B}(p,p'\gamma)^{10}\text{B}$ reaction were measured by Kiss *et al.* [4.2], Anttila *et al.* [4.1] and Savidou *et al.* [4.17] for the same energies as in the case of the $^{10}\text{B}(p,\alpha\gamma)^7\text{Be}$ reaction. Differential cross-sections were measured by Segel *et al.* [4.32], Day *et al.* [4.33], Hunt *et al.* [4.36] and Ophel *et al.* [4.37]. While the new measurements are in excellent agreement with the data from Day *et al.*, there are major disagreements in regards to the data from other laboratories. The discrepancies between these datasets can be explained using the same reasoning as in the case of the 429 keV gamma-rays, in the section labeled $^{10}\text{B}(p,\alpha\gamma)^7\text{Be}$: 429 keV γ -ray. The datasets are illustrated in Fig. 4.17 for easy visual comparison.

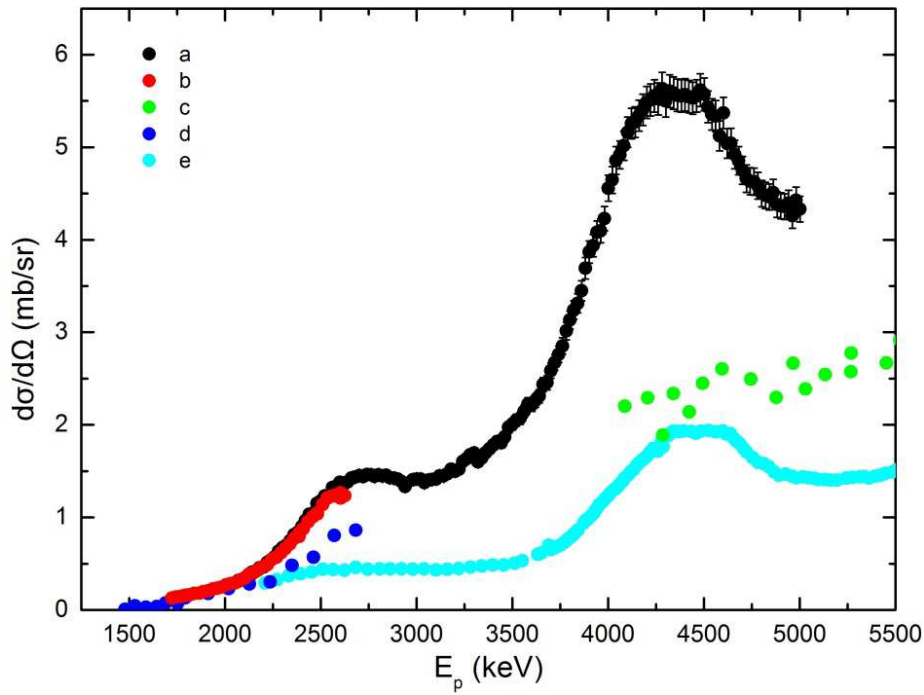


FIG. 4.17. Comparison of the available differential cross-sections of the 718 keV $^{10}\text{B}(p,p'\gamma)^{10}\text{B}$ resonance as a function of proton energy. Data from: (a) [4.34] at 55° , (b) [4.33] at 90° , (c) [4.32], (d) [4.36] at 0° and (e) [4.37] at 55° .

(c) Recommended data

Since the new measurements of the 718 keV γ -ray are correlated with the 429 keV γ -ray, the new measurements that were made in the proton energy range from 2.0 to 5.0 MeV are recommended. For proton energies below 2.0 MeV, the data of Day *et al.* [4.33] are recommended. The validity of these two datasets is additionally supported by comparing their integrated γ -ray yields with the thick-target yields found in the literature [4.1, 4.2, 4.17] and with the new ones by Chiari *et al.* [4.35], as shown in Fig. 4.18. Concerning thick-target yields, the new data from Chiari *et al.* are recommended because they are in agreement with the data from both Day *et al.* and Lagoyannis *et al.* [4.34].

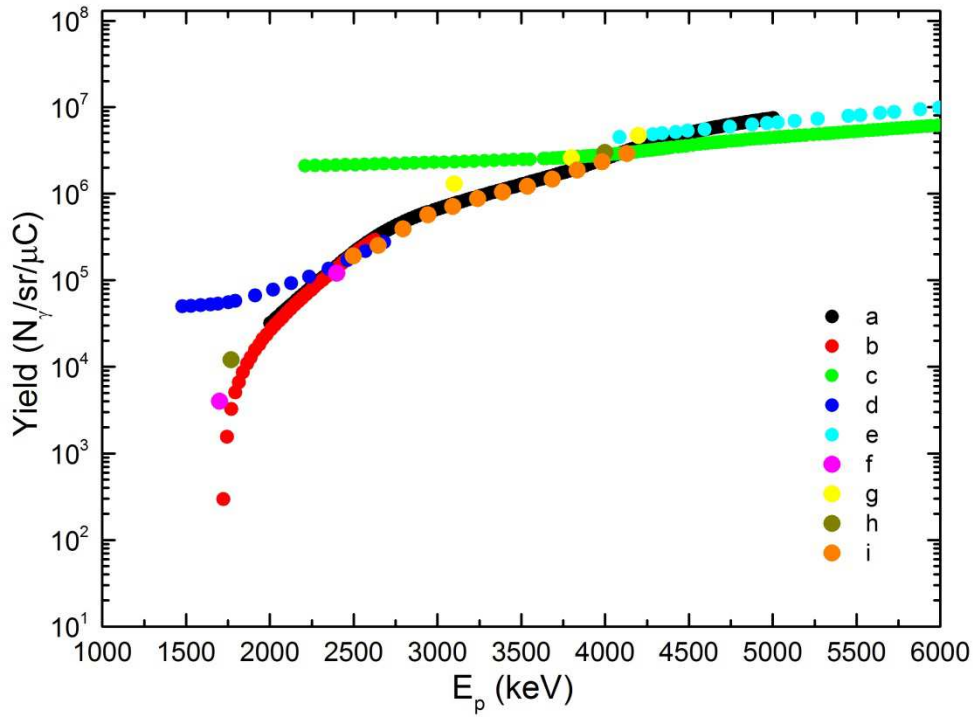


FIG. 4.18. Comparison of the thick target yields of the 718 keV $^{10}\text{B}(p,p'\gamma)^{10}\text{B}$ resonance as a function of proton energy. Data obtained from (a) [4.34], (b) [4.33], (c) [4.36], (d) [4.36], (e) [4.32], (f) [4.1], (g) [4.2], (h) [4.17], and (i) [4.35]. Yields were measured at 0° with respect to the beam axis and normalized to elemental yields.

4.3.1.3. $^{10}\text{B}(p,p'\gamma)^{10}\text{B}$: 1020, 1430, 2860 and 4440 γ -rays

These γ -rays were studied at proton energies above 4.0 MeV by Segel *et al.* [4.32] and are emitted by the de-excitation of the second, third, fourth and seventh excited state of ^{10}B to the first (see Fig. 4.19). The experimental setup is the same as that described in the section labeled $^{10}\text{B}(p,\alpha\gamma)^7\text{Be}$: 429 keV γ -ray. Since there are no other data available for these γ -rays, no evaluation can be performed.

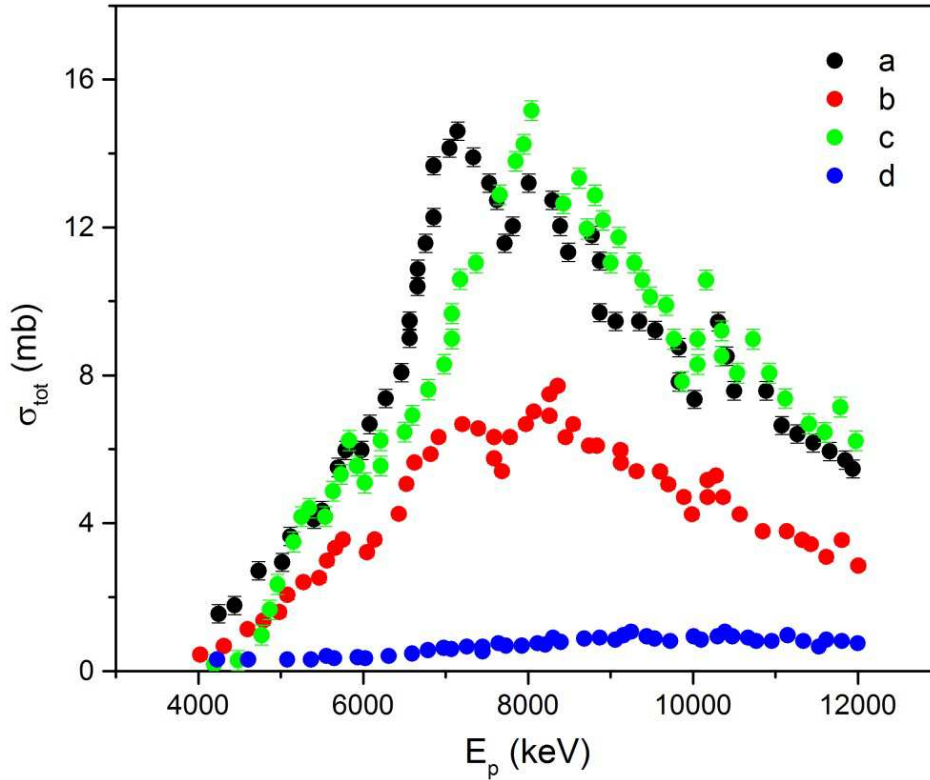


FIG. 4.19. Total cross-section measurements of the (a) 1020 keV (b) 1430 keV (c) 2860 keV and (d) 4440 keV γ -rays produced by the $^{10}\text{B}(p,p'\gamma)^{10}\text{B}$ reaction as a function of proton energy. All data are taken from [4.32].

4.3.1.4. $^{11}\text{B}(p,p'\gamma_{1-0})^{11}\text{B}$: 2125 keV γ -ray

At proton energies above 2.5 MeV the cross-section of the $^{11}\text{B}(p,p'\gamma_{1-0})^{11}\text{B}$ becomes important and can be used for the PIGE technique. The first excited state of ^{11}B ($T_{1/2} = 3.8$ fs) emits an isotropic γ -ray of 2125 keV. As illustrated in Fig. 4.20, the $^{11}\text{B}(p,p'\gamma_{1-0})^{11}\text{B}$ reaction appears to have a double peak, which is due to a combination of the Doppler shift and that the reaction has a double kinematic solution.

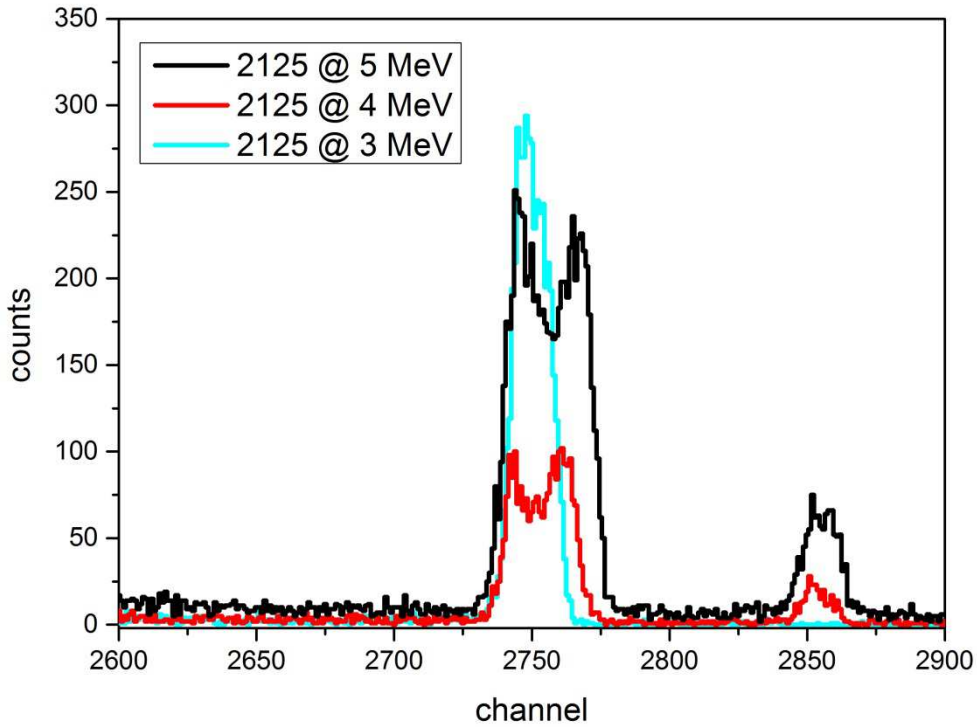


FIG. 4.20. The shape of the 2125 keV gamma-ray at different proton energies as noted in the legend.

(a) New measurements

The only known differential cross-section measurement was made by Boni *et al.* [4.5] at an angle of 90° and for the energy range 2.6 to 3.8 MeV. The lack of experimental data, as well as the underestimation of the cross-sections for the proton-induced reactions of ^{10}B , which were measured with the same experimental setup, led to the necessity of a new experiment by Preketes-Sigalas *et al.* [4.39]. The experimental setup consisted of three HPGe mounted on a motorized turntable and initially placed at 0° , 90° and 165° . The proton energy varied from 2.58 to 5.0 keV with an energy step of 20 keV. After each energy step, the turntable was rotated by 15° , thus placing the detectors in three new angles, i.e. 15° , 105° and 150° . The accuracy in the determination of the energy was 0.1% since it was measured using the narrow resonances of $^{27}\text{Al}(p,\gamma)^{28}\text{Si}$ and $^{13}\text{C}(p,\gamma)^{14}\text{N}$ at $E_p = 991.9$ and 1746.9 keV, respectively. A thin $^{\text{nat}}\text{B}$ target mounted on a Ta backing was used throughout the experiment. The thickness of the target was found to be 577×10^{15} at/cm² by using a combination of the RBS and NRA techniques. The results of this experiment are shown in Fig. 4.21 and the uncertainty budget is summarized in Table 4.14.

Since there were very few datasets concerning thick-target yields for the 2125 keV γ -ray, Chiari *et al.* [4.35] performed a new experiment using the experimental conditions described in the section labeled $^{10}\text{B}(p,\alpha\gamma)^7\text{Be}$: 429 keV γ -ray and using a thick BN target. The results are presented in Fig. 4.22 and the uncertainty budget of this experiment can be found in Table 4.14.

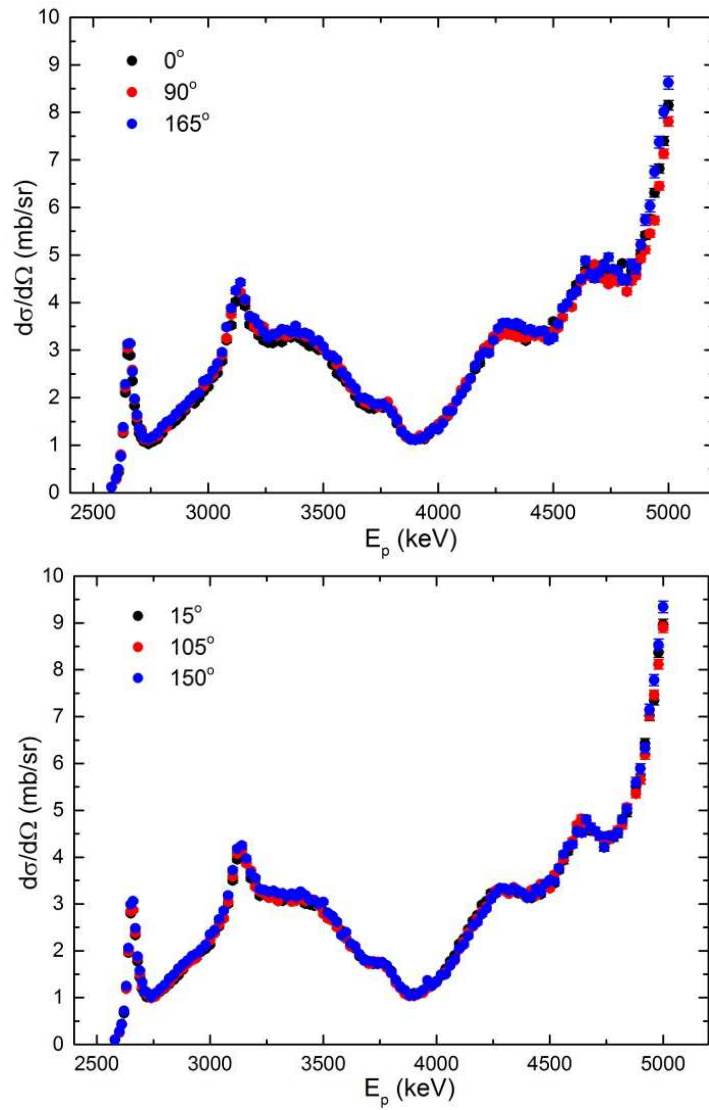


FIG. 4.21. Differential cross-sections of the 2125 keV $^{11}\text{B}(p, p\gamma_{1-0})^{11}\text{B}$ resonance as a function of proton energy, deduced from [4.39]. Yield measured at 15° , 105° and 150° with respect to the beam axis.

TABLE 4.14. UNCERTAINTY BUDGET FOR THE NEW DIFFERENTIAL CROSS-SECTION MEASUREMENTS OF $^{11}\text{B}(p, p\gamma_{1-0})^{11}\text{B}$.

| Quantity | Uncertainty |
|-----------------------|-------------|
| Peak Integration | 3–5% |
| Beam charge | 3.5 % |
| Target thickness | 5% |
| Detector's efficiency | 4% |

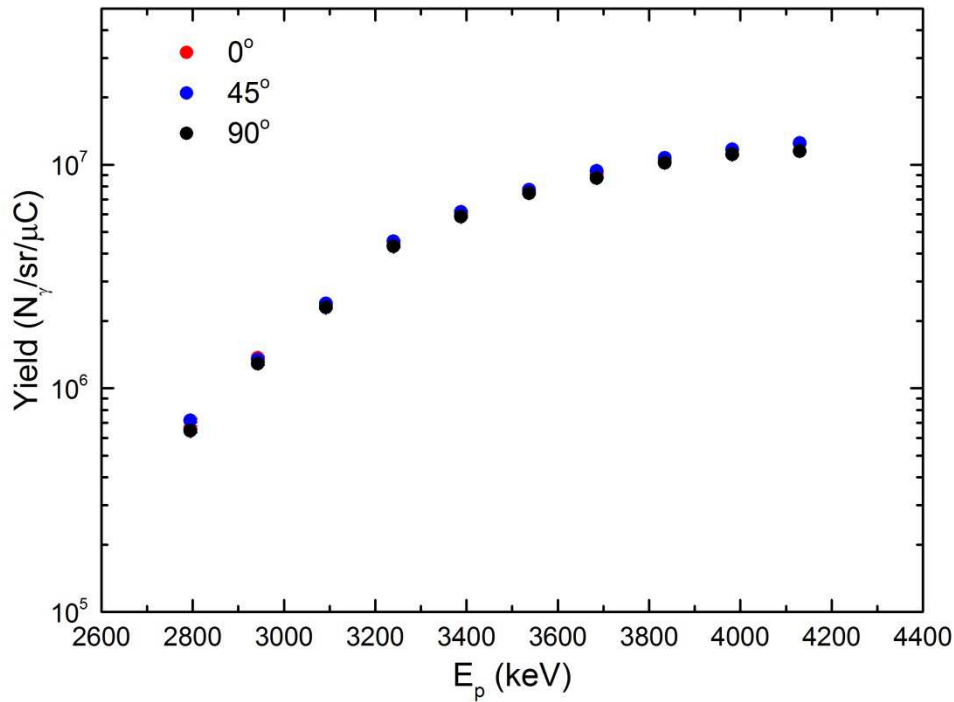


FIG. 4.22. Thick-target yields of the 2125 keV $^{11}\text{B}(p, p\gamma_{1-0})^{11}\text{B}$ resonance as a function of proton energy. Data from [4.35]. Yields measured at 0° , 45° and 90° , with respect to the beam axis.

(b) Data in the literature and assessment

As previously stated, the only existing data in the literature is from Boni *et al.* [4.5], measured at 90° for the energy range between 2.6 and 3.8 MeV. Details of the experimental setup can be found in section labeled $^{10}\text{B}(p, \alpha\gamma)^7\text{Be}$: 429 keV γ -ray. The differential cross-sections shown in Fig. 4.23 are a factor of ~ 5 lower than the new ones. There is no apparent reason for this difference and the lack of additional data means that there is not enough information to recommend one set of data over the other. On the other hand, the shape of the integrated yields obtained from the new measurements are in agreement with the thick-target yields from Kiss [4.2] and Savidou [4.17], while the ones from Boni *et al.* exhibit a different trend (see Fig. 4.24).

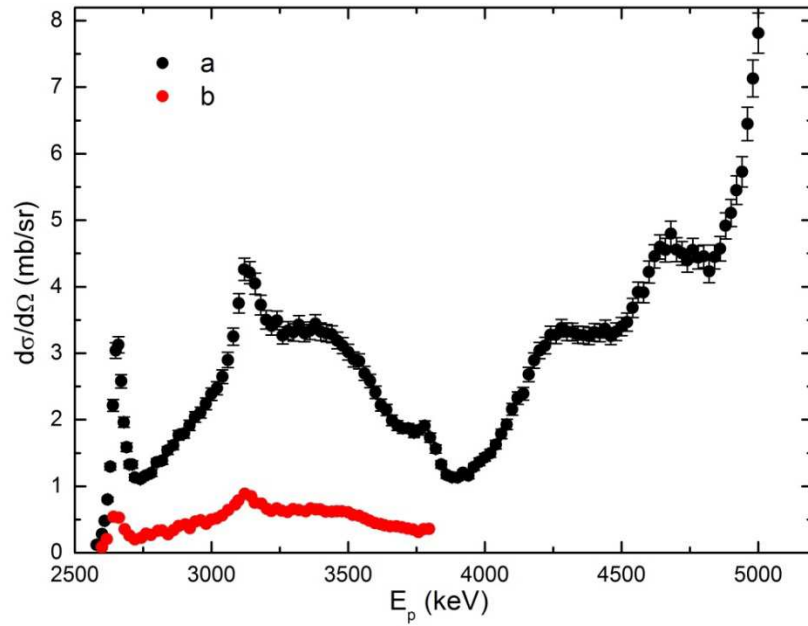


FIG. 4.23. Comparison of the differential cross-sections of the 2125 keV $^{11}\text{B}(p,p\gamma_{1-0})^{11}\text{B}$ resonance between the two available datasets, recorded at 90° with respect to the beam axis, as a function of proton energy. Data taken from a) [4.39] and b) [4.5].

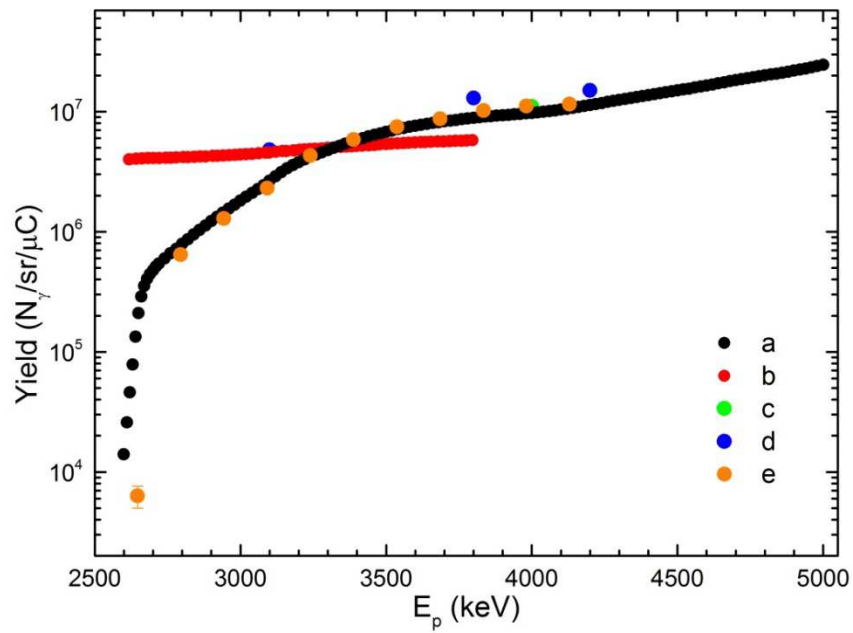


FIG. 4.24. Comparison of the thick target yields of the 2125 keV $^{11}\text{B}(p,p\gamma_{1-0})^{11}\text{B}$ resonance as a function of proton energy. Data taken from (a) [4.39], (b) [4.5], (c) [4.17], (d) [4.2] and (e) [4.35], measured at 0° and normalized to elemental yields.

(c) Recommended data

The data of Preketes – Sigalas *et al.* are recommended, since they successfully reproduce the trend of measured thick-target yields from earlier works [4.2], as well as the ones from Chiari *et al.* [4.35].

4.3.2. Gamma-ray production cross-sections of boron from deuteron-induced nuclear reactions

Contrary to the proton-induced reactions with boron, there are only limited cross-section data for the deuteron-induced reactions. The higher γ -ray yields of the proton-induced reactions compared to the deuteron ones are the main reason for this lack of data. Only the ^{11}B isotope has been studied via deuterons and more specifically, the two first excited states of ^{12}B through the $^{11}\text{B}(d,p\gamma)^{12}\text{B}$ reaction.

4.3.2.1. $^{11}\text{B}(d,p\gamma)^{12}\text{B}$: 953 and 1674 keV γ -rays

These γ -rays originate from the $^{11}\text{B}(d,p\gamma_{1-0})^{12}\text{B}$ and $^{11}\text{B}(d,p\gamma_{2-0})^{12}\text{B}$ transitions, respectively, and are expected to have anisotropic angular distributions. Their cross-sections at 60° have been studied by Sziki *et al.* [4.19] for the deuteron energies between 0.6 and 2.0 MeV. The energy calibration of the accelerator was performed using the narrow resonance at 991.9 keV of the $^{27}\text{Al}(p,\gamma)^{28}\text{Si}$ reaction and the γ -rays were detected by a HPGe detector placed at an angle of 60° and at a distance of 10 cm from the target. Various thin targets were used with thicknesses around 800×10^{15} at/cm². The resulting differential cross-sections along with their corresponding errors are presented in Fig. 4.25. The thick-target γ -ray yield of the same reaction was investigated by Elekes *et al.* [4.18] using a HPGe detector placed at the same distance from the target, but at an angle of 135° . The thick-target yields are shown in Fig. 4.26. In the absence of any other experimental data, additional measurements are recommended, especially with thick-targets, for validation purposes.

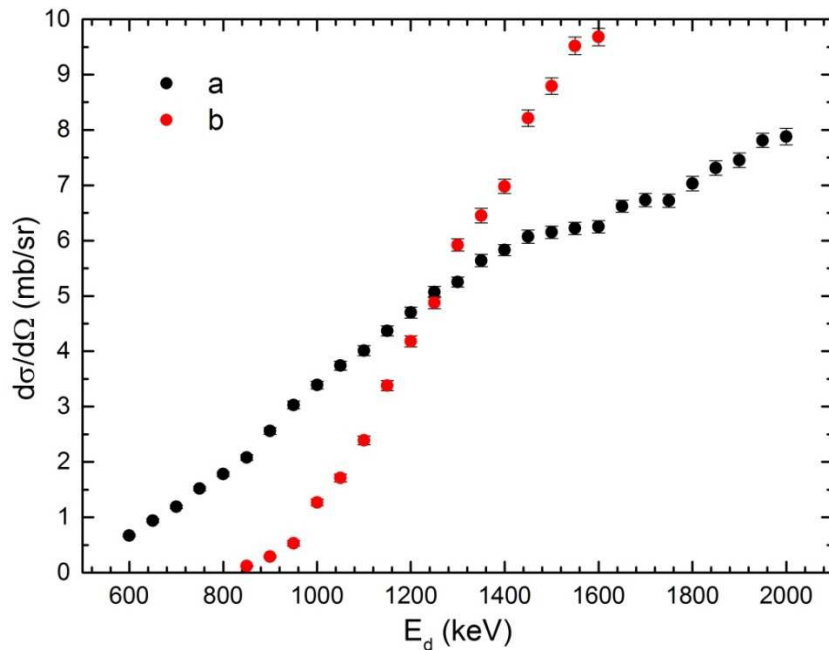


FIG. 4.25. Differential cross-sections of the (a) 953 and (b) 1674 keV γ -rays produced by the $^{11}\text{B}(d,p\gamma)^{12}\text{B}$ reaction as a function of proton energy, measured at an angle of 55° . Data from [4.19]

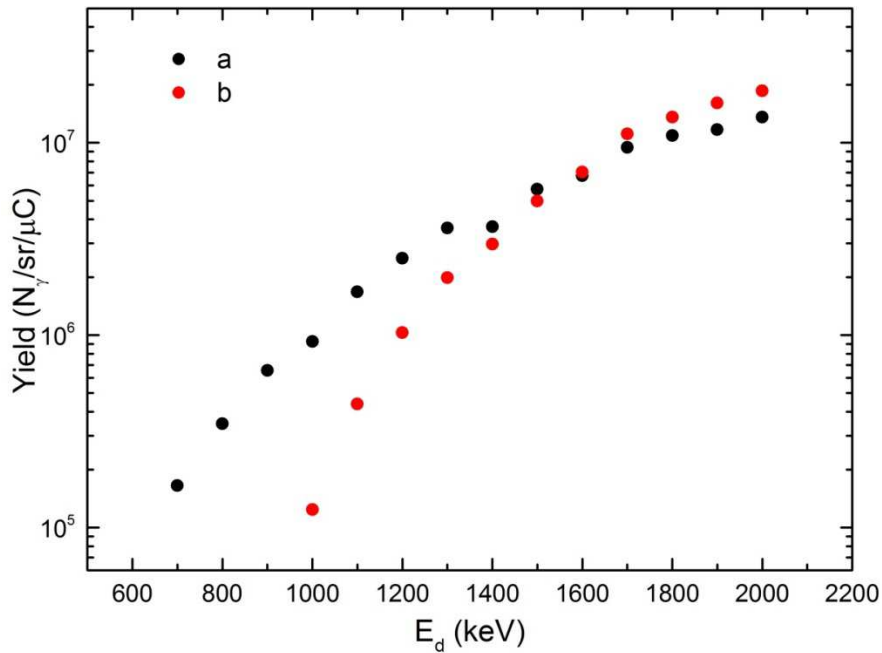


FIG. 4.26. Thick target yields of the (a) 953 and (b) 1674 keV γ -rays produced by the $^{11}\text{B}(d,p\gamma)^{12}\text{B}$ reaction as a function of proton energy, measured at an angle of 135° . Data from [4.18].

4.4. CARBON

Particle-induced γ -ray reactions with carbon isotopes prove most useful for material analysis purposes when induced with protons or deuterons. When using proton beams with ^{12}C and ^{13}C in the lower energy region, (p, γ) reactions occur; while at higher energies, the (p,p' γ) reactions are dominant. If a laboratory can produce a deuteron beam, however, the deuteron-induced ^{12}C (d,p γ) reaction is more frequently used and is more important. In the following subsections, the methods and parameters for each reaction are discussed, i.e. energy dependence of the cross-section, typical beam energies used, γ -ray energies and resonances that can be employed for depth profiling. Examples of studies within material science are provided in order to illustrate the use and capabilities of each specific reaction. At the end, the available data are presented and assessed.

4.4.1. Gamma-ray production cross-sections of carbon from proton-induced nuclear reactions

4.4.1.1. $^{12}\text{C}(p,\gamma)^{13}\text{N}$

This reaction is governed by a direct capture process that interferes with two broad resonances at 457 keV and 1699 keV for beam energies of up to 2.5 MeV (Fig. 4.27). The primary γ -rays that are emitted from de-excitation to the ground and first excited state have the energy provided by the sum of the Q value of the reaction and the proton beam, which is equivalent to 1.6 MeV and 3.422 MeV, respectively, at a beam energy of 1.056 MeV. Therefore, in practice, these primary lines are not narrow, but rather broad, depending also on the energy loss of the protons in the sample. The shape of the line is given by a convolution of the depth profile of ^{12}C and the cross-section of the reaction. The width of the resonance at 457 keV allows for a moderate depth resolution, a technique which has been used successfully for the

depth profiling of carbon in steel [4.40]. The sensitivity to this reaction is less than the sensitivity to the competitive (p, p') reaction at higher energies and to the deuteron-induced reactions. The advantage, however, is that at low beam energies, background contributions from other constituents of the sample are small. This method has been used in [4.41, 4.42] for tracing studies of carbon. The cross-section of the capture reaction to the ground state has been investigated at the angles of 0° and 90° over a wide range of energies by Rolfs and Azuma [4.43] in 1974. The results for 90° are displayed in Fig. 4.27.

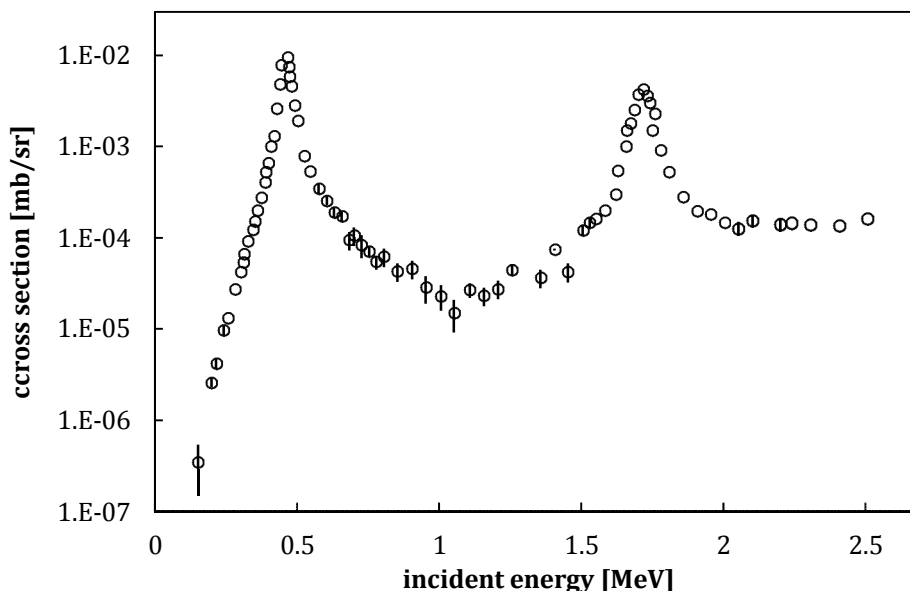


FIG. 4.27. Cross-section of $^{12}\text{C}(p,\gamma)^{13}\text{N}$ for a detection angle of 90° as a function of incident beam energy. Data taken from the work of [4.43].

In the work of [4.43], the absolute cross-section was determined relative to the Rutherford cross-section using a carbon foil target. With this approach, the measurement is independent from the target stoichiometry and stopping power data, and only an additional relative measurement of the beam charge is necessary, which reduces the overall uncertainty. The majority of the uncertainty comes from the efficiency calibration of the γ -detector. The authors quote an error of 12 % for the absolute determination of a cross-section of 125 μb at the maximum of the 457 keV resonance.

More recent measurements at selected beam energies have been performed by [4.44], resulting in a peak cross-section of $124 \pm 12 \mu\text{b}$ at 460 keV. Since the reaction is important for nuclear astrophysics, the energy dependence of the cross-section has been investigated thoroughly by detailed R-matrix calculations [4.44, 4.45]. To improve knowledge of the reaction rates, a new absolute measurement of the cross-section was initiated during the course of the CRP, with the goal to further reduce the error. This work is still under way [4.45].

For measurements on thick samples, the γ -yields for the first ($E_\gamma = 2.366 \text{ MeV}$) and second ($E_\gamma = 3.511 \text{ MeV}$) excited state of ^{13}N have been measured at beam energies of 1.0 MeV, 1.7 MeV and 2.4 MeV by Anttila *et al.* [4.1] and at 2.4 MeV and 3.1 MeV by Kiss *et al.* [4.2]. From the measured spectra provided by [4.1, 4.2], it is clear that these γ -rays are suitable for

material analysis. Both measurements were performed at a detection angle of 55 °. The results are summarized in Table 4.15.

TABLE 4.15. GAMMA-YIELD AT GAMMA ENERGIES 2.366 MeV AND 3.511 MeV FOR $^{12}\text{C}(p,\gamma)^{13}\text{N}$ AT DIFFERENT BEAM ENERGIES AT AN ANGLE OF 55°.

| E_γ (MeV) | γ -yield ($N_\gamma/(\mu\text{C}\cdot\text{sr})$) | | | | |
|------------------|--|----------------------|----------------------|----------------------|----------------------|
| | 1.0 MeV ^a | 1.7 MeV ^a | 2.4 MeV ^a | 2.4 MeV ^b | 3.1 MeV ^b |
| 2.366 | 260 | 220 | 230 | 230 | 270 |
| 3.511 | — | 230 | 210 | 210 | — |

^a [4.1]

^b [4.2]

4.4.1.2. $^{13}\text{C}(p,\gamma)^{14}\text{N}$

Due to the low cross-section and the low abundance of ^{13}C found in nature, the $^{13}\text{C}(p,\gamma)^{14}\text{N}$ reaction is only used in special cases [4.41, 4.42], e.g. for ion beam analysis below beam energies of 1 MeV. The reaction is governed by a broad resonance at 558 keV and is overall similar to the $^{12}\text{C}(p,\gamma)^{13}\text{N}$ reaction. Since the Q value is much higher than for the $^{12}\text{C}(p,\gamma)^{13}\text{N}$ reaction, several primary γ -lines with energies up to more than 8 MeV and several secondary transitions are available for analysis, which have the advantage of being isotropic when they come from the first excited state. The cross-section and angular distributions have been studied in this energy range by King *et al.* [4.46]. The absolute cross-section was determined using inverse kinematics relative to a resonance in the $^1\text{H}(^{19}\text{F},\alpha\gamma)^{16}\text{O}$ reaction employing a hydrogen gas target and relative to a resonance in $^{14}\text{N}(p,\gamma)^{15}\text{O}$. The authors quote an overall error of 12%. More recent measurements [4.47] are in good agreement with these results and give angular distributions at selected proton energies.

Despite being only rarely used, the reaction is important for materials analysis because it has a strong, narrow and almost completely isolated resonance at a beam energy of 1747 keV, which is ideally suited for high-resolution depth profiling. Several γ -ray lines are appropriate for material analysis purposes. Since the γ -line to the ground state has an energy of 9.169 MeV, interferences originating from γ -lines emitted from reactions of other elements possibly contained in the sample can be avoided. The resonance has been used in various studies such as isotopic tracing investigations of fusion reactor walls [4.48] and the study of implantation profiles in silver [4.49] and silicon [4.50].

The resonance parameters, such as branching ratios and angular distributions, are known very accurately [4.51]. Therefore this resonance is proposed as an alternative to the 992 keV resonance of $^{27}\text{Al}(p,\gamma)^{28}\text{Si}$, for the relative efficiency calibration of detectors and the energy calibration of the beam. Since no recent data on the resonance strength or the cross-section can be found in literature for this resonance, it is used only in combination with standards.

4.4.1.3. $^{12}\text{C}(p,p'\gamma)^{12}\text{C}$: 4400 keV γ -ray

The $^{12}\text{C}(p,p'\gamma)^{12}\text{C}$ inelastic scattering has been studied over a wider range of energies, e.g. by Dyer *et al.* [4.52], by analyzing the 4.4 MeV γ -ray from the first excited state. The spin value of the latter is 2+. Therefore, the angular distribution of the γ -ray is expected to be anisotropic. The data in Fig. 4.28 show a strong resonance at a proton energy of 5.370 MeV. In the energy range above this resonance, the sensitivity is high. However, for much higher

energies (> 8 MeV) the gamma and neutron background often becomes a severe problem. The reaction has been employed for the investigation of carbon in steel [4.53, 4.54], where sensitivities of 10 ppm of carbon have been accomplished. It has also been used for the determination of carbon in biomedical samples [4.55].

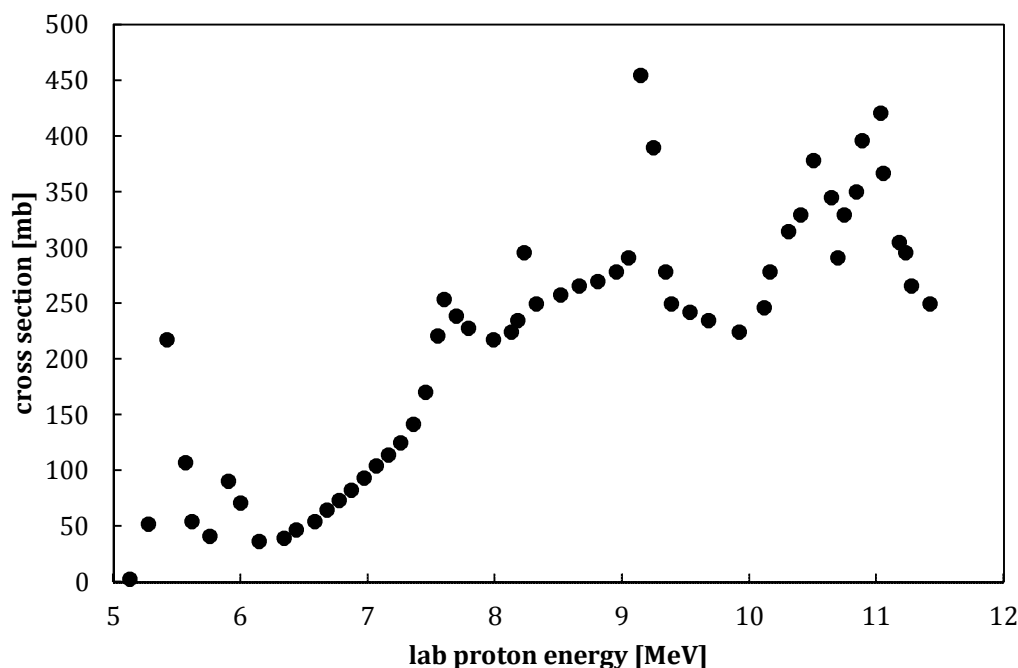


FIG. 4.28. Cross-section of inelastic scattering of protons on a ^{12}C target as a function of proton energy. Data from [4.52].

In the measurements of [4.52], the absolute value for the inelastic scattering cross-section was determined from detailed measurements of angular distributions of the particle exit channel relative to the Rutherford cross-section, using a thin foil target. This method cancels out errors in the beam charge integration and the determination of the absolute efficiency of the γ -detector. An error of 5% for the absolute cross-section was obtained. Unfortunately, detailed information about the angular distribution measured during the course of the experiment is not given in [4.52].

4.4.1.4. $^{13}\text{C}(p,p'\gamma)^{13}\text{C}$: 3090 keV and 3680 keV γ -rays

Inducing the reaction with a low energy beam is not ideal for material analysis, because of the moderate sensitivity. Two γ -rays emitted from this reaction are normally observed, at 3.09 MeV and 3.68 MeV, with the first one being isotropic. In samples containing traces of ^{12}C , these γ -rays will be obscured by the strong 4.4 MeV line emitted from the $^{12}\text{C}(p,p'\gamma)^{12}\text{C}$ reaction at beam energies above 5 MeV. Therefore, the use of these γ -rays is limited to beam energies below 5 MeV.

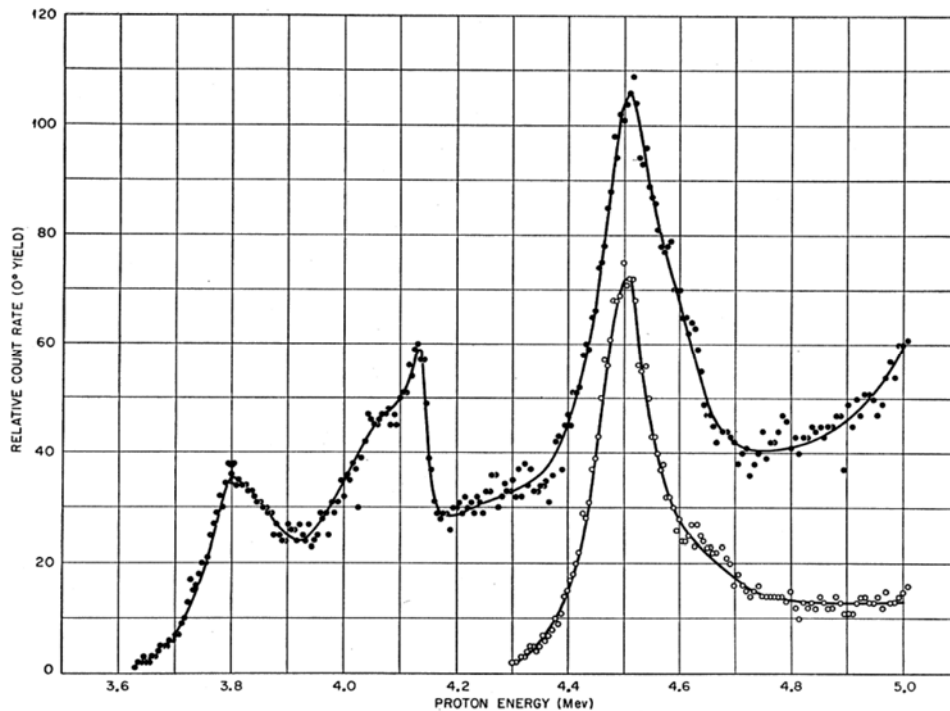


FIG. 4.29. Relative yield for the 3.09 MeV γ -line (solid points) and the 3.68 MeV line (open points) produced by $^{13}\text{C}(p,p'\gamma)^{13}\text{C}$ as a function of proton energy. Reproduced courtesy of *Physical Review* (1893–1969) [4.56].

The energy dependence of the reaction, as measured by Bair *et al.* [4.56], is displayed in Fig. 4.29. The authors give relative yields only. Fortunately, Kiss *et al.* [4.2] have measured the absolute yield for a thick-target at the beam energies of 3.8 MeV and 4.2 MeV for the 3.09 MeV γ -line. These values were calculated to be 6.2×10^3 and 4.1×10^4 $\text{N}_\gamma/(\mu\text{C}\cdot\text{sr})$, respectively, and can be used to normalize the relative yields of [4.56].

4.4.2. Gamma-ray production cross-sections of carbon from deuteron-induced nuclear reactions

4.4.2.1. $^{12}\text{C}(d,p\gamma_{1-0})^{13}\text{C}$: 3089 keV γ -ray

The deuteron-induced γ -emission on ^{12}C is generally the preferred method for the detection of carbon in material analysis because it has a high detection efficiency and the deuteron beam allows for the simultaneous detection of other light elements such as nitrogen and oxygen. The technique has many applications, such as for the detection of carbon in steel [4.54] or the investigation of layers produced by metal-organic chemical vapor deposition (MOCVD) [4.57].

The dominant γ -ray is emitted from the first excited state in ^{13}C with an energy of 3.089 MeV. For beam energies above 1.5 MeV, the γ -lines from the second and third state can be seen, but they are weaker and not used in material analysis. The 3.089 MeV γ -line has the additional advantage of being isotropic.

(a) New measurements

The differential cross-sections have been studied by several groups, with the most recent measurements given by Csedreki *et al.* [4.59], which were performed during this CRP. In this paper a complete and careful comparison with previous data is presented, an assessment of the data is given and a benchmarking measurement is performed.

The experiments were performed at ATOMKI using the 5 MV Van de Graaff accelerator. The energy calibration of the beam was determined with an uncertainty of 3 keV. The experimental set-up consisted of a target chamber with a long Faraday cup, a co-axial HPGe detector of 170 cm³ volume positioned at an angle of 55° relative to the beam direction. This detector was shielded from γ -rays originating from the Faraday cup. The absolute efficiency was determined with calibrated radioactive sources (¹³³Ba, ⁵⁶Co, ⁶⁰Co, ¹³⁷Cs and ¹⁵²Eu). Backscattered particles for an RBS analysis with an alpha beam as well as the particles from the reaction with a deuteron beam were observed at an angle of 135° with an ion-implanted silicon particle detector that has a 500 μ m active depth and 13 keV energy resolution.

The target was a thin self-supporting natural carbon foil with an evaporated palladium layer on its back surface. The number of target nuclides was determined with the α -RBS technique. The simultaneous RBS monitoring of the Pd layer made it possible to determine the absolute charge independently from a charge measurement from within the target chamber. The γ -ray yield measurements were performed in the 740–2000 keV deuteron energy range with 2–20 keV steps, depending on the structure of the excitation function. The obtained γ -ray production cross-sections, as a function of the bombarding deuteron energy are presented in Fig. 4.30 along with the results of previous measurements.

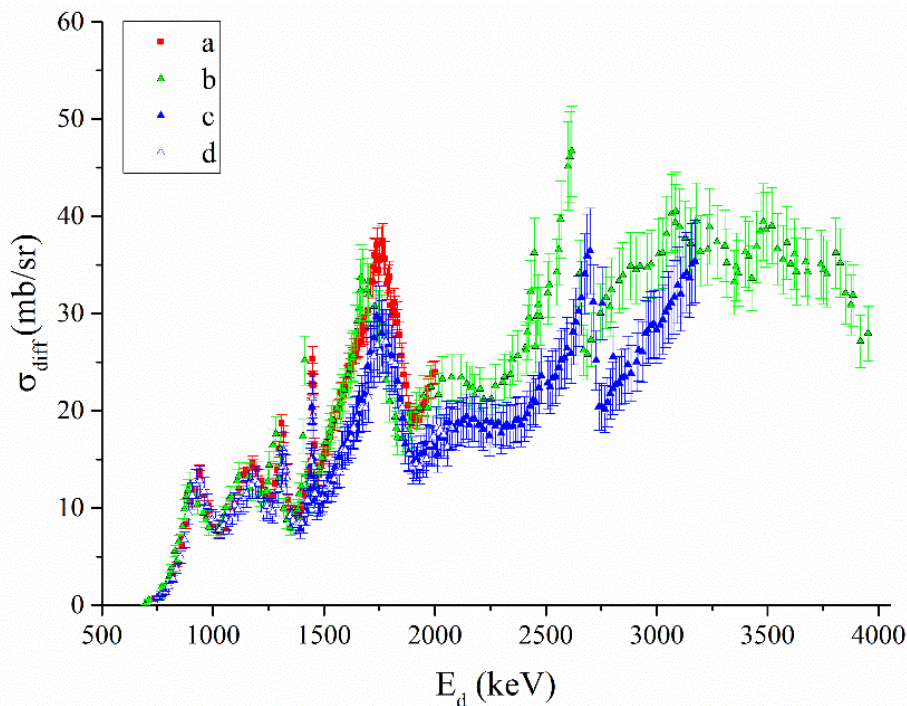


FIG. 4.30. Differential γ -ray production cross-sections of the 3089 keV γ -ray produced by $^{12}\text{C}(d,p\gamma)^{13}\text{C}$ as a function of deuteron energy, deduced from the work of a) [4.59] and literature data b) [4.60], c) [4.61] and d) [4.62].

(b) Data from the literature and assessment

There are three previous measurements reported in the literature in which the γ -ray production cross-sections were measured in a large deuteron energy interval. Both of the studies by Tryti *et al.* [4.60, 4.61] primarily explored the nuclear physics aspects of this reaction, while the aim of the third investigation [4.62] was the application of the results for elemental analysis.

In the measurements of Tryti, the electrostatic beam energy analyzer of the Van de Graaff generator was calibrated relative to the $^{13}\text{C}(p,\gamma)^{14}\text{N}$: 1747 keV resonance. The γ -rays were detected with a planar 10 cm^3 Ge(Li) detector. The carbon target was a sooted tantalum backing. No other details were given for the first measurement [4.60]. In [4.62], the targets were carbon films of 9 keV thickness for 2 MeV deuterons covered with a thin gold layer. Particles were detected by two surface barrier detectors at angles of 90° and 135° . The elastically scattered deuterons from gold were used as a beam current monitor and the target stability was controlled by comparing the yield from carbon and gold at regular intervals.

Papillon *et al.* used a 2 MV Pelletron tandem accelerator [4.61]. Its generating voltmeter was calibrated with the well-known $^{27}\text{Al}(p,\gamma)^{28}\text{Si}$ resonance at 992 keV. The integrated charge was measured in the insulated chamber with a low-impedance current integrator. For the target, a thin layer of carbon was deposited onto a solid Ta backing. The detector was a HPGe with an efficiency of 22.7%. The absolute efficiency of the detector, below 1408 keV, was determined with a ^{152}Eu source placed in the position of the target, while above this energy the efficiency was obtained from an extrapolation. At 3.1 MeV, the uncertainty of the efficiency was taken as 5–10%. Table 4.16 shows the uncertainty budget of the new measurement in comparison with the above two literature data. The final uncertainties for the new measurement are significantly smaller than the ones from earlier measurements.

TABLE 4.16. COMPARISON OF THE ESTIMATED UNCERTAINTY BUDGET FOR DIFFERENTIAL CROSS-SECTION VALUES FROM THE MEASUREMENTS OF CSEDREKI *et al.* [4.59] AND LITERATURE DATA FOR 3089 keV $^{12}\text{C}(d,p\gamma)^{13}\text{C}$

| Quantity | [4.60, 4.61] | [4.62] | [4.59] |
|---|--------------|-----------|--------|
| Beam energy spread (keV) | | ~0.6 | 1.0 |
| Straggling in the target | | | |
| Charge collection | | not given | — |
| Target inhomogeneity | | 2–5% | |
| N_T number of target nuclei per square centimeter | | 5% | 3.0% |
| γ -ray peak area | | 1–2% | < 1–2% |
| γ -ray detector absolute efficiency | | 5–10% | 2.0% |
| particle detector solid angle | | — | 2.5% |
| d+Au/Pd elastic peak area | | — | < 1.0% |
| d+Au/Pd Rutherford cross sect. | | — | 2.0% |
| Final uncertainty | 12% | 10% | 6% |

The experimental conditions of the new [4.59] and three previous works [4.60– 4.62] are given in Table 4.17.

TABLE 4.17. EXPERIMENTAL CONDITIONS OF THE NEW [4.59] AND THREE PREVIOUS MEASUREMENTS FOR 3089 keV $^{12}\text{C}(\text{d},\text{p}\gamma)^{13}\text{C}$

| Parameter | [4.60] | [4.61] | [4.62] | [4.59] |
|---|-----------------------------|-----------------------------|-----------------------|-----------------------|
| Target thickness (at./cm ²) | $\sim 0.36 \times 10^{18*}$ | $\sim 2.00 \times 10^{18*}$ | 0.52×10^{18} | 1.90×10^{18} |
| Energy loss in target at $E_d = 1.45$ MeV (keV) | 2.1 | 11.2 | 2.9 | 10.5 |
| Target backing | Ta | Ta | Ta | self supp. |
| Target other | — | Au | — | Pd |
| Target current (nA) | 1000 | 700 | 70–130 | 25 |
| Method of charge collection | not given | Au-RBS | Brookhaven IC | Pd-RBS |
| Collected charge (μC) | 1800 | not given | 30 | 7 |
| Target-detector distance (cm) | 15 | 16 | 7 | 9.5 |
| Ge detector volume | planar 10 cm ³ | planar 10 cm ³ | 115 cm ³ | 170 cm ³ |
| Ge detector angle | 0° | 0° | 135° | 55° |
| Particle detector | no | 90° and 135° | no | 135° |
| E_d range (MeV) | 0.8–2.2 | 1.4–3.2 | 0.5–4.0 | 0.74–2.0 |
| Cross-section unit | arbitrary | mbarn | mbarn | mbarn |
| Uncertainty | not given | 12% | 10% | 6% |

As it is illustrated in Table 4.17, Tryti *et al.* [4.61] gave their cross-section values in arbitrary units in their first paper. Because the experimental conditions in the second measurement were practically the same as in the first and because there is a large overlap between the deuteron energy intervals, it was possible to normalize the two curves and then use them for comparison with other results.

Figure 4.30 shows substantial differences with regard to the energy scale as well as the cross-section values between the measurements. The energy shift in the data of [4.62] is most likely caused by an error in the energy calibration of the accelerator. If the data are shifted in energy, they agree, for beam energies below 2 MeV, with the measurements of [4.59]. For the energy range above 2 MeV, the situation is not so satisfactory and needs further investigation. However, work with deuteron beams is mostly performed below 2 MeV, due to an increasing neutron background at higher energies and for radiation safety reasons.

Thick-target yields for the analysis of infinite thick samples has been measured by Elekes *et al.* [4.18] in the beam energy range of 0.7 to 3.4 MeV and an explicit value is given with an error of $\sim 5\%$ for the beam energy of 1.8 MeV. These data are in an excellent agreement with the results from integrating the thin-target differential data from [4.59].

(c) Recommended data

Based on the assessed experimental differential cross-section data, the calculation of an evaluated cross-section function would be advisable, at least for the 0.7–2.0 MeV deuteron energy range. For the energy range above 2 MeV, further cross-section measurements are needed, as mentioned above.

4.4.2.2. $^{13}\text{C}(d,p\gamma)^{14}\text{C}$

The deuteron induced γ -emission on ^{13}C has a low cross-section and is therefore not of importance for material analysis. Though the γ -energies of the first and third excited state in ^{14}C are higher than those from the $^{12}\text{C}(d,p\gamma)^{13}\text{C}$ reaction, they will be practically covered by γ -lines from other light constituents in the given sample. Very few cross-section data exist in the literature. Elekes *et al.* [4.18] gave a γ -spectrum at a deuteron energy of 1.8 MeV on a solid natural carbon sample, where the lines from the $^{13}\text{C}(d,p\gamma)^{14}\text{C}$ reaction can be seen. No value for the cross-section, however, is given.

4.5. NITROGEN

4.5.1. Gamma-ray production cross-sections of nitrogen from proton-induced nuclear reactions

Previous thick-target yield measurements on natural nitrogen showed that there are essentially two γ -rays which have a yield large enough to be suitable for analytical purposes [4.2]. These are the 2313 keV γ -ray from the $^{14}\text{N}(p,p\gamma_{1-0})^{14}\text{N}$ reaction and the 4439 keV γ -ray from the $^{15}\text{N}(p,\alpha\gamma_{1-0})^{12}\text{C}$ reaction. The (p,γ) radiative capture reactions have only astrophysical significance. There are only a few previous thin-target cross-section measurements for nitrogen, which is likely due to the low yields of the above-mentioned γ -rays. The aim of these previous studies was more to study basic nuclear physics than to apply them to ion beam analysis. Therefore, it was important to have new thin-target cross-section measurements included within the CRP [4.63].

4.5.1.1. $^{14}\text{N}(p,p\gamma_{1-0})^{14}\text{N}$: 2313 keV γ -ray

(a) New measurements

Since the $E_x = 2.31$ MeV excited state of ^{14}N has a 0 spin value, the angular distribution of that γ -ray is isotropic, and this excited state has a $\tau_m = 98.7$ fs mean life causing a Doppler broadening in the gamma spectrum [4.64]. Recent γ -ray production cross-section measurements were performed by the Helsinki group and were published in Marchand *et al.* [4.63]. The proton beam was generated by the 5 MV belt-driven tandem accelerator of the University of Helsinki. The $^{14}\text{N}(p,p'\gamma)^{14}\text{N}$ reaction with resonances at 3903, 3996, and 5937 keV were exploited in the calibration of the absolute proton beam energy at 4–6 MeV, with precision better than 1 keV. The calibration procedure is described in detail in [4.65]. The γ -rays were detected with a 38% efficient HPGe germanium detector positioned 20 mm from the target. The detection angle was fixed to 55° relative to the beam direction. The absolute efficiency curve for the detector was determined by using Eu-152, Co-60 and Co-56 calibration sources placed at the position of the target. For more details on energy calibration, see Section 3.1.

A thin self-supporting Si_3N_4 membrane, obtained from Silson Ltd, was used as the target for cross-section measurements. The nominal foil thickness was $100 \text{ nm} \pm 10\%$ and the window area of the membrane was $5 \times 5 \text{ mm}^2$. The composition and areal density of the target was determined accurately by ERDA. The collected charge was measured from a shielded Faraday cup equipped with secondary-electron suppression. The excitation function was measured in the proton energy range of 3586–6920 keV with 100 keV energy steps for the regions that are farther away from the reaction resonance and narrower steps for regions that are closer to the reaction resonance. The obtained γ -ray production cross-sections are presented in Fig. 4.31 as

a function of proton energy. Special care was taken to accurately determine the composition and areal density of the Si_3N_4 membrane. Possible sources of error in the measured yield values include current integration, detection efficiency and the stopping power correction.

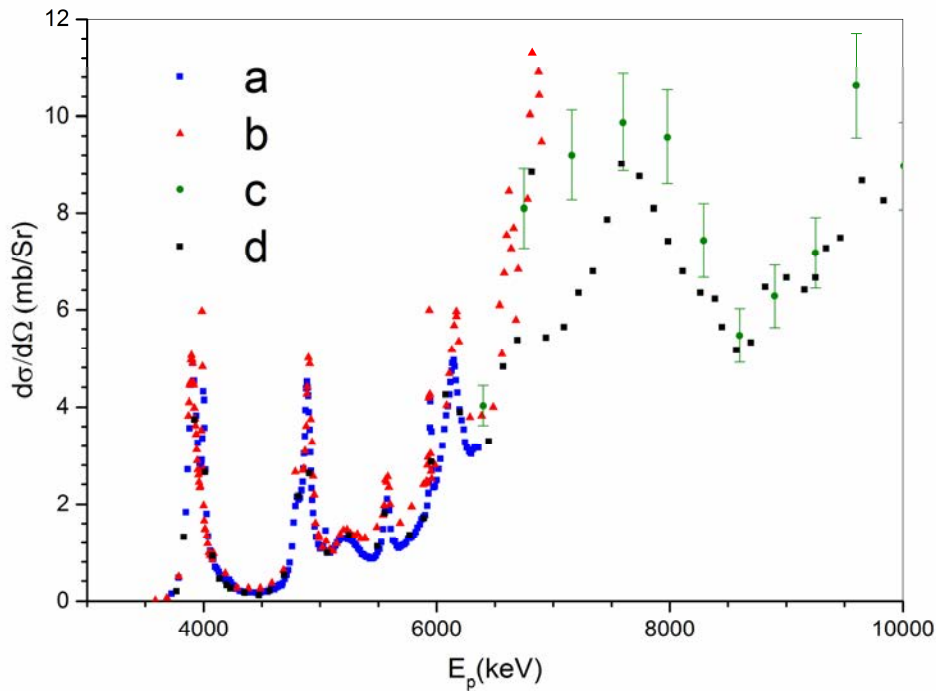


FIG. 4.31. Differential γ -ray production cross-sections of the 2313 keV γ -ray $^{14}\text{N}(p,p\gamma_{1-0})^{14}\text{N}$ resonance as a function of proton energy deduced from the work of b) [4.63] and from the literature a) [4.66], c) [4.67] and d) [4.52].

(b) Data in the literature and assessment

In Fig. 4.31, the results of the new measurement and also the values of three previous cross-section measurements are shown.

Phillips *et al.* [4.66] used melanin ($\text{C}_3\text{H}_6\text{N}_6$) as a nitrogen target, which was evaporated onto thin carbon backings. No other details about the target were given. The excitation curve was taken from 3750 to 5220 keV proton energies with steps around 15 keV with a NaI(Tl) detector. Later, the measurement was repeated but with smaller steps and extended to a proton energy of 6360 keV using a Ge(Li) detector placed at 90° with respect to the beam direction. The curve was normalized to an inelastic cross-section of 61 mb for the 3.90 MeV resonance [4.68]. Systematic uncertainty for the normalization was estimated at less than 10%.

Dyer *et al.* [4.52] performed γ -ray producing cross-sections measurements that are relevant to γ -ray astronomy including for the $^{14}\text{N}(p,p'\gamma)^{14}\text{N}$ reaction. Experimental details are as follows. Proton energies varied from 3.7 to 23 MeV with an energy resolution of a few keV. Charge determination was performed through the integration of the beam in a Faraday cup. The γ -rays were detected by two Ge(Li) detectors at $\sim 31^\circ$ and 110° with respect to the beam direction. For the target, a gas cell was filled with high purity natural nitrogen. Uncertainties arise from yield determination (generally 5%), beam current integration ($\sim 3\%$), target

thickness measurement (5%) and Ge(Li) efficiency measurement (estimated at 5%). These uncertainties were added quadratically to give the approximate absolute uncertainty of 10%.

Table 4.18 shows the uncertainty budget of the new measurement in comparison with the two literature data mentioned above. Final uncertainties are in the same range for all three results.

A recent paper, the aim of which was to produce data for nuclear reaction models [4.67], also contained measured γ -ray production cross-sections of nitrogen in the proton energy range 6550–26200 keV, using a gas target. The γ -rays were detected with four high-purity Ge detectors between 30° and 135°. Possible sources of error, including from the gas cell and gamma detector efficiency, were carefully studied. The deduced cross-section values are also presented in Fig. 4.31 (10 MeV was set as an upper limit of proton energy, which is a usual limit in IBA applications).

TABLE 4.18. ESTIMATED UNCERTAINTY BUDGET FOR THE ABSOLUTE DIFFERENTIAL CROSS-SECTION VALUES FOR 2313 keV $^{14}\text{N}(p,p\gamma_{1-0})^{14}\text{N}$ FROM THE MEASUREMENT OF [4.63] AND LITERATURE DATA.

| Quantity | [4.66] | [4.52] | [4.63] |
|---|--------|---------|-------------|
| Beam energy spread (keV) | | „a few” | ~2.5 keV |
| Charge collection | | 3% | 3% |
| Target inhomogeneity | | 5% | < 1.0% |
| N_T number of target nuclei per square centimeter | | — | 3% |
| Target stoichiometry | | — | 0.5% |
| γ -ray peak area | | 5% | 1.5*–3.0**% |
| γ -ray detector absolute efficiency | | 5% | 5% |
| Final uncertainty | 10% | 10% | 10% |

* at resonance

** off-resonance

The comparison of the measured cross-section data shows that the present values of Marchand *et al.* [4.63] are generally higher throughout the entire energy range than the data of Phillips *et al.* [4.66] and Dyer *et al.* [4.52]. However, up to energies of 5 MeV, the discrepancies do not exceed the experimental uncertainties. Two of the measured cross-section values of Benhabiles-Mezhoud *et al.* [4.67] are in the range of Marchand’s values and match up well. Between these data and the data of Dyer *et al.*, however, there is a large discrepancy within the energy range 7–8.5 MeV. In the new measurements [4.63], the resonances are narrower and stronger than in the previous ones.

To check the reliability of thin-target cross-sections, Marchand *et al.* made thick-target measurements on different nitrogen containing samples (BN and Si₃N₄) at several proton energies. The measured thick-target yields were compared with corresponding calculated thick-target yields deduced from γ -ray producing cross-sections that were measured by the same group and Phillips *et al.* The results are presented in Fig. 4.32. For the sake of completeness, Fig. 4.32 also shows the results of an old absolute thick-target γ -yield measurement made by the Helsinki group [4.3] and a very new measurement of Chiari *et al.* [4.69]. It was found that the trends for the experimental and calculated values are similar. However, the present experimental values are systematically lower than the calculated thick-target yields by 45–30%. The experimental thick-target yields obtained by the Si₃N₄ target are

systematically slightly lower than the values obtained by the BN target. The values obtained by using the cross-section data of Phillips *et al.* are in good agreement with the values obtained by calculating the thick-target yields from the present cross-section data.

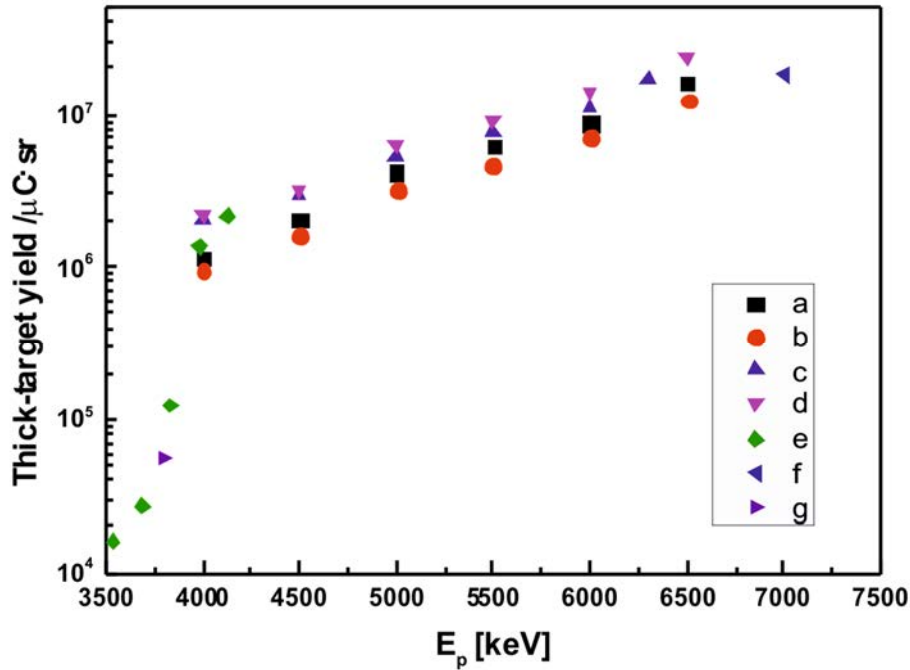


FIG. 4.32. Comparison of measured thick-target yields of the 2313 keV γ -ray $^{14}\text{N}(p,p\gamma_{1-0})^{14}\text{N}$ resonance as a function of proton energy: (a) BN exp [4.63], b) Si₃N₄ exp [4.63], with calculated thick-target yields deduced from the corresponding γ -ray producing cross-sections measured by c) [4.66] and d) [4.63]. Some measured thick-targets yields from literature are also included for comparison: e) [4.2], f) [4.3] and g) [4.69].

(c) Recommended data

Based on the results of the above four γ -ray production cross-sections, it can be concluded that the measurements of Marchand *et al.* [4.63] are recommended for PIGE analysis due to the narrower resonances and good agreement with other data, for proton energy up to 6.5 MeV. The large discrepancies between the experimental values above 6.5 MeV suggests that re-measurement of these cross-sections is advisable.

4.5.1.2. $^{14}\text{N}(p,p\gamma_{2-1})^{14}\text{N}$: 1635 keV γ -ray

(a) Data in the literature and assessment

The transition from the second excited state ($E_x = 3.95$ MeV) to the first one produces the 1635 keV γ -ray. Its cross-section as a function of proton energy was extracted from the measurements of Phillips *et al.* [4.66], Dyer *et al.* [4.52] and Benhabiles-Mezhoud *et al.* [4.67]. Their results are compared in Fig. 4.33. As demonstrated in Fig. 4.33, there is good agreement between the values of Phillips *et al.* and Dyer *et al.* below 6.5 MeV. The measured cross-section values of Dyer *et al.* and Benhabiles-Mezhoud *et al.* show large discrepancies above this energy. The 3.95 MeV state has a spin value of 1, which means that the angular distribution of the 1635 keV γ -ray is anisotropic. Because of the higher reaction threshold, its

yield becomes measurable around 5 MeV, and its cross-section is about 50% of the 2313 keV γ -ray at higher energies.

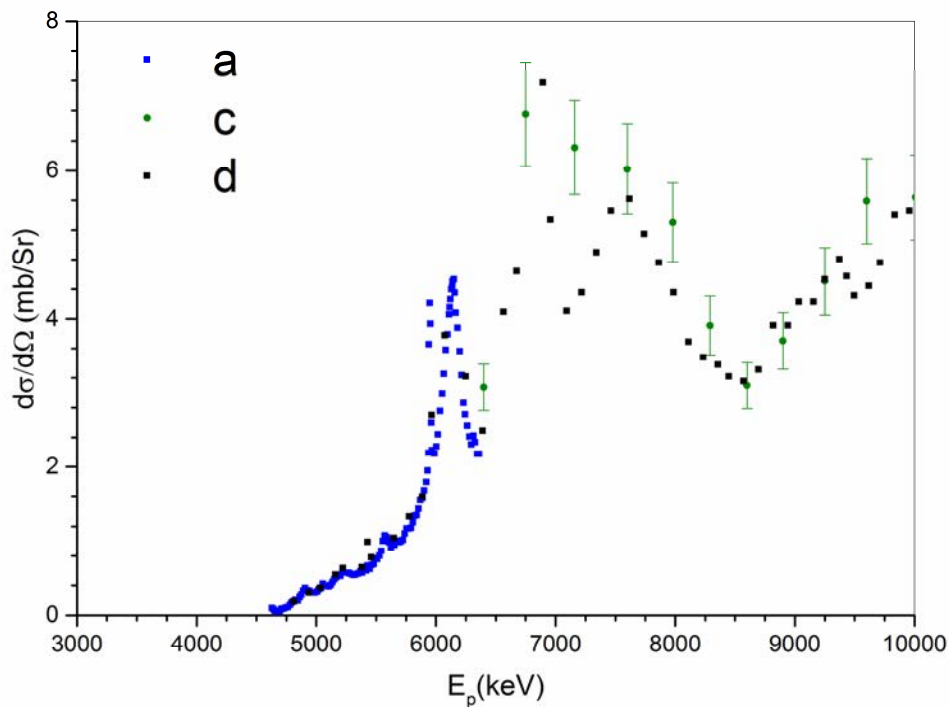


FIG. 4.33. Differential γ -ray production cross-sections of the 1635 keV $^{14}\text{N}(p,\gamma_{2-1})^{14}\text{N}$ resonance as a function of proton energy, deduced from the work of a) [4.66] at 90° , c) [4.67] and d) [4.52].

(b) Recommended data

The laboratories that have large accelerators, with energies larger than 6 MeV, have the additional possibility to use the γ -ray for PIGE analysis. For proton beams with an energy above 6.5 MeV, there are large discrepancies between the measured cross-sections of Dyer *et al.* [4.52] and Benhabiles-Mezhoud *et al.* [4.67]. A re-measurement of the 1635 keV γ -ray production cross-sections at proton energies above 6.5 MeV could result in resolving the discrepancies and provide a reliable cross-section for this γ -ray as well.

4.5.1.3. $^{15}\text{N}(p,\alpha\gamma_{1-0})^{12}\text{C}$: 4439 keV γ -ray

(a) Data in the literature and assessment

Thick-target yield measurements on natural nitrogen sample show that the intensity of the 4439 keV γ -ray is not negligible in comparison with the intensity of the 2313 keV γ -ray. In spite of that, the abundance of ^{15}N in natural nitrogen samples is only 0.368 % as compared to the abundance of ^{14}N , which is 99.632 %. Gorodetzky *et al.* [4.70] measured γ -ray production cross-sections from 350 to 1910 keV, using a gas target enriched by ^{15}N to 99.6 %. Rolfs and Rodney [4.71] took measurements within the 150–2500 keV proton energy range and also used a gas target. More recently, Imbriani *et al.* [4.72] repeated the cross-section measurements in the 150–1910 keV proton energy range. The ^{15}N enriched TiN target was created by sputtering Ti onto Ta backings under nitrogen atmosphere that had been enriched

to 99.95% ^{15}N . The reaction γ -rays were detected using a HPGe clover detector. The results are presented in Fig. 4.34 for comparison.

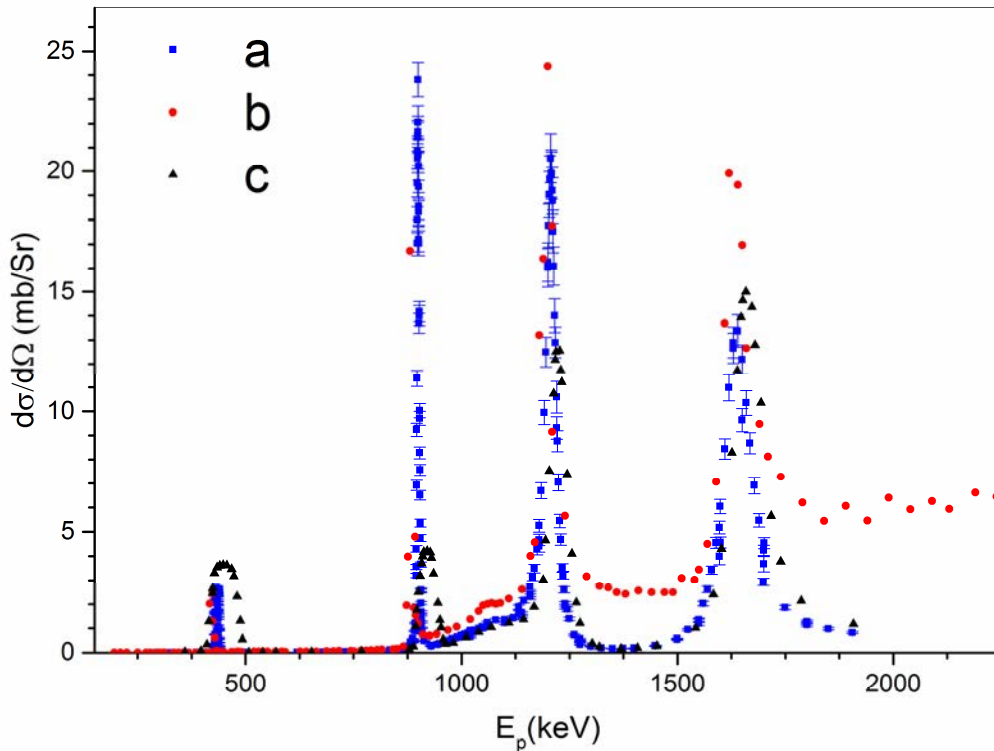


FIG. 4.34. Differential γ -ray production cross-sections of the $4439 \text{ keV } ^{15}\text{N}(p, \alpha \gamma_{1-0})^{12}\text{C}$ resonance as a function of proton energy, deduced from the work of a) [4.72], b) [4.71] and c) [4.70] at 90° . As the former two cross-section data [4.72, 4.71] were given as total cross-sections, they were divided by 4π to obtain differential cross-sections assuming isotropy.

The target of Gorodetzky *et al.* [4.70] was too thick (47 keV) for a precise cross-section measurement. The resonances of the other two measurements are narrow. The background between the resonances in the measurement made by Rolfs and Rodney [4.71] is quite high due to a contamination in the target.

(b) Recommended data

From the discussion in the previous section, it follows that only the cross-section values of Imbriani *et al.* [4.72] can be recommended for further application. It should be noted, however, that the purpose of these cross-section measurements was to provide data for astrophysical use and the beam current was around $10 \mu\text{A}$, which is much higher than usual for the PIGE technique. Nevertheless, there are possibilities to use this γ -ray for PIGE analysis, e.g. for biological applications with an external beam. Although the yield from this reaction increases for proton beam energies greater than 2 MeV, the background increases even more rapidly. For practical use, the optimum E_p region is about 1900–2100 keV [4.73].

4.5.2. Gamma-ray production cross-sections of nitrogen from deuteron-induced nuclear reactions

Thick target yield measurements [4.18] showed that, contrary to what was observed for proton-induced γ -ray yields, deuteron-induced γ -ray yields with nitrogen are very intense, even at low deuteron energies, since there are several γ -rays in both the high and low energy regions that produce high yields. The dominant nuclear reaction is the $^{14}\text{N}(d,p\gamma)^{15}\text{N}$, with a Q value of 8.609 MeV. Therefore the ^{15}N nucleus decays from highly excited states. Before this CRP, there was only one measurement of a thin target γ -ray production cross-section available in the literature [4.74]. It was therefore imperative that new measurements were performed and included in IBANDL in a timely manner.

4.5.2.1. $^{14}\text{N}(d,p\gamma_{7-0})^{15}\text{N}$: 8310 keV γ -ray

The 8310 keV γ -ray originates from the $^{14}\text{N}(d,p\gamma_{7-0})^{15}\text{N}$ transition. Due to the spin $\frac{1}{2}$ value of the initial state, from which the γ -ray is emitted, the angular distribution of the 8310 keV γ -ray is isotropic.

(a) New measurement

In the work of Csedreki *et al.* [4.75], the experiments were carried out using the 5 MV Van de Graaff accelerator of MTA ATOMKI, Debrecen. Energy calibration of the beam was determined with an uncertainty of 3 keV. The target chamber had several diaphragms in the long entrance tube that formed a beam of 1 mm diameter, ending in a long Faraday cup and was insulated from the rest of the beam pipe. This provided the possibility to measure accumulated beam charge on the set-up, which was performed by a digital current integrator. The γ -rays were detected using a 170 cm³ HPGe detector at 55° with respect to the beam direction and 9.5 cm from the target, and it was shielded from γ -rays originating from the Faraday cup. In order to determine the absolute efficiency of the γ -ray detector for every nitrogen γ -ray, radioactive sources supplemented with narrow resonance reactions were used. For $E_\gamma < 3500$ keV, calibrated radioactive sources (^{133}Ba , ^{56}Co , ^{60}Co , ^{137}Cs and ^{152}Eu) were placed at the exact position of the target. For $E_\gamma > 3500$ keV, the detector efficiency was determined using γ -ray cascades from the $^{23}\text{Na}(p,\gamma)^{24}\text{Mg}$ and $^{27}\text{Al}(p,\gamma)^{28}\text{Si}$ reactions at 1417 and 992 keV resonance energies, respectively. The absolute double escape efficiency was also calculated. With this knowledge, the contribution of the double escape line of the 8310 keV γ -ray could be separated from the 7299 keV γ -line in the γ -ray production cross-section calculations. The target chamber had an inlet at an angle of 135° for an ion-implanted silicon particle detector with 500 μm active depth, 35 keV energy resolution and a 3 mm diameter collimator positioned in front. The Si detector was used to detect backscattered particles simultaneously with γ -rays from the target. The description of the experimental set-up, accelerator energy calibration, particle detector solid angle determination and the absolute efficiency determination of the γ -ray detector are described in [4.76]. The target was a thin self-supporting silicon-nitride film with a nominal thickness of 200 ± 14 nm and an area of 5×5 mm², obtained from Norcada Inc. The number of target nuclides was determined with the detection of backscattered deuterons from nitrogen, within the energy region where the backscattering is considered Rutherford. The results were checked with the α -RBS technique. Since nitrogen has complicated deuteron-induced PIGE spectra, only relatively intense γ -rays were selected for yield measurements. The excitation function measurements were carried out with 50 keV steps from 2.0 to 0.65 MeV and, at certain points, the measurement was repeated twice. The obtained γ -ray production cross-sections for the 8310 keV γ -ray are presented in Fig. 4.35 as a function of deuteron energy. The main sources of uncertainties are collected in

Table 4.19. The errors were added quadratically. The average uncertainty of the nitrogen γ -ray production cross-sections is 5%.

(b) Data in the literature and assessment

In Fig. 4.35, the data of Bebber *et al.* [4.74], which is the only data found in the literature for nitrogen, is presented for comparison. Gamma-yields of the $^{14}\text{N}(d,p\gamma)^{15}\text{N}$ reaction were measured by bombarding thin Si_3N_4 films on silicon substrates prepared by plasma sputtering. The thicknesses of the targets were determined by ellipsometry and the areal density of ^{14}N was obtained by using the nominal density of Si_3N_4 . The areal density was confirmed by nuclear reaction analysis. Ion charge was collected on the wings of a beam chopper, which allowed the determination of the dose with a precision better than 2%. The γ -rays were detected by a high-efficiency detection system (solid angle around 4π , photo-peak-efficiency 47% for 8 MeV γ -rays) including a $12'' \times 12''$ NaI(Tl) bore hole detector. Due to the summing property of the detection system, practically no escape peaks appeared and the Compton background was significantly reduced. This feature was especially advantageous in the case of nitrogen, where the presence of escape peaks of high-energy γ -rays make the γ -spectrum and its evaluation more complicated. Total cross-section curves for the γ -rays of 7299 and 8310 keV were obtained in the deuteron energy range of 0.5–1.5 MeV. In Fig. 4.35, following convention, differential γ -ray cross-sections are obtained by dividing the given total cross-section values by 4π . The errors of the cross-section values contain the inaccuracies that resulted from the beam current and detection efficiency measurements as well as the error in the determination of surface atomic density. Table 4.19 details the uncertainty budget of the new measurement in comparison with the above literature data. Final uncertainties are in the same range for both results. A rather large discrepancy between the two results can be seen.

TABLE 4.19. ESTIMATED UNCERTAINTY BUDGET FOR THE ABSOLUTE DIFFERENTIAL CROSS-SECTION VALUES OF THE 8310 keV $^{14}\text{N}(d,p\gamma_{7-0})^{15}\text{N}$ FROM THE MEASUREMENTS OF [4.75] AND [4.74].

| Quantity | [4.74] | [4.75] |
|---|----------|---------|
| Beam energy spread (keV) | | 3.0 keV |
| Charge determination | < 2% | 3.0% |
| N_T number of target nuclei per square centimeter | 2.0–3.0% | 2.5% |
| γ -ray peak area | | < 4.0% |
| γ -ray detector absolute efficiency | ~2.0% | 2.0% |
| Final average uncertainty | 5.6% | 5.0% |

In Fig. 4.35, γ -ray production cross-section data of the new measurement are compared with the data of Bebber *et al.* [4.74]. Following convention, differential γ -ray cross-sections are obtained by dividing the total cross-section values given in [4.74] by 4π . A large discrepancy between the two results can be observed.

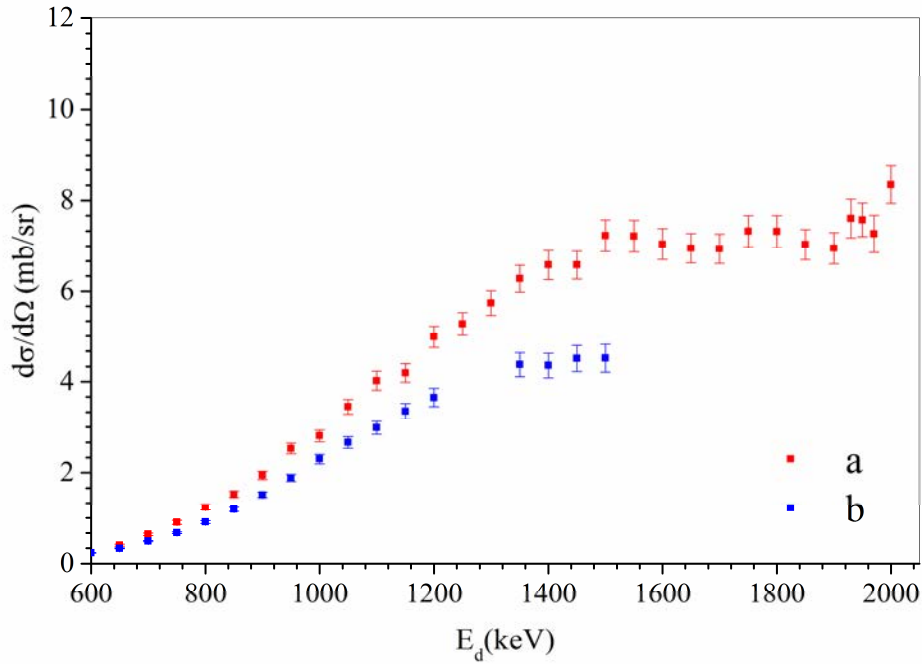


FIG. 4.35. Differential γ -ray production cross-sections of the 8310 keV $^{14}\text{N}(d,p\gamma_{7-0})^{15}\text{N}$ resonance as a function of deuteron energy, taken from the works of a) [4.75], b) [4.74].

A comparison of the integrated cross-section data with previously reported thick-target yields confirms one of the differential cross-section curves from Fig. 4.35. For the 8310 keV γ -ray, only the thick-target γ -yields of Elekes *et al.* [4.18] are available in the literature. Figure 4.36 illustrates that the data of Csedreki *et al.* [4.75] follow the tendency of the measured curve, while Bebbler's data [4.74] gradually deviates from it. From a detailed comparison [4.77], it was deduced that although both the calculated thick-target yields show large variances, most of Csedreki's data are within the 25% uncertainty band of the experimental thick-target curve. Data from [4.74] has a systematic shift on the negative scale that gradually increases in deviation. Furthermore, it was found that the evaluation of the large Doppler broadened 8310 keV peak could cause an additional uncertainty in the elimination of the background for both thick and thin target γ -spectra. After removing data points charged with this possible additional uncertainty, the data of Csedreki *et al.* remain within the 0–15 % uncertainty band, while the data of Bebbler *et al.* are 10–25 % lower than the measured thick-target yield.

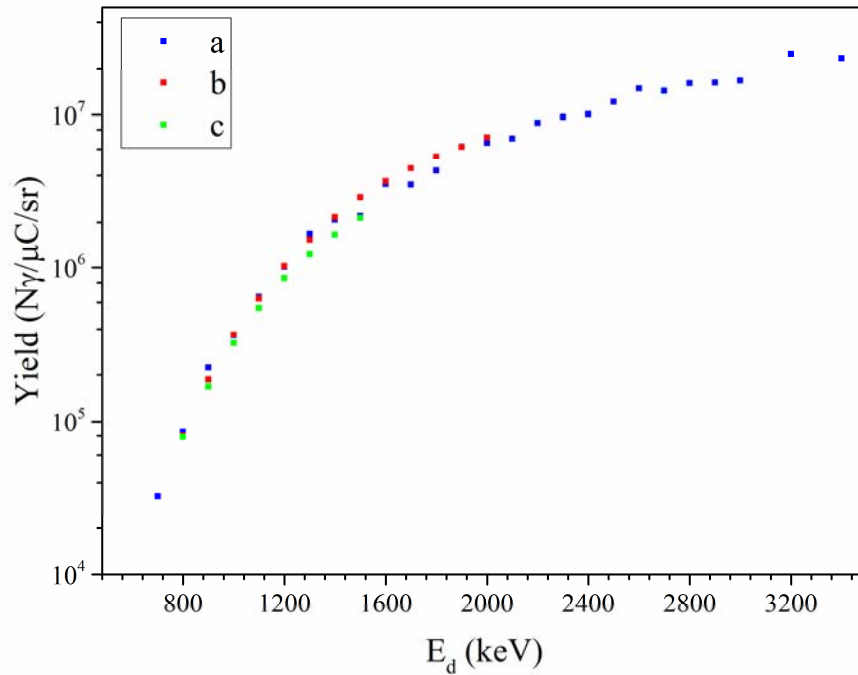


FIG. 4.36. Thick-target yields of the 8310 keV $^{14}\text{N}(d,p\gamma)^{15}\text{N}$ resonance as a function of deuteron energy. Data obtained from a) measured yields [4.18], b) and c) calculated yields using cross-sections of [4.75] and [4.74], respectively.

(c) Recommended data

The γ -ray production cross-sections measured for the 8310 keV γ -ray from the $^{14}\text{N}(d,p\gamma)^{15}\text{N}$ nuclear reaction by Csedreki *et al.* [4.75] during this CRP cover a larger deuteron energy region and contain more data points than previous measurements. However, the large discrepancy between the new and the old data, which are beyond the quoted experimental uncertainties, still cannot be explained. To resolve the problem and be able to recommend suitable cross-section data, an evaluation of the measured cross-sections is necessary. Further validation, by comparing the results with measured thick-target yields, is suggested. Additional differential cross-section measurements would also be useful.

4.5.2.2. $^{14}\text{N}(d,p\gamma_{5-0})^{15}\text{N}$: 7299 keV γ -ray

The 7299 keV γ -ray originates from the $^{14}\text{N}(d,p\gamma_{5-0})^{15}\text{N}$ reaction. The initial state from which the γ -ray is emitted has a 3/2 spin value. Therefore, an anisotropic angular distribution is expected to be observed for this γ -ray.

(a) New measurement

In the work of Csedreki *et al.* [4.75], the differential cross-sections for the 7299 γ -ray and the 8310 keV γ -ray from the $^{14}\text{N}(d,p\gamma)^{15}\text{N}$ reaction were measured simultaneously. The 7299 keV γ -ray is the strongest, however its full energy (FE) peak is contaminated by the double escape (DE) peak of the 8310 keV γ -ray. For the determination of the cross-section of this γ -ray, the above mentioned DE peak was subtracted based on the known absolute DE efficiency curve of the HPGe detector. The resulting differential γ -ray production cross-sections and the corresponding errors are presented in Fig. 4.37 as a function of beam energy.

(b) Data in the literature and assessment

The γ -ray production cross-sections of the 7299 keV γ -ray were also measured by Bebbler *et al.* [4.74]. These data are compared with the new measurements in Fig. 4.37. The advantage of using a 4π γ -detector [4.74] was exploited in the case of this γ -ray, i.e. determining cross-sections from the measured spectra without having to deal with the problem of disturbing escape peaks. Moreover, the obtained total cross-sections are independent from anisotropic angular distributions. However, there is a large discrepancy between the new and old results, like in the case of the 8310 keV γ -ray. The total cross-sections of [4.74] were divided by 4π to give differential cross-sections for comparison with the new data of [4.75]. The underlying assumption is that this γ -line has negligible anisotropy within the experimental uncertainties.

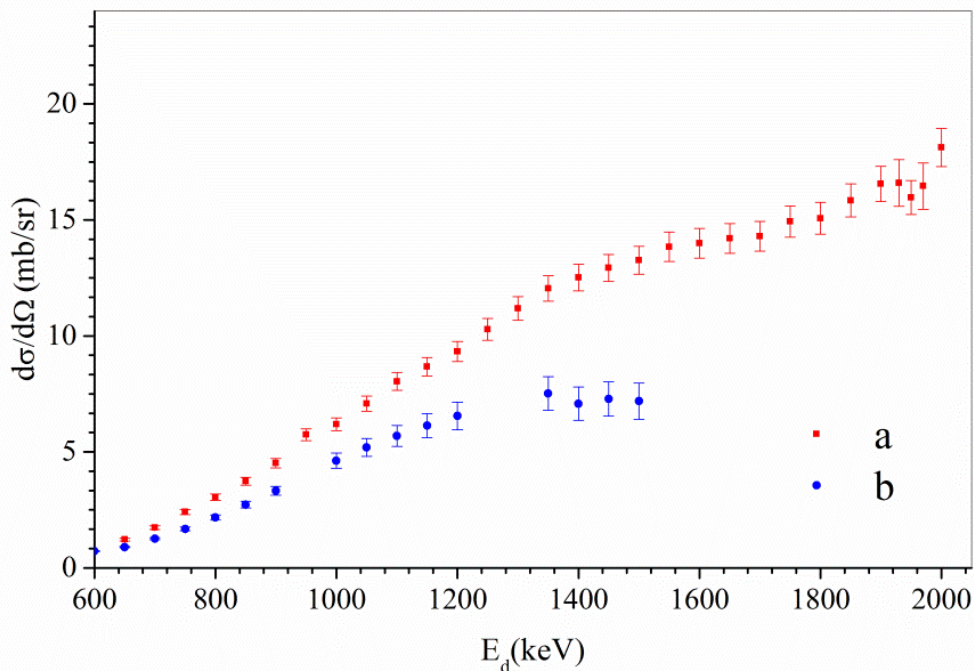


Fig. 4.37. Differential γ -ray production cross-sections of the 7299 keV $^{14}\text{N}(d,p\gamma_{5-0})^{15}\text{N}$ resonance as a function of deuteron energy. Data obtained from the works of a) [4.75] at 55° and b) [4.74].

(c) Recommended data

The measurement of the γ -ray production cross-section for the 7299 keV γ -ray in the $^{14}\text{N}(d,p\gamma)^{15}\text{N}$ nuclear reaction by Csedreki *et al.* [4.75] was compared with the only existing data [4.74] prior to the CRP. Because these new cross-section data are ‘clean’ from the contamination of the second escape peak of the 8310 keV γ -ray, they can not generally be applied directly to PIGE analysis. Instead, the use of the 8310 keV γ -ray production cross-section is recommended. Alternatively, the differential γ -ray producing cross-section of the 7299 + 8310 DE keV peak can be measured. The yield of this composed peak is much higher than the yield of the 8310 keV γ -line, however the determination of the ratio of the DE/FE peak depends strongly on the detector geometry.

4.5.2.3. $^{14}\text{N}(d,p\gamma_{6-1})^{15}\text{N}$: 2297 keV γ -ray

The initial state from which the 2297 keV γ -ray is emitted has 7/2 spin value. Therefore the angular distribution of the 2297 keV γ -ray is expected to be anisotropic.

(a) New measurement

The cross-section for the production of the 2297 keV γ -ray from the $^{14}\text{N}(d,p\gamma_{6-1})^{15}\text{N}$ reaction was measured by [4.75] and the results are plotted in Fig. 4.38. No previous measurement exists in the literature.

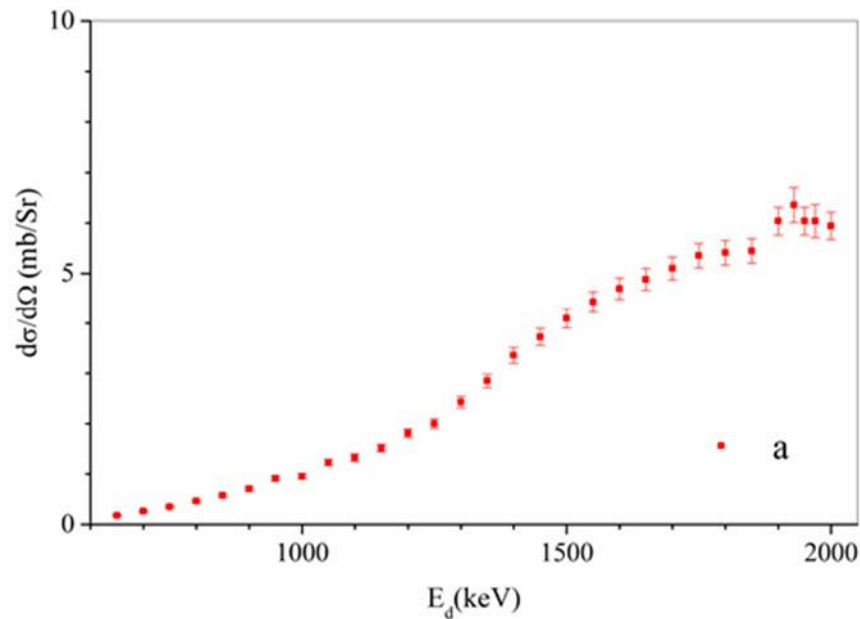


FIG. 4.38. Differential γ -ray production cross-section of the 2297 keV $^{14}\text{N}(d,p\gamma_{6-1})^{15}\text{N}$ resonance measured at an angle of 55° as a function of deuteron energy. Data obtained from the work of a) [4.75].

(b) Assessment

The integrated cross-section data were compared with previously reported thick-target yields [4.18]. From the result presented in Fig. 4.39, one can conclude that the calculated yield is systematically larger than the measured thick-target yield. However, this deviation remains within the 25% uncertainty band.

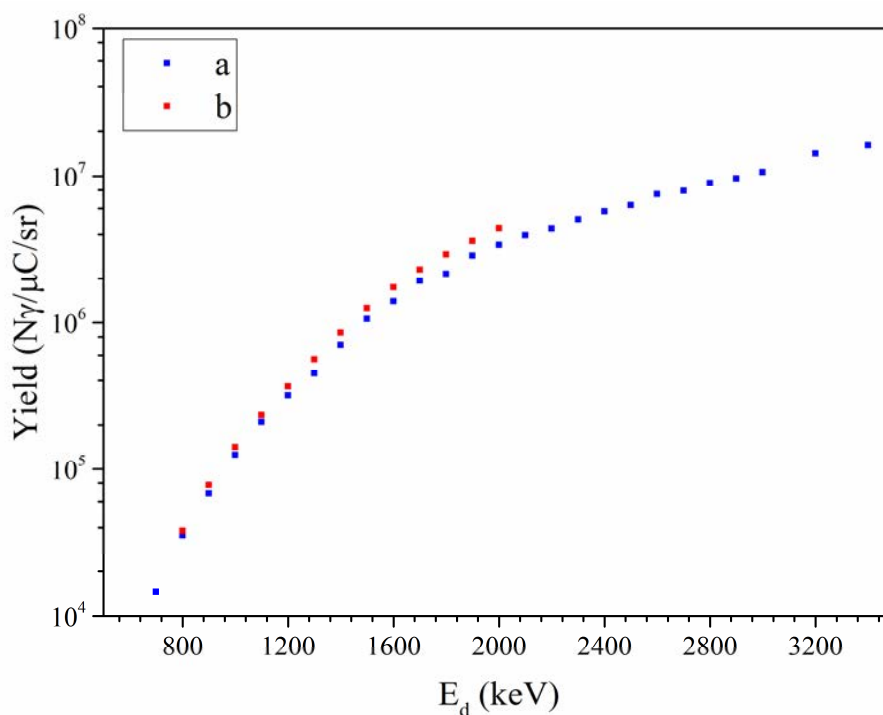


FIG. 4.39. Thick-target yields of the 2297 keV $^{14}\text{N}(d,p\gamma_{6-1})^{15}\text{N}$ resonance as a function of deuteron energy. Data obtained from thick target yields a) measured at 135° [4.18] and b) calculated from the differential cross-sections of [4.75] measured at 55° .

(c) Recommended data

The differential γ -ray production cross-section values of the 2297 keV γ -ray are about 70% of the corresponding values of the 8310 keV γ -ray when induced by deuteron beam with energy around 2 MeV. However, there are some advantages in using this γ -ray for PIGE analysis, e.g. its Doppler broadening is smaller due to its lower energy, which makes it easier to subtract the background. The determination of the efficiency of the γ -detector is also straightforward, since, at lower γ -energy, it can be performed solely with radioactive sources without the need to use nuclear reactions.

4.5.2.4. $^{14}\text{N}(d,p\gamma_{4-1})^{15}\text{N}$: 1885 keV γ -ray

For the 1885 keV γ -ray of the $^{14}\text{N}(d,p\gamma_{4-1})^{15}\text{N}$ reaction, the initial state emitting the γ -ray has a $5/2$ spin value, which indicates that an anisotropic angular distribution is expected for this γ -ray. The γ -ray is also Doppler broadened due to the 18 fs lifetime of the initial state.

(a) New measurement

Csedreki *et al.* [4.75] also measured these cross-sections for γ -rays and results are plotted in Fig. 4.40. No other measurement can be found in the literature.

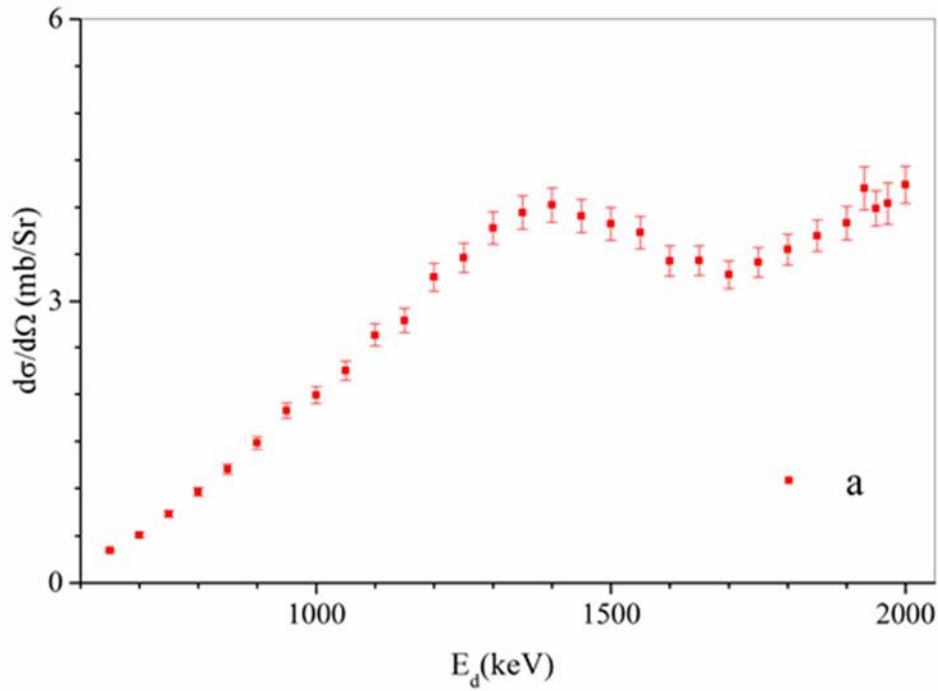


FIG. 4.40. Differential γ -ray production cross-sections of the 1885 keV $^{14}\text{N}(d,p\gamma_{+1})^{15}\text{N}$ resonance measured at an angle of 55° as a function of deuteron energy. Data obtained from a) [4.75].

(b) Assessment

The resulting differential γ -ray production cross-sections and corresponding errors are presented in Fig. 4.40 as a function of incident beam energy. The energy dependence of the obtained cross-sections shows deviations from the direct reaction mechanism. This is clearly observed for the 1885 keV γ -ray, where a pronounced maximum is seen in the cross-section function in the studied energy interval.

The integrated cross-section data was compared with previously reported thick-target yields [4.18]. From the result presented in Fig. 4.41, it can be concluded that the calculated yield is systematically larger than the measured thick-target yield. However, this deviation is not higher than 15%.

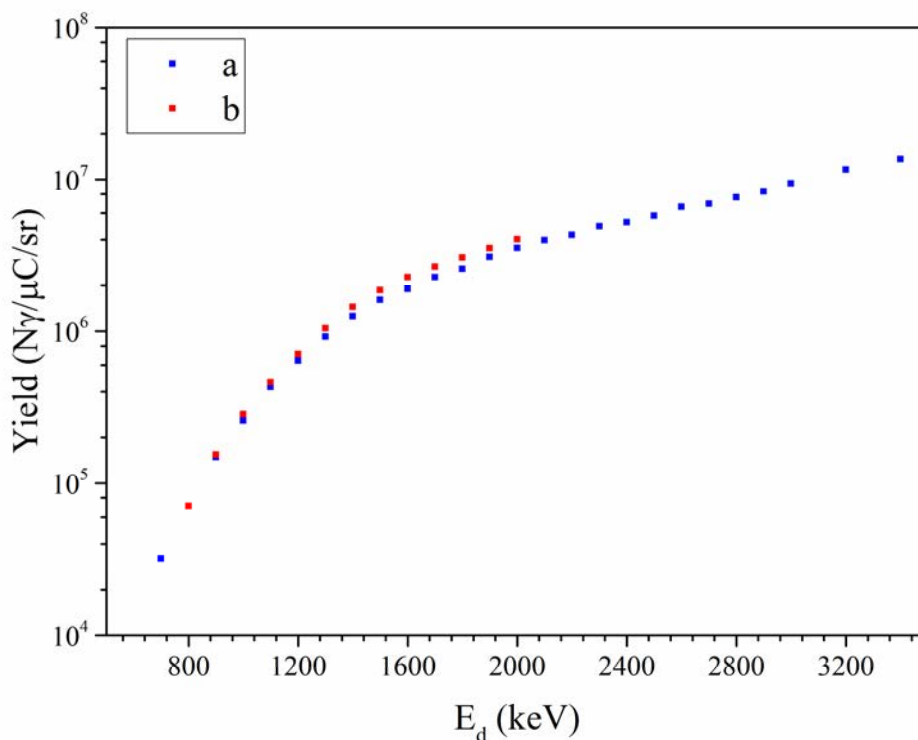


FIG. 4.41. Thick target yields of the 1885 keV $^{14}\text{N}(d,p\gamma_{+1})^{15}\text{N}$ resonance as a function of deuteron energy. Data obtained from a) measured yields at 135° [4.18] and b) calculated yields from the differential cross-sections of [4.75] measured at angle of 55° .

(c) Recommended data

The advantage of using the resulting cross-section values for PIGE analysis is that for the determination of the γ -detector efficiency, no use of nuclear reaction measurement is required. It is recommended that the 1885 keV γ -ray be used, e.g. in simultaneous measurement of nitrogen and oxygen containing samples.

One additional remark is that the calculated thick-target yields for all four γ -rays of the $^{14}\text{N}(d,p\gamma_{+1})^{15}\text{N}$ reaction are higher than the measured γ -yields of Elekes *et al* [4.18]. In the absence of any other experimental data, additional measurements are recommended for both thin and thick targets in order to properly validate the results.

4.6. FLUORINE

4.6.1. Gamma-ray production cross-sections of fluorine from proton-induced nuclear reactions

4.6.1.1. $^{19}\text{F}(p,p'\gamma)^{19}\text{F}$: 110 keV and 197 keV γ -rays

(a) New measurements

Four laboratories, RBI, LABEC-INFN, CTN/IST, and CMAM-UAM, took responsibility for measuring cross-sections for PIGE emission produced by protons on ^{19}F . Two different γ -rays were considered: the $^{19}\text{F}(p,p\gamma_{1-0})^{19}\text{F}$ ($E_\gamma = 110$ keV) and the $^{19}\text{F}(p,p\gamma_{2-0})^{19}\text{F}$ ($E_\gamma = 197$ keV), while two other γ -rays, the $^{19}\text{F}(p,p\gamma_{3-1})^{19}\text{F}$ ($E_\gamma = 1236$ keV) and $^{19}\text{F}(p,p\gamma_{4-1+5-2})^{19}\text{F}$ ($E_\gamma = 1349/1357$ keV), have been measured so far only by the group at RBI [4.79]. The yield of the

latter two γ -rays was known to be significantly lower than those for the first two. Since the first two γ -rays are more suitable for PIGE analysis, they were the only ones included in the list of planned measurements for the CRP.

The 110 keV γ -ray has an isotropic angular distribution (due to the spin -1/2 of the initial first excited state) while the 197 keV γ -ray is expected to have an anisotropic angular distribution (spin -5/2 of the initial second excited state of ^{19}F). The cross-sections have been measured for proton energies spanning from 815 keV to 4415 keV. Each group covered a different energy range with a common overlap between 2133 and 3022 keV. As a result, there are at least two measurements for any given part of the explored region. The laboratories used different experimental conditions, which are summarized in Table 4.20 and have produced, as a consequence, different uncertainty budgets, which are summarized in Table 4.21.

RBI measured target areal densities ratios by 1.8 MeV a BS obtaining $N^{19}\text{F}/\text{NAu} = 47 \pm 1$, $N^{24}\text{Mg}/\text{NAu} = 18.3 \pm 0.4$ $N^{25}\text{Mg}/\text{NAu} = 2.32 \pm 0.05$. The detector efficiency was measured by placing calibrated sources of ^{60}Co , ^{133}Ba , ^{137}Cs and ^{152}Eu in the exact target position. Afterward, the absolute efficiency at 110, 197, 1236 and 1349 keV was obtained from a third degree polynomial fit in the argument $1/E_\gamma$. To avoid absolute collected charge measurements, the RBI, LABEC-INFN and CTN/IST groups extracted PIGE differential cross-sections, relative to the known values of the proton Rutherford backscattering cross-sections and the known quantity of high Z element (Au or Ag) present in the target. In this case, the particle detector was a Si surface barrier whose solid angle was determined by the RBS of 1.8 MeV protons of thick single element targets (Ni, Sn, Ta, Au). The energy calibration was performed using the resonance at 991.88 ± 0.04 keV of the $^{27}\text{Al}(p,\gamma)^{28}\text{Si}$ reaction and the $^7\text{Li}(p,n)^8\text{Be}$ reaction threshold at 1880.44 ± 0.02 keV. After calibration, the proton beam energy was known with an accuracy of 0.06%.

LABEC-INFN used the same targets as the CTN/IST, i.e. a NaF film evaporated on a self-supporting Ag film. The target thickness was $\text{NaF} = 34.9 \pm 1.5$ $\mu\text{g}/\text{cm}^2$ and $\text{Ag} = 51.0 \pm 1.8$ $\mu\text{g}/\text{cm}^2$ and the atomic ratio was $\text{F}/\text{Ag} = 1.73 \pm 0.05$, as measured by 2.0 MeV α scattering. They performed the same absolute efficiency calculation as RBI, using calibrated sources of ^{133}Ba and ^{152}Eu . For normalization purposes and to avoid absolute charge measurement, elastic scattered protons were collected simultaneously using a Si-PIN diode detector with a 10 mm^2 area, 300 mm thickness and 13 keV FWHM energy resolution, placed at a backward angle of 150° and collimated by a 1×13 mm^2 vertical slit. The subtended solid angle was 3.37 ± 0.08 msr, while the spread in the scattering angle was 1.0° due to beam size on the target and detector finite aperture. The proton beam energy was calibrated using an aluminum thick target and the resonances at 991.86 keV and 1683.57 keV in the (p, γ) and (p,p' γ) reactions, respectively, on ^{27}Al . The proton beam energy was also calibrated using a native silicon oxide thin target and the resonance at 3470 keV in the proton elastic scattering from ^{16}O . After the calibration, the proton beam energy was known with an accuracy of 0.15%.

The CTN/IST group produced the NaF targets that were also used by LABEC-INFN. Analysis by a particle RBS at 165° and incident energies of 1600 and 1800 keV gave the following thicknesses: $\text{F} = 5.1 \times 10^{17}$ at/cm^2 , $\text{Ag} = 3.2 \times 10^{17}$ at/cm^2 with an atomic ratio $\text{F}/\text{Ag} = 1.59$, about 9% lower than the Florence independent measurements average. The absolute efficiency versus γ -ray energy was obtained by measuring the yields of γ -rays produced by ion sources (^{133}Ba and ^{153}Eu) calibrated in activity as well as by Monte Carlo simulations using GEANT and PENELOPE. For normalization purposes, scattered protons were detected at 157° to the incident beam by Camberra PIPS detectors with an active area of 50 mm^2 and a depletion layer of 100 mm. The detector was located at 88 mm from the target,

following Cornell geometry, with solid angles defined by apertures of 6.00 ± 0.05 mm. Proton energy was calibrated using the 1645 and 1931 keV resonances of the $^{23}\text{Na}(p,p'\gamma)^{23}\text{Na}$ reaction and the 3470 keV resonance of the $^{16}\text{O}(p,p)^{16}\text{O}$ reaction.

TABLE 4.20. COMPARISON OF EXPERIMENTAL CONDITIONS OF THE FOUR LABORATORIES MEASURING THE CROSS-SECTIONS OF THE PROTON-INDUCED ^{19}F REACTIONS

| Parameters | RBI | LABEC-INFN | CTN/IST | CMAM-UAM |
|--|--|---|---|--------------------------------|
| Gamma-detector absolute-efficiency at 110KeV | 1.30% ± 7–10% (relative) | $0.252 \pm 0.018\%$ | Not explicitly quoted | 0.40% ± 4.6% (relative) |
| Gamma-detector absolute-efficiency at 197KeV | 1.04% ± 7–10% (relative) | $0.213 \pm 0.013\%$ | Not explicitly quoted | 0.28% ± 1.9% (relative) |
| Gamma-detector angle | 135° | 45° | 130° | 135° |
| Gamma-detector distance to target | 6.6 cm | 18.6 cm | 5.6 cm | 21.1 cm |
| Target | MICROMATTER™ MgF ₂ 54.1 μg/cm ² on 6.3 mm Mylar foil + 4 nm Au layer evaporated on top | NaF evaporated on Ag film self-supporting. NaF 34.9 ± 1.5 μg/cm ² , Ag 51.0 ± 1.8 μg/cm ² | NaF evaporated on Ag film self-supporting. NaF 34.9 ± 1.5 μg/cm ² , Ag 51.0 ± 1.8 μg/cm ² | Various LiF targets (see text) |
| Beam size | 4 mm Ø | $1.0 \times 1.0 \text{ mm}^2$ | Not reported | 1.5–3 mm Ø |
| Energy range | 1950–3050 keV | 2463–4101 keV | 2144–4059 keV | 815–4415 keV |
| Beam Currents | 10–20 nA | 70–140 nA | < 200 nA | 150–300 nA |
| Particle detector solid angle | 7.7 +/- 0.2 msr | $3.37 \pm 0.08 \text{ msr}$ | $3.65 \pm 0.06 \text{ msr}$ | Not used |

TABLE 4.21. RELATIVE ERRORS AND UNCERTAINTY BUDGET FOR THE FOUR LABORATORIES MEASURING THE CROSS-SECTIONS OF THE PROTON-INDUCED ^{19}F REACTIONS

| Parameters | RBI | LABEC-INFN | CTN/IST | CMAM-UAM |
|--|---|---------------------------------------|--|-------------------------|
| γ -detector absolute-efficiency | $\pm 7\text{--}10\%$ | $\pm 7\%$ | $\pm 5\%$ | $\pm 1.9\text{--}4.6\%$ |
| Particle detector solid angle | $\pm 2\%$ | $\pm 2.4\%$ | $\pm 2.5\%$ | |
| γ -ray peak area | $< \pm 1\%$ (110–197 KeV) $< \pm 4\%$ (1236–1349 + 1357 KeV at $E_p > 2.2\text{MeV}$) $< \pm 22\%$ (1236 at $E_p < 2.\text{MeV}$) $< \pm 36\%$ (1349 + 1357 KeV at $E_p < 2.2\text{MeV}$) | $\pm 2\text{--}3\%$ | $\pm 1.4\%$ (resonances) $\pm 3.2\%$ (between resonances) | $\pm 1\%$ |
| Scattered particles peak area | $\pm 1\%$ | $\pm 1\%$ | $\pm 1\%$ | |
| Target Thickness | $\pm 5\%$ (MgF2) | $\pm 4.3\%$ (NaF) $\pm 3.5\%$ (Au) | $\pm 4.3\%$ (NaF) $\pm 3.5\%$ (Au) (as measured at LABEC-INFN) | $\pm 20\%$ |
| Atomic ratio | $\pm 2\%$ | $\pm 2\%$ | $\pm 3\%$ | |
| Rutherford cross-section | $\pm 1\%$ | $\pm 1\%$ | | |
| Collected charge | | | | $\pm 2.5\%$ |
| Cumulative error | $\pm 10\%$ (110 and 197 KeV) $\pm 10\text{--}24\%$ (1236keV) $\pm 10\text{--}38\%$ (1349 +1357keV) | $\pm 8\text{--}8.3\%$ | $\pm 6.5\text{--}7.1\%$ | $\pm 20\text{--}21\%$ |

The CMAM-UAM lab measured the absolute detector efficiency using the same procedure and sources as the RBI group. However, due to the fact that the entrance window of the REGe Canberra detector was a polymer, the efficiency had a maximum value at the 80.9979 keV of the ^{133}Ba line. Various targets were used to measure in different energy regions: LiF/Ag/C (nominal thickness: $13\mu\text{g}/\text{cm}^2$ LiF + $40\mu\text{g}/\text{cm}^2$ Ag), Au/LiF/C ($50\mu\text{g}/\text{cm}^2$ Au + $20\mu\text{g}/\text{cm}^2$ LiF + $15\mu\text{g}/\text{cm}^2$ C) LiF/Ag/C ($20\mu\text{g}/\text{cm}^2$ LiF + $40\mu\text{g}/\text{cm}^2$ Ag + $30\mu\text{g}/\text{cm}^2$ C). The first target was supplied by CTN/IST and the other two were supplied by the Laboratori Nazionali di Legnaro (INFN-LNL). The target thickness measured by RBS and γ -yield, could not be accurately reproduced and the estimated systematic error is $\pm 20\%$. With such a high systematic error dominating the cumulative error, this dataset was not suitable for fixing absolute values. However, it remains useful for studying the structure of the excitation function, since it covers the largest energy range among all the measured datasets. The proton beam energy was calibrated using the resonances at 991.86 keV and 1316.83 keV in the $^{27}\text{Al}(p,\gamma)^{28}\text{Si}$ reaction as well as the non-resonant reactions $^{55}\text{Mn}(p,p)^{55}\text{Mn}$, $^{\text{nat}}\text{Sn}(p,p)^{\text{nat}}\text{Sn}$, and $^{11}\text{B}(p,\alpha)^8\text{Be}$. After the calibration, the proton beam energy was known with an accuracy of 0.07%.

(b) Assessment

The data from Chiari *et al.* (LABEC-INFN) [4.78], Jesus *et al.* (CTN/IST) [4.10], and Zamboni *et al.* (RBI) [4.79] are shown in Figs. 4.42 and 4.43. All the data are available in IBANDL, however, at the present stage, only the latter has been published. While the RBI and CTN/IST energy scales coincide, the LABEC-INFN data and the CMAM-UAM data needed to be shifted up by 10 keV. After the correction, the 110 keV data are all within $\pm 8\%$ at the energy around 3200 keV and therefore fully within the evaluated cumulative errors. Below 3 MeV, the data are in close agreement. Above 3 MeV, only two data sets can be compared, which differ in shape in some energy regions (3.4–3.5 and 3.7–3.9 MeV). The overall agreement, however, is within quoted uncertainties.

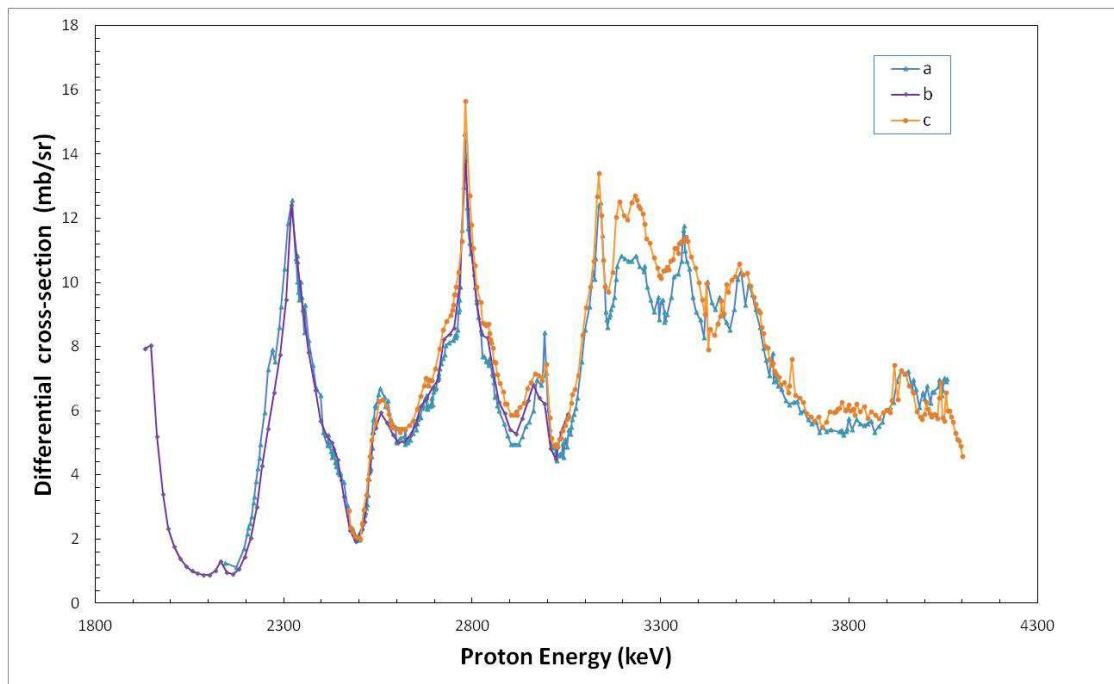


FIG. 4.42. Differential cross-sections for the $110\text{KeV } ^{19}\text{F}(p,p'\gamma)^{19}\text{F}$ resonance as a function of proton energy. Data measured during the CRP by a) Jesus *et al.* [4.78], b) [4.79] and c) Chiari *et al.* [4.78]

The situation is different for the 197 keV data, where the difference between datasets is a factor of 2 outside the quoted cumulative errors. Since the two yields have been measured from the same spectra, such a different behavior in the 197 keV case with respect to the 110 keV case requires an explanation. The only factors which are different for the 110 keV and the 197 keV line are: the γ -ray angular anisotropy (according to Allegro *et al.* [4.80] the anisotropy of the 197 keV γ -line can be very strong), relative detector efficiency, peak background subtraction and the possible presence of background peaks coming from the F presence in the experimental setup (even at the trace level such as in Ta collimators) or beam stoppers. The pile-up might affect the two peaks differently but it has been maintained at a low level. A systematic error of 25% or even 50% in the efficiency of the 197 keV peak would be unexpected given that the two energies are very similar and the experimental efficiency values should not be that different.

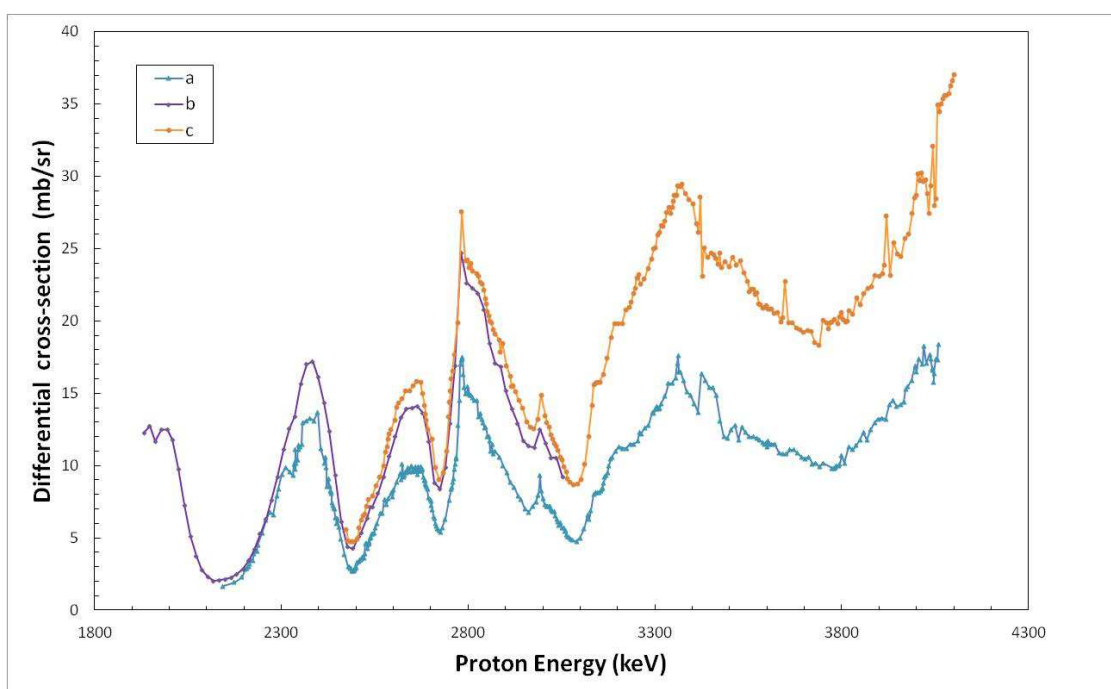


FIG. 4.43. Differential cross-sections for 197 keV $^{19}\text{F}(p,p'\gamma)^{19}\text{F}$ resonance as a function of proton energy. Data as measured within the CRP by a) Jesus *et al.* (130°) [4.78], b) [4.79] (135°) and c) Chiari *et al.* (45°) [4.78].

(c) Data in literature

Already in 1986, Chaudri [4.81] observed that “in spite of the inherent advantage of the $\text{F}(p,p'\gamma)\text{F}$, its use for analytical and depth profiling purposes has been rather limited, probably due to the non-availability of accurate cross-section data”. The situation represented in Fig. 4.44, where all the published data [4.5, 4.6, 4.9, 4.79, 4.81–4.83] are compared to the CRP produced data, still supports Chaudri’s statement. It is worthwhile noting that a correlation analysis performed on the 110 keV gamma cross-sections and interpolated at all the measured energies gives Pearson correlation coefficients (Table 4.22) that are high in all cases except for the data of Ranken [4.84]. The Pearson coefficient between two variables (in our case the two cross-section functions that are compared) depends on the standard deviation of the two variables and on their covariance, but is independent of the measure units. A value of 1

indicates perfect correlation and 0 indicates no correlation at all. In other words, the relative heights of structures in the excitation functions are constant from one set to the other but the absolute values are evidently affected in many cases by large systematic errors.

The work of Boni *et al.* [4.5] is one of the most complete in regards to the number of elements investigated. A LiF target of thickness 1000 Å deposited on a Nuclepore™ film was used. Precision is quoted at 15% for the absolute values of their differential cross-sections, but an uncertainty budget is not provided. It is reported that the germanium detector was calibrated with ²²⁶Ra. The lowest line of ²²⁶Ra, however, is at 186 KeV, which means that the efficiency for the 110 keV F line had to be extrapolated. The Faraday cup was rather distant from the target, which might have enhanced transmission problems due to the multiple scattering of the beam in the target. Several authors have found that their data, in cases other than F, can differ by a factor of up to 5 from those of Boni *et al.*

The work of Ranken *et al.* [4.84] was a pioneer one. The CaF₂ targets were evaporated on tungsten and supported by a 3.175 mm aluminium plate. Having set the detector at 45° to the beam direction, the photons were partially absorbed by the target backing. Protons stop in the target and the charge was collected through a calibrated integrator. Photons were detected by a 1" × 1" NaI scintillator. Both the detector efficiency and the photon absorption in the target were computed from tables and diagrams. An accuracy of 10–15% is quoted for the absolute values of the total cross-sections. No uncertainty budget is detailed. The consistency of the data is claimed to have come from the comparison with the 110 keV data of Barnes [4.85] at 1.70 MeV. While the NaI absolute efficiency is good, the resolution is not comparable to that of a germanium detector and the background/signal ratio is much higher. A cumulative error of 10–15% compared to a cumulative error of 7–8% (CRP data) might be optimistic.

Chaudri [4.44] covered a large energy range from 0.5 to 4.3 MeV in steps of 20 keV. He used a CaF₂ target on a carbon foil and measured the thickness with RBS (probably protons), with an uncertainty < 5%. He used a large volume NaI scintillator at 125°, which covered an angular range of 63.5°. It is demonstrated that the yield obtained in his set-up from the anisotropic 197 keV emission is only 3% different from the yield obtained from an isotropic emission. The detector efficiencies are calculated to be 4.2% ± 0.27% at 110 keV and 3.71% ± 0.24% at 197 keV. No detail is given on this calculation and no check with a calibrated source has been done. Given the use of a NaI scintillator, the same considerations as for the work of Ranken *et al.* [4.1] hold. It is worth noting that Chaudri's data are not available in tabular form and have been digitized from the publication plots (in log scale), which introduces a further source of error.

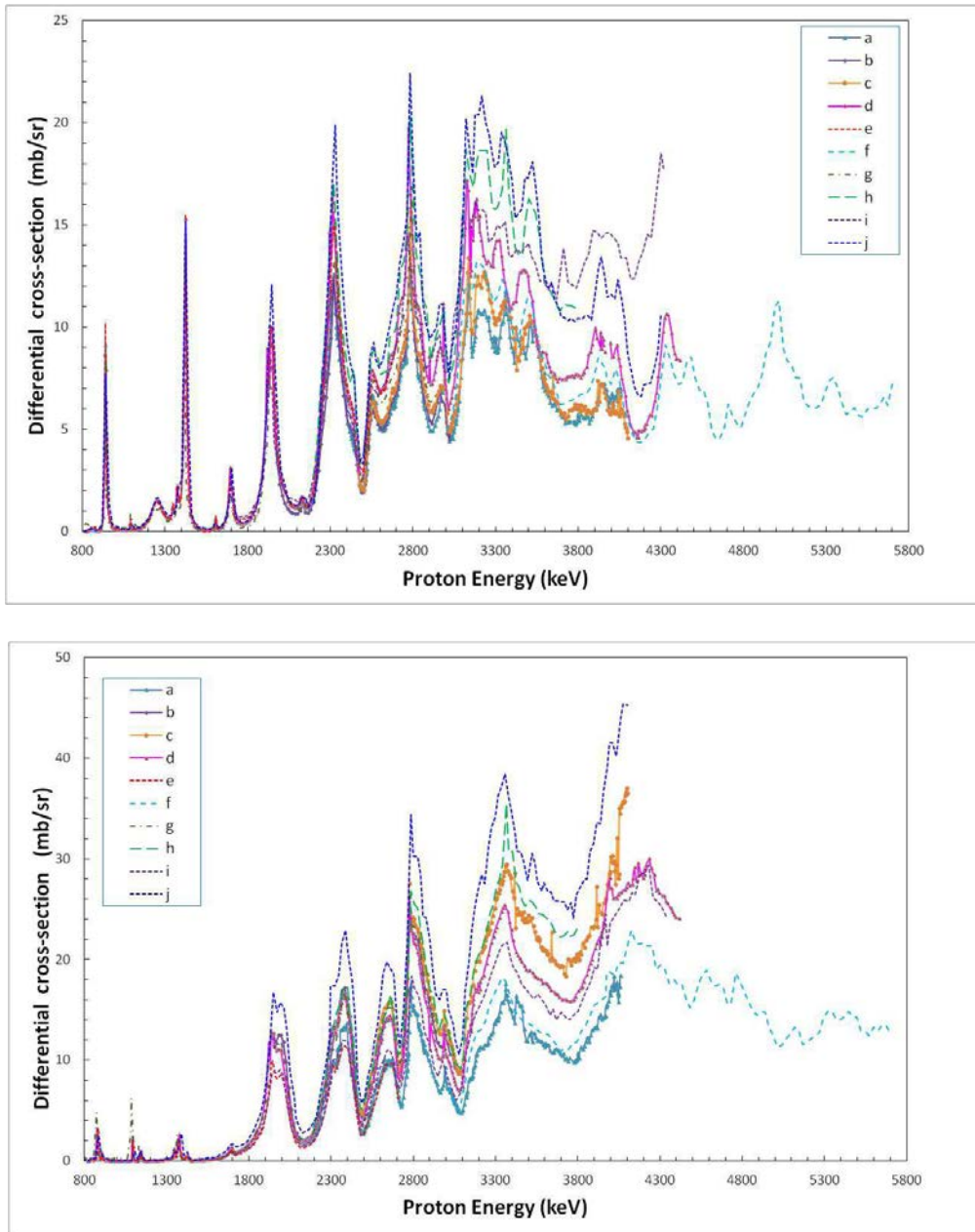


FIG. 4.44. Differential cross-sections for the 110 keV $^{19}\text{F}(p,p')^{19}\text{F}$ resonance (TOP) and 197 keV $^{19}\text{F}(p,p')^{19}\text{F}$ (BOTTOM) as a function of proton energy. Data from all the published and CRP produced datasets: a) Jesus et al. at 130° [4.78], b) [4.79] at 135° , c) Chiari et al. at 45° [4.78], d) CMAM-UAM at 135° , e) [4.82] at 130° , f) [4.6] at 135° , g) [4.83] at 90° , h) [4.5] at 90° , i) [4.84] at 45° and j) [4.81].

TABLE 4.22. THE PEARSON CORRELATION COEFFICIENTS OF THE AVAILABLE SETS OF DATA, INTERPOLATED AT ALL MEASURED ENERGIES FOR THE 110 keV $^{19}\text{F}(p,p'\gamma)^{19}\text{F}$ RESONANCE

| | CHAUDRI | CACIOLLI | CTN/IST2000 | CTN/IST | BONI | RANKEN | RBI | GRAMBOLE | LABEC-INFN | CMAM-UAM |
|--------------------|----------------|-----------------|--------------------|----------------|-------------|---------------|------------|-----------------|-------------------|-----------------|
| CHAUDRI | | 0.993 | 0.992 | 0.956 | 0.986 | 0.995 | 0.994 | 0.990 | 0.988 | 0.992 |
| CACIOLLI | 0.988 | | 0.959 | 0.944 | 0.988 | 0.988 | 0.960 | | 0.975 | 0.992 |
| CTN/IST2000 | 0.987 | | 0.986 | 0.987 | 0.988 | 0.988 | 0.993 | 0.981 | 0.983 | 0.992 |
| CTN/IST | 0.956 | 0.951 | 0.981 | 0.928 | 0.942 | 0.942 | 0.971 | 0.953 | 0.968 | 0.971 |
| BONI | 0.984 | 0.960 | 0.989 | 0.949 | 0.987 | 0.987 | 0.988 | 0.989 | 0.984 | 0.966 |
| RANKEN | 0.863 | 0.604 | 0.973 | 0.758 | 0.921 | 0.921 | 0.992 | 0.993 | 0.980 | 0.984 |
| RBI | 0.994 | 0.949 | 0.997 | 0.978 | 0.983 | 0.938 | | 0.987 | 0.985 | 0.983 |
| GRAMBOLE | 0.966 | | 0.945 | 0.969 | 0.981 | 0.978 | 0.985 | | 0.986 | 0.990 |
| LABEC-INFN | 0.962 | 0.978 | 0.969 | 0.950 | 0.962 | 0.704 | 0.978 | 0.987 | | 0.984 |
| CMAM-UAM | 0.976 | 0.961 | 0.992 | 0.947 | 0.941 | 0.825 | 0.982 | 0.969 | 0.967 | |

Grambole *et al.* [4.83] used a 20 nm CaF₂ target on a Ta backing and detected low energy photons with a Ge(Li) X-ray detector with a 16 mm diameter and a 7 mm thickness. The detector was placed at 90° with respect to the beam direction, with the target tilted at 45°. The excitation curves range from 0.69 to 2.94 MeV and are given in relative units. No errors are quoted. Although the numerical values are quite close to the differential cross-section values of the other authors, the use of relative units is indicative of possible systematic errors. The Grambole data below 1600 keV appear shifted by about -10 keV.

The two other published sets of data [4.82, 4.6] are much more recent and were produced by groups taking part in the CRP. Both were obtained using a set-up very similar to the set-up in the CRP data collection. Both produced an uncertainty budget, with a cumulative, conservative error of $\pm 15\%$ for Caciolli *et al.* [4.6] and 9.6–12.6 % for Jesus *et al.* [4.82].

As previously stated, with the exclusion of [4.84] for the 110 keV channel, there is a clear correlation between the different data sets. Considering that, due to the coordination that the CRP has assured, the data produced by Zamboni *et al.* [4.79], Jesus *et al.* [4.78] and Chiari *et al.* [4.78] for the 110 keV case are accurate, the previous data can be renormalized to these results, as is seen in Table 4.23.

TABLE 4.23. LINEAR COEFFICIENTS OF THE AVAILABLE SETS OF DATA, INTERPOLATED AT ALL MEASURED ENERGIES.

| Data Set | Normalization to 110 KeV | Note for 110 keV | Normalization to 197 KeV | Note for 197 keV |
|-------------|--------------------------|---|--------------------------|---|
| CTN/IST | N/A | N/A | 1.3–1.7 | Dependent on energy and outside errors |
| CTN/IST2000 | 0.85 | Within the errors | 1.4 | Outside the errors |
| Caciolli | 0.89 | Within the errors | 1.15 | Within the errors |
| CMAM-UAM | 0.80 | Outside the errors quoted for the reference data. | 1.08–1.15 | Depending on energy but within the errors quoted for the reference data |
| Grambole | 0.95 | Within the errors | 1.0 | Within the errors |
| Boni | 0.6–0.7 | Dependent on energy and outside errors | 0.9 | Within the errors |
| Chaudri | 0.57–0.72 | Dependent on energy and outside errors | 0.78 | Outside errors |
| Ranken | N/A | Poor correlation | 1.3 | Outside errors |

In the case of the 197 keV line, there is no agreement between the CRP produced data and the data-spread gets wider with increasing energy, up to a maximum of $\pm 25\%$. It is surprising to note that the two series measured at CTN/IST (Jesus *et al.* [4.78] and [4.82]) match for the 110 keV and the 197 keV case but only the 110 keV measurements agree with the rest of the CRP data. Since the data of Zamboni *et al.* and Chiari *et al.* [4.78] for the 197 keV γ -ray agree in the common energy range, it is assumed that they are accurate. Therefore, the re-normalization process, as reported in Table 4.23, is repeated. The data of Chaudri [4.81] and Ranken [4.84] do not fit with the rest because their discrepancy is energy dependent for the 110 keV case. Except for the case of Grambole [4.83], where it is assumed that their relative

units are indeed mb/sr, the normalization coefficients are remarkably different for the two cases, 110 keV and 197 keV γ -lines, which is probably due to an unexpectedly large difference in the measurement of the absolute detector efficiency for the two photons.

The data included in this detailed analysis had a cut-off date of December 2016. Since then, there has been an additional publication of new data from the CMAM group [4.78]. These data were not considered in our assessment; however they are available in IBANDL.

4.6.2. Thick target yields

In addition to the normalization procedure, differential cross-section data were compared to the existing measured thick-target yields. For that purpose, an integration routine developed by Lagoyannis [4.85] was used.

4.6.2.1. $^{19}\text{F}(p,p\gamma_{1-0})^{19}\text{F}$: 110 keV γ -ray

For the 110 keV γ -ray, only three experimental datasets exist for thick-target yield (Kenny [4.86], Antilla [4.1], and Kiss [4.2]) Fig. 4.45 shows thick-target yields calculated using the experimental data measured in the present CRP and the available thick-target yield data [4.86, 4.1, 4.2]. In order to compare the new measured differential cross-sections with the thick-target yield data sets, the integrated cross-section data were normalized to the data of Kenny *et al.* [4.86] at the energy of 2.5 MeV. The normalization was performed by adding a constant number to the integral to take into account that the measured differential cross-sections do not extend to zero energy. It is worth noting that it is not possible to normalize the integrated differential cross-section data to the thick-target yields of Antilla [4.1] and Kiss [4.2], since the latter's absolute value is smaller than the integrated cross-sections and would therefore require subtracting a constant instead of adding it, which is not physically possible.

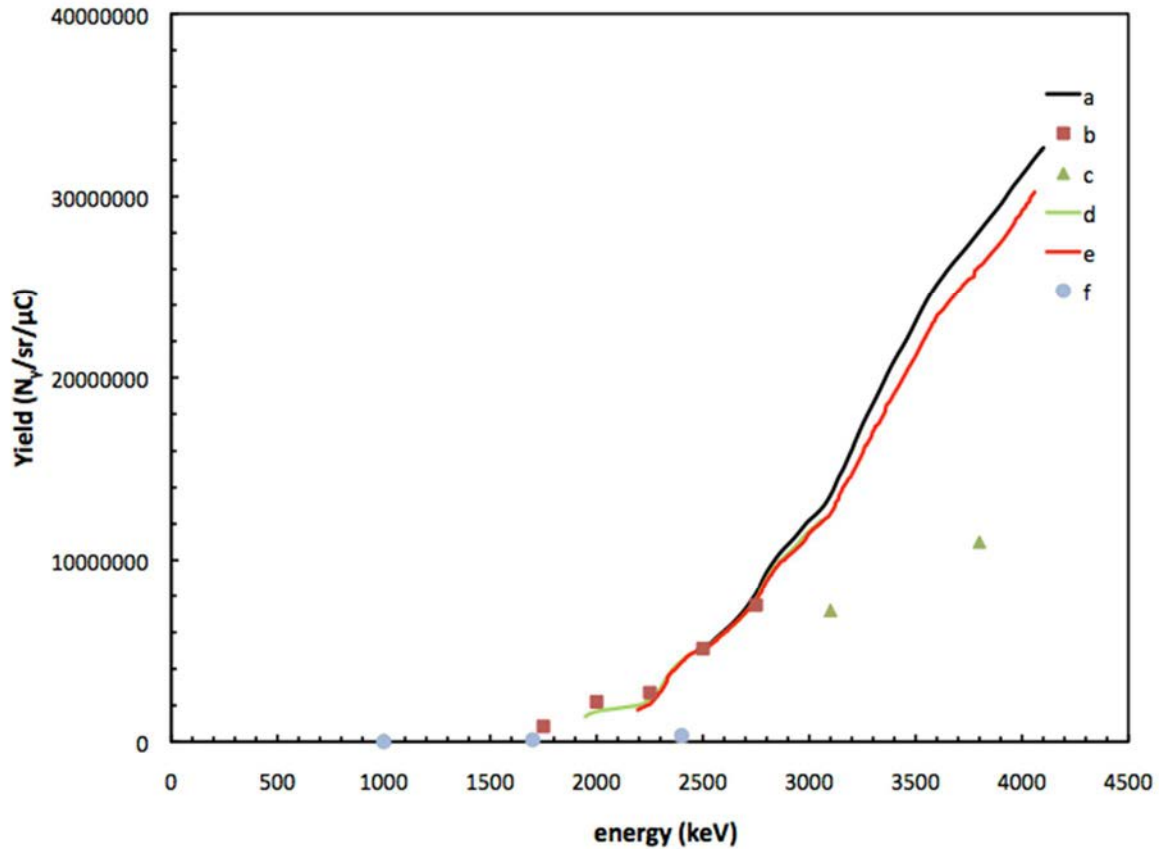


FIG. 4.45. Comparison of thick target yields for the 110 keV $^{19}\text{F}(p,p')^{19}\text{F}$ resonance as a function of energy. Calculated yields are obtained with cross-section data from (a) Chiari et al. [4.78], (d) [4.79], (e) Jesus et al. [4.78], while measured yields are taken from (b) [4.86], (c) CTN/IST [4.2] (f) [4.1].

In Fig. 4.46 thick-target yields are compared just as in Fig. 4.45, but with the addition of thick-target yields calculated using old experimental data from IBANDL. To compare new and old measured differential cross-sections with thick-target yield datasets, the integrated data were normalized to Kenny's data [4.86] at 2.5 MeV, by adding a constant to take into account that the measured differential cross-sections do not extend to zero energy. Again, this normalization procedure cannot be applied to the thick-target yields of Kiss [4.2] and Antilla [4.1] for the same reason mentioned above.

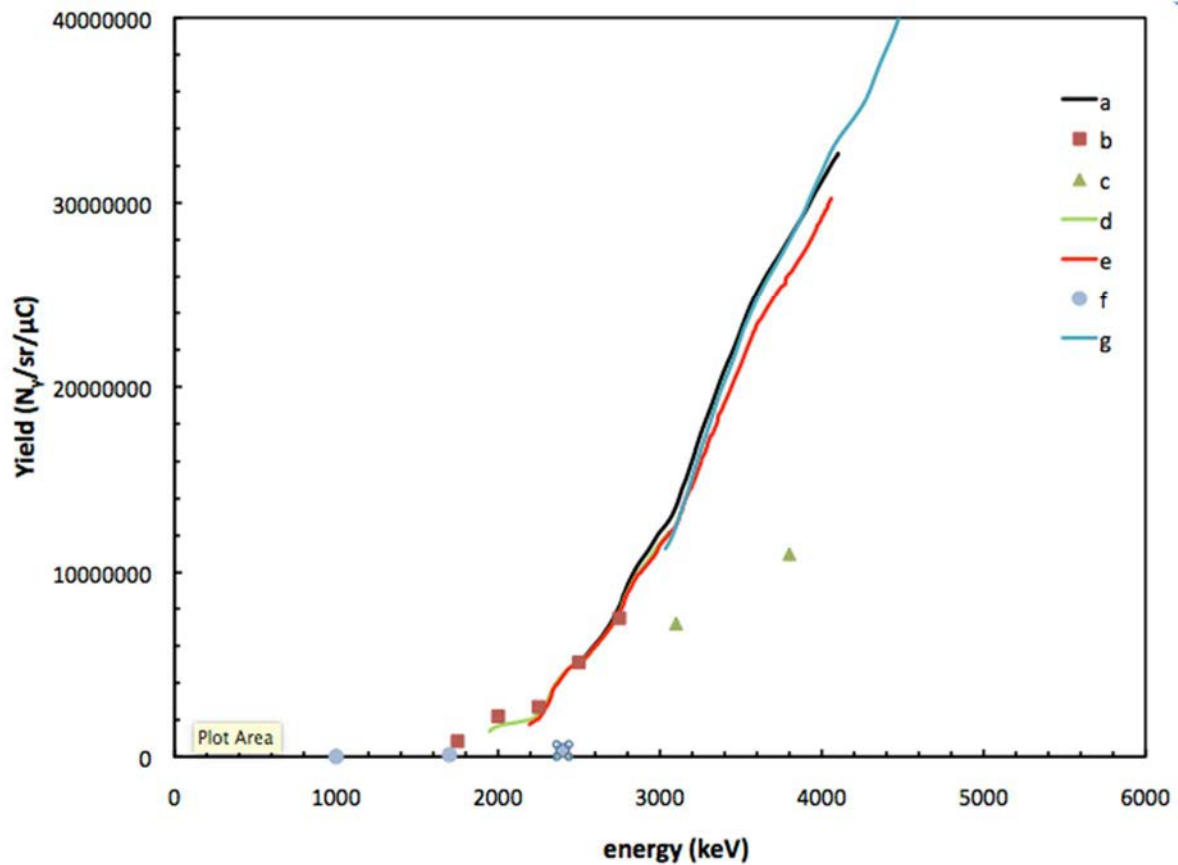


FIG. 4.46. Comparison of the thick-target yields for the 110 keV $^{19}\text{F}(p,p'\gamma)^{19}\text{F}$ resonance as a function of energy. Calculated yields are obtained with cross-section data from (a) Chiari *et al.* [4.78], (d) [4.79], (e) Jesus *et al.* [4.78], and (g) [4.6] and measured yields are taken from (b) [4.86], (c) [4.2], and (f) [4.1].

4.6.2.2. $^{19}\text{F}(p,p\gamma_{2-0})^{19}\text{F}$: 197 keV γ -ray

For the 197 keV line, there are four experimental data sets for thick-target yields (Kenny [4.86], Kiss [4.2], Antilla [4.1] and Savidou [4.17]), which are compared with calculated yields obtained from the various experimental differential cross-section data (new and old) available in the literature and shown in Fig. 4.47. The same normalization procedure was applied as in the case of the 110 keV γ -ray described in the previous section. The data of Savidou *et al.* [4.17] suffer from the same deficiency as those of Kiss [4.2] and Antilla [4.1], as described above for the 110 keV γ line. For this reason, the comparison is limited to the data of Kenny *et al.* [4.86]. All datasets agree in the shape of the yield curve produced up to an energy of 2.5 MeV. Furthermore, the previous low energy data of Jesus *et al.* [4.82], extending up to 2.7 MeV, have been validated by an independent benchmark performed by Matheus *et al.* [4.87]. At energies above this low energy region, however, the datasets diverge. This is expected, given the divergence of the differential cross-section data observed in Fig. 4.44. In the absence of any reliable experimental thick-target yields, it is not possible to draw any definite conclusions for this energy region.

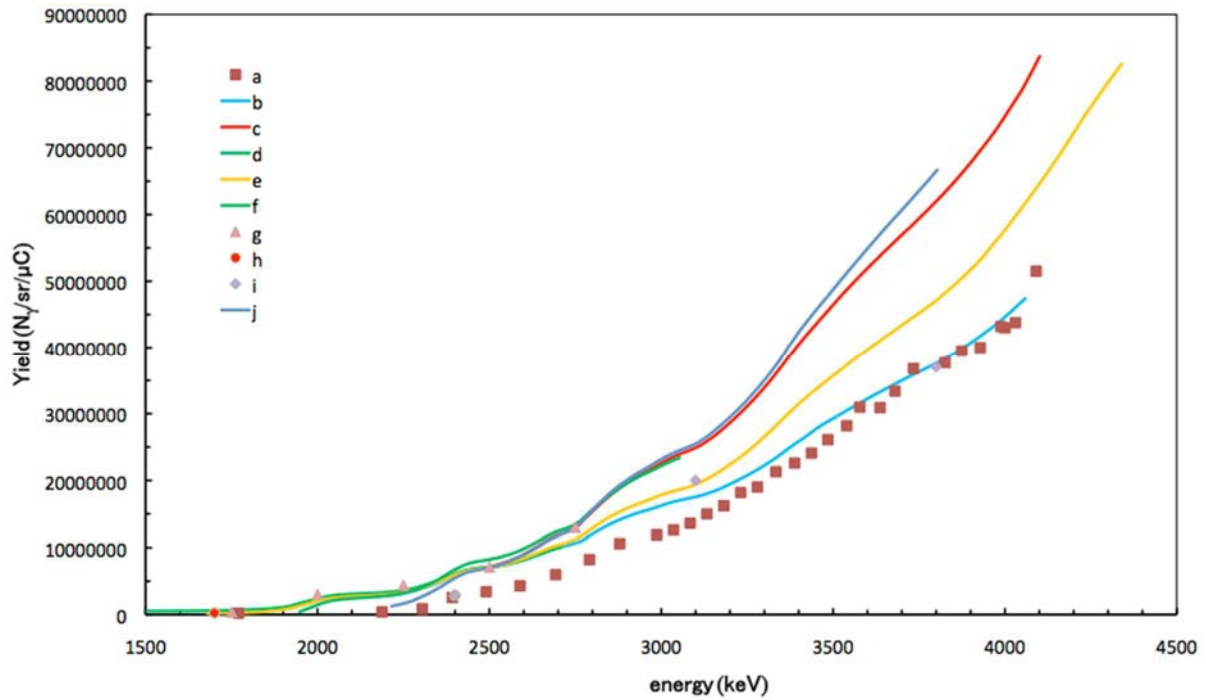


FIG. 4.47. Comparison of the thick target yields for the 197 keV $^{19}\text{F}(p,p'\gamma)^{19}\text{F}$ resonance as a function of energy. Calculated yields are obtained from cross-section data of (b) Jesus et al. [4.78], (c) Chiari et al. [4.78], (d) [4.82], (e) [4.84], (f) [4.79], and (j) [4.5]. Measured yields are taken from (a) [4.17], (g) [4.86], (h) [4.1], (i) [4.17].

(d) Recommended data

PIGE bulk analysis requires knowing the gamma emission cross-section from the beam proton energy down to zero in order to calculate the integral that provides elemental concentrations.

From the above analysis, it is clear that the 110 keV γ -line is best suited for bulk analysis. It is recommended to use any of the three new datasets that were measured during the CRP up to 3.2 MeV. At higher energies, the cross-sections have uncertainties of approximately 8%.

Another possibility is to use a combination of datasets from Chiari et al. [4.78], Zamboni et al. [4.79], and Jesus et al. [4.78], that were produced in the CRP and combine them with the two datasets at low energy, [4.82] and [4.6], using the normalization constants shown in Table 4.23. According to Table 4.23, the low energy data [4.82] should be multiplied by a factor 0.85 while the data at high energy [4.6] should be multiplied by a factor 0.89. The recommended cross-section is shown in Fig. 4.48. This will cover a wide energy range, corresponding to the most used PIXE energies and extending to 5.7 MeV for deeper bulk analysis.

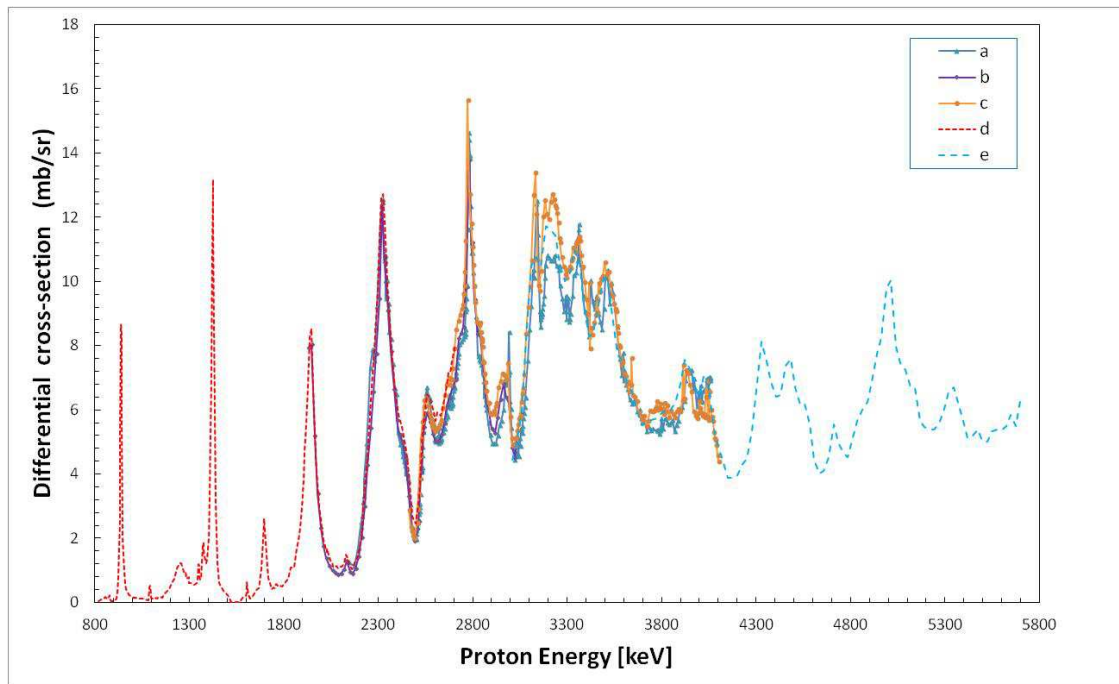


FIG. 4.48. Differential cross-sections for the 110 keV $^{19}\text{F}(p,p'\gamma)^{19}\text{F}$ resonance, including data from the CRP and previous work [4.82, 4.6] as a function of proton energy. Data from a) Jesus *et al.* [4.78], b) [4.79], c) Chiari *et al.* [4.78], d) [4.82] and e) [4.6].

For the 197 keV γ -line, the comparison of differential cross-section data and thick-target yields have shown divergencies at energies above 3 MeV that cannot be explained. Therefore, no recommendation can be made for those high energies. At lower energies up to 3 MeV, the data are in better agreement; in particular the data of Jesus *at al.* [4.82] have already been benchmarked, which enables it to be used for bulk analysis. Nevertheless, to resolve the above-mentioned discrepancies, it is recommended that an evaluation of the differential cross-section data and additional measurements of thick-target yields are performed, over the whole energy range, in order to validate the evaluated data.

4.7. SODIUM

4.7.1. Gamma-ray production cross-sections of sodium from proton-induced nuclear reactions

(a) New measurements

In the framework of the CRP, differential cross-sections for proton-induced γ -ray emission from $^{23}\text{Na}(p,p'\gamma)^{23}\text{Na}$ ($E_\gamma = 441$ and 1636 keV) and $^{23}\text{Na}(p,\alpha'\gamma)^{20}\text{Ne}$ ($E_\gamma = 1634$ keV) have been measured by five different laboratories LABEC-INFN, CTN/IST, ATOMKI, NSTRI and RBI. Measurements were performed in the energy range between 1.0 to 4.1 MeV and at several angles in the laboratory frame of reference, since these γ -rays have anisotropic angular distributions.

The measurements at the HVEE 3 MV Tandatron accelerator at the LABEC-INFN laboratory in Florence were done using + 30° beam line chamber. The groups at LABEC-INFN and CTN/IST have used NaF films evaporated on a self-supporting Ag film. Targets were produced at CTN/IST. The ratio between Na and Ag atoms was determined using 2 MeV He

RBS and was found to be 1.79 ± 0.04 . The LABEC-INFN lab used three HPGe detectors to detect γ -rays at 90° , 45° and 0° . They performed the same absolute efficiency calculation as RBI, using calibrated sources of ^{133}Ba and ^{152}Eu . To avoid absolute charge measurement and for the normalization procedure, elastic scattered protons were collected simultaneously using a Si-PIN diode detector with 13 keV energy resolution, area 10 mm^2 and thickness 300 μm . Detector was placed at 150° and collimated by a $1 \times 13 \text{ mm}^2$ vertical slit; the subtended solid angle was $3.37 \pm 0.08 \text{ msr}$. The proton beam energy was calibrated using an aluminum thick target and the resonances at 991.86 keV and 1683.57 keV, in the (p,γ) and $(p,p'\gamma)$ reactions on ^{27}Al respectively, as well as a native silicon oxide thin-target on the resonances at 3470 keV in the proton elastic scattering from ^{16}O . After calibration, the proton beam energy was known with an accuracy of 0.1%.

RBI measurements were performed using a conventional ion beam analysis scattering chamber, installed at the -15° line of the 6 MV Tandem Van de Graaff accelerator. The proton beam energy was calibrated using the 991.86 keV resonance of the $^{27}\text{Al}(p,\gamma)^{28}\text{Si}$ reaction and the $^7\text{Li}(p,n)^7\text{Be}$ reaction threshold at 1880.44 keV on thick aluminum and lithium targets respectively. After calibration, a beam energy accuracy of 0.06% was determined. Micromatter™ thin reference standard ($53.7 \mu\text{g}/\text{cm}^2$ of NaCl deposited on 6.3 μm Mylar) was used for the measurements. For normalization purposes, a 3.5 nm Au layer was evaporated on top of the target. In order to determine the ratio r between the Na and Au areal densities, assuming Rutherford cross-sections, 1.8 MeV α particles were used. The ratio r was measured to be 28.4 ± 0.7 .

At ATOMKI, the measurements were carried out using the 5 MV Van de Graaff accelerator. After energy calibration with the 991.86 keV resonance of the $^{27}\text{Al}(p,\gamma)^{28}\text{Si}$ nuclear reaction, beam energy uncertainty was 1.5 keV. The absolute HPGe detector efficiency was determined using radioactive sources (^{60}Co and ^{152}Eu , calibrated by the Hungarian National Office of Measures) that were placed at target position. The target used for the measurements was produced at CTN/IST (NaCl thick $41 \mu\text{g}/\text{cm}^2$ and evaporated on Ag foil). The ratio r between Na and Ag was determined from the 1.5 MeV He RBS to be 2.52 ± 0.08 .

At CTN/IST, measurements were performed using the 3.0 MV Tandemtron accelerator and a scattering chamber electrically insulated from the rest of the beamline. Proton beam energy was calibrated with an accuracy of 0.1% using the 1645 keV and 1930.7 keV resonances of the $^{23}\text{Na}(p,p'\gamma)^{23}\text{Na}$ reaction and by the 3470 keV resonance of the $^{16}\text{O}(p,p)^{16}\text{O}$ reaction. The NaF target evaporated on thin Ag was used for the measurement and was analysed by 1.6 and 1.8 MeV RBS at 165° scattering angle. Atomic ratio of Na to Ag was found to be 1.60 ± 0.05 . The HPGe detector absolute efficiency was obtained by measuring the yields of γ -rays produced by radioactive sources (^{133}Ba and ^{153}Eu) calibrated in activity as well as by Monte Carlo simulations using GEANT and PENELOPE codes.

The proton beam from the 3.0 MV Van de Graaff of NSTRI was used for the measurements. Proton energy was calibrated by the resonance at 991.86 keV of $^{27}\text{Al}(p,\gamma)^{28}\text{Si}$ and the $^7\text{Li}(p,n)^7\text{Be}$ reaction threshold at 1880.44 keV. After calibration, the proton beam energy was known to an accuracy $< 0.2\%$. Thin films of sodium chloride were evaporated onto thin films of self-supporting Ag. The targets obtained this way were analysed by alpha RBS at 165° for alpha particle incident energies of 2.0 MeV. Thicknesses of $1.9 \times 10^{17} \text{ at}/\text{cm}^2$ and $4.8 \times 10^{17} \text{ at}/\text{cm}^2$ were obtained for Na and Ag, respectively.

More details about the experimental set-ups used by different groups can be found in Table 4.24 and in [4.88]. The uncertainty budget, as estimated for the measurements performed in the different laboratories, can be found in Table 4.25. It includes the statistical errors from the peak areas with subtracted background, and different systematic errors. From there, it can be estimated that an overall uncertainty of 7–8% can be expected for the cross-section of the 441 keV γ -ray line from the $^{23}\text{Na}(p,p'\gamma)^{23}\text{Na}$ reaction, and of 8–12% for the cross-section of the 1634–1636 keV γ -ray lines from the $^{23}\text{Na}(p,\alpha'\gamma)^{20}\text{Ne}$ and $^{23}\text{Na}(p,p\gamma_{2-1})^{23}\text{Na}$ reactions.

TABLE 4.24. EXPERIMENTAL CONDITIONS USED IN THE FIVE LABORATORIES MEASURING THE DIFFERENTIAL CROSS-SECTIONS OF THE $^{23}\text{Na}(p,\gamma)^{23}\text{Na}$: 441 keV & 1636 keV γ -rays AND $^{23}\text{Na}(p,\alpha'\gamma)^{20}\text{Ne}$: 1634 keV γ -ray

| Experimental Condition | Laboratory | | | |
|---|--|------------------------------------|------------------------------------|--|
| | LABEC-INFN | RBI | ATOMKI | CTN/IST NSTRI |
| γ -ray detector absolute efficiency at 441 keV | (1.88 \pm 0.11) $\times 10^{-3}$ (1.17 \pm 0.07) $\times 10^{-3}$ (6.70 \pm 0.36) $\times 10^{-4}$ | (5.40 \pm 0.38) $\times 10^{-3}$ | (4.40 \pm 0.13) $\times 10^{-3}$ | (1.07 \pm 0.05) $\times 10^{-2}$ (1.58 \pm 0.08) $\times 10^{-4}$ |
| γ -ray detector absolute efficiency at 1634–1636 keV | (8.03 \pm 0.46) $\times 10^{-4}$ (4.33 \pm 0.26) $\times 10^{-4}$ (2.98 \pm 0.18) $\times 10^{-4}$ | (1.60 \pm 0.18) $\times 10^{-3}$ | (1.68 \pm 0.13) $\times 10^{-3}$ | (3.94 \pm 0.20) $\times 10^{-3}$ (0.61 \pm 0.03) $\times 10^{-4}$ |
| γ -Detector angle | 90° 45° 0° | 135° | 55° | 130° 90° |
| γ -Detector distance to target | Ranging from 18–20 cm | 6.6 cm | 9.5 cm | 5.55 cm 5.19 cm |

TABLE 4.24. EXPERIMENTAL CONDITIONS USED IN THE FIVE LABORATORIES MEASURING THE DIFFERENTIAL CROSS-SECTIONS OF THE $^{23}\text{Na}(p,\gamma)^{23}\text{Na}$: 441 keV & 1636 keV γ -rays AND $^{23}\text{Na}(p,\alpha'\gamma)^{20}\text{Ne}$: 1634 keV γ -ray (cont.)

| Experimental Condition | Laboratory | | | |
|---|---|---|---|--|
| | LABEC-INFN | RBI | ATOMKI | CTN/IST NSTRI |
| Target | NaF evaporated on Ag film self-supporting | 53.7 $\mu\text{g}/\text{cm}^2$ of NaCl on 6.3 μm Mylar + 3.5 nm Au layer | NaCl layer (41 $\mu\text{g}/\text{cm}^2$) evaporated on a thin Ag foil | NaF evaporated on Ag self-supporting thin film. NaCl evaporated on Ag self-supporting thin film. |
| | NaF $34.9 \pm 1.5 \mu\text{g}/\text{cm}^2$, Ag $51.0 \pm 1.8 \mu\text{g}/\text{cm}^2$ | | | Thicknesses of $5.12 \cdot 10^{17}$ at/cm ² and $3.21 \cdot 10^{17}$ at/cm ² were obtained for Na and Ag Na and Ag |
| Beam size | 1.0 x 1.0 mm ² | 4 mm ϕ | Not reported | Not reported |
| Energy range | 2463–4101 keV | 1890–3050 keV | 1770–3020 keV | 2150–4070 keV |
| Energy step | 3–10 keV | 15 keV | 1–10 keV | 2–20 keV |
| Beam Currents | 70–140 nA | 10–20 nA | 37 nA | < 200 nA |
| Particle detector angle and solid angle | 150° 3.37 \pm 0.08 msr | 165° 7.5 \pm 0.2 msr | 135° 4.3 \pm 0.2 msr | 157° not reported |
| | | | | < 100 nA 165° 0.746 \pm 0.007 msr |

TABLE 4.25. UNCERTAINTY BUDGET FOR THE MEASUREMENTS PERFORMED IN THE FIVE LABORATORIES MEASURING THE DIFFERENTIAL CROSS-SECTIONS OF THE $^{23}\text{Na}(p,p'\gamma)^{23}\text{Na}$: 441 keV & 1636 keV γ -rays AND $^{23}\text{Na}(p,\alpha'\gamma)^{20}\text{Ne}$: 1634 keV γ -ray

| Quantity | Uncertainty | | | | |
|--|--------------------------|------|--------|----------|-------------------|
| | LABEC-INFN | RBI | ATOMKI | CTN/IST | NSTRI |
| 441 keV γ -ray peak area | < 2.0% | 1.0% | < 1.5% | 1.4–3.2% | 1.4% |
| 1634–1636 keV γ -ray peak area | 1–3%, 9–11% ^b | 1–5% | 2.0% | 1.4–3.2% | 3.2% ^d |
| p+Ag/Au elastic peak area | 1.0% | 1.0% | < 1.0% | < 1.0% | 1.0% |
| p+Ag/Au Rutherford cross-section ^c | 1.0% | 1.0% | 3% | 1.0% | 1.0% |
| Na-to-Ag/Au atomic ratio | 2.0% | 2.5% | 3% | 3% | 3.7% |
| Particle detector solid angle | 2.4% | 2.0% | 4.6% | 2.5% | 1.0% |
| <i>γ-ray detector absolute efficiency:</i> | | | | | |
| at 441 keV | 6% | 7% | 3% | 5% | 5% |
| at 1634–1636 keV | 6% | 11% | 8% | 5% | 5% |

4.7.1.1. $^{23}\text{Na}(p,p\gamma_{1-0})^{23}$: 441 keV γ -ray

The excitation function for the 441 keV γ -ray line that was measured by the five laboratories, is presented in Fig. 4.49. In the energy region below 2500 keV, data from RBI and ATOMKI are in good agreement. In the energy range from 2500–3000 keV, data from all involved laboratories can be compared and the difference among the different data sets for similar angles is less than 20%. In this energy region, the average differential cross-section would be within an uncertainty range of $\pm 10\%$, which is comparable to the uncertainty of the individual experimental sets. Small energy shifts of 4 keV and 8 keV, which are within the quoted uncertainties, should be applied to the RBI and LABEC-INFN data, respectively, so that they match with the other datasets. In the energy range above 2500 keV, NSTRI data are about 30–40% higher than the other data sets, which are in good agreement with each other. Above 3000 keV, data have been measured only by LABEC-INFN and CTN/IST and they agree within 15% except for a small energy region from 4000 to 4050 keV, where the difference is 25%. Again the average differential cross-section agrees with the individual data within $\pm 7.5\%$, i.e. within the stated experimental uncertainties.

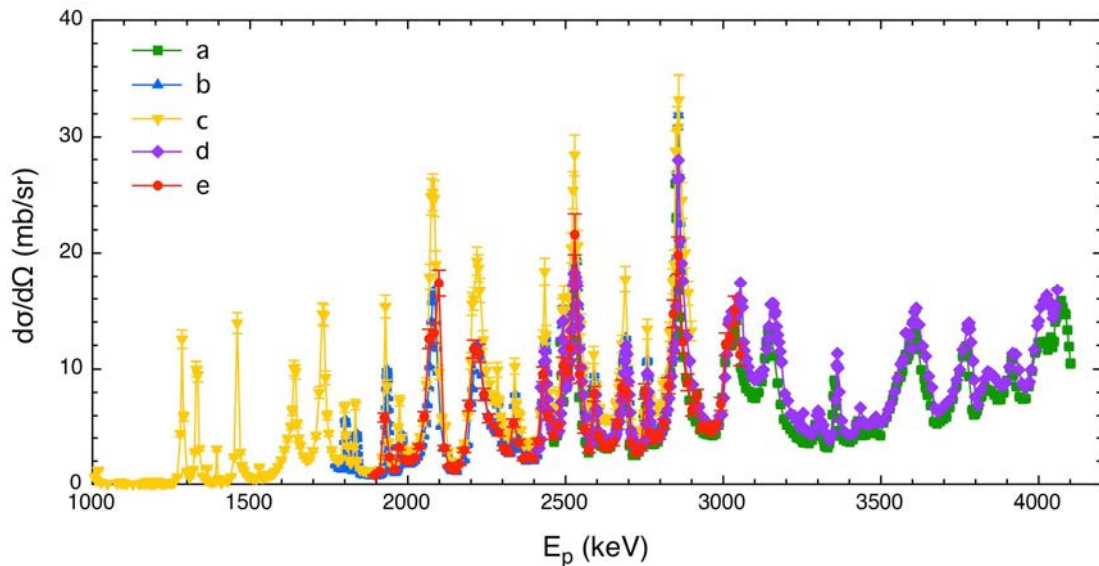


FIG. 4.49. Measured differential cross-sections values for the production of 441 keV $^{23}\text{Na}(p,p\gamma_{1-0})^{23}\text{Na}$ resonance as a function of proton energy [4.88]. Measurements by five laboratories: a) LABEC-INFN (45°), b) ATOMKI (55°), c) NSTRI (90°), d) CTN/IST (130°) and e) RBI (135°).

4.7.1.2. $^{23}\text{Na}(p,p\gamma_{2-1})^{23}\text{Na}$: 1636 γ -ray and $^{23}\text{Na}(p,\alpha\gamma_{1-0})^{20}\text{Ne}$: 1634 keV γ -ray

Differential cross-sections for the 1634–1636 keV γ -ray lines from the $^{23}\text{Na}(p,\alpha\gamma_{1-0})^{20}\text{Ne}$ and $^{23}\text{Na}(p,p\gamma_{2-1})^{23}\text{Na}$ reactions were measured by five laboratories and the results are shown in Fig. 4.50. At energies below 2500 keV, the data from NSTRI are higher by 20–25% than the data measured from other groups in this energy region. The reason for that could be attributed to an angular anisotropy of the emitted γ -ray. The differential cross-sections measured at RBI, CTN/IST and ATOMKI in the energy range from 2500–3000 keV are in good agreement, since their differences are well within quoted uncertainties. The only exception is the data from LABEC-INFN, which are systematically lower by 20–25%. In the same energy region, the data from NSTRI are about 20–25% higher than the data from ATOMKI, CTN/IST and RBI. As in the case of the 441 γ -ray line, the same shift in energy should be applied to the data from RBI and LABEC-INFN so that the resonance energies match the data from the other three groups. For energies above 3000 keV, there exist data from two groups, LABEC-INFN and CTN/IST, which differ by about 20–25%. The systematic difference observed between the data from LABEC-INFN and CTN/IST is not the same for the two γ -ray lines, therefore it is most likely attributable to an error in the determination of the absolute efficiency of the detector, since this is the only parameter that depends on the γ -ray energy.

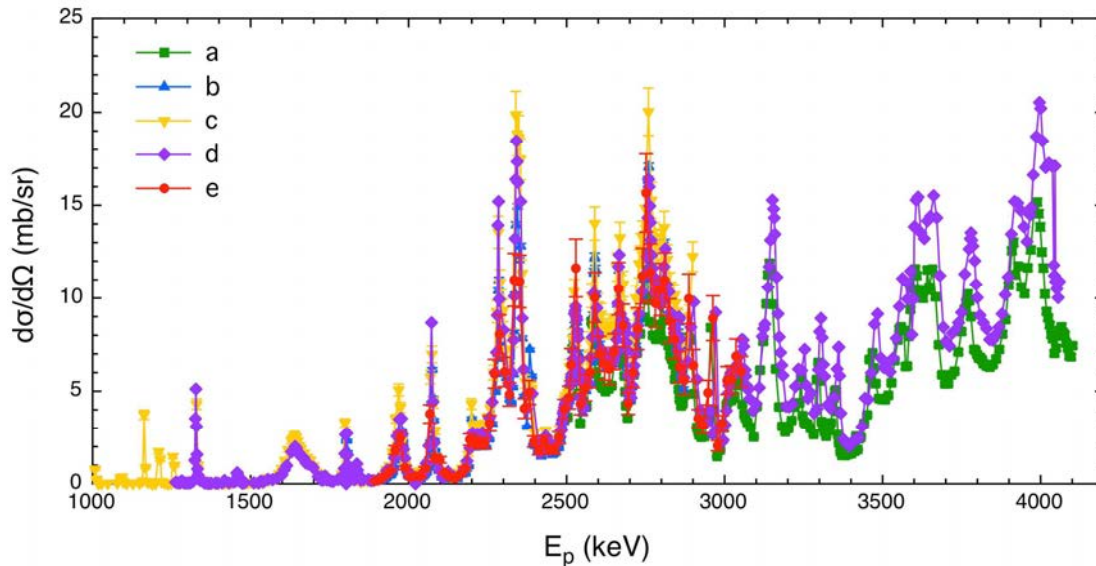


FIG. 4.50. Measured differential cross-sections values for the production of 1636 and 1634 keV γ -rays produced by the $^{23}\text{Na}(p,p\gamma_{2-1})^{23}\text{Na}$ and $^{23}\text{Na}(p,\alpha\gamma_{1-0})^{20}\text{Ne}$ reactions, respectively, as a function of proton energy, measured by five laboratories [4.88]: a) LABEC-INFN (45°), b) ATOMKI (55°), c) NSTRI (90°), d) CTN/IST (130°) and e) RBI (135°).

(b) Data in the literature

Several publications that are dedicated to measurements of proton-induced γ -ray emission from sodium exist in the literature. These include one measurement of differential cross-sections [4.89], two different measurements of total cross-sections [4.90, 4.91], and several measurements of thin [4.92–4.95] and thick target yields [4.1, 4.2, 4.17, 4.96], in the proton energy range 1–5 MeV, which is of interest for PIGE applications. Recently, evaluated cross-sections were also published for the $^{23}\text{Na}(p,p'\gamma)^{23}\text{Na}$ reaction, for energies up to 2400 keV [4.97]. This evaluation, however, only took into account the data that were available in the literature until 2013. Consequently, not all the data that were measured within this CRP were included in that evaluation. A new evaluation that includes all the published data from this CRP is recommended.

Figure 4.51 illustrates the measured differential cross-sections for the production of 441 keV γ -ray from the $^{23}\text{Na}(p,p\gamma_{1-0})^{23}\text{Na}$ reaction that were available in the literature and IBANDL, prior to the CRP [4.89–4.91]. Since the latter two are given as total cross-sections in the articles, they have been subsequently divided by a factor 4π to obtain differential cross-sections. The data from [4.91] are higher than the two other datasets by about a factor of 7 and are therefore omitted from the subsequent comparison. In Fig. 4.52, the above-mentioned data from the literature are compared with the data measured in this CRP. As can be seen in the figure, the data from NSTRI are about 10% higher than the data from Mateus *et al.* [4.90], in the low energy region. This difference could be attributed to the angular anisotropy of the emitted γ -ray, since the two measurements were performed at different angles: 90° by NSTRI and 120° by [4.90]. At proton energies below 2.5 MeV, the data from ATOMKI and RBI are in good agreement, however they are about 30% lower than the data from [4.90]. The angles at which the various measurements have been performed are comparable (55° at ATOMKI, 135° at RBI and 120° by [4.90]). Therefore, the deviations cannot be due only to the anisotropy in the angular distribution. Data from Caciolli *et al.* [4.89], which were measured at an angle of 135°, with quoted overall uncertainty 9%, are systematically lower than the

presently measured data, by a relative factor ranging from about 15% (compared to data from LABEC-INFN) to about 35% (compared to data from ATOMKI). Compared to the older data, the present CRP measurements were made with smaller energy steps and using thinner targets, thus revealing a finer structure in the excitation function. The observed fine structure makes these new data particularly valuable for the extension of the theoretical evaluation of the $^{23}\text{Na}(p,p'\gamma)^{23}\text{Na}$ cross-section to higher energies.

Figure 4.53 compares the data measured by this CRP with the dataset of Cacioli *et al.* [4.89] for the production of 1636 and 1634 keV γ -rays from the $^{23}\text{Na}(p,p\gamma_{2-1})^{23}\text{Na}$ and $^{23}\text{Na}(p,\alpha\gamma_{1-0})^{20}\text{Ne}$ reactions. The data of [4.89], which has a quoted overall uncertainty of 12% for the 1634–1636 keV γ -ray lines, are systematically lower than the presently measured data. The underestimation ranges from about 15% (compared to the data from LABEC-INFN) to about 50% (compared to the other data). As already noted above for the differential cross-section of the 441 keV γ -ray, the large energy steps employed by Cacioli *et al.* [4.89] lead to excitation curves that miss the fine structure and sharp resonance features that are clearly observed in the more detailed new measurements performed during this CRP.

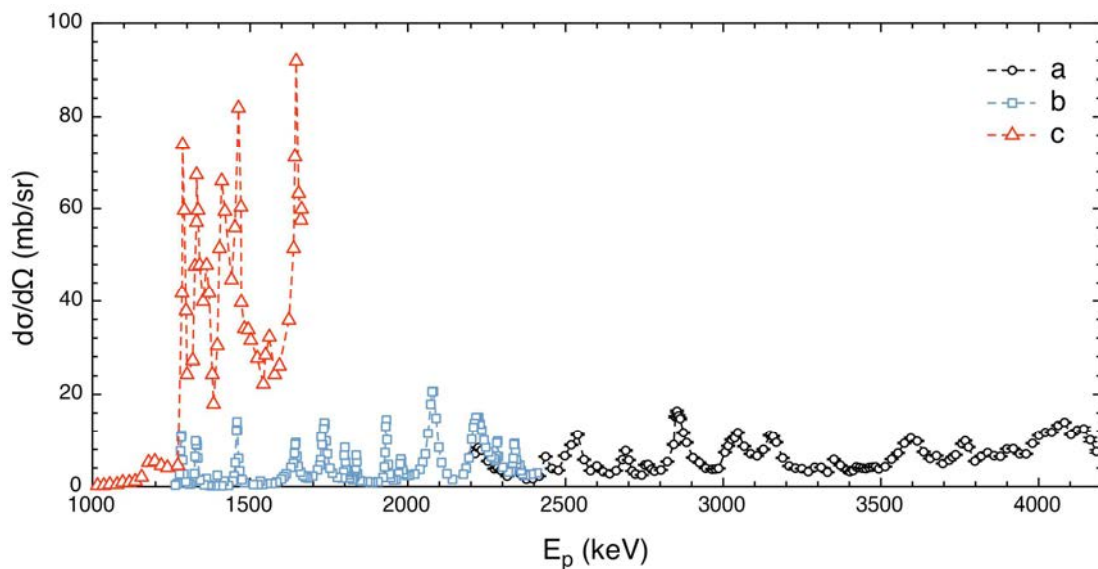


FIG. 4.51. Differential cross-sections for the 1636 keV $^{23}\text{Na}(p,p\gamma_{2-1})^{23}\text{Na}$ and 1634 keV $^{23}\text{Na}(p,\alpha\gamma_{1-0})^{20}\text{Ne}$ resonances as a function of proton energy. Data taken from the literature a) [4.89] at 135° , b) [4.90] at 120° and c) [4.91] at 90° . The latter two are given as total cross-sections and must be divided by a factor 4π to obtain differential cross-sections.

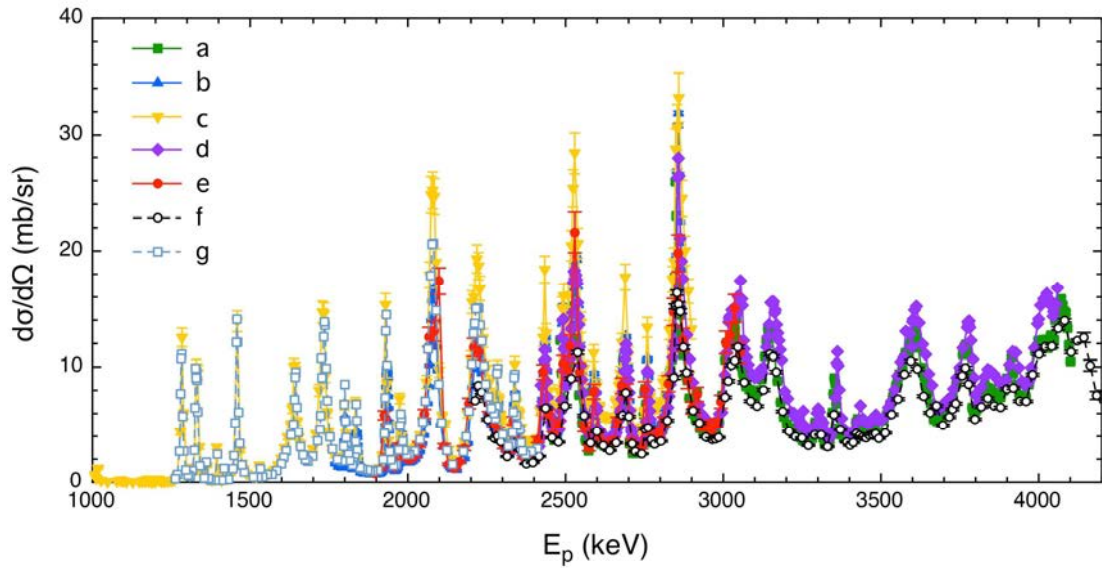


FIG. 4.52. Measured differential cross-sections for the 441 keV $^{23}\text{Na}(p, p\gamma_{1-0})^{23}\text{Na}$ resonance as a function of proton energy. Data obtained from the laboratories in the CRP [4.88]: a) LABEC-INFN (45°), b) ATOMKI (55°), c) NSTRI (90°), d) CTN/IST (130°), e) RBI (135°) and from other sources: f) [4.89] (135°) and g) [4.90] (120°).

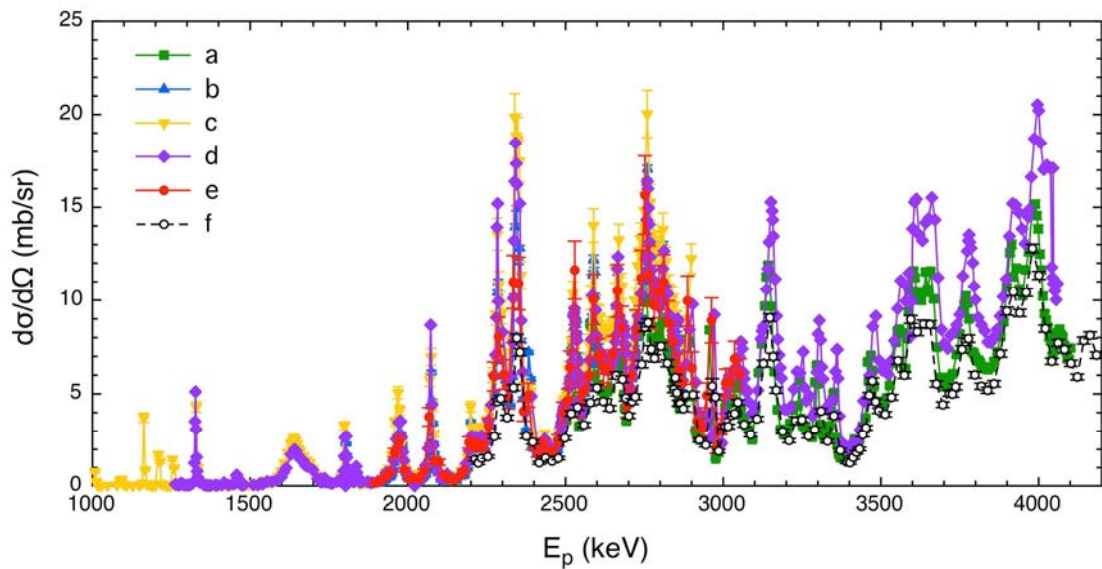


FIG. 4.53. Measured differential cross-sections for 1636 keV $^{23}\text{Na}(p, p\gamma_{2-1})^{23}\text{Na}$ and 1634 keV and $^{23}\text{Na}(p, \alpha\gamma_{1-0})^{20}\text{Ne}$ as a function of proton energy. Data obtained from laboratories in the CRP [4.88]: a) LABEC-INFN (45°), b) ATOMKI (55°), c) NSTRI (90°), d) CTN/IST (130°), e) RBI (135°) and from other sources: f) [4.89] (135°).

4.7.2. Thick target yields

4.7.2.1. $^{23}\text{Na}(p,p\gamma_{1-0})^{23}$: 441 keV γ -ray

For the 441 keV γ -ray line, there are five different datasets for thick-target yields available in the literature [4.1, 4.2, 4.17, 4.88, 4.96]. Chiari *et al.* [4.88] reported thick-target yields for three different laboratory angles (0° , 45° and 90°) and showed that the difference in the thick-target yield that exists for these three angles is due to the anisotropic emission of 441 keV γ -ray line. Thick-target yields were also calculated from the new experimental differential cross-section data using the same computer program distributed to CRP participants by [4.34]. This program computes the number of γ -rays produced by a certain reaction, assuming a homogeneous thick target and taking into account the beam energy loss and the differential cross-section of the reaction. Figure 4.54 shows thick-target yields calculated using the experimental data measured in the present CRP and the available thick-target yield data [4.1, 4.2, 4.17, 4.88, 4.96]. In order to compare differential cross-sections with the thick-target yield datasets, the integrated cross-section data were normalized to the data of Kiss *et al.* [4.2] at the energy of 2.4 MeV. The normalization was performed by adding a constant number to the integral to take into account that the measured differential cross-sections do not extend down to zero energy. However, it can be seen that some sets of data can't be normalized to the data of Kiss *et al.* [4.2] at the energy of 2.4 MeV without subtracting some value, which is physically not possible.

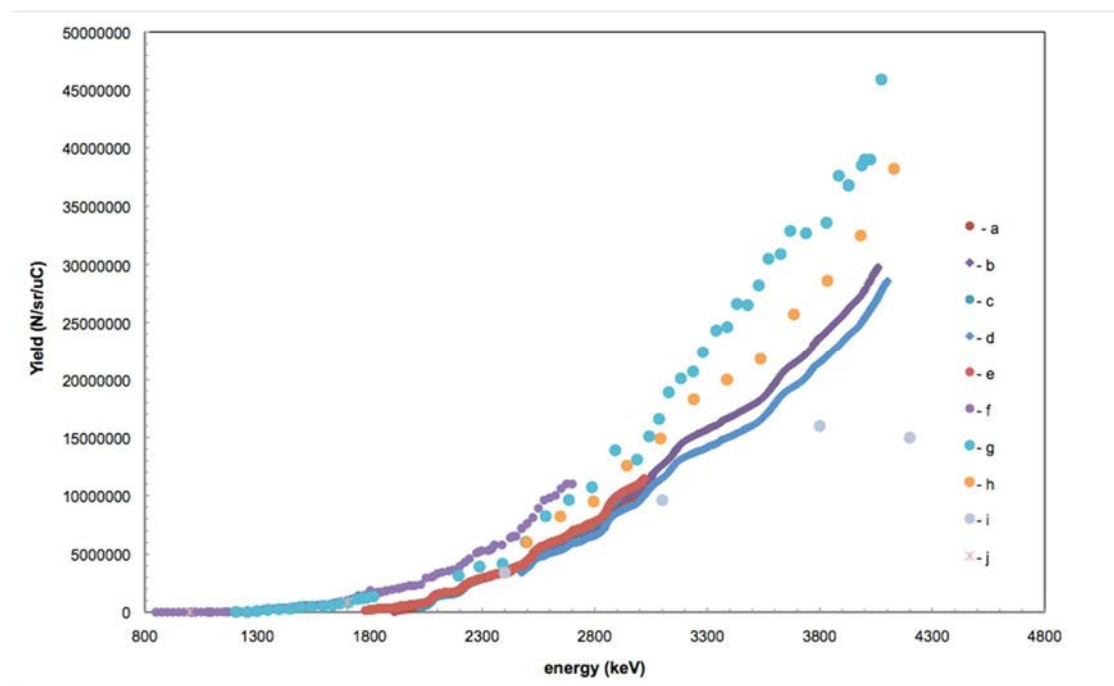


FIG. 4.54. Comparison of the thick-target yields for 441 keV $^{23}\text{Na}(p,p'\gamma)^{23}\text{Na}$ as a function of energy. Calculated yields taken from measured cross-sections from laboratories in the CRP [4.88]: (a) RBI (135°), (b) CTN/IST (130°), (c) NSTRI (90°), (d) LABEC-INFN, (e) ATOMKI (55°), and measured yields taken from (f) [4.96] (90°), (g) [4.17] (90°), (h) [4.88] (90°), (i) [4.2] (55°) and (j) [4.1] (55°).

Figure 4.55 shows thick-target yields calculated using the experimental data measured in the present CRP, thick-target yields calculated using previously measured experimental data [4.17, 4.89–4.91, 4.96] and the available thick-target yield data [4.1, 4.2, 4.17, 4.88, 4.96].

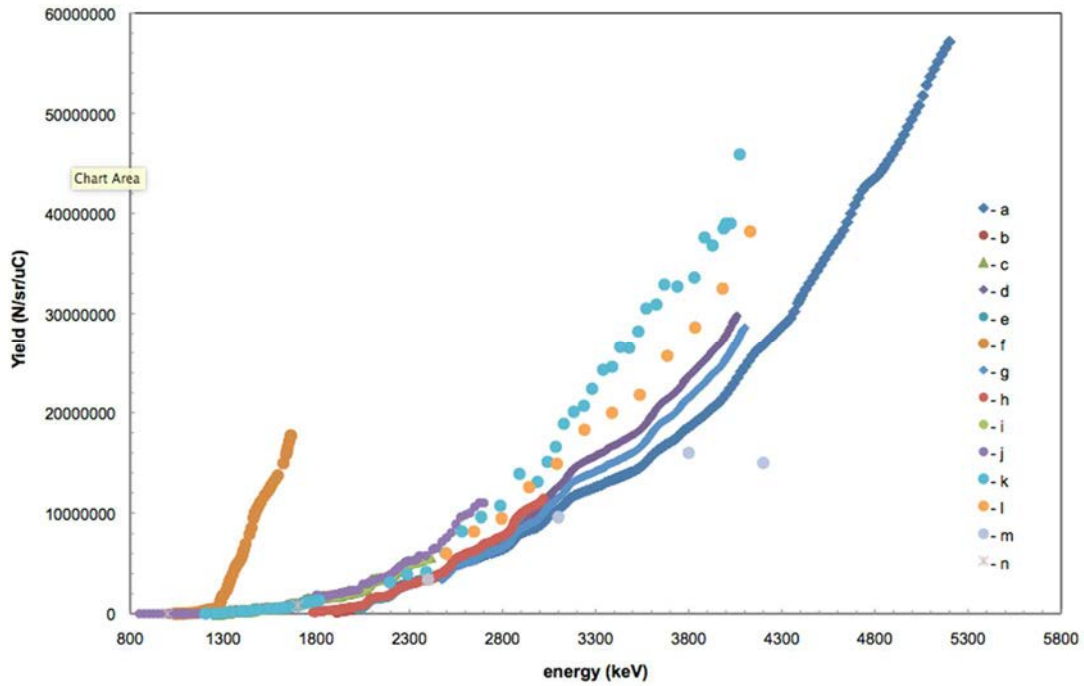


FIG. 4.55. Comparison of the thick target yields for 441 keV $^{23}\text{Na}(p,p'\gamma)^{23}\text{Na}$ as a function of incident energy. Calculated yields are from measured cross-sections of laboratories in the CRP [4.88]: (b) RBI (135°), (c) [4.90] (120°), (d) CTN/IST (130°), (e) NSTRI (90°), (g) LABEC-INFN (90°), (h) ATOMKI (55°) and from other sources: (a) [4.89] (135°), (f) [4.91] (90°) and (i) SigmaCalc. Measured yields are from (j) [4.96] (90°), (k) [4.17] (90°), (l) [4.88] (90°), (m) [4.2] (55°) and (n) [4.1] (55°).

(c) Recommended data

It should be noted that ^{23}Na is one of the cases where the data for the γ -ray production cross-sections are in good agreement, and have relatively low uncertainties. All the new measurements agree within the quoted uncertainties in the measured energy range and therefore can be used for analytical purposes. Since slight anisotropy was observed, it is advisable to use the cross-sections at the appropriate angle.

4.7.2.2. $^{23}\text{Na}(p,p\gamma_{2-1})^{23}\text{Na}$: 1636 γ -ray and $^{23}\text{Na}(p,\alpha\gamma_{1-0})^{20}\text{Ne}$: 1634 keV γ -ray

For the 1636 and 1634 keV γ -rays lines, there is only one dataset for thick-target yields available in the literature. Chiari *et al.* [4.88] reported thick-target yields for three different laboratory angles: 0°, 45° and 90°. Differences in the thick-target yield are due to the anisotropic emission of the γ -ray line. Figure 4.56 shows thick-target yields calculated using the experimental data measured in the present CRP, thick-target yields calculated using previously measured experimental cross-sections [4.89] and the available measured thick-target yield data [4.88] for 90°.

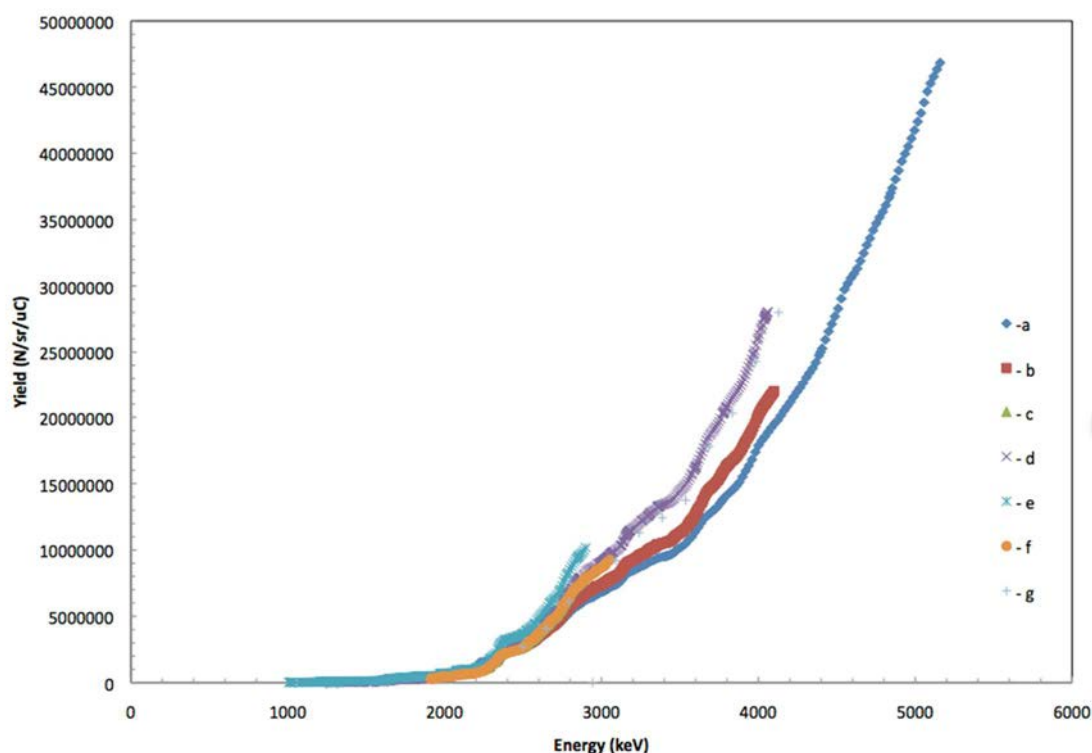


FIG. 4.56. Comparison of the thick target yields for the 1636 keV $^{23}\text{Na}(p,p\gamma_{2-1})^{23}\text{Na}$ and 1634 keV $^{23}\text{Na}(p,\alpha\gamma_{1-0})^{20}\text{Ne}$ γ -rays as a function of energy. Calculated yields from cross-section data from laboratories in the CRP [4.88]: b) LABEC-INFN (90°), c) ATOMKI (55°), d) CTN/IST (130°), e) NSTRI (90°), f) RBI (135°) and other sources a) [4.89] (135°). Measured yields from g) [4.88] (90°).

(d) Recommended data

All the new measurements agree within the quoted uncertainties in the low energy range (up to 3 MeV) and therefore can be used for analytical purposes in this energy region. However, care should be taken when analysis is performed at energies higher than 3 MeV since discrepancies are observed between existing datasets.

It is recommended that data for both γ -lines are evaluated over the entire measured energy range as well as for the γ -line 1636 + 1634. In addition, it is recommended that thick-target yield measurements be performed to resolve existing differences.

4.8. MAGNESIUM

4.8.1. Gamma-ray production cross-sections of magnesium from proton-induced nuclear reactions

For the analysis of Na, Mg and Al elements, which are common components of archaeological and cultural heritage materials such as ceramic, glass, obsidian and paper, it is recommended that PIGE analysis be performed simultaneously with PIXE [4.98, 4.99], since the two are considered to be complementary techniques. However, γ -ray producing cross-section data, which is required for PIGE analysis of Mg, are rarely found in the literature. Therefore, measurements of these cross-sections were considered a priority for the CRP.

A review of the literature that existed prior to the CRP revealed the following publications on Mg: “A study of relative thick-target yield of prompt γ -rays at some specific proton energies” by Anttila *et al.* [4.1], in which the most suitable γ -rays for elemental analysis have been suggested. Excitation function measurements of thick-target γ -ray yield for Mg have been presented by Savidou *et al.* [4.17] in the proton energy interval 1.0–4.1 MeV at $\theta_{\text{lab}} = 90^\circ$. Lastly, Boni *et al.* [4.5] have measured differential cross-sections of 390, 585, 975, 1612, 1809 and 1369 keV γ -rays from Mg at $\theta_{\text{lab}} = 90^\circ$ at 2.2–3.8 MeV proton energies.

(a) New measurements

Four laboratories were involved in measurements of γ -ray producing cross-sections from the reactions $^{24}\text{Mg}(p,p'\gamma)^{24}\text{Mg}$ ($E_\gamma = 1369$ keV γ -ray) and $^{25}\text{Mg}(p,p'\gamma)^{25}\text{Mg}$ ($E_\gamma = 390, 585$ and 975 keV γ -rays): CTN/IST, RBI, NCSR “Demokritos”, and NSTRI. One laboratory, NSTRI (Iran), performed measurements of the 1014 keV γ -ray from the $^{26}\text{Mg}(p,\gamma_2-0)^{27}\text{Al}$ reaction.

In a typical measurement of differential cross-sections using Mg targets, the sources of the systematic uncertainties are: the γ -ray detector absolute efficiency (due to the uncertainties of calibration for radioactive sources and fitting the experimental data), the stoichiometric ratio, particle detector solid angle. The total systematic uncertainty was obtained by taking the quadratic sum of all these uncertainties. The uncertainties in the proton scattering cross-section values of Ag can be considered negligible, since these cross-sections are purely Rutherford. Different methods can be used to prepare a thin target of Mg if the target is not purchased from a commercial company, which may lead to different uncertainties in the quoted target thickness. The laboratories participating in the CRP adopted different experimental conditions, which are summarized in Table 4.26.

TABLE 4.26. EXPERIMENTAL CONDITIONS OF THE LABORATORIES INVOLVED IN THE DIFFERENTIAL GAMMA-RAY PRODUCTION CROSS-SECTION MEASUREMENTS FOR Mg

| Reference | Data source | Angle | E_p (MeV) | Target | Quoted uncertainties | Data presentation |
|-----------|-------------|----------------------------|---------------|--|-------------------------------|--------------------|
| [4.78] | IBANDL | 130° | 0.86– 4.02 | Mg thin film evaporated on Ag thin film | 7% systematic | Tabular (R33 file) |
| [4.39] | IBANDL | 55° , 90° | 2.41– 4.55 | — | statistical, systematic | Tabular (R33 file) |
| [4.100] | Author | 90° | 1.98–3.0 | Mg ($60 \mu\text{g}/\text{cm}^2$) evaporated on Ag ($40 \mu\text{g}/\text{cm}^2$) | 5% statistical, 6% systematic | Tabular (R33 file) |
| [4.79] | IBANDL | 135° | 1.93– 3.05 | Au (4nm) deposited on MgF_2 ($54.1 \mu\text{g}/\text{cm}^2$) deposited on (6.3 μm) Mylar foil | Overall uncertainty 8–42% | Tabular (R33 file) |

4.8.1.1. $^{24}\text{Mg}(p,p\gamma_{1-0})^{24}\text{Mg}$: 1369 keV γ -ray

The 1369 keV γ -ray is emitted from the first excited state of ^{24}Mg , which has a 2+ spin. Therefore the angular distribution of this γ -ray is anisotropic. The measured PIGE differential cross-sections of the 1369 keV γ -ray from the $^{24}\text{Mg}(p,p'\gamma)^{24}\text{Mg}$ reaction are shown in Fig. 4.57. As illustrated in the figure, the PIGE cross-sections in the 1.0–3.0 MeV energy range are low and nearly smooth, except around energies 2409, 2919 and 2979 keV, where strong resonances are observed. The 2919 keV and 2979 keV resonances have also been reported by Boni *et al.* [4.5] and all three resonances have been observed by Zamboni *et al.* [4.79]. Furthermore, a weak resonance at 2009 keV has been reported by [4.79], although the results could not be validated by [4.100], since the selected energies were not coincident with this specific energy.

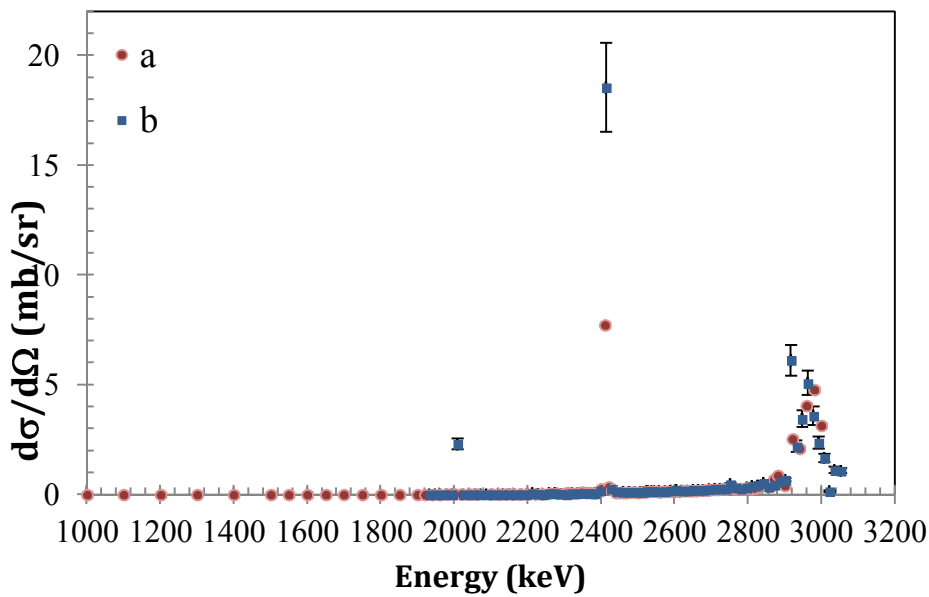


FIG. 4.57. Differential γ -ray production cross-sections of 1369 keV $^{24}\text{Mg}(p,p'\gamma)^{24}\text{Mg}$ as a function of proton energy. Data obtained from a) [4.100] (90°) and b) [4.79] (135°).

As can be seen in Fig. 4.57, the measured data are in close agreement in both the energy position of the resonances and the cross-section values with the data of Zamboni [4.79]. As mentioned in [4.79], the cross-section data values in [4.5] should be multiplied by a factor of 2π in order to compare them to the measured data.

4.8.1.2. $^{25}\text{Mg}(p,p'\gamma)^{25}\text{Mg}$: 390, 585, 975 keV γ -rays

Cross-sections for $E_\gamma = 390, 585$ and 975 keV from the $^{25}\text{Mg}(p,p'\gamma)^{25}\text{Mg}$ reaction show narrow resonances at proton energies higher than 1850 keV. In Figs. 4.58–5.60, the data of Shirifzadeh *et al.* [4.100] are compared with those reported by Zamboni *et al.* [4.79] and Preketes-Sigalas *et al.* [4.39]. In the case of the 585 keV γ -ray line, the comparison also includes the data of Jesus *et al.* [4.78].

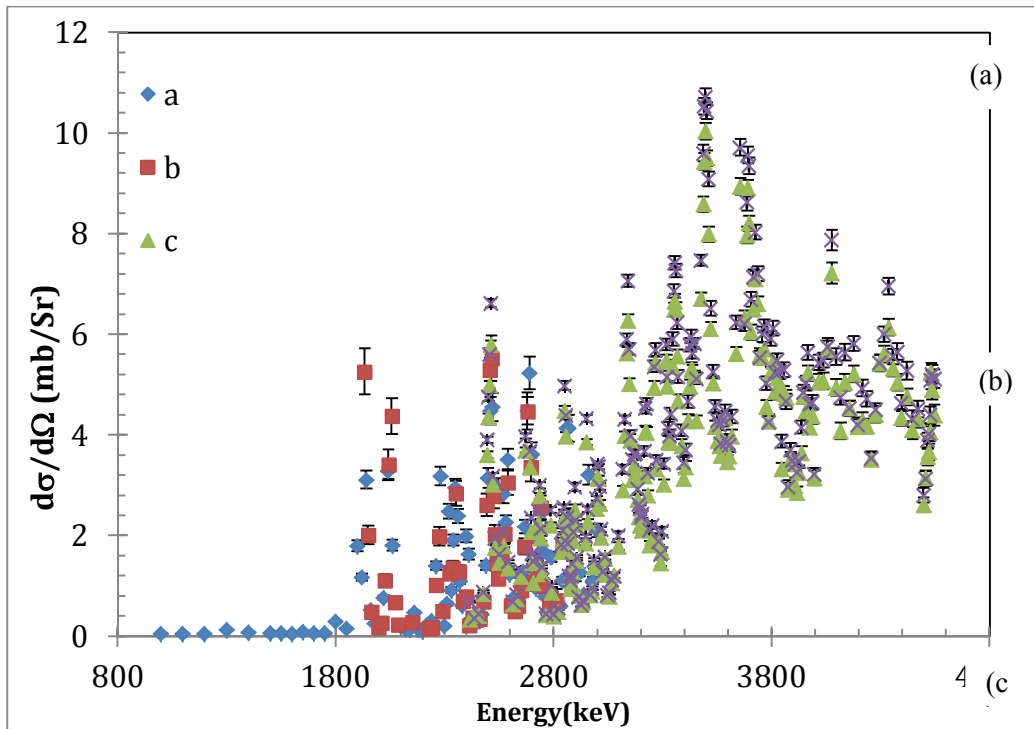


FIG. 4.58. Differential γ -ray production cross-sections of 390 keV $^{25}\text{Mg}(p,p'\gamma)^{25}\text{Mg}$ as a function of proton energy. Data obtained from a) [4.100] (90°) b) [4.79] (135°), c) [4.39] (90°) and d) [4.39] (55°).

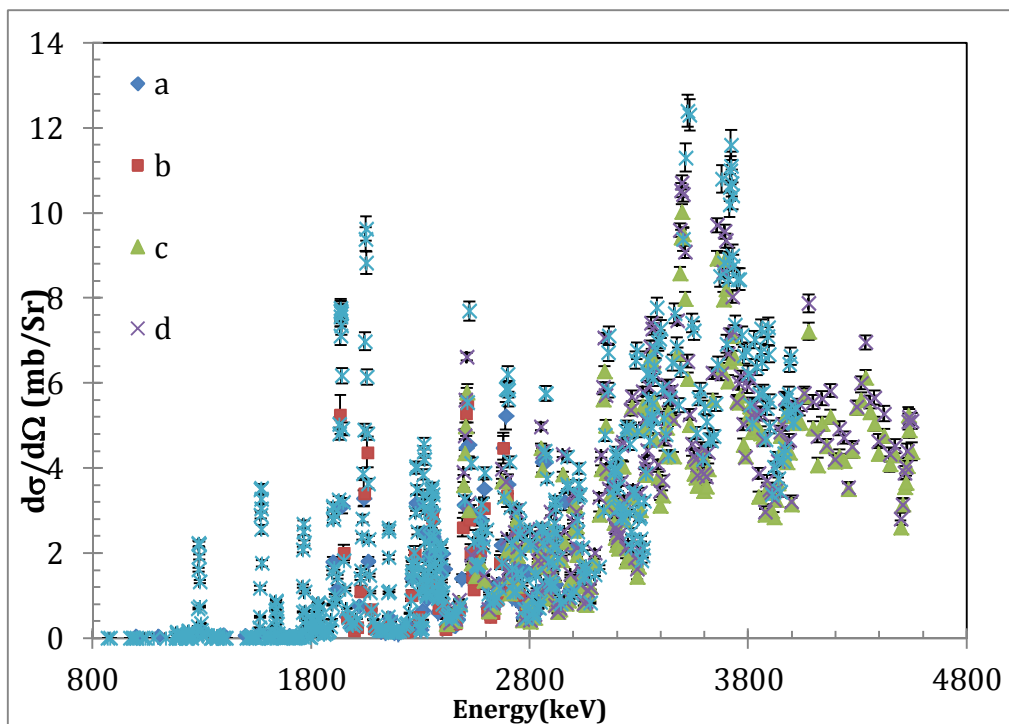


FIG. 4.59. Differential γ -ray production cross-sections of 585 keV $^{25}\text{Mg}(p,p'\gamma)^{25}\text{Mg}$ as a function of proton energy. Data obtained from a) [4.100] (90°) b) [4.79] (135°), c) [4.39] (90°), d) [4.39] (55°) and e) [4.78] (130°).

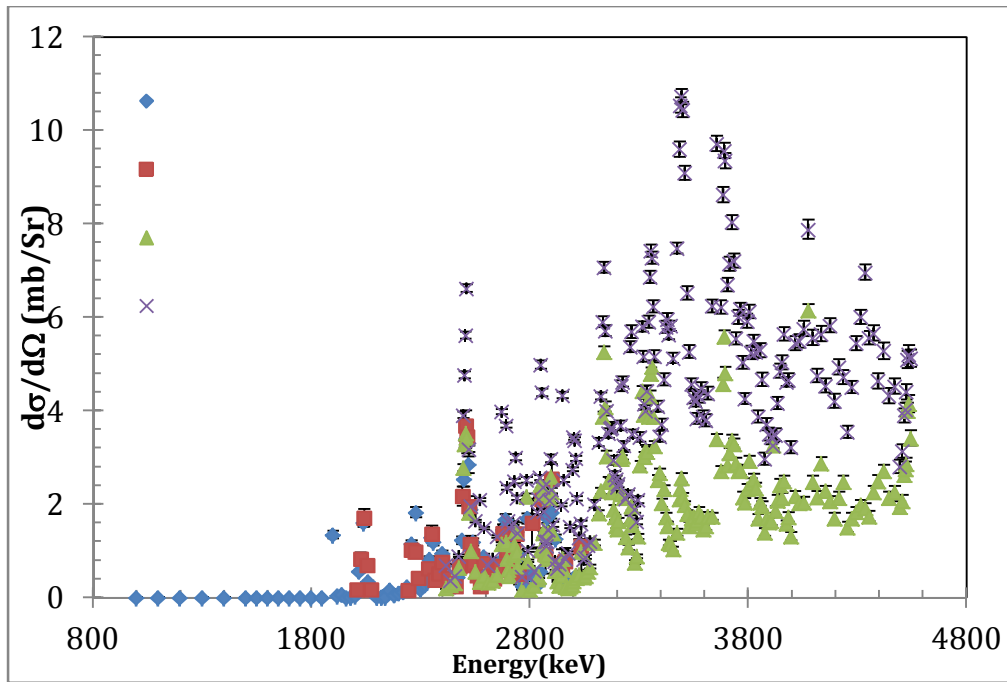


FIG. 4.60. Differential γ -ray production cross-sections of 975 keV $^{25}\text{Mg}(p,p'\gamma)^{25}\text{Mg}$ as a function of proton energy. Data obtained from a) [4.100] (90°), b) [4.79] (135°), c) [4.39] (90°) and d) [4.39] (55°).

(b) Assessment

In Fig. 4.58, at energies higher than 2.24 MeV, the excitation function is dominated by resonances. The data of Shirifzadeh *et al.* [4.100] reveal the presence of two resonances for 390, 585 and 975 keV γ -rays from the $^{25}\text{Mg}(p,p'\gamma)^{25}\text{Mg}$ reaction at 2159 keV and 2789 keV as well as two more resonances for 585 keV γ -rays observed at 2319 and 2569 keV, which are missing in the data of [4.79], due to their larger energy steps.

Table 4.27 compares the measured energy resonances of $^{25}\text{Mg}(p,p'\gamma)^{25}\text{Mg}$ reaction in the data of [4.100] with those published in [4.5] and [4.79]. As mentioned in [4.17], the 585 keV γ -line is a suitable choice for the elemental Mg analysis over the whole energy range, due to its relative high cross-section values compared to the other γ -lines. Other reasons include the low background underneath this peak and the absence of overlapping reaction channels from other light elements. Moreover, the 2.60–2.65 keV proton energy interval for the analysis of thin multi-element samples containing Mg is recommended. This energy range is greater than the energy loss of protons in thin samples and furthermore the PIGE cross-section values are high and constant enough within this range.

TABLE 4.27. COMPARISON OF THE ENERGY RESONANCES OF THE $^{25}\text{Mg}(p,p'\gamma)^{25}\text{Mg}$ REACTION: PUBLISHED IN THE LITERATURE VS MEASURED

| Measured E_p (keV) | Published E_p [4.5, 4.79] | | |
|----------------------|-----------------------------|------------|------------|
| | 390 keV | 585 keV | 975 keV |
| 2039 | 2041 | 2060 | 2041 |
| 2159 | — | — | — |
| 2279 | 2259 | 2275 | 2259 |
| 2319 ^a | — | — | — |
| 2349 | 2351 | 2351 | 2352 |
| 2399 | 2399 | 2399 | 2399 |
| 2509 | 2507 | 2514 | 2507 |
| 2569 ^a | — | — | — |
| 2589 | 2589 | 2589 | 2589 |
| 2689 | 2678 | 2678 | 2678 |
| 2739 | 2740 | 2740 | 2740 |
| 2789 | — | — | — |
| 2864 | 2857 | 2857 | 2857 |
| | 2858 ± 5 b | 2856 ± 5 b | 2855 ± 5 b |
| 2899 | 2901 | 2901 | 2901 |
| | 2900 ± 5 b | 2902 ± 5 b | 2897 ± 5 b |
| 2959 | 2962 | 2947 | — |
| | 2960 ± 5 b | 2956 ± 5 b | — |

^a only visible for the 585 keV γ -line

^b resonance energies from Ref. [4.5]

4.8.1.3. $^{26}\text{Mg}(p,\gamma_{2-0})^{27}\text{Al}$: 1014 keV γ -ray

The measured PIGE differential cross-sections of the 1014 keV γ -rays from the $^{26}\text{Mg}(p,\gamma_{2-0})^{27}\text{Al}$ reaction are shown in Fig. 4.61 [4.100]. To the best of our knowledge, there was no previous cross-section data in the literature for the 1014 keV γ -line. The PIGE cross-sections for this γ -ray line are low and smooth over almost the entire energy range, except at $E_p = 2879$ keV where a strong resonance is observed.

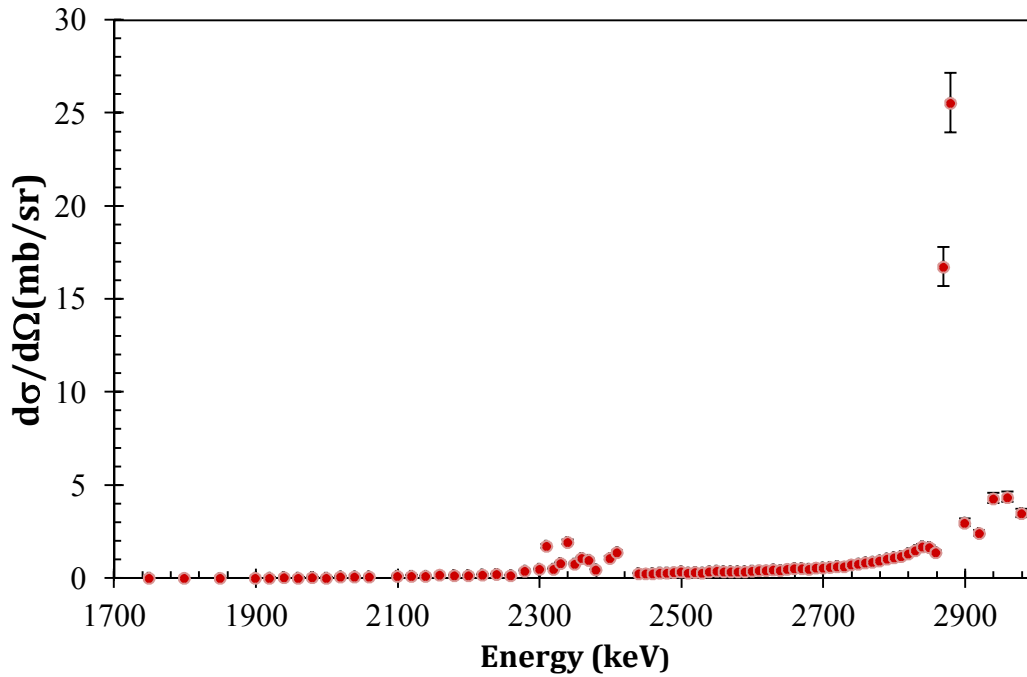


FIG. 4.61. Differential γ -ray production cross-sections of 1014 keV $^{26}\text{Mg}(p, \gamma_{2-0})^{27}\text{Al}$ measured at an angle of 90° as a function of proton energy [4.100].

4.8.2. Thick target yields

The differential cross-section data shown in Figs. 4.58–4.60 were used to calculate thick-target yields using the computer program of [4.34]. In the calculation of thick-target yields, if the energy in the integration starts from a certain energy above zero that corresponds to a given reaction cross-section value, the measured thick-target yields up to that certain energy, have to be added to the integral. For this purpose, the data sets reported by Kiss *et al.* [4.2] were employed. The resulting thick-target yields are compared in Figs. 4.62–4.66.

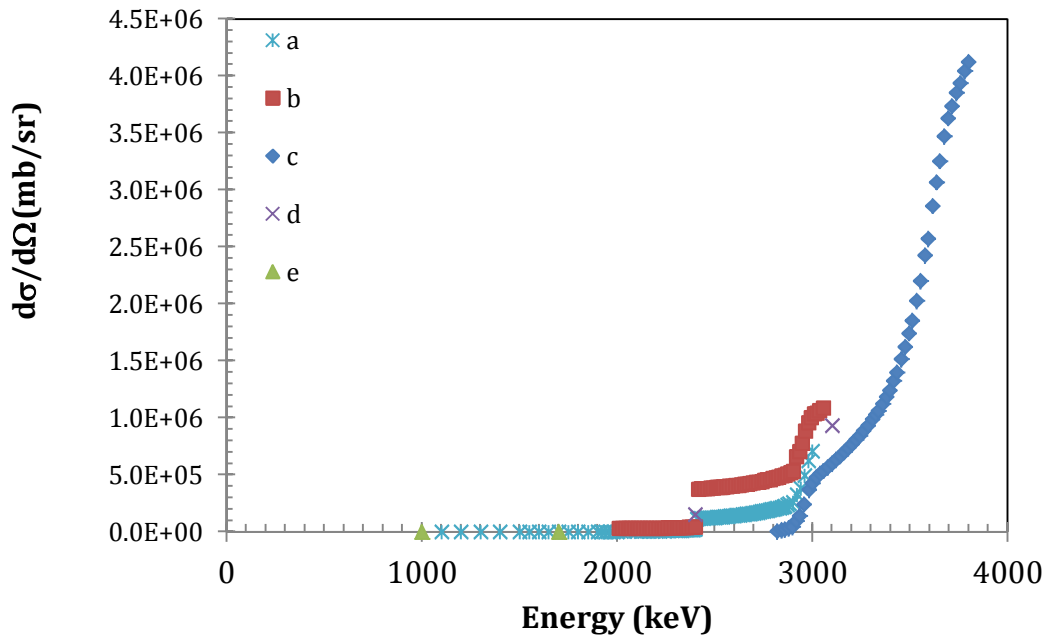


FIG. 4.62. Comparison of measured and calculated thick-target yields for the 1369 keV γ -ray produced by the $^{24}\text{Mg}(p,p')^{24}\text{Mg}$ reaction as a function of energy. Calculated yields obtained from: a) [4.100] (90°), b) [4.79] (135°), c) [4.5] (90°), while measured yields are taken from: d) [4.2] (55°) and e) [4.1] (55°).

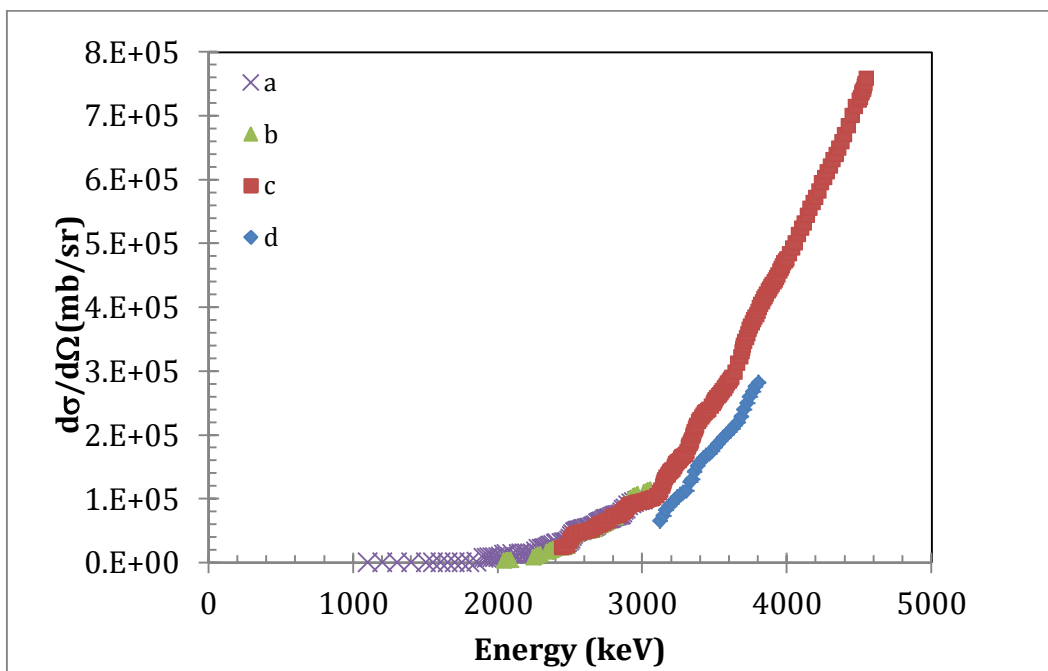


FIG. 4.63. Comparison of measured and calculated thick-target yields for the 390 keV γ -ray produced by the $^{25}\text{Mg}(p,p')^{25}\text{Mg}$ reaction as a function of energy. Calculated yields obtained from: a) [4.100] (90°), b) [4.79] (135°), c) [4.39] (55°) and d) [4.5] (90°).

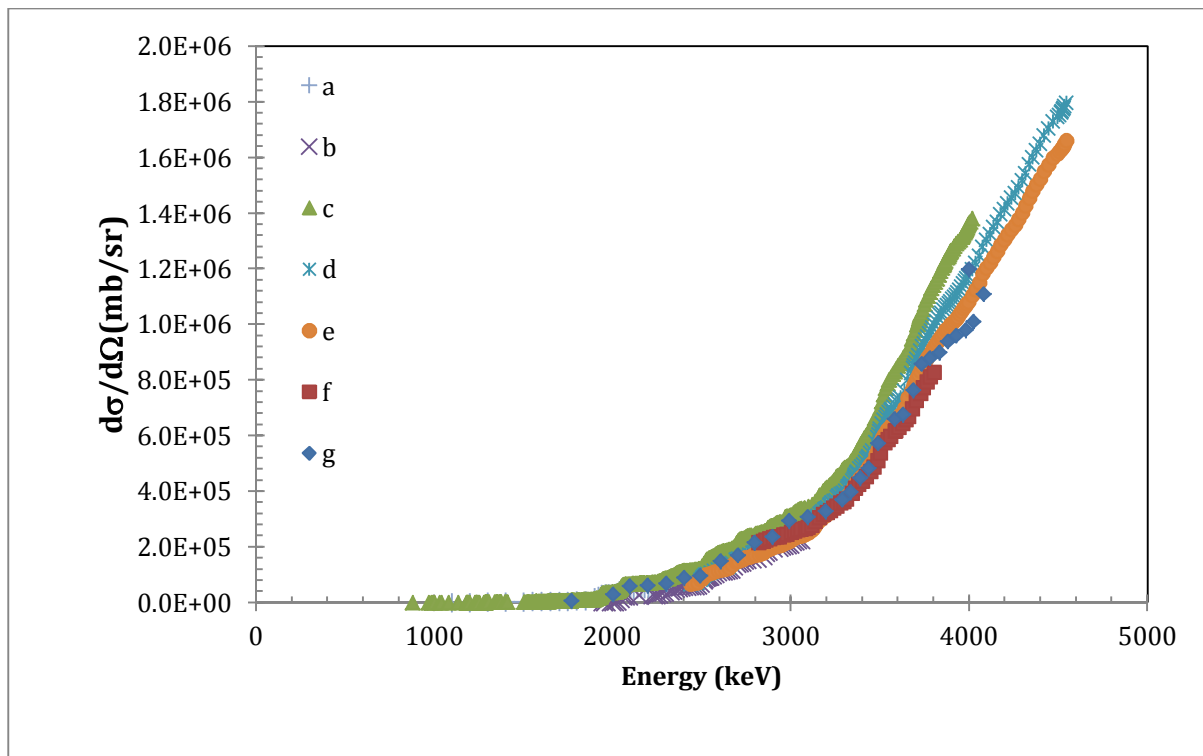


FIG. 4.64. Comparison of measured and calculated thick-target yields for the 585 keV γ -ray produced by the $^{25}\text{Mg}(p,p'\gamma)^{25}\text{Mg}$ reaction as a function of energy. Calculated yields obtained from: a) [4.100], b) [4.79], c) [4.78], d) 55° [4.39], e) 90° [4.39], f) [4.5] and measured yields taken from g) [4.17].

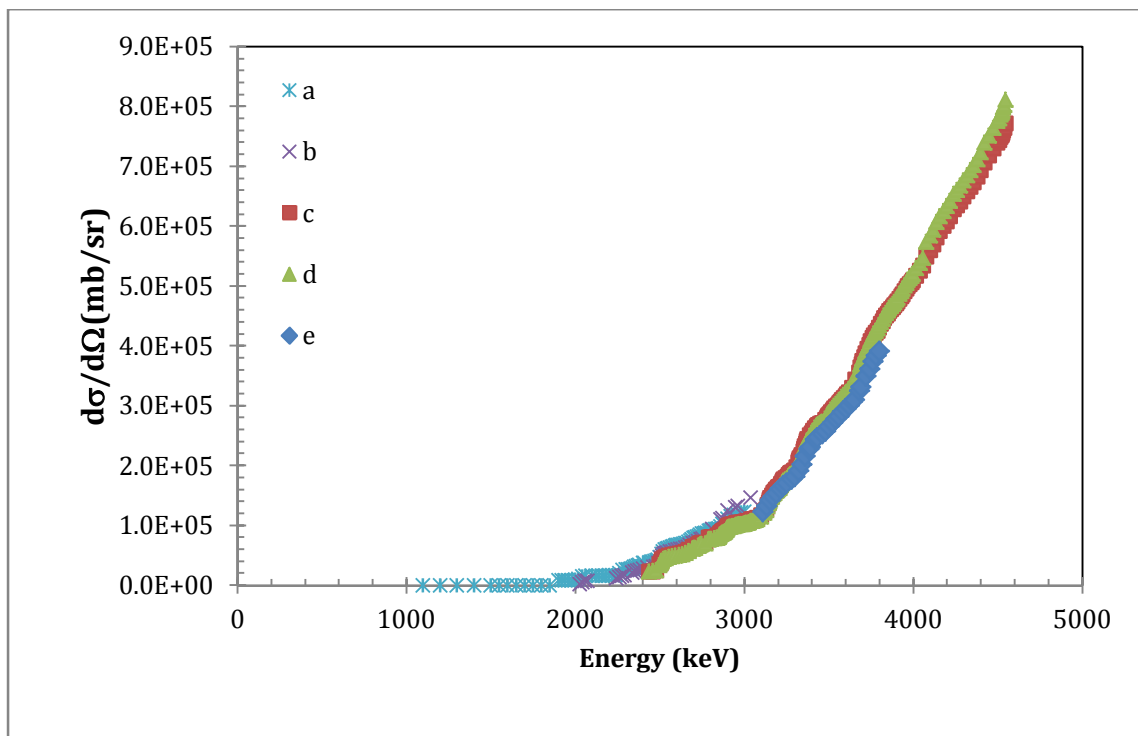


FIG. 4.65. Comparison of measured and calculated thick-target yields for the 975 keV γ -ray produced by the $^{25}\text{Mg}(p,p'\gamma)^{25}\text{Mg}$ reaction as a function of energy. Calculated yields obtained from: a) [4.100] (90°), b) [4.79] (135°), c) [4.39] (55°), d) [4.39] (90°) and e) [4.5] (90°).

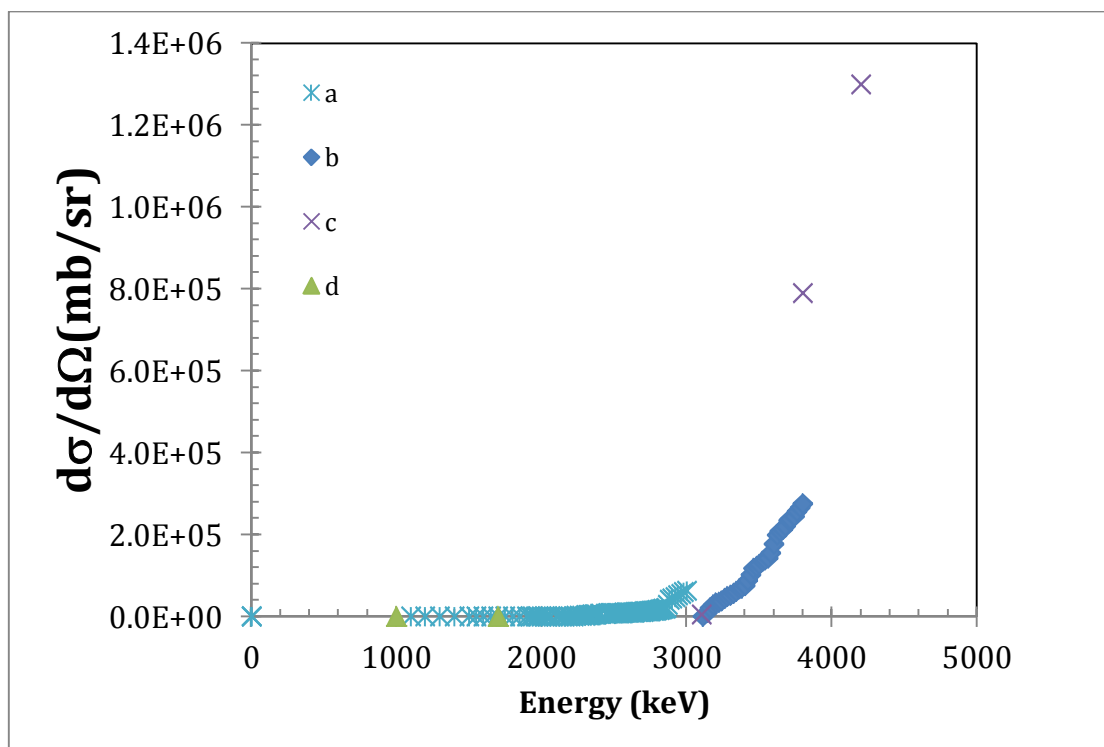


FIG. 4.66. Comparison of measured and calculated thick-target yields for the 1014 keV γ -ray produced by the $^{26}\text{Mg}(p,\gamma_{2-0})^{26}\text{Mg}$ reaction. Calculated yields taken from a) [4.100] (90°), b) [4.5], while measured yields from c) [4.2] (55°), and d) [4.1] (55°).

(c) Recommended data

From Fig. 4.62, it is clear that the calculated thick-target yields for the 1369 keV - ray from $^{24}\text{Mg}(p,p'\gamma)^{24}\text{Mg}$ reaction are neither in agreement with each other, nor with the yields derived from the data reported by Boni *et al* [4.5]. The reason is that there are some narrow resonances around 2010 keV and 2410 keV, but the cross-sections are not measured with small enough energy steps to be sensitive to them. As a result, none of these measured differential cross-sections are recommended for PIGE analysis.

According to the results shown in Figs. 4.63–4.65 for the 390, 585 and 975 keV γ -rays produced from the $^{25}\text{Mg}(p,p'\gamma)^{25}\text{Mg}$ reaction, the data of Shafifzadeh *et al.* [4.100] is recommended for proton energies less than 3 MeV, due to good agreement with the thick-target yield measurements over an extended energy range. For energies above 2.5 MeV, the measured data by K. Preketes-Sigalas *et al.* [4.39] give the best agreement with the thick-target yields and therefore they are recommended. Furthermore, in the energy region from 2.0 to 3.0 MeV, the data measured by Zamboni *et al.* [4.79] are in good agreement with the measured data of Savidou *et al.* [4.17]. However, for the 585 keV γ -ray line, the data reported by Jesus *et al.* [4.78] seem to overestimate the thick-target yields that are calculated and those that are measured by Savidou *et al.* [4.17].

For the 1014 keV γ -ray produced by the $^{26}\text{Mg}(p,\gamma_{2-0})^{26}\text{Mg}$ reaction, there is no reasonable overlap between the energy ranges of the various thick-target yield measurements and the energy range of the differential cross-sections measurements by [4.100]. Therefore no comparison can be performed and hence none of these data are recommended for PIGE analysis.

4.9. ALUMINUM

4.9.1. Gamma-ray production cross-sections of aluminum from proton-induced nuclear reactions

Gamma-rays of 844 and 1014 keV are produced following the inelastic scattering of protons by aluminum. The cross-sections of these processes are large, which leads to high γ -ray yields that may be used to quantify aluminum concentrations in a large variety of samples when using proton beams. Other γ -rays (of higher energy) are also produced during the bombardment, by the process called proton capture. However, since this process has a much smaller cross-section than the inelastic scattering process and the efficiency of the γ -ray detector decreases with increasing γ -ray energy, inelastic scattering gives a much higher sensitivity for analysis of in-depth homogeneous samples. In contrast, proton capture excites several very narrow and rather isolated resonances, which are frequently used for the purpose of depth analysis. Another nuclear reaction that may occur is the (p,α) reaction, but the γ -ray produced by this reaction may also be obtained by bombardment of magnesium by protons. Therefore, it is not suitable for analytical purposes, unless it can be ensured that magnesium is not present in the sample. Furthermore, $^{26}\text{Mg}(p,\gamma)^{27}\text{Al}$ may also produce the 844 and 1014 keV γ -ray lines, but since this reaction is less likely to occur, its contribution will be significant only for samples very rich in magnesium. The amount of magnesium may be controlled by the $^{25}\text{Mg}(p,p'\gamma)^{25}\text{Mg}$ reaction, which produces a different γ -ray line.

Regarding the availability of cross-section data, inelastic scattering cross-sections and proton capture cross-sections are scarce. Although this reaction has been thoroughly studied, most of the studies have focused on measuring resonance strengths. As a result, considerable effort was made during this CRP to measure γ -ray producing cross-sections and thick-target yields for the inelastic scattering of protons by aluminum.

4.9.1.1. $^{27}\text{Al}(p,p'\gamma_{1-0})^{27}\text{Al}$: 844 keV γ -ray

Some of the results of these measurements have been described in the section on the interlaboratory exercise (Section 3.6). In this section, more details of the different experimental set-ups, the complete datasets as well as a comparison with datasets found in the literature are presented.

(a) New measurements

Measurements of the $^{27}\text{Al}(p,p'\gamma_{1-0})^{27}\text{Al}$ reaction were performed in the following laboratories: CTN/IST, LABEC-INFN, RBI and NSTRI. The experimental conditions for the different laboratories are presented below.

CTN/IST

The proton beams were accelerated by a 2.5 MV Van der Graaff accelerator and a 3 MV Tandemron accelerator. The 2.5 MV Van der Graaff accelerator delivered proton beams with energies in the range 0.30 to 2.40 MeV. Proton beam currents of 250 nA were employed. The proton energy was calibrated by the 668.0, 872.1 and 1373.2 keV resonances produced by the $^{19}\text{F}(p,\alpha\gamma)^{16}\text{O}$ reaction and also by the 1645.1 and 1930.7 keV resonances produced by the $^{23}\text{Na}(p,p'\gamma)^{23}\text{Na}$ reaction. Proton beams, produced by a Duoplasmatron source, were accelerated by the 3 MV Tandemron accelerator, with energies in the range of 2.0 to 3.0 MeV. Proton beam currents of the order of 100 nA were employed. The proton energy was calibrated by the 1645.1 and 1930.7 resonances produced by the $^{23}\text{Na}(p,p'\gamma)^{23}\text{Na}$ reaction and by the 3470 keV resonance produced by the $^{16}\text{O}(p,p)^{16}\text{O}$ reaction. The same reaction chamber

was used for the two sets of measurements. The reaction chamber is electrically insulated from the beam line and works together with the target holder and beam stopper as one Faraday cup for beam charge collection. Scattered protons at 157° to the incident beam were detected by Canberra PIPs detectors with active area of 50 mm^2 and depletion layer 100 mm, located in Cornell geometry at 88 mm from the target, with solid angles defined by apertures of $6.00 \pm 0.05 \text{ mm}$. Gamma-rays were detected by a 45% Ge(HP) detector located at 130° in relation to the incident beam direction and at a distance of 55.5 mm from the target. The absolute efficiency versus γ -ray energy was obtained by measuring the yields of γ -rays produced by ion sources (^{133}Ba and ^{152}Eu) that were calibrated in activity as well as by Monte Carlo simulations using GEANT and PENELOPE. The target was produced by evaporating a thin film of pure Al onto a thin self-supporting Ag film. RBS performed on the Ag film was used to normalize the cross-sections. The uncertainty budget can be found in Table 4.28.

LABEC – INFN

The measurement was performed with a 3 MV Tandatron accelerator. Proton beam currents of 100 nA were employed. The proton energy was calibrated by the resonances at the 992 keV γ -ray produced by the $^{27}\text{Al}(p,\gamma)$ reaction, the 1683 keV γ -ray produced by the $^{27}\text{Al}(p,p'\gamma)$ reaction, the 2876 keV γ -ray produced by the $^{27}\text{Al}(p,p)$ reaction and the 3470 keV resonance produced by the $^{16}\text{O}(p,p)^{16}\text{O}$ reaction. Gamma-rays were detected by a 50% Ge(HP) detector located at 90° in relation to the incident beam direction and at a distance of 205 mm from the target. The absolute efficiency versus γ -ray energy was obtained by measuring the yields of γ -rays produced by ion sources (^{152}Eu). Elastically scattered protons were collected simultaneously using a Si-PIN diode detector with area of 10 mm^2 , thickness of 300 μm and energy resolution 13 keV FWHM, placed at a backward angle of 150° and collimated by a $1 \times 13 \text{ mm}^2$ vertical slit. The subtended solid angle was $3.37 \pm 0.08 \text{ msr}$. The target was produced by evaporating a thin film of pure Al onto a thin self-supporting Ag film. RBS by the Ag film was used to normalize the cross-sections. The uncertainty budget can be found in Table 4.28.

RBI

The protons were accelerated by a 6.0 MV Tandem Van der Graaff. The energy was calibrated by the 992 keV resonance produced by the $^{27}\text{Al}(p,\gamma)$ reaction and the $^7\text{Li}(p,n)^7\text{Be}$ threshold at $E_p = 1880.7 \pm 0.4 \text{ keV}$. Gamma-rays were detected by a 20% Ge(HP) detector located at 135° in relation to the incident beam direction and at a distance of 100 mm from the target. The absolute efficiency versus γ -ray energy was obtained by measuring the yields of γ -rays produced by ion sources (^{60}Co , ^{133}Ba , ^{137}Cs and ^{152}Eu). Elastically scattered protons were collected simultaneously using a silicon surface barrier detector placed at the backward scattering angle of 165° , with a solid angle of $7.5 \pm 0.2 \text{ msr}$. The target was a thin film of pure Al evaporated onto a thin self-supporting Mylar™ film, with a 4 nm Au layer. RBS by the Au layer was used to normalize the cross-sections. The uncertainty budget can be found in Table 4.28.

NSTRI

The protons were accelerated by a 3.0 MV Van der Graaff accelerator. The proton energy was calibrated by the 992 keV resonance produced by the $^{27}\text{Al}(p,\gamma)$ reaction and the $^7\text{Li}(p,n)^7\text{Be}$ threshold at $E_p = 1880.7 \pm 0.4 \text{ keV}$. Gamma-rays were detected by a 50% Ge(HP) detector located at 90° in relation to the incident beam direction and at a distance of 51.9 mm from the target. The absolute efficiency versus γ -ray energy was obtained by measuring the yields of γ -rays produced by ion sources (^{60}Co , ^{133}Ba , ^{137}Cs , ^{152}Eu and ^{241}Am). Elastically scattered protons were collected simultaneously using a silicon surface barrier detector placed at the backward scattering angle of 165° , with a solid angle of 0.746 msr . The target was created by

evaporating a thin film of pure Al onto a thin self-supporting Ag film. RBS by the Ag film was used to normalize the cross-sections. The uncertainty budget may be found in Table 4.28.

Since every laboratory used the same method to measure the cross-sections, the uncertainty budget is the same for all the laboratories and is listed in Table 4.28.

TABLE 4.28. UNCERTAINTY BUDGET FOR THE MEASUREMENTS OF THE CROSS-SECTIONS OF Al MADE IN ALL LABS

| Quantity | Uncertainty |
|-----------------------------------|-------------|
| γ -ray peak area | 1–3% |
| p+Ag elastic peak area | 1% |
| p+Ag Rutherford cross-section | 1% |
| Al/Ag atomic ratio | 3% |
| Particle detector solid angle | 2.5% |
| γ -ray detector efficiency | 6% |
| Proton beam energy | 0.1% |
| Overall uncertainty | 8–10% |

Figure 4.67 shows a comparison of cross-section values obtained by the above listed groups. These values may also be found in the IBANDL database: Jesus *et al.* (CTN/IST) [4.78] from 1497 to 3000 keV in steps from 1 keV (on resonance) to 10 keV (off resonance); Chiari *et al.* (LABEC-INFN) [4.101] from 2507 to 4089 keV in steps from 5 keV (on resonance) to 10 keV (off resonance); Zamboni *et al.* (RBI) [4.79] from 1932 to 2507 keV in 16 keV steps and from 2507 to 3053 keV in steps from 5 keV (on resonance) to 15 keV (off resonance); Jokar *et al.* (NSTRI) [4.102] from 1497 to 2388 keV in 20 keV steps and from 2388 to 2998 keV in steps from 5 keV (on resonance) to 10 keV (off resonance). Figure 4.67 pertains to an energy region covered by the four measurements. The energy region from 2.5 to 3.0 MeV has been covered by all four measurements and, as is illustrated in Fig. 4.67, these measurements agree within the experimental uncertainty for both on and off resonance. Around 2.5 MeV, the proton energy scales seem to be correct for all the measurements except Jokar *et al.*, which are 3 keV lower. However around 2.9 MeV, Jokar *et al.* and Jesus *et al.* present energies 3 keV higher than Chiari *et al.* and 6 KeV higher than Zamboni *et al.* At an energy range lower than 2.5 MeV, as illustrated in Fig. 4.68, the energy steps of Zamboni *et al.* and Jokar *et al.* are too large to pick up most of the resonances. However, with respect to some gross features of the excitation function, the results of Zamboni *et al.* and Jokar *et al.* agree with Jesus *et al.* within the experimental uncertainty.

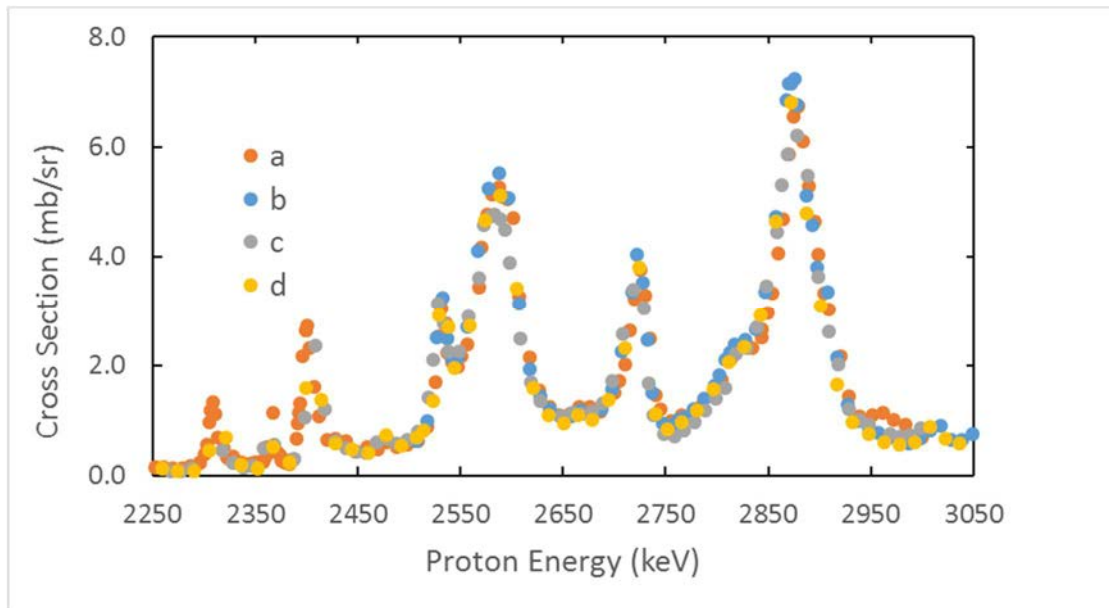


FIG. 4.67. Comparison of cross-sections for the 844 keV γ -ray produced by the $^{27}\text{Al}(p,p\gamma_{1-0})^{27}\text{Al}$ reaction, as a function of proton energy in the range of 2250 – 3050 keV. Data obtained within the CRP: a) [4.78], b) [4.101], c) [4.102] and d) [4.79]

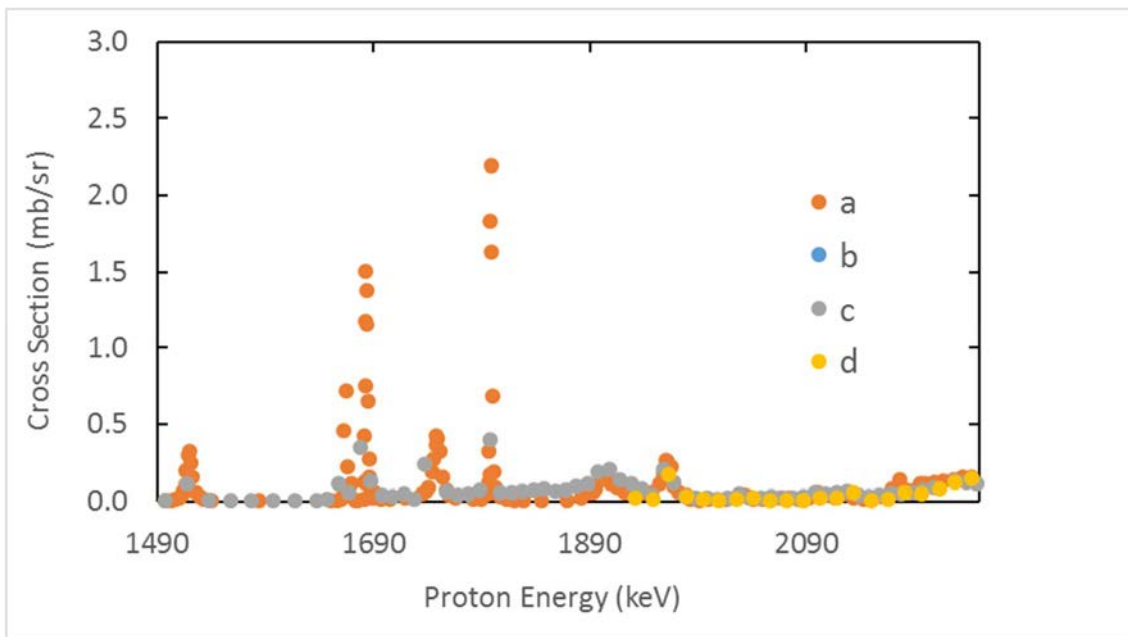


FIG. 4.68. Same as Fig. 4.67 but for the proton energy range 1490–2250 keV.

Only Chiari *et al.* [4.101] have made measurements for the energy range above 3050 keV.

(b) Data in the literature

A review of the existing literature produced one dataset measured by Boni *et al.* [4.5] (values may be found in the IBANDL database). Cross-sections were measured in the proton energy range from 2190 to 3800 keV in steps of around 27 keV. In the energy range from 2190 to 3050 keV, Boni *et al.* missed most of the resonances due to the very large energy step they

employed. The cross-section values between the resonances, however, agree with the new measured values within the experimental uncertainty. Their results are compared with the data by Chiari *et al.* [4.101], in the energy range from 3050 to 4100 keV, in Fig. 4.69. As can be seen in the figure, the data agree within the experimental uncertainties. At 3050 keV, there is a discrepancy larger than 10 keV that decreases with increasing energy.

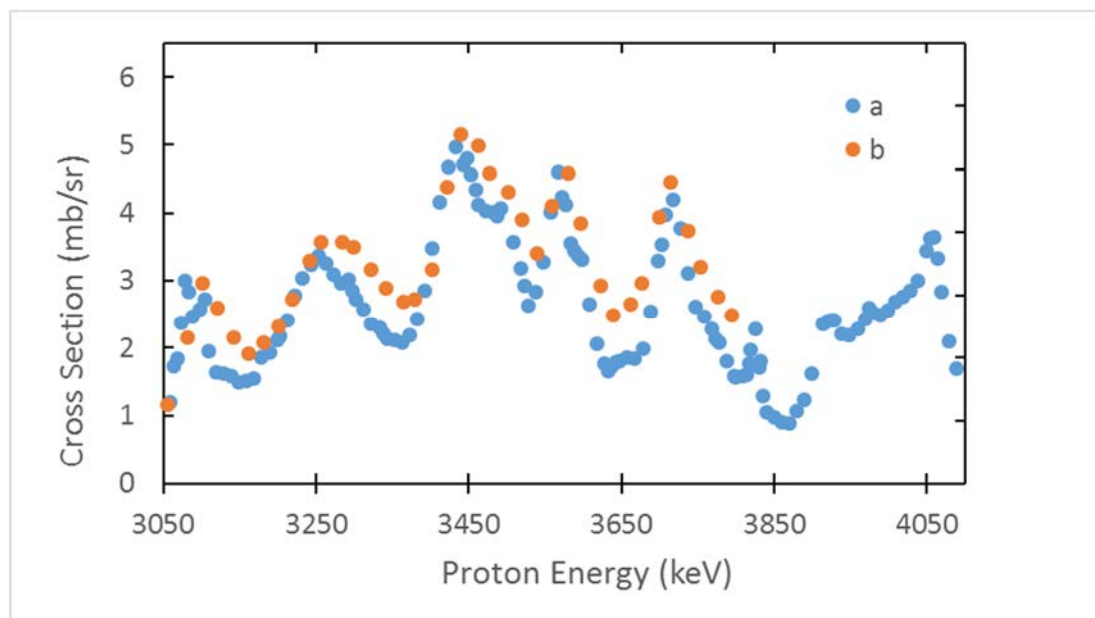


FIG. 4.69. Comparison of cross-sections for the 844 keV γ -ray produced by the $^{27}\text{Al}(p,p\gamma_{1-0})^{27}\text{Al}$ reaction, as a function of proton energy in the proton energy range 3050 – 4050 keV. Data obtained within the CRP a) [4.101] and previous results: b) [4.5].

(c) Recommended data

From the comparison of the results from new and previous measurements, one may conclude that there is an overall agreement among the data within the experimental uncertainty. Therefore, it is recommended to use a combined excitation function in the energy range from 1490 to 4100 KeV, composed of the data of Jesus *et al.* [4.78] from 1490 to 2500 keV and the data of Chiari *et al.* [4.101] from 2500 to 4100 keV, in PIGE bulk analysis.

4.9.1.2. $^{27}\text{Al}(p,p\gamma_{2-0})^{27}\text{Al}$: 1014 keV γ -ray

(a) New measurements

Measurements of the $^{27}\text{Al}(p,p\gamma_{2-0})^{27}\text{Al}$ reaction were performed simultaneously with the 844 keV γ -ray at the same laboratories, with the same conditions and uncertainty budget mentioned above. The energy range and steps are also the same. Additionally, results from Kiss *et al.* (ATOMKI) [4.78] were also obtained. The measurement was performed with a 5 MV Van de Graaff accelerator. Proton beam currents of 300 nA were employed. The proton energy was calibrated using the 992 keV γ -ray produced by the $^{27}\text{Al}(p,\gamma)$ reaction. Gamma-rays were detected by a 40% Canberra GR4025–7600SL detector located at 55° in relation to the incident beam direction and at a distance of 95 mm from the target. The absolute efficiency versus γ -ray energy was obtained by measuring the yields of γ -rays produced by ion sources (^{152}Eu and ^{60}Co). Elastically scattered protons were collected simultaneously using an ion implanted Si detector with active depth 500 μm and energy resolution 13 keV,

placed at an angle of 135° relative to the incident beam direction and at a distance of 4.3 ± 0.1 cm from the target. A copper collimator with a circular aperture of 3.2 mm diameter was mounted in front of the Si detector. The solid angle of the Si detector was 4.3 ± 0.2 msr, from geometrical calculations. The target was produced by evaporating a thin film of pure Al onto a thin self-supporting C film. The absolute values of the charge and of the areal density of Al atoms were used to calculate the cross-sections.

Although the 844 keV γ -line, which originates from a spin 1/2 state, is expected to be isotropic, the same does not apply to the 1410 keV γ -line, which originates from a spin 3/2 state and which may display anisotropy. Two of the measurements were set at an angle of 90° and the other two measurements at angles of 130° and 135° . Since the latter two angles are very similar, the measurements are considered to be performed under the same conditions. Chiari *et al.* also measured at 45° , and the results were shown to agree, within the experimental uncertainty, with the data obtained at 90° .

Figures 4.70 and 4.71 show a comparison of the results obtained within this CRP. As can be seen in Fig. 4.70, in the energy range from 2.5 to 3.0 MeV, for both on and off resonance regions, the measurements agree within the experimental uncertainty, although they correspond to different angles. However, it is not clear whether there is a discrepancy in the energy scale, since some of the measurements seem to have missed the maxima of the resonances.

In the energy range below 2.5 MeV, the energy steps of Zamboni *et al.* [4.79] and Jokar *et al.* [4.102] were too large. Consequently, their results miss some of the resonances as can be seen in Fig. 4.71. Overall, however, the gross features of these excitation functions agree with the results of Jesus *et al.* [4.78], within the experimental uncertainty.

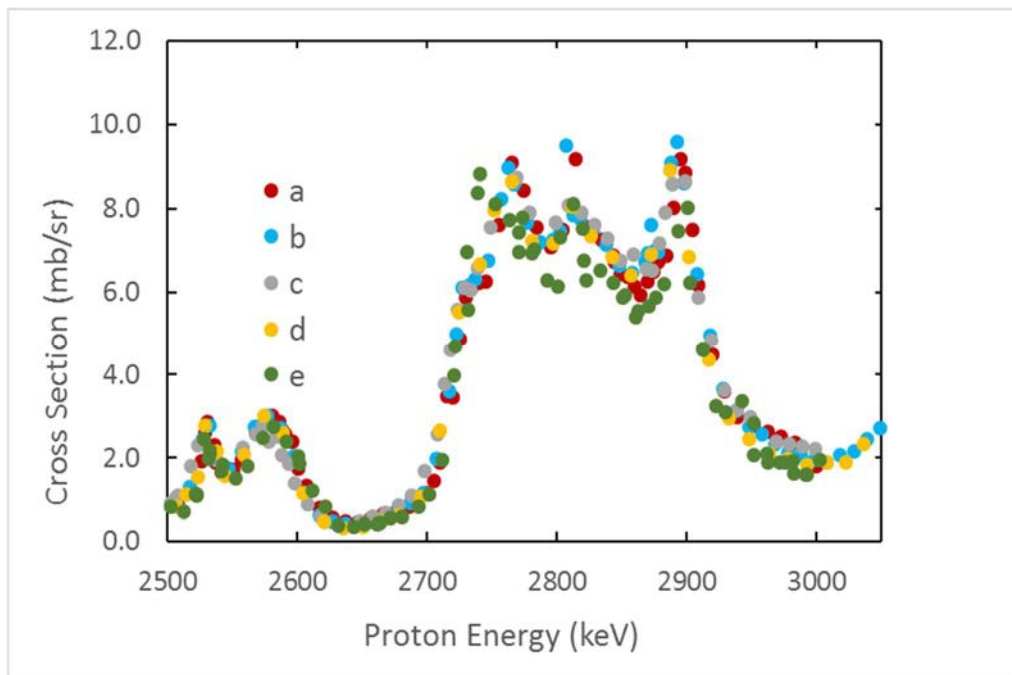


FIG. 4.70. Comparison of cross-sections for the 1014 keV γ -ray produced by the $^{27}\text{Al}(p, p\gamma_{2-0})^{27}\text{Al}$ reaction, as a function of proton energy in the range 2500 – 3050 keV. Data obtained within the CRP: a) [4.78] (130°), b) [4.101] (45°), c) [4.102] (90°), d) [4.79] (135°), and e) [4.78] (55°).

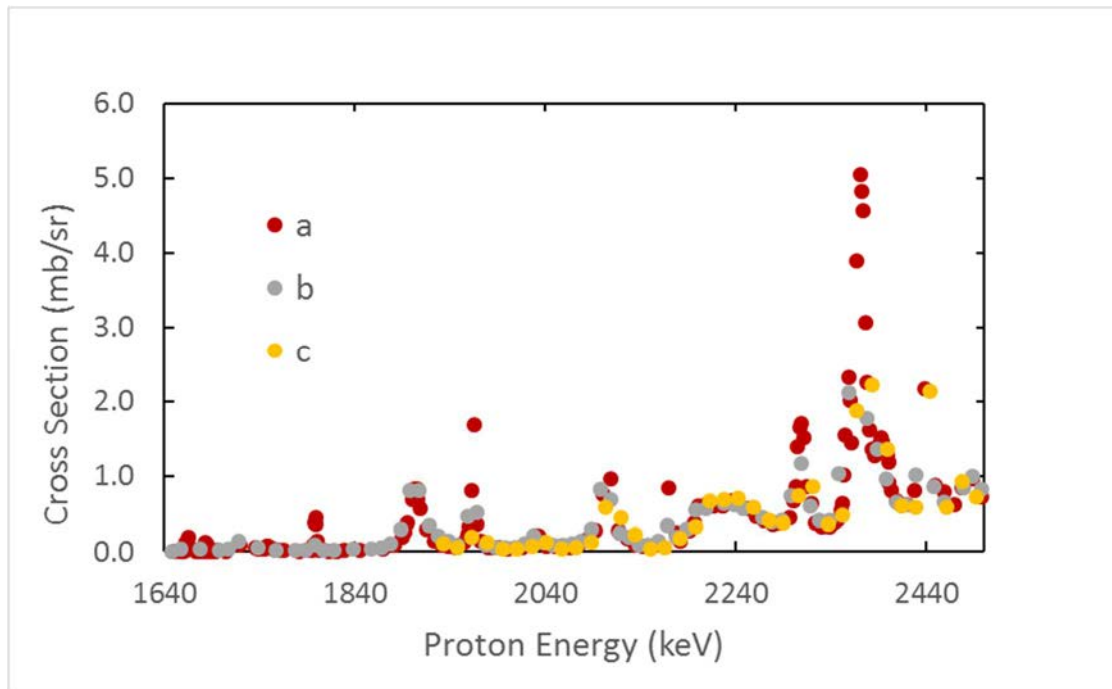


FIG. 4.71. Comparison of cross-sections for the 1014 keV γ -ray produced by the $^{27}\text{Al}(p,p\gamma_{2-0})^{27}\text{Al}$ reaction, as a function of proton energy in the range 1640 – 2500 keV. Data obtained within the CRP by: a) [4.78] (130°), b) [4.102] (90°), and c) [4.79] (135°).

(b) Data in the literature

A review of the existing literature on similar measurements resulted in one published set of measurements [4.5] (data available in IBANDL). The measurements were performed in the proton energy range from 2190 to 3800 keV in steps of around 27 keV, with a detection angle at 90° . In the energy range 2190 to 3050 keV, the data of Boni *et al.* miss most of the resonances due to the very large energy step employed, but between resonances, the cross-sections agree with the new measured cross-sections, within the experimental uncertainty. At the energy range from 3000 to 4100 keV, the Boni data [4.5] are compared with the data of Chiari *et al.* [4.101] (Fig. 4.72). Overall, there is good agreement within the experimental uncertainty, although there is a discrepancy of more than 10 keV in the energy scale at around 3050 keV, which decreases with increasing energy.

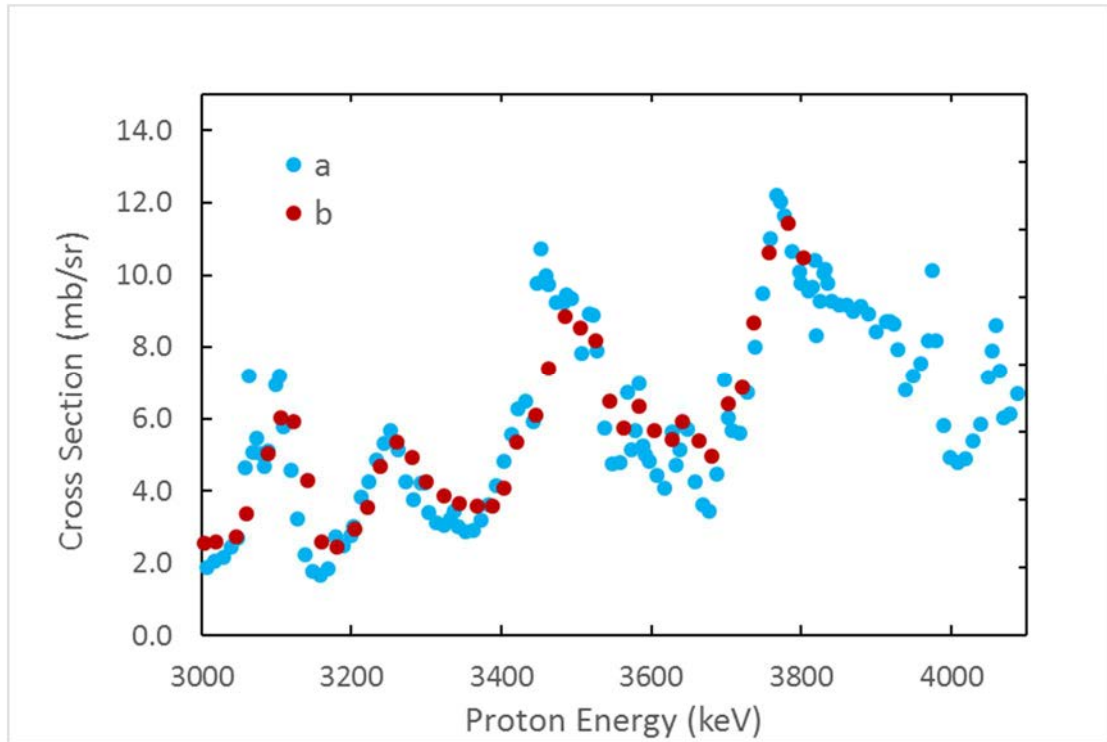


FIG. 4.72. Same as Fig. 4.71, but for the range of 3000 – 4100 keV. Data obtained within the CRP a) [4.101] (45°) and previous results b) [4.5] (90°).

(c) Recommended data

From the above comparison of results from new measurements and previous measurements, it can be concluded that there is an overall agreement within the experimental uncertainty, which is independent of the detection angles and implies isotropy at the covered energy range for the 1014 keV γ -line.

4.9.1.3. $^{27}\text{Al}(p, \alpha \gamma_{1-0})^{24}\text{Mg}$: 1369 keV γ -ray

(a) New measurements

Although not very useful for analysis, the 1369 keV γ -line produced from the $^{27}\text{Al}(p, \alpha \gamma_{1-0})^{24}\text{Mg}$ reaction is obtained in the same spectra as the 844 keV and 1014 keV γ -ray lines produced from the $^{27}\text{Al}(p, p' \gamma)^{27}\text{Al}$ reaction, as previously mentioned. However, the 1369 keV γ -line has only been quantified by Jokar *et al.* [4.102], Zamboni *et al.* [4.79], and Cedreki *et al.* [4.78]. A comparison of the different results is shown in Fig. 4.73. As can be seen, in the energy range from 1.9 to 2.65 MeV, for both on and off resonance regions, the measurements agree within the experimental uncertainty, even if they correspond to different detection angles. At higher energies, however, there are discrepancies in the proton energy scale among the different measurements. In addition, since the energy step that was used is larger than the width of some resonances, the measurements have missed the resonances. Therefore, it is not possible to compare the data in any meaningful way. Although this γ -ray is anisotropic based on the spin of the initial excited state of ^{24}Mg being 2+, the effect of anisotropy (which may differ from resonance to resonance) is not expected to be significant, since the thick-target yields obtained by Chiari *et al.* [4.101] at different angles indicate very small anisotropies (see following sections).

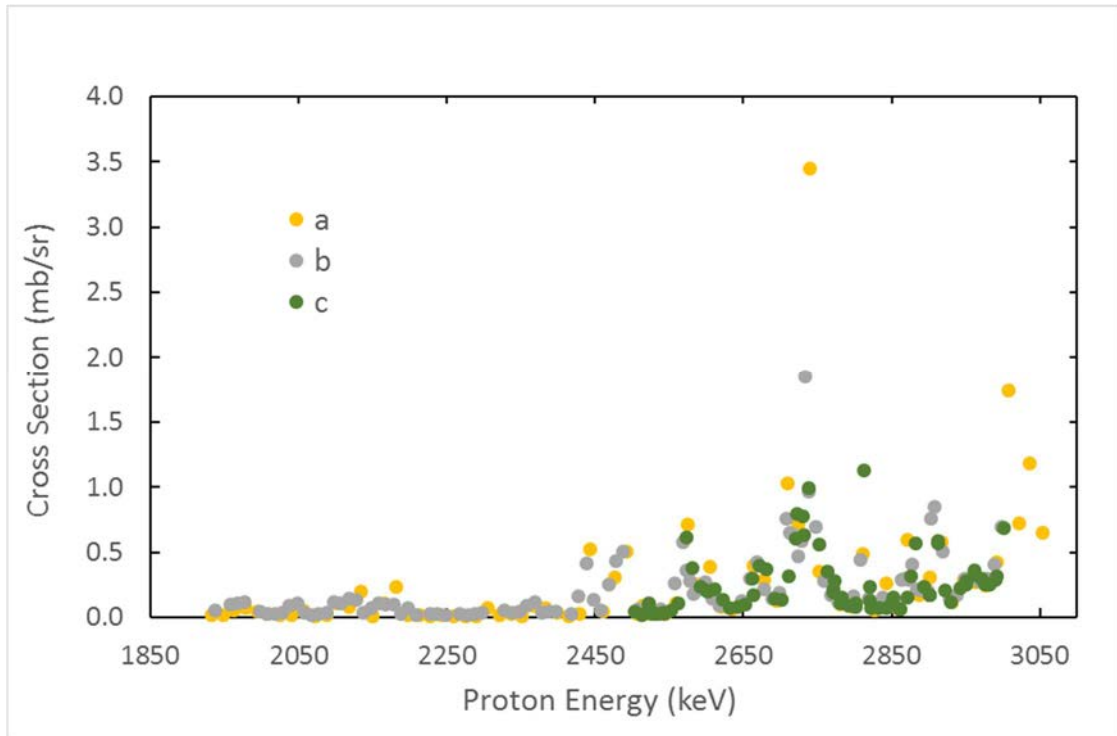


FIG. 4.73. Comparison of cross-sections for the 1369 keV γ -ray from the $^{27}\text{Al}(p,\alpha)^{24}\text{Mg}$ reaction as a function of the proton energy in the range of 1850 – 3050 keV. Data obtained within the CRP by a) [4.79] (135°), b) [4.102] (90°) and c) [4.78] (55°).

(b) Data in the literature

A review of the existing literature revealed two different measurements, those of Boni *et al.* [4.5] and Warsh *et al.* [4.104] (available in IBANDL), which covered the proton energy range from 2200 to 3800 keV and 3474 to 12152 keV, respectively. In both measurements, an energy step between 20 to 30 keV was used and the detection angle was 90° . In Fig. 4.74, one can see the comparison of new and previous measurements for the energy range from 2150 to 3800 keV. Boni *et al.* [4.5] miss some of the resonances due to the very large step employed, but between resonances, the different data sets agree within the experimental uncertainty. In the energy range from 3000 to 3800 keV, the results are compared with the data of Warsh *et al.*, which reveals a large discrepancy in the energy scale that does not allow for a meaningful comparison of the two measurements. However, the cross-sections of Warsh *et al.* [4.104] seem to be higher than the ones of Boni *et al.* [4.5].

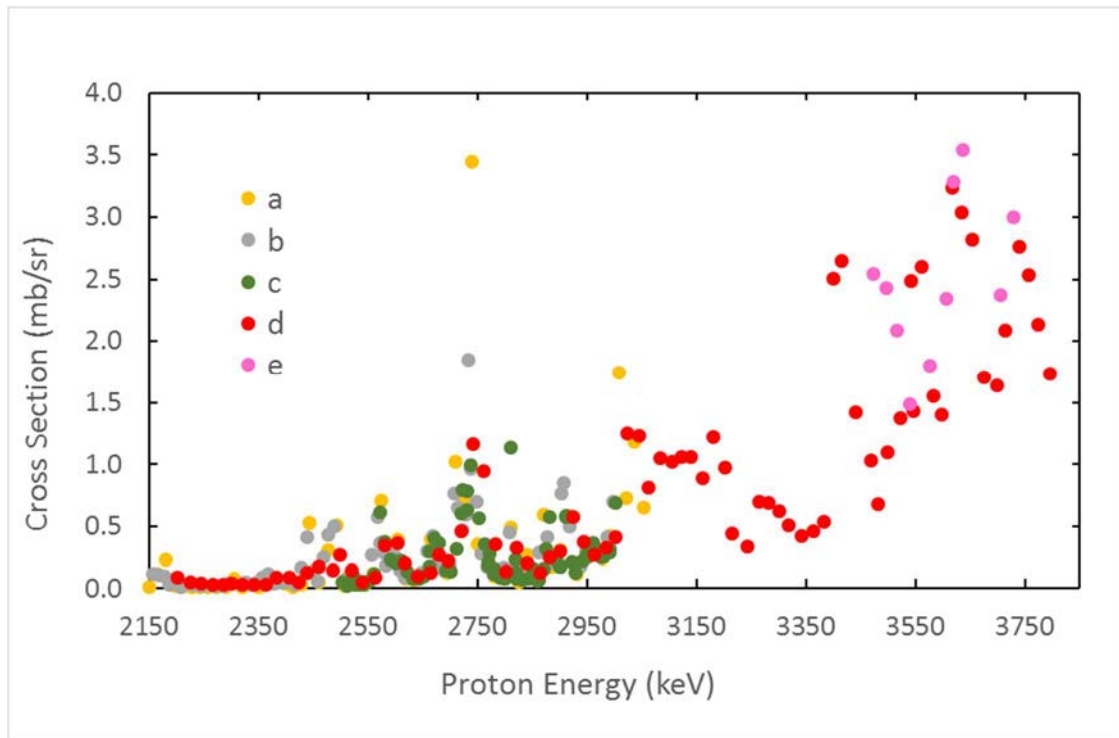


FIG. 4.74 Comparison of cross-sections for the 1369 keV γ -ray from the $^{27}\text{Al}(p,\alpha)^{24}\text{Mg}$ reaction as a function of proton energy in the range of 2150 – 3800 keV. Data obtained within the CRP are, from a to c, the same as for Fig. 4.73, while previous results are obtained from: d) [4.5] (90°) and e) [4.104] (90°).

(c) Conclusions

From the results above, it can be concluded that it is essential to use an adequate energy step and appropriate target thickness, in order to obtain a detailed excitation function of a nuclear reaction. As it stands, it is not possible to employ the results shown above for new and old measurements for PIGE analysis.

(d) Other γ -ray lines

Although the $^{27}\text{Al}(p,\gamma)^{28}\text{Si}$ reaction produces several γ -rays that have been thoroughly studied, most of the published results refer to resonance strengths. There is one exception: the work by Harissopoulos *et al.* [4.105] (available in IBANDL), which provides γ -ray yields corresponding to a combined γ -ray measurement. In order to convert these yields to an individual γ -ray producing cross-section at a particular angle, one must use branching ratios and angular distributions. For analysis of in-depth homogeneous samples, there is no advantage in using this reaction since the cross-sections are much lower than the inelastic scattering cross-sections. Furthermore, the lowest energy γ -ray line that can be extracted is 1779 keV, which is more energetic than the other widely used (p,p' γ) γ -ray lines and therefore has a lower detection efficiency. However, the (p, γ) cross-section has very narrow resonances that have often been used for depth analysis or profiling, e.g. the resonance at 991.92 keV, which is used as a reference resonance for accelerator calibration.

4.9.2. Thick target yields

4.9.2.1. $^{27}\text{Al}(p,p\gamma_{1-0})^{27}\text{Al}$: 844 keV γ -ray

(a) New measurements

Thick-target yields were also obtained during this CRP, at the same laboratories and using the same experimental conditions referred in previous sections. Thick-target yield results depend on the absolute value of the collected charge, on the detector efficiency and on the collected gamma-ray yield. Hence, the uncertainty budget presented in Table 4.29 is to be expected.

TABLE 4.29. UNCERTAINTY BUDGET FOR THE THICKE-TARGET YIELD MEASUREMENTS OF Al

| Quantity | Uncertainty |
|--|-------------|
| γ -ray peak area | 1% |
| γ -ray detector efficiency | 6% |
| Absolute value of the collected charge | 10% |
| Overall uncertainty | 12% |

Results pertaining to the emitted yield per steradian of a pure aluminum target are shown in Fig. 4.75. In the case of the CTN/IST laboratory [4.78], yields were also measured for (a) Al_2TiO_5 and (b) Al_2O_3 , both of which were then converted to 100% Al, taking into consideration the stoichiometry and the stopping power. These converted yields are in agreement with the ones obtained for (c) a pure Al target.

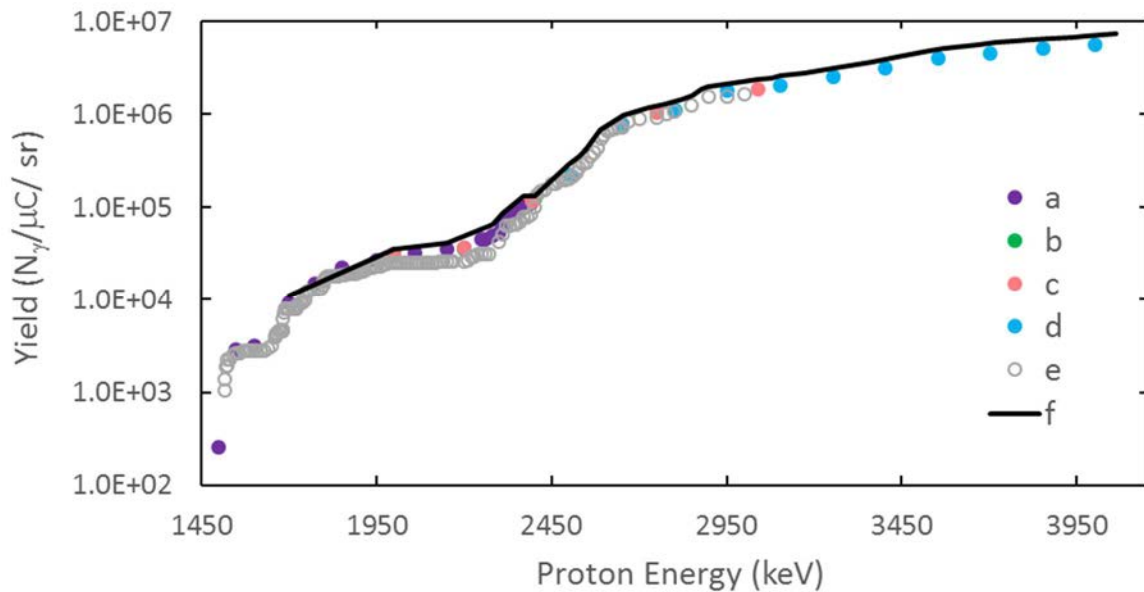


FIG. 4.75. Thick target yields corresponding to the 844 keV γ -line of the $^{27}\text{Al}(p,\gamma_{1-0})^{27}\text{Al}$ reaction, emitted by a pure Al target, as a function of proton energy. Data obtained from the CRP: a) measurements performed with Al_2TiO_5 and then converted to 100% Al [4.78], b) measurements performed with Al_2O_3 and then converted to 100% Al [4.78], c) measurements with a pure Al target [4.78], d) [4.101], e) [4.103] and f) calculated thick target yield obtained from a combination of measured cross-sections (see text).

In the common energy range, Jesus *et al.* [4.78] values are in agreement with Chiari *et al.* values [4.101] within 5%. Jokar *et al.* [4.103] data are lower by 15 to 25% than [4.78] below 2.5 MeV and around 15% lower than [4.101] near 3 MeV. The discrepancy with [4.78] may be, in part, due to a mismatch of the energy scales, as indicated in Fig. 4.75. Chiari *et al.* have also obtained yields at 0° and 45° . Considering that the uncertainty of the yields, at a given angle relative to the yields at other angles, depends only on the relative uncertainty of the detection efficiency of the different detectors, these measurements can be considered to be in agreement, as expected for an isotropic line.

A combined excitation function was produced by adopting the cross-sections of Jesus *et al.* [4.78] up to 3.0 MeV and those of Chiari *et al.* [4.101] from 3 to 4.1 MeV (Figs. 4.67–4.69). This combined excitation function was introduced in the ERYA code (for details see Section 5) in order to obtain thick-target yields for a pure aluminum target, from 1.5 to 4.1 MeV proton energy. These results are also shown as a solid black line in Fig. 4.75. As can be seen from the figure, the calculated yields agree with the experimental results within the experimental uncertainties.

(b) Data in the literature

Several previous measurements of thick-target yields were found. The ones of Anttila *et al.* [4.1] and Kiss *et al.* [4.2] were included in the Handbook of Ion Beam Analysis [4.106]. These results, together with the ones by Deconninck *et al.* [4.107], are now in the IBANDL database. Figure 4.76 displays these previous results with the ones measured in this CRP. Deconninck's results seem to lay in-between the results from [4.78] and the results below 2.5 MeV from [4.103]. They are 15% higher than [4.103] around 3 MeV and are in agreement with [4.101]. Kiss *et al.* [4.2] results at 2.4 MeV are 18% higher than the results from [4.78]

(or there is an energy scale mismatch) and at higher energies his results are 10% higher than the ones by [4.101]. The result from Anttila [4.1] at 1.7 MeV is 10% higher than the [4.78] value.

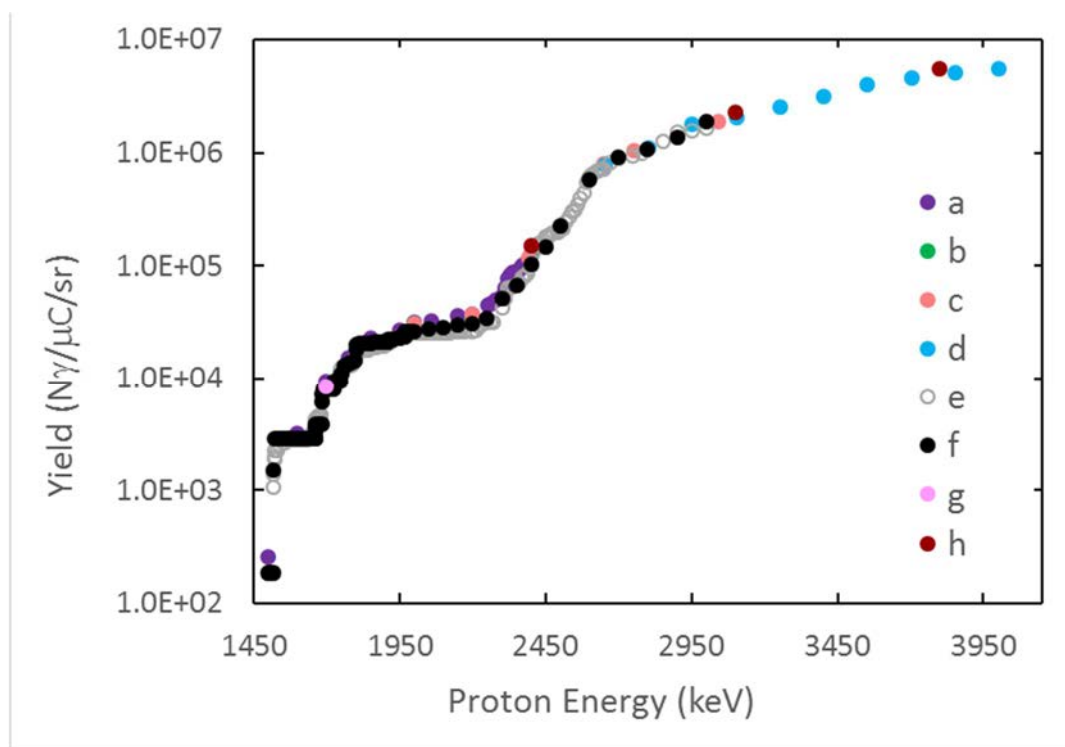


FIG. 4.76. Thick target yields corresponding to the 844 keV γ -line, emitted by a pure Al target as a function of proton energy. Data obtained in this CRP (from a to e, the same as for Fig. 4.75) and from the literature: f [4.107], g [4.1] and h [4.2].

(c) Recommended data

Taking into consideration the uncertainty of the yield results mentioned above, all new and old thick-target yield results are within reasonable agreement, apart from possible discrepancies in the energy scale. Hence they may be used as supplementary information in PIGE analysis of Al, by providing (i) data for a PIGE system calibration, (ii) data for the determination of $E_{1/2}$, i.e. the energy at which the yield is half of that obtained at incident energy, and (iii) an indication of the yield to be expected.

4.9.2.2. $^{27}\text{Al}(p,p\gamma_{2-0})^{27}\text{Al}$: 1014 keV γ -ray

(a) New measurements

The same experiments that measured the yields of the 844 keV γ -ray line also measured the yields of the 1014 keV γ -ray line. The comparison of the results shown in Fig. 4.77 leads to similar conclusions as in the previous paragraphs. The data from Jokar *et al.* [4.103] are lower than data from Jesus *et al.* [4.78] and Chiari *et al.* [4.101], although overall there is slightly better agreement than in the case of the 844 keV γ -ray line. To be more precise, the data of [4.103] are lower by 15% compared to [4.78], for data below 2.5 MeV, and around 5% lower than [4.101] around 3 MeV. Again, the discrepancy with [4.78] values may be partly due to a mismatch of the energy scales.

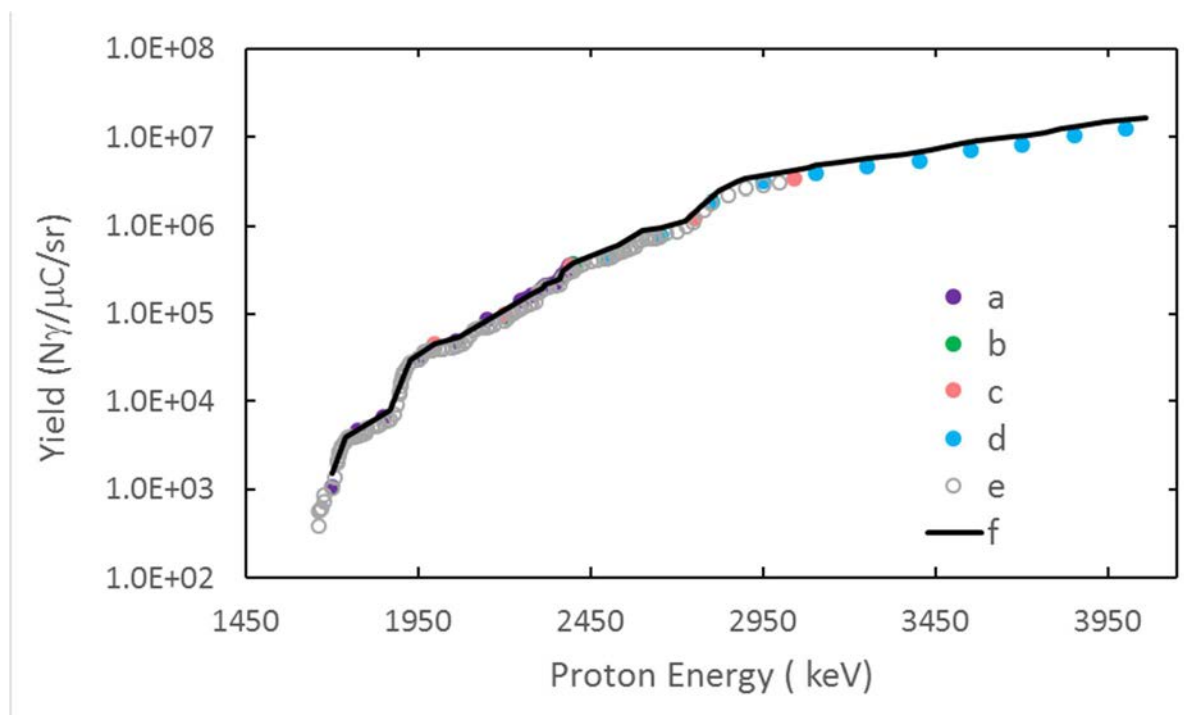


FIG. 4.77. Same as in Fig. 4.75, but for the 1014 keV γ -line, emitted by a pure Al target as a function of proton energy.

Chiari *et al.* [4.101] have also measured the yields at 0° and 45° . These thick-target yield data are in good agreement with the ones at 90° , indicating that any anisotropy related to the 1014 keV γ -ray line is small.

A combined excitation function consisting of data from Jesus *et al.* [4.78], up to an energy of 3.0 MeV, and data from [4.101], at energies from 3 to 4 MeV (Figs. 4.67–4.69), was introduced in the ERYA analysis code (see Section 5 for details) in order to obtain thick-target yields for a pure aluminum target, for an energy range from 1.6 to 4.1 MeV. These results are also shown in Fig. 4.77 as a solid black line. The agreement with the experimental results is within the experimental uncertainties.

(b) Data in the literature

Several previous measurements of thick-target yields for the 1014 γ -ray line were found. The data of Kiss *et al.* [4.2] were included in the Handbook of Ion Beam Analysis [4.106]. These results, together with the data of Deconninck *et al.* [4.107] and Savidou *et al.* [4.17], are available in the IBANDL database. Figure 4.78 shows a comparison of these previous thick-target yield data with the data measured in this CRP.

Similar conclusions to those regarding the 844 keV γ -ray line may be drawn from the results of Kiss *et al.* [4.2]. The data of Deconninck *et al.* [4.107] are now lower than the data of Jokar *et al.* [4.103] by around 15%, for energies lower than 2050 keV; however they converge at higher energies. The data of Savidou *et al.* [4.17] are in good agreement with the data of Jesus *et al.* [4.78] at low energy, however they become increasingly higher than the data of Chiari *et al.* [4.101] with increasing proton energy (10 % at 3 MeV and 25% at 4 MeV).

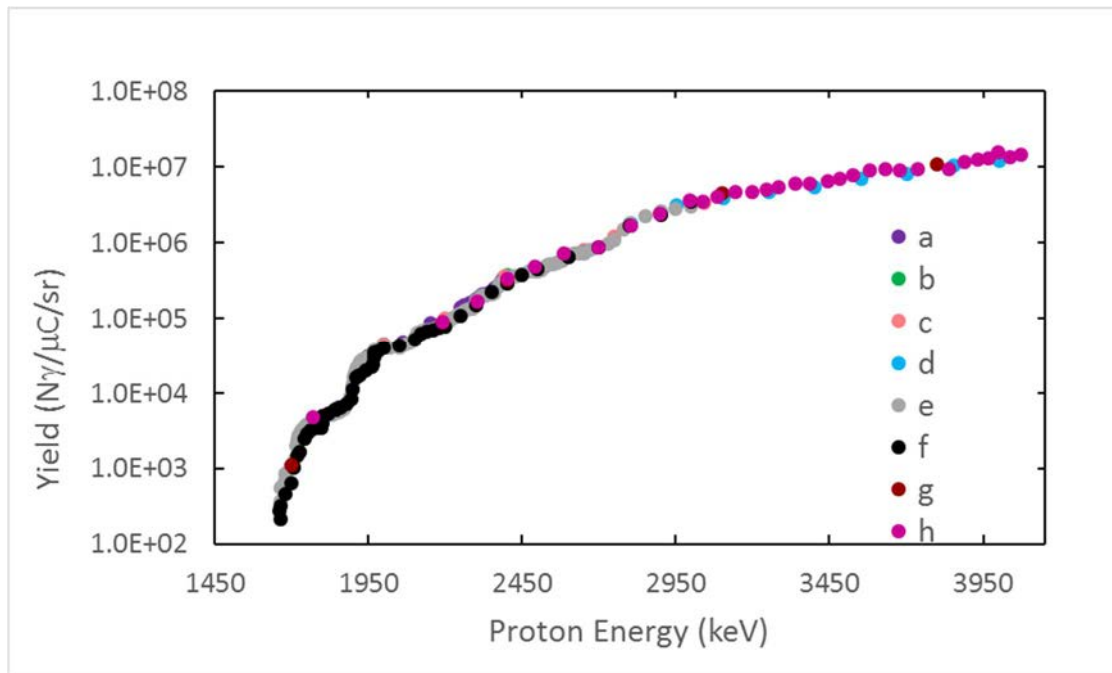


FIG. 4.78. Thick target yields corresponding to the 1014 keV gamma-line, emitted by a pure Al target as a function of proton energy. Data obtained in this CRP are from a to e, the same as for Fig. 4.77, and previous measurements from: f) [4.107] (90°), g) [4.2] (55°) and h) [4.17] (90°).

(c) Recommended data

The same conclusions drawn for the 844 keV γ -ray line apply here.

4.9.2.3. $^{27}\text{Al}(p, \alpha\gamma_{1-0})^{24}\text{Mg}$: 1369 keV γ -ray

(a) New measurements

Along with determining yields related to the 844 and 1014 keV γ -lines, two of the laboratories also determined yields of the 1369 keV γ -line (Fig. 4.79). Within the energy range 2500–2800 keV, results from Jokar *et al.* [4.103] are around 10% lower than the results from Chiari *et al.* [4.101], however the discrepancy rises to 26% at 2950 keV.

Cross-section data were combined to produce an excitation function for the $^{27}\text{Al}(p, \alpha\gamma)^{24}\text{Mg}$ reaction which was then introduced in the ERYA code (see Section 5) in order to obtain thick-target yields for a pure aluminum target, from 1.7 to 3.05 MeV proton energy. The combined data used the measurements of [4.102] for energies up to 2.940 MeV and of Zamboni *et al.* [4.79] from 2.940 MeV up to 3.05 MeV (Fig. 4.73 and as a solid black line in Fig. 4.79). The ERYA values are larger than the measured thick-target yields from [4.103] by 50–80% in the region from 1.8 to 2.4 MeV. From 2.4 MeV, this difference decreases with increasing energy. From 2.6 MeV, ERYA calculated yields agree with the ones measured by [4.101] within 10%.

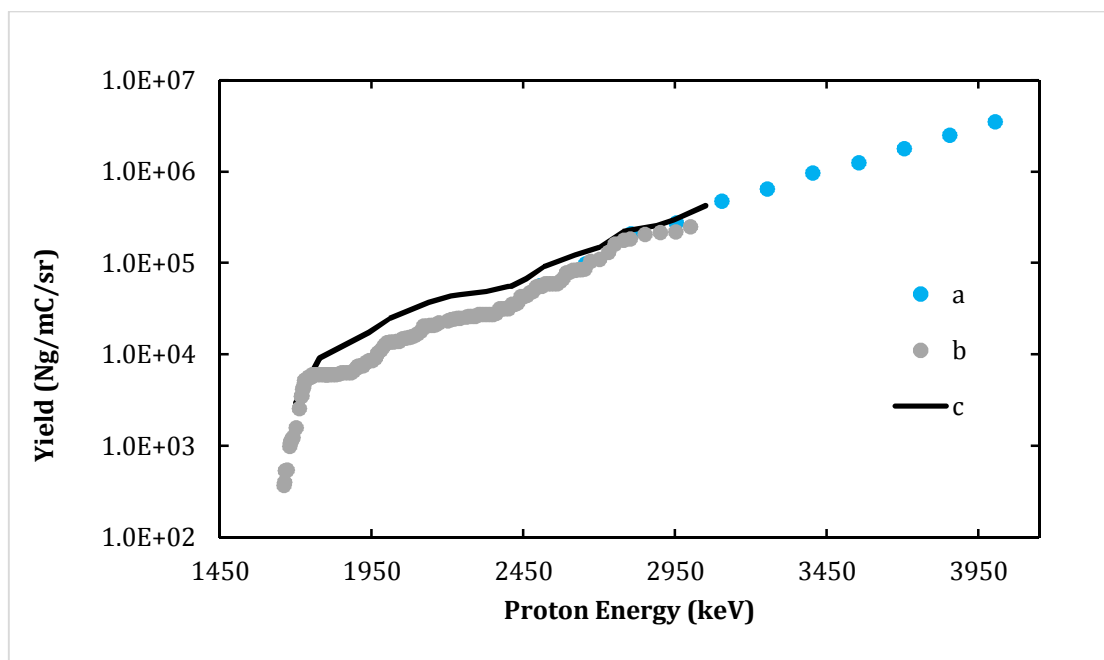


FIG. 4.79. Thick target yields per steradian corresponding to the 1369 keV γ -line, emitted by a pure Al target as a function of proton energy. Data obtained in this CRP: a) [4.101] (45°), b) [4.103] (90°), and c) calculated thick target yield using the ERYA code (see text and Section 5 for more details).

(b) Data in the literature

Several previous measurements were found in the literature. The thick-target yields of Anttila *et al.* [4.1] and Kiss *et al.* [4.2] have been included in the Handbook of Ion Beam Analysis [4.106]. These results together with results of Deconninck *et al.* [4.107] are also available in the IBANDL database. In Fig. 4.80, the previous results are compared with the new measured thick-target yields.

The results in Fig. 4.80 suggest that, at energies lower than 2000 keV, there is a difference in energy scale between Deconninck *et al.* [4.107] and Jokar *et al.* [4.103] of about +20 keV, which decreases with energy. The results of Anttila [4.1] and Kiss *et al.* [4.2] at 2400 keV agree with the data of [4.103], if a +10 keV is applied to Jokar's energy scale (or -10 keV to the one of Anttila and Kiss). Kiss's result [4.2] at 3100 keV is 20% higher than Chiari's [4.101], but there is fair agreement at 3800 keV.

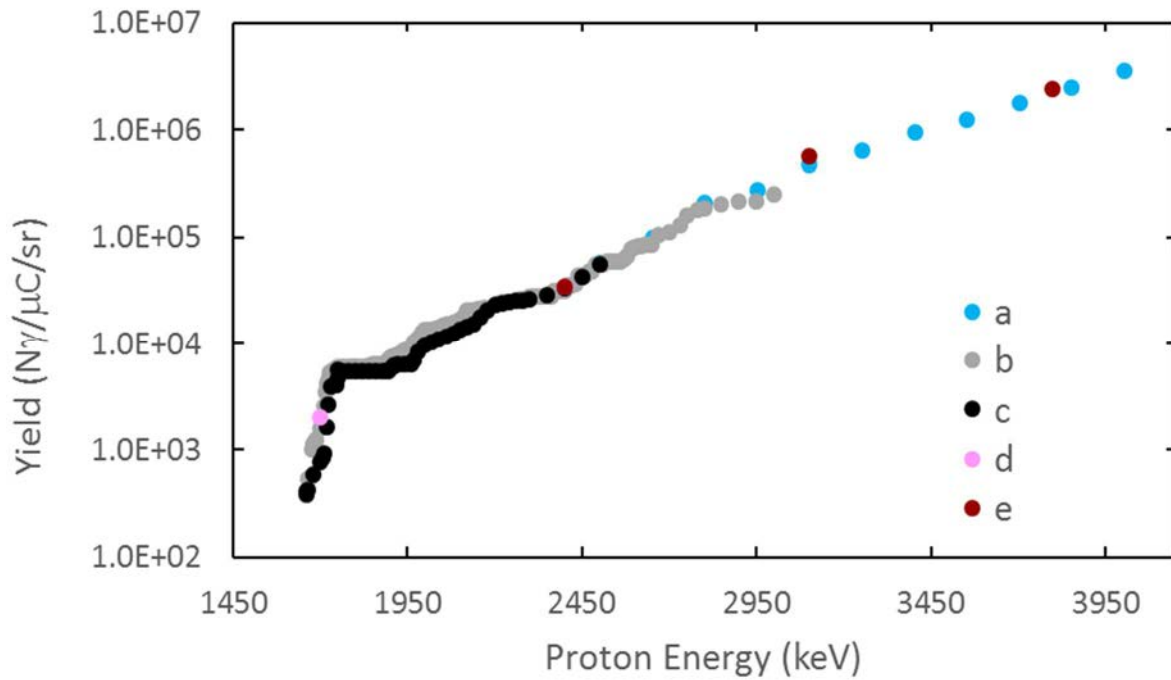


FIG. 4.80. Thick target yields corresponding to the 1369 keV γ -line emitted by a pure Al target as a function of proton energy. Data obtained in this CRP a) [4.101] (45°), b) [4.103] (90°) and found in the literature c) [4.107] (90°), d) [4.1] (55°) and e) [4.2] (55°).

(c) Conclusions

The discrepancy between ERYA (see Section 5) calculated yields and the results from Jokar *et al.* [4.103], at energies between 1.8 and 2.4 MeV, point to an overestimation of the measured cross-sections measured by [4.102]. Although it is not recommended, if a standardless PIGE analysis is performed with the help of this γ -ray line, this overestimation should be taken into account.

Nevertheless, in spite of the above remarks, due to the fair agreement among new and old yield results, these measurements are still useful for PIGE analysis of Al as they provide (i) values for a PIGE system calibration, (ii) a determination of $E_{1/2}$, i.e. the energy at which the yield is half of the one obtained at incident energy, and (iii) an indication of the yield to be expected.

(d) Summary remarks

The following is a summary of the main findings for the individual γ -ray lines mentioned in the previous sections:

- Good agreement between the new and previous measurements of cross-section values for the 844 and 1014 keV γ -ray lines of the $^{27}\text{Al}(p,p'\gamma)^{27}\text{Al}$ nuclear reaction;
- Fair agreement between calculated values of combined excitation functions, which are obtained from [4.78] for values between 1490 to 3000 keV and from [4.101] for values between 3000 to 4100 keV, with measured thick-target yields relative to the same γ -lines;
- Possibility to perform PIGE analysis by inserting these composed excitation functions into a PIGE analysis code such as ERYA (see Section 5) or other similar codes.

From these findings, it can be concluded that there is sufficient consistent experimental information available for these γ -ray lines in order to perform a complete and comprehensive theoretical evaluation.

4.10. SILICON

4.10.1. Gamma-ray production cross-sections of silicon from proton-induced nuclear reactions

Silicon can be analysed by the PIGE technique by employing either the $^{28}\text{Si}(p,p'\gamma)^{28}\text{Si}$ reaction or the $^{29}\text{Si}(p,p'\gamma)^{29}\text{Si}$ reaction, which produce the 1779 keV and 1273 keV γ -rays, respectively. Within the frame of this CRP, new measurements were performed to determine cross-section data for silicon analysis via PIGE, as well as the corresponding thick-target γ -ray yields. All the new data, as well as the older data found in the literature, have been uploaded in IBANDL.

4.10.1.1. $^{28}\text{Si}(p,p'\gamma)^{28}\text{Si}$: 1779 keV γ -ray and $^{29}\text{Si}(p,p'\gamma)^{29}\text{Si}$: 1273 keV γ -ray

New measurements in the energy range of 3.6 – 6.9 MeV

Cross-sections for the proton-induced nuclear reactions of $^{28}\text{Si}(p,p'\gamma)^{28}\text{Si}$ and $^{29}\text{Si}(p,p'\gamma)^{29}\text{Si}$ have been determined in the proton energy range 3.6–6.9 MeV, at a detection angle of 55° [4.63]. The proton beam was generated by the 5 MV belt-driven tandem accelerator of the University of Helsinki. The $^{14}\text{N}(p,p'\gamma)^{14}\text{N}$ reaction with resonances at 3903, 3996, and 5937 keV were exploited in the calibration of the absolute proton beam energy at 4–6 MeV, with precision better than 1 keV. The calibration procedure is described in detail in [4.65]. The γ -rays were detected with a 38% efficient HPGe germanium detector positioned 20 mm from the target. The detection angle was fixed to 55° relative to the beam direction. The absolute efficiency curve for the detector was determined by using Eu-152, Co-60 and Co-56 calibration sources placed at the position of the target. For more experimental details, such as charge collection and target preparation, see Section 4.5.1. The same thin self-supporting Si_3N_4 membrane targets were used as in the corresponding nitrogen cross-section measurements.

The selected membrane thickness of 100 nm was chosen to ensure sufficient counting rate of the γ -ray detector and still enable the membrane to be considered a thin target for the present experiments. The estimated energy loss of 4 MeV protons in the Si_3N_4 target is ~ 2.5 keV and the energy straggling is ~ 3 keV, based on SRIM calculations. The sample composition and areal densities were determined by ERDA.

The reaction excitation functions were measured with energy steps of 100 keV, except for the energy regions provided in Table 4.30, where the energy steps were narrower. The collected charge for each measurement point was ~ 12 μC . Carbon buildup at the membrane surface was regularly checked for and reduced by frequently changing the irradiation spot on the membrane.

TABLE 4.30. MEASURED ENERGY POINTS FOR THE MEASURED CROSS-SECTIONS OF 1779 keV $^{28}\text{Si}(p,p'\gamma)^{28}\text{Si}$ AND 1273 keV $^{29}\text{Si}(p,p'\gamma)^{29}\text{Si}$

| Energy interval (MeV) | Energy step (keV) |
|-----------------------|-------------------|
| 3.871 - 4.016 | 5 |
| 4.016 - 4.086 | 10 |
| 4.850 - 4.960 | 10 |
| 4.960 - 5.380 | 30 |
| 5.540 - 5.600 | 10 |
| 5.912 - 5.957 | 5 |
| 6.110 - 6.192 | 20 |
| 6.540 - 6.840 | 20 |

The obtained cross-section data are presented in Figs. 4.81 and 4.82. The possible sources of error in the cross-section values are:

- Absolute efficiency of the γ -ray detector. This is mainly due to the uncertainties of the calibrated radioactive source activities;
- Determination of the absolute value of the collected charge. Despite appropriate electron suppression, systematic deviations may occur;
- The determination of the target atomic thickness by ERDA;
- Accuracy of available stopping power data as provided by SRIM.

The uncertainty budget is summarized in Table 4.31.

TABLE 4.31. UNCERTAINTY BUDGET OF CROSS-SECTION MEASUREMENTS OF 1779 keV $^{28}\text{Si}(p,p'\gamma)^{28}\text{Si}$ AND 1273 keV $^{29}\text{Si}(p,p'\gamma)^{29}\text{Si}$

| Quantity | Uncertainty |
|---|--------------------------------------|
| Beam energy spread | ~2.5 keV |
| Energy straggling in target | ~3 keV |
| Charge collection | 3 % |
| Peak unfolding including dead time correction | 1.5% at resonance; 3 % off-resonance |
| Detection efficiency x solid angle | 5 % |
| Target stoichiometry | 0.5% |
| Cross-section uncertainty: | 10% at resonance; 13% off-resonance |

The proton-induced thick-target γ -ray yields were measured at an angle of 55° relative to the beam direction at 4.0, 4.5, 5.0, 5.5, 6.0 and 6.5 MeV using a thick Si_3N_4 target. In the thick-target yield measurements, the collected charge was measured directly from the sample using electron suppression. The uncertainty budget of the thick-target γ -ray yield measurements is provided in Table 4.32.

TABLE 4.32. UNCERTAINTY BUDGET OF THICK-TARGET YIELD MEASUREMENTS OF 1779 keV $^{28}\text{Si}(p,p'\gamma)^{28}\text{Si}$ AND 1273 keV $^{29}\text{Si}(p,p'\gamma)^{29}\text{Si}$

| Quantity | Uncertainty |
|---|-------------|
| Charge collection | 6% |
| Peak unfolding including dead time correction | 1% |
| Detection efficiency x solid angle | 5% |
| Target stoichiometry | 0.5% |
| Thick-target yield uncertainty | 10% |

(a) New measurements in the energy range of 2.0 – 3.2 MeV

In the framework of this CRP, differential cross-sections for γ -ray emission from the $^{28}\text{Si}(p,p'\gamma)^{28}\text{Si}$ ($E_\gamma = 1779$ keV) and the $^{29}\text{Si}(p,p'\gamma)^{29}\text{Si}$ ($E_\gamma = 1273$ keV) nuclear reactions were measured in the energy range of 2.0–3.2 MeV and 2.0–3.0 MeV, respectively, by Jokar *et al.* [4.108]. The experiments were performed using the 3 MV Van de Graaff accelerator of the Nuclear Science and Technology Research Institute (NSTRI) in Tehran. The excitation functions were measured with energy steps of 1–2 keV in resonance regions and variable energy steps of 10–40 keV in off-resonance regions. The proton beam energy was calibrated using the 991.9 keV resonance of the $^{27}\text{Al}(p,\gamma)^{28}\text{Si}$ reaction and the 1880.4 keV threshold energy of the $^7\text{Li}(p,n)^7\text{Be}$ reaction. Gamma-rays were detected by a 50% P-type HPGe detector located at 90° with respect to the incident beam direction at a distance of 51.9 mm from the target center and subtending an angle of 65° . The absolute efficiency curve of the γ -ray detector was determined using ^{133}Ba , ^{152}Eu , ^{137}Cs , ^{60}Co and ^{241}Am calibration radioactive sources, which were placed at the exact position of the target. Backscattered protons were detected simultaneous with γ -rays using an ion implanted Si detector placed at a scattering angle of 165° , with a solid angle of 0.746 msr. The targets were created from two films of natural SiO evaporated onto thin self-supporting Ag layers. The stoichiometry and the thickness of the target films were determined by RBS measurements with a 2 MeV alpha-beam. By simulation of the RBS spectra with the SIMNRA code, composition of the SiO layer was found to be 45% natural Si and 55% O. The thickness of the SiO film of the first target was found to be 25.6 ± 1.8 $\mu\text{g}/\text{cm}^2$. The first target was used in the 2.0–3.0 MeV incident beam energy range, while the second one, consisting of 53 ± 4 $\mu\text{g}/\text{cm}^2$ SiO, was employed in the beam energy range of 3.0–3.2 MeV. Based on SRIM calculations, the proton beam energy loss in SiO layers was found to be 4.3–3.2 keV and 6.5–6.2 keV for the first and second targets, respectively. The target was oriented inside the reaction chamber so that the incident beam direction made an angle of 45° with respect to the normal of the target. The accumulated beam charge was chosen to be between 5 and 400 μC at each energy point, depending on the statistics. In this way, statistical errors in the on-resonance and off-resonance regions were found to be 1–3% and 5–10%, respectively. In order to remove large systematic uncertainty due to the direct measurement of absolute value of the collected beam charge, RBS of the Ag film was used for normalization of the cross-sections. To avoid excessive carbon build up on target, the beam spot position was changed by fine adjustment of target location several times during the measurements. The systematic uncertainty budget is summarized in Table 4.33.

TABLE 4.33. SYSTEMATIC UNCERTAINTY BUDGET: CROSS-SECTION MEASUREMENTS OF THE 1779 keV $^{28}\text{Si}(p,p'\gamma)^{28}\text{Si}$ AND 1273 keV $^{29}\text{Si}(p,p'\gamma)^{29}\text{Si}$

| Quantity | Uncertainty |
|--|-------------|
| The γ -ray detector absolute efficiency | 7% |
| The stoichiometric ratio | 4% |
| Particle detector solid angle | 2.8% |
| Rutherford cross-section on Ag | 1% |
| Cross-section uncertainty | 9% |

The thick target γ -ray yields for the $^{28}\text{Si}(p,p'\gamma)^{28}\text{Si}$ ($E_\gamma = 1779$ keV) and the $^{29}\text{Si}(p,p'\gamma)^{29}\text{Si}$ ($E_\gamma = 1273$ keV) nuclear reactions were also measured at the laboratory angle of 90° , from 2.38–3.0 MeV in 10 keV energy steps and 2.2–3.0 MeV with 10 keV energy steps, respectively [4.103]. The target was a thick Si plate, in a single-element form. Additionally, a 70×10^{15} atoms/cm² Au layer was evaporated on the surface of the target in order to measure the collected charge. The experiments were performed in the same experimental set-up used for cross-section measurements. The uncertainty budget of the thick-target γ -ray yields is presented in Table 4.34.

TABLE 4.34. UNCERTAINTY BUDGET: THICK-TARGET YIELD MEASUREMENTS OF 1779 keV $^{28}\text{Si}(p,p'\gamma)^{28}\text{Si}$ AND 1273 keV $^{29}\text{Si}(p,p'\gamma)^{29}\text{Si}$

| Quantity | Uncertainty |
|--|-------------|
| Charge collection | 3% |
| The gamma-ray detector absolute efficiency | 7% |
| Stopping power | 4% |
| Thick-target yield uncertainty | 9% |

(b) Data in the literature and assessment

The available PIGE cross-section data in the literature for silicon is scarce. Only the studies of Dyer *et al.* [4.52] and Boni *et al.* [4.5] can be found for the energy range covered by the present differential cross-section measurements. The values of Jokar *et al.* are for proton energies below 3.2 MeV [4.108]. The available previous cross-section values, together with the present values for the reaction $^{28}\text{Si}(p,p'\gamma)^{28}\text{Si}$, are shown in Fig. 4.81. When comparing the different data sets, it should be kept in mind that the associated angular distributions of the γ -rays are not isotropic [4.52]. The data of [4.5] and [4.108] are differential cross-section values obtained at specific detection angles and in Fig. 4.81, the data have been plotted as total cross-section values, taking into account the appropriate angular distribution determined by [4.52].

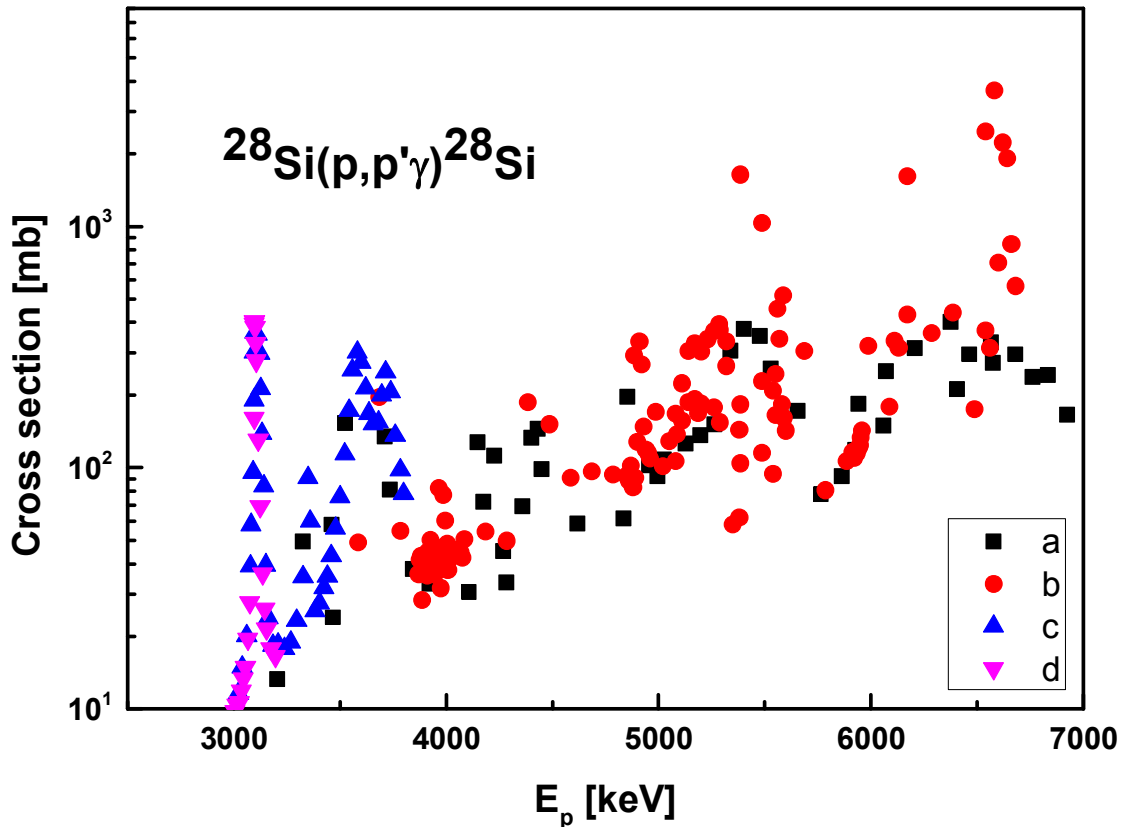


FIG. 4.81. Cross-sections for production of 1.78 MeV γ -rays from the reaction $^{28}\text{Si}(p,p'\gamma)^{28}\text{Si}$ as a function of proton energy. Data obtained from: a) [4.52], b) [4.63] (55°), c) [4.5] (90°), and d) [4.108] (90°).

The work of Dyer *et al.* [4.52] covers the proton energy range from 3 MeV to 23 MeV. In this study, the γ -ray angular distribution was determined by measuring yields at several detection angles and by fitting them with a series of Legendre polynomials. The estimated uncertainty in the Dyer *et al.* cross-section values is 15% for proton energies below 5 MeV and 10% for values above 5 MeV. The experimental points are in reasonable agreement with the other data, in the lower part of the energy range. Within the energy range 4.4–5.1 MeV, the values of Dyer *et al.* are clearly lower than the new data of Marchand *et al.* [4.63]. In the high energy region, the agreement becomes better.

In the study of Boni *et al.* [4.5], cross-section data is provided for the energy range 2.2 – 3.8 MeV, measured at a 90° angle [4.5], with energy steps of 20 keV. The data points of [4.63], in the overlapping energy region, are in reasonable agreement with those of Boni *et al.* A shift of 30–35 keV in the proton energy would yield completely overlapping data points.

The present values of [4.108] range from 2 MeV to 3.2 MeV proton energy. The data has been collected at a detection angle of 90° . A detailed comparison between the values of this study and those of Boni *et al.* can be found in the original article by Jokar *et al.* [4.108].

The comparison shows that, in the proton energy range of 3.0–3.2 MeV, there is a very good agreement between the measured cross-section values of [4.108] and those of Boni *et al.*

However, due to using thinner target and smaller energy steps in the resonance region, the obtained resonance in the present data [4.108] is sharper than results from Boni *et al.* [4.5].

Except for the 1.78 MeV γ -line produced by ^{28}Si , no other cross-section data for proton reactions with silicon, within the presently considered energy range, are available in the literature.

The present data for the $^{29}\text{Si}(p,p'\gamma)^{29}\text{Si}$ reaction is shown in Fig. 4.82. The data of [4.108] are differential cross-section values obtained at a 90° detection angle. The data has been plotted in Fig. 4.82 as total cross-section values, assuming isotropic angular distribution.

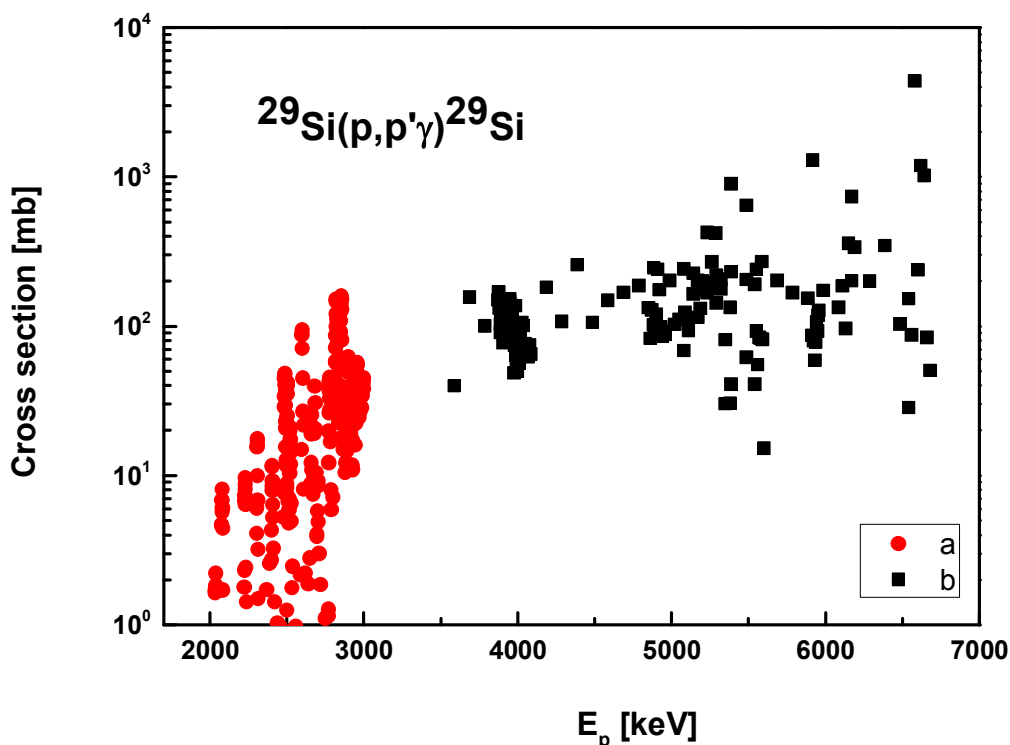


Fig. 4.82. Cross-sections for production of the 1.27 MeV γ -rays from the reaction $^{29}\text{Si}(p,p'\gamma)^{29}\text{Si}$ as a function of proton energy. Data obtained within CRP: a) [4.108] (90°) and b) [4.63] (55°).

Even though PIGE analysis of silicon is solely based on the isotopes of ^{28}Si and ^{29}Si , depth profiling of silicon by nuclear reaction resonances is typically carried out by utilizing the ^{30}Si isotope and the $E_p = 620$ keV resonance of the $^{30}\text{Si}(p,\gamma)^{31}\text{P}$ reaction [4.109–4.111].

4.10.2. Thick target yields

For silicon, the following individual thick-target γ -ray yield data points are available in the literature: at 2.4 MeV [4.1], 3.1 and 3.8 MeV [4.2], 7 MeV [4.3], 3.05–4.09 MeV [4.17] and 2.65 – 4.13 MeV [4.112]. A more systematic approach has recently been taken by Jokar *et al.* with yield values measured from 2.2 MeV to 3 MeV with energy steps of 10 keV [4.108]. In the work of Marchand *et al.* [4.63], additional points have been obtained at 4.0, 4.5, 5.0, 5.5, 6.0 and 6.5 MeV. In Fig. 4.83, the present yield values for silicon are compared with available literature data. The data of [4.2], [4.3] and [4.1] have been obtained at an angle of 55° (as is the case of data from [4.63]), the data of [4.112] at angles of 0° , 45° , 90° and those of [4.17]

and [4.108] at 90° . It should be noted that, in this case, the yields can be very anisotropic and the comparison between the values is only indicative. The yields calculated from the measured differential cross-sections shown in Figs. 4.81 and 4.82 have not been included in the comparison, since the measured excitation functions have missed the narrow resonances and therefore provide only rough estimates.

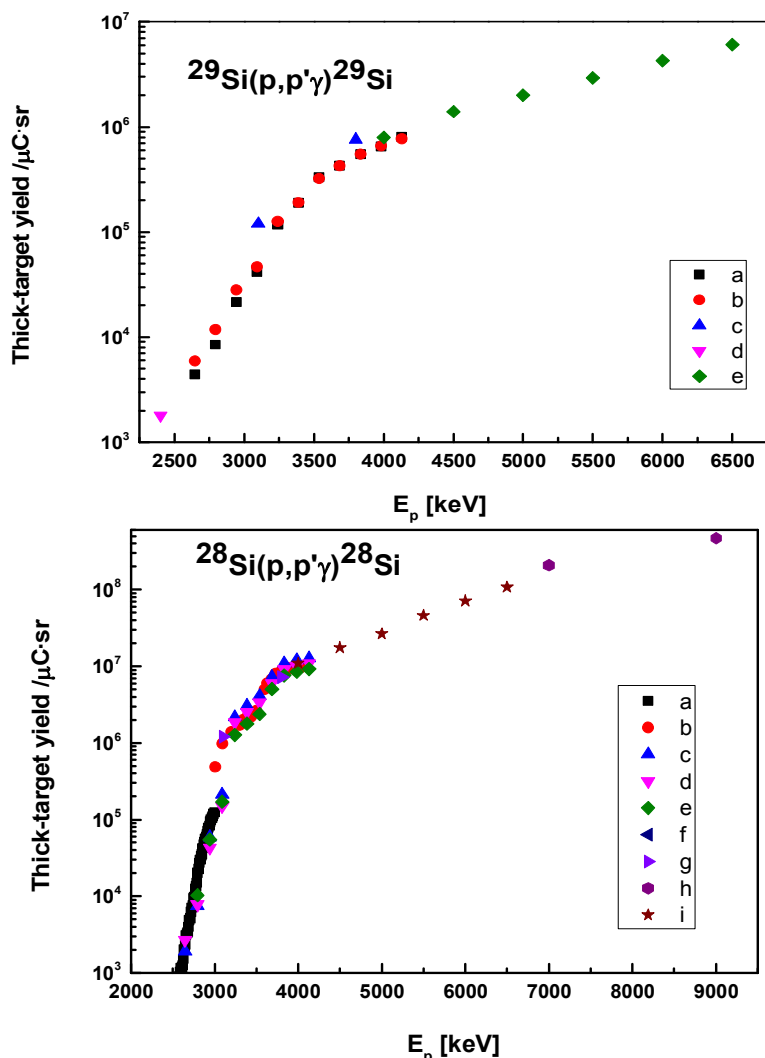


FIG. 4.83. Comparison of the measured thick-target yields with available previous literature data corresponding to natural isotopic abundance as a function of proton energy. Upper figure illustrates the γ -ray line 1779 keV from the reaction $^{28}\text{Si}(p,p'\gamma)^{28}\text{Si}$: a-b) [4.112] (0° , 45° , 90°), c) [4.2] (55°), d) [4.1] (55°), and e) [4.63] (55°). Lower figure illustrates the 1273 keV line from the reaction $^{29}\text{Si}(p,p'\gamma)^{29}\text{Si}$: a) [4.108] (90°), b) [4.17] (90°), c-e) [4.112] (0° , 45° , 90°), f) [4.1] (55°), g) [4.2] (55°), h) [4.3] (55°) and i) [4.63] (55°).

(c) Recommended data

Both γ -ray lines are suitable for silicon analysis, specifically for detection of the two separate isotopes. Since the excitation curves for both reactions indicate the presence of several narrow resonances, more accurate data obtained with narrow energy steps and good resolution are recommended. The available thick-target yield data is still rather limited.

4.10.3. Gamma-ray production cross-sections of silicon from deuteron-induced nuclear reactions

The deuteron-induced gamma-emission is mainly applied to the analysis of light elements, but it also simultaneously detects silicon. As previous thick-target measurements [4.18] indicate, many states are excited, mainly in the $^{28}\text{Si}(d,p\gamma)^{29}\text{Si}$ reaction, which produces a rather complicated gamma-spectrum even at low deuteron energies. The most intense γ -rays from this reaction are the 1273 keV, 2028 keV, 2426 keV and the 4934 keV from the de-excitation of the 1st, 2nd, 3rd and 10th excited states, respectively, to the ground state. The only available cross-section measurements for these γ -rays were performed in the frame of this CRP [4.113].

(a) New measurements

Differential cross-sections for γ -ray emission from the $^{28}\text{Si}(d,p\gamma)^{29}\text{Si}$ reaction ($E_\gamma = 1273, 2028, 2426$ and 4934 keV) have been determined for deuteron energies ranging from 0.65 to 2.0 MeV, at the detection angle of 55° . The details of the experiment are the same as for nitrogen (see Section 4.5), since the same thin self-supporting Si_3N_4 film target was used [4.113].

The main source of uncertainty was the measured γ -peak area, which varied between 1% and 40% for the silicon γ -lines, depending on the incident deuteron energy and the silicon reaction channel. Average uncertainties of the silicon γ -ray production cross-sections are 12%. The uncertainty budget is presented in Table 4.35.

TABLE 4.35. UNCERTAINTY BUDGET: SILICON ABSOLUTE DIFFERENTIAL CROSS-SECTION VALUES

| Quantity | Uncertainty |
|--|-------------|
| Beam energy spread (keV) | 3 keV |
| Charge determination | 3.0 % |
| N number of target nuclei/cm ² | 2.5 % |
| γ -ray peak area | 1–40 % |
| γ -ray detector absolute efficiency | 2.0 % |
| Uncertainty | 12 % |

The resulting differential γ -ray cross-sections are rather small and have large uncertainties in the measured energy region. Only the 1273 keV and 4934 keV γ -rays are suitable for PIGE analysis.

4.10.3.1. $^{28}\text{Si}(d,p\gamma)^{29}\text{Si}$ reaction: 1273 γ -ray

The cross-sections for the 1273 keV γ -ray from the $^{28}\text{Si}(d,p\gamma)^{29}\text{Si}$ reaction are plotted in Fig. 4.84.

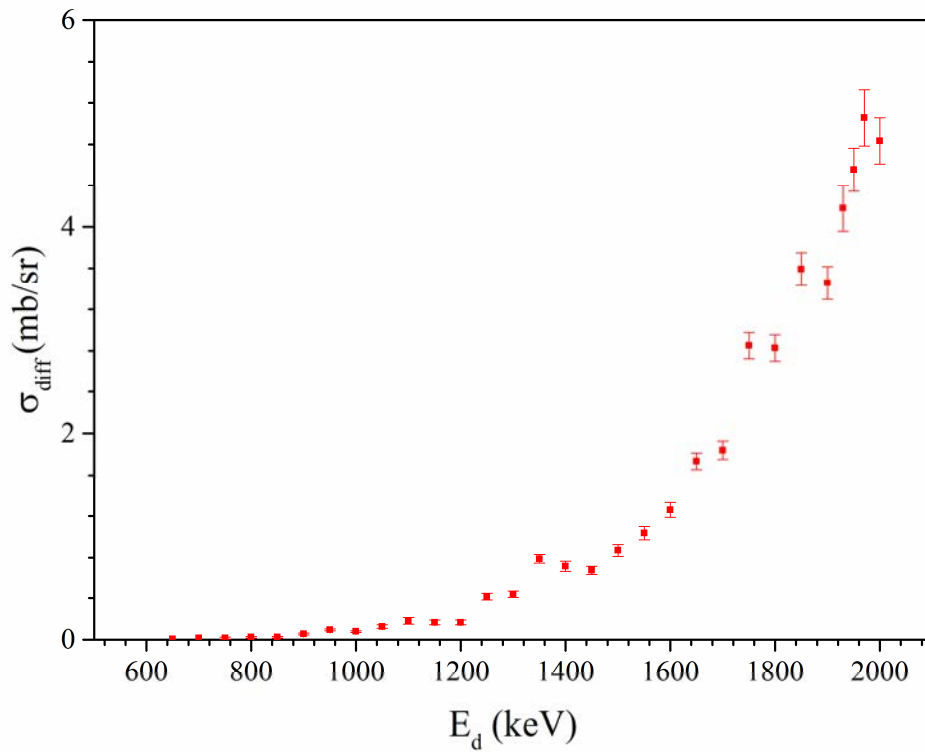


FIG. 4.84. Differential cross-sections of the 1273 keV γ -ray produced by the $^{28}\text{Si}(d,p\gamma)^{29}\text{Si}$ reaction at 55° , as a function of deuteron energy [4.113].

A critical assessment cannot be performed since this is the only existing measured dataset. Yet validation can be performed through a comparison of the calculated yields from the differential cross-section values with the only existing measured thick-target gamma-yield. In Fig. 4.85, a comparison with the thick-target yields of Elekes *et al.* [4.18] is presented. The comparison shows that there is a large discrepancy between the calculated and measured yield data, below 1300 keV. Above 1300 keV, the calculated yields gradually converge with the measured thick-target gamma-yield data. The discrepancy remains within the 15 % uncertainty band of the measured curve in the entire energy range.

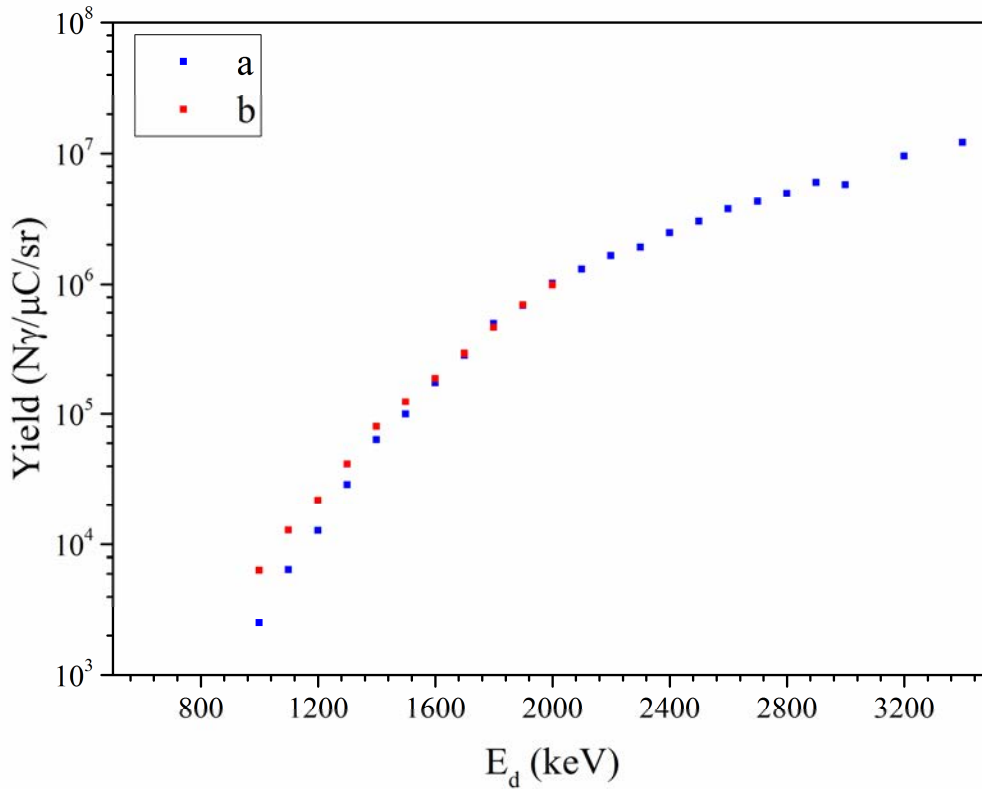


FIG. 4.85. Comparison of the thick target yields of the 1273 keV γ -ray produced by the $^{28}\text{Si}(d,p\gamma)^{29}\text{Si}$ reaction as a function of deuteron energy. Data obtained from a) [4.18] (135°) and b) [4.113] (55°).

4.10.3.2. $^{28}\text{Si}(d,p\gamma)^{29}\text{Si}$ reaction: 4934 γ -ray

The 4934 keV excited state has a 3/2 spin value, which results in the angular distribution being anisotropic (although the anisotropy is not very large [4.113]). The 1.2 fs lifetime of the excited state results in a Doppler broadening of the shape of the γ -ray. The measured γ -ray production cross-sections are plotted in Fig. 4.86 as a function of deuteron energy. The cross-section values increase rapidly, but are still quite low in this deuteron energy region. Because of the high energy of this γ -ray, it can be identified easily in a bulk spectrum containing several elements.

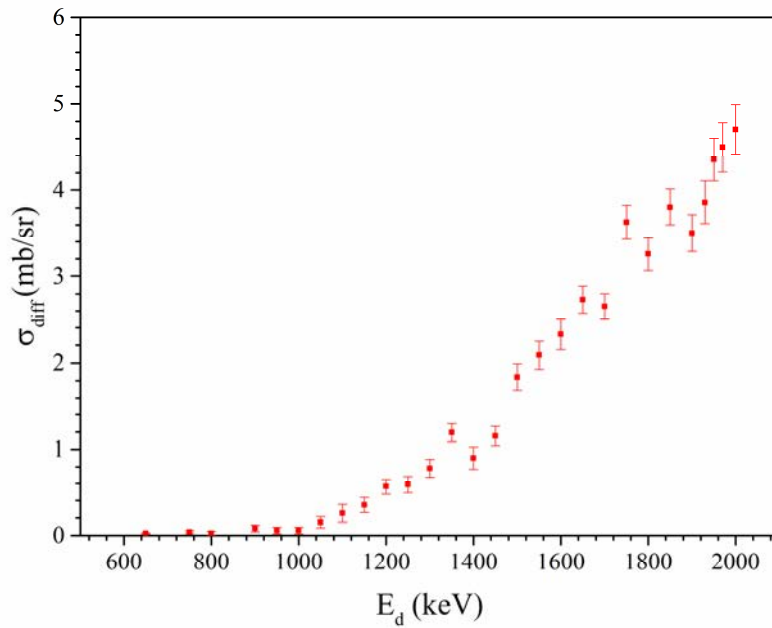


FIG. 4.86. Differential γ -ray production cross-sections of the 4934 keV γ -ray produced by the $^{28}\text{Si}(d,p\gamma)^{29}\text{Si}$ reaction at 55° as a function of deuteron energy [4.113].

As in the case of the 1273 keV γ -ray, a comparison of the calculated yields from the differential cross-section values with the only existing measured thick-target γ -yield can help validate these cross-section values. In Fig. 4.87, a comparison with the thick-target yields of Elekes *et al.* [4.18] is presented. The comparison shows a good agreement between the calculated and measured thick-target gamma-yields. The discrepancy between the calculated and measured yield data remains within the 15 % band uncertainty for the measured curve, along the whole deuteron energy region.

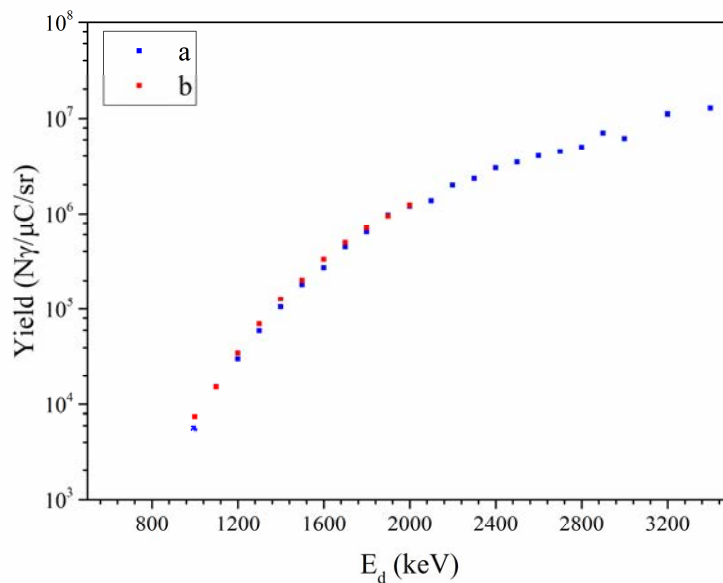


FIG. 4.87. Comparison of the thick target yields of the 4934 keV γ -ray produced by the $^{28}\text{Si}(d,p\gamma)^{29}\text{Si}$ reaction as a function of deuteron energy. Data obtained from: a) [4.18] (135°) and b) [4.113] (55°).

(b) Recommended data

Although both γ -ray lines have intensities large enough for silicon analysis using deuteron energies at or above 1.8 MeV, the application of the 4934 keV γ -ray is more highly recommended because of its easy identification in a bulk spectrum containing several elements. Because of the absence of any other experimental data, additional measurements with both thin and thick targets are also recommended.

4.11. PHOSPHORUS

4.11.1. Gamma-ray production cross-sections of phosphorus from proton-induced nuclear reactions

Proton-induced nuclear reactions on the single stable isotope of Phosphorus, ^{31}P , produce several γ -rays. Among them, the 1266 keV γ -ray, which is emitted following the inelastic scattering of protons by phosphorus, is the most useful one for analysis of in-depth homogeneous samples, since it has the highest yields. It is also expected to have an anisotropic angular distribution due to the spin 3/2 of the first excited state of ^{31}P . The other γ -ray lines produced by the same process have higher energies and the detectors respond with lower efficiencies. Other γ -rays are also produced by proton radiative capture reactions. However, since the cross-sections of these capture reactions are much smaller than the inelastic scattering cross-sections and have lower sensitivity, the inelastic scattering cross-sections are preferred for in-depth homogeneous sample analysis. In contrast, for depth analysis, proton capture is preferred since it exhibits narrow and rather isolated resonances, which are more suitable for depth profiling purposes.

Regarding the available data for γ -ray production, cross-sections from phosphorus proton inelastic scattering and capture reactions are scarce in the energy region of interest. In view of this situation, it was decided to perform measurements of γ -ray production cross-sections of phosphorus from proton inelastic scattering.

4.11.1.1. $^{31}\text{P}(p,p\gamma_{1-0})^{31}\text{P}$: 1266 keV γ -ray

(a) New measurements

Measurements of $^{31}\text{P}(p,p\gamma_{1-0})^{31}\text{P}$ reaction were performed at CTN/IST (Lisbon) and at the NSTRI (Tehran). The experimental conditions for the different experiments are presented below.

CTN /IST (Lisbon)

The proton beams were accelerated by a 3 MV Tandatron accelerator, with energies in the range of 2.5 to 4.0 MeV. Proton beam currents to the order of 100 nA were employed. The proton energy was calibrated by the 1645.1 keV and 1930.7 keV resonances of the $^{23}\text{Na}(p,p'\gamma)^{23}\text{Na}$ reaction and by the 3470 keV resonance of the $^{16}\text{O}(p,p)^{16}\text{O}$ reaction. The reaction chamber was electrically insulated from the beam line and worked together with the target holder and beam stopper as one Faraday cup for beam charge collection. Scattered protons at 155° with respect to the incident beam were detected by Camberra PIPs detectors with active area of 50 mm^2 and a 100 mm depletion layer, located in Cornell geometry at 88 mm from the target, with solid angles defined by apertures of 6.00 ± 0.05 mm. Gamma-rays were detected by a 45% Ge(HP) detector located at 130° with respect to the incident beam direction and at a distance of 55.5 mm from the target. The absolute efficiency versus γ -ray

energy was obtained by measuring the yields of γ -rays produced by ion sources (^{133}Ba and ^{152}Eu) calibrated in activity as well as by Monte Carlo simulations using GEANT and PENELOPE.

The target was made from a thin film of $\text{Ca}_3(\text{PO}_4)_2$ evaporated onto a thin self-supporting Ag film. RBS of the Ag film was used to normalize the cross-sections. The uncertainty budget is presented in Table 4.36.

TABLE 4.36. UNCERTAINTY BUDGET FOR THE CROSS-SECTION MEASUREMENTS OF 1266 keV $^{31}\text{P}(p,p\gamma_{1-0})^{31}\text{P}$ – CTN/IST

| Quantity | Uncertainty |
|-----------------------------------|-------------|
| γ -ray peak area | 1–3% |
| p+Ag elastic peak area | 1% |
| p+Ag Rutherford cross-section | 1% |
| P/Ag atomic ratio | 10% |
| Particle detector solid angle | 2.5% |
| γ -ray detector efficiency | 6% |
| Proton beam energy | 0.1% |
| Overall uncertainty | 12% |

NSTRI (Tehran)

The cross-sections were measured [4.12] in the proton energy range of 1886–3007 keV at the laboratory angle of 90° , employing a thin Zn_3P_2 target evaporated onto a self-supporting C. Beam intensities of the order of 50 nA were used. The accelerator beam energy was calibrated using the 991.88 keV resonance of the $^{27}\text{Al}(p,g)^{28}\text{Si}$ reaction and the 1880.44 keV threshold energy of the $^7\text{Li}(p,n)^7\text{Be}$ reaction. The γ -rays and backscattered protons were detected simultaneously. A 50 % HPGe detector placed at 51.9 mm collected the γ -rays while an ion implanted Si detector placed at a scattering angle of 165° detected the scattered particles. The uncertainty budget may be found in Table 4.37.

TABLE 4.37. UNCERTAINTY BUDGET FOR THE CROSS-SECTION MEASUREMENTS OF 1266 keV $^{31}\text{P}(p,p\gamma_{1-0})^{31}\text{P}$ – NSTRI

| Quantity | Uncertainty |
|-----------------------------------|-------------|
| γ -ray peak area | 1-3% |
| p+Ag elastic peak area | 1% |
| p+Ag Rutherford cross-section | 1% |
| P/Ag atomic ratio | 4% |
| Particle detector solid angle | 2% |
| γ -ray detector efficiency | 7% |
| Overall uncertainty | 9% |

Figure 4.88 presents values obtained by the referred measurements. These values may be found in the IBANDL database: CTN/IST – Jesus *et al.* [4.12] from 2621 to 3950 keV in steps from 1 keV (on resonance) to 10 keV (off resonance); NSTRI – Jokar *et al.* [4.114] from 1886 to 3007 keV in steps from 2 (on resonance) to 10 keV (off resonance).

In the common energy range, the energy scales of the two new measurements are in agreement within 1 keV. The cross-sections differ by an average of 12%, well within the quoted uncertainties.

(b) Data in the literature

A review of the existing literature only produced the measurements of Boni *et al.* [4.5] (data available in IBANDL). The cross-section data were measured in the proton energy range from 2648 to 3799 keV, in steps ranging from 15 to 20 keV. Due to the large energy step, some of the resonance maxima may have been missed, which hinders comparison with results obtained in this CRP. Nevertheless, it can be concluded that the results from Boni are higher by 10 to 20% (see Fig. 4.88), considering the quoted uncertainties.

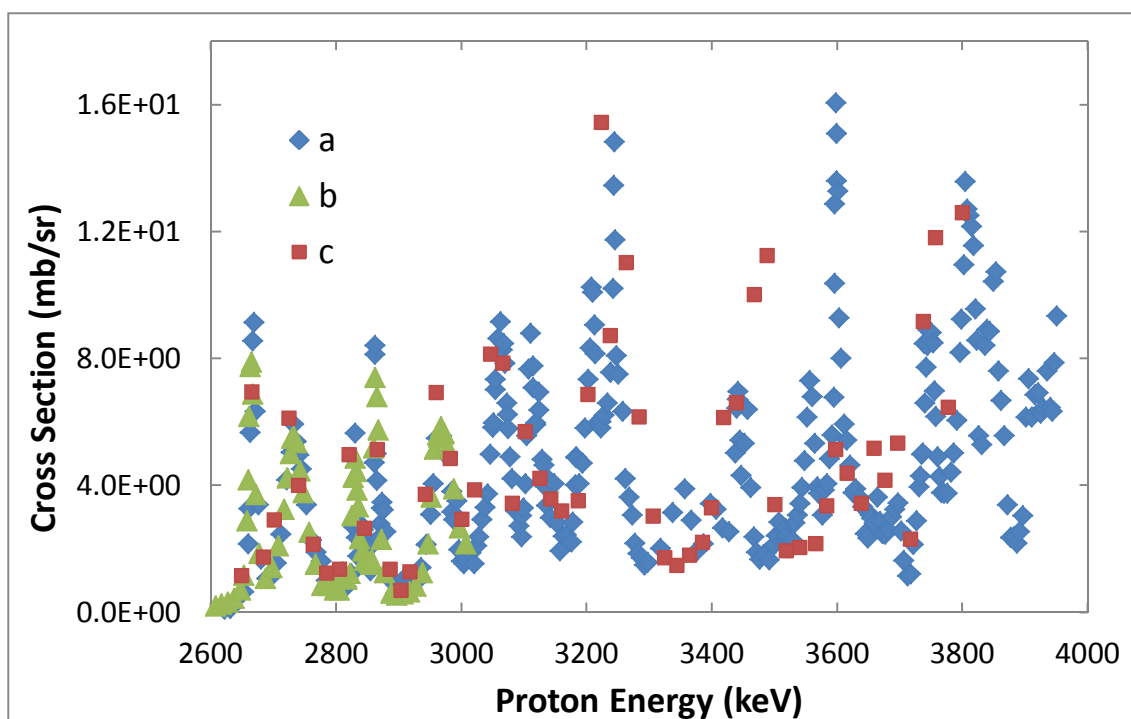


FIG. 4.88. Comparison of cross-sections of the $^{31}\text{P}(p, p\gamma_{1-0})^{31}\text{P}$ reaction obtained within the CRP: a) Jesus *et al.* [4.12] (130°), b) Jokar *et al.* [4.114] (90°) with previous results c) Boni *et al.* [4.5] (90°) in the proton energy range 2640 – 3950 keV.

(c) Recommended data

From the above comparison of new and old measurements, it can be concluded that there is an overall agreement within the experimental uncertainty. However, to be fully confident in the results, more measurements should be made to confirm the structure that was observed, to identify possible missed structures and to consolidate the absolute values of the excitation function.

4.11.2. Thick target yields

4.11.2.1. $^{31}\text{P}(p,p\gamma_{1-0})^{31}\text{P}$: 1266 keV γ -ray

(a) New measurements

Thick-target yields were also measured during this CRP by Jesus *et al.* [4.12] and Jokar *et al.* [4.114] at the same laboratories and with the same experimental conditions described in the previous section. Thick-target yield results depend on the absolute value of the collected charge, on the detector efficiency and on the collected γ -ray yield. The uncertainty budget for the yields of [4.12] is presented in Table 4.38. In this case, the yields were measured for $\text{Ca}_3(\text{PO}_4)_2$ and then converted to 100% phosphorus, taking into consideration the stoichiometry and the stopping power.

TABLE 4.38. UNCERTAINTY BUDGET FOR THE THICK-TARGET YIELD MEASUREMENTS OF 1266 keV $^{31}\text{P}(p,p\gamma_{1-0})^{31}\text{P}$

| Quantity | Uncertainty |
|--|-------------|
| γ -ray peak area | 1% |
| γ -ray detector efficiency | 6% |
| Absolute value of the collected charge | 10% |
| Overall uncertainty | 12% |

The measured thick-target yields per steradian of a pure phosphorus target are shown in Fig. 4.89.

(b) Data in the literature

Several previous measurements of thick-target yields for phosphorus were found in the literature. The data of Anttila *et al.* [4.1] and Kiss *et al.* [4.2] were included in the Handbook of Ion Beam Analysis [4.106]. These results, together with the data of Demortier *et al.* [4.115] and Savidou *et al.* [4.17], are now available in the IBANDL database. Figure 4.89 shows a comparison of the previous thick-target yield data with the new data measured in this CRP.

The results are in good agreement, within uncertainties, with the new data of Jesus *et al.* [4.12] and Jokar *et al.* [4.114]. The data of Jesus *et al.* becomes progressively larger than the results of Savidou *et al.* until finally reaching a maximum disagreement of around 22% at the highest energies. However, this 22% disagreement is still within the quoted uncertainties.

The excitation function of Jesus *et al.* [4.12], shown in Fig. 4.88, was introduced in the ERYA analysis code (see Section 5) in order to obtain thick-target yields for a pure phosphorus target, from 2.7 to 4.0 MeV proton energy. These results are also shown in Fig. 4.89 as a solid black line. The agreement with the experimental thick-target yields is within the experimental uncertainties.

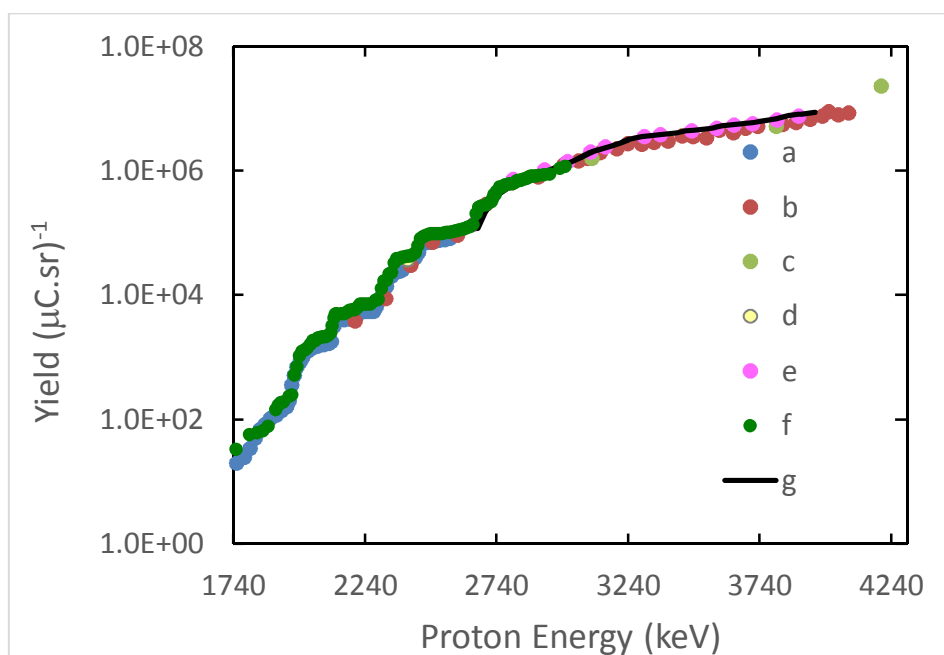


FIG. 4.89. Thick target yields, per steradian, corresponding to the 1266 keV γ -line, emitted by a pure phosphorus target as a function of proton energy. Data obtained in previous measurements: a) Demortier *et al.* [4.115] (90°), b) Savidou *et al.* [4.17] (90°) c) Kiss *et al.* [4.2] (55°), d) Anttila *et al.* [4.1] (55°), f) Jokar *et al.* [4.114] and in this CRP: e) Jesus *et al.* [4.12] (130°). The new measurements were done with $\text{Ca}_3(\text{PO}_4)_2$ and then converted to 100% phosphorus. The solid line g represents calculated values by the ERYA code (see text).

(c) Conclusions

Considering the uncertainty on the yield measurements, all the new and old results seem to be in fair agreement, apart from possible discrepancies in the energy scale. Hence they may be used in PIGE analysis of phosphorus as complementary data for (i) a PIGE system calibration, (ii) the determination of $E_{1/2}$, i.e. the energy at which the yield is half of the one obtained at incident energy, and (iii) an indication of the yield to be expected.

(d) Recommended data

Although it has been shown that there is (i) good agreement between the two sets of cross-section data for the $^{31}\text{P}(p,p'\gamma)^{31}\text{P}$ nuclear reaction producing the 1266 keV γ -ray, (ii) good agreement between calculated thick target yields using the cross-section data of Jesus *et al.* from 2600 to 4000 keV with measured thick-target yields for the same gamma line and (iii) the possibility to perform PIGE analysis by inserting this excitation function into the ERYA code (see Section 5) or similar code, it can be argued that a theoretical evaluation is also necessary, followed by further validation by benchmark measurements.

4.12. SULPHUR

4.12.1. Gamma-ray production cross-sections of sulphur from proton-induced nuclear reactions

Most of the IBA techniques are well suited for the proper quantification of Sulphur. The one most commonly used, because of its multi-elemental capabilities, is PIXE. However, only a few of the nuclear techniques can provide depth profile information and, in most cases, only

when sulphur is present in suitable matrices. On the other hand, resonant PIGE can fill this gap by providing accurate depth profile quantification, due to the strong resonances that are present in the $^{32}\text{S}(p,p'\gamma)^{32}\text{S}$ reaction. However, since recently published data disagree on the energy and strength of these resonances, a new set of measurements was considered necessary.

4.12.1.1. $^{32}\text{S}(p,p\gamma_{1-0})^{32}\text{S} : 2230 \text{ keV } \gamma\text{-ray}$

(a) New measurements

The $^{32}\text{S}(p,p'\gamma)^{32}\text{S}$ reaction was studied at the 5.5 MV Tandem Accelerator installed at the Institute of Nuclear and Particle Physics, NCSR “Demokritos” by Lagoyannis *et al.* [4.116]. The energy calibration of the accelerator was performed at $E_p = 991.9$ and 1746.9 keV using the resonances of the $^{27}\text{Al}(p,\gamma)^{28}\text{Si}$ and $^{13}\text{C}(p,\gamma)^{14}\text{N}$ reactions, respectively.

Two targets were used: a thin MoS_2 film deposited on a tantalum backing and a thick MoS_2 pellet. The primary goal of using the thin target was to measure the off-resonance cross-section of the reaction, while the thick target was used to determine the exact energy of the resonances and their strength. The targets were placed at the centre of a cylindrical chamber, which also acted as a Faraday cup. The beam charge was collected using a current integrator, while a suppression voltage of +300 volts was applied onto a tantalum collimator placed ~1 meter before the chamber.

The produced γ -rays were detected using four HPGe detectors placed at 0° , 55° , 90° and 165° with respect to the beam direction and at a distance of ~ 25 cm from the target covering an angular acceptance of $\pm 10^\circ$. The detectors were then rotated by 15° to a set of four new angles, i.e. 15° , 40° , 105° and 150° , in order to measure the angular distribution of the 2230 keV γ -ray.

The energy and efficiency calibration of the HPGe detectors were performed using a calibrated point source of ^{226}Ra .

The statistical error from the integration of the accumulated spectrum peaks did not exceed 5% and the overall systematic error was estimated at 8%, taking into account the uncertainties in the beam charge collection, efficiency calibration and target thickness. An analytical breakdown of the uncertainties is shown in Table 4.39.

TABLE 4.39. UNCERTAINTY BUDGET FOR PROTON-INDUCED SULFUR REACTIONS

| Quantity | Uncertainty |
|-----------------------|-------------|
| Peak Integration | 3–5% |
| Beam charge | 3.5% |
| Detector’s efficiency | 3% |

The measured relative yield at 55° with respect to the proton beam, is presented in Fig. 4.90.

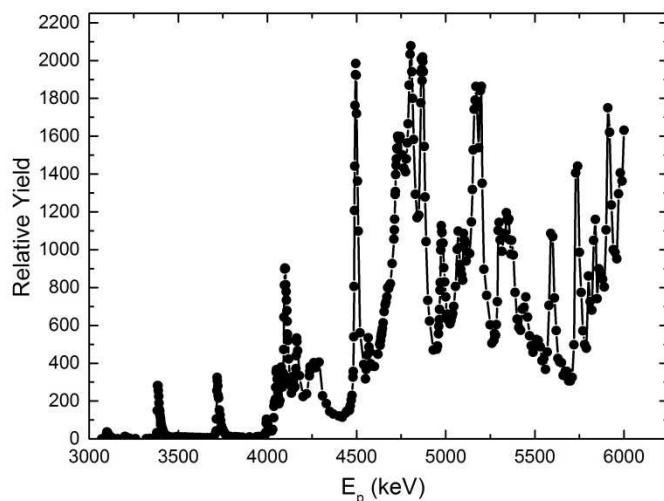


FIG. 4.90. Relative yield of the 2230 keV γ -ray at 55° as a function of proton energy [4.116].

The angular distributions of the 2230 γ -ray on the first four resonances, along with their fit with Legendre polynomials, are shown in Fig. 4.91. Because of the complexity of the excitation function of the $^{32}\text{S}(p,p'\gamma)^{32}\text{S}$ reaction, which exhibits numerous overlapping resonances, no cross-sections were derived.

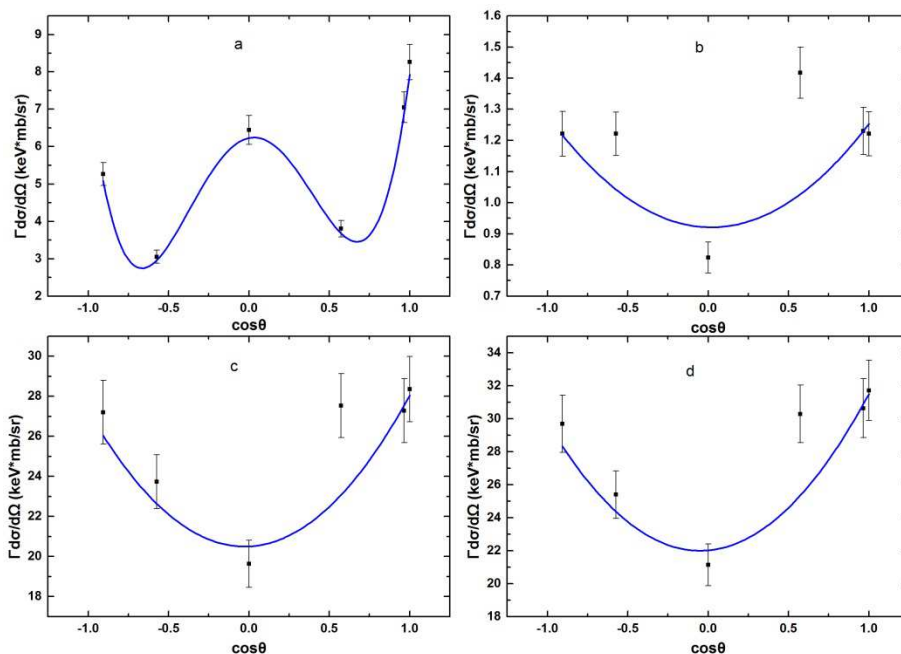


FIG. 4.91. Angular distributions of the first four resonances at (a) 3094 keV (b) 3195 keV (c) 3379 keV and (d) 3714 keV of the 2230 keV γ -ray [4.116].

(b) Data in the literature and assessment

The only existing data in the literature, except from those referring to the energy and the strength of the first three resonances, are thick-target yields by Kiss *et al.* [4.2] shown in Fig. 4.92.

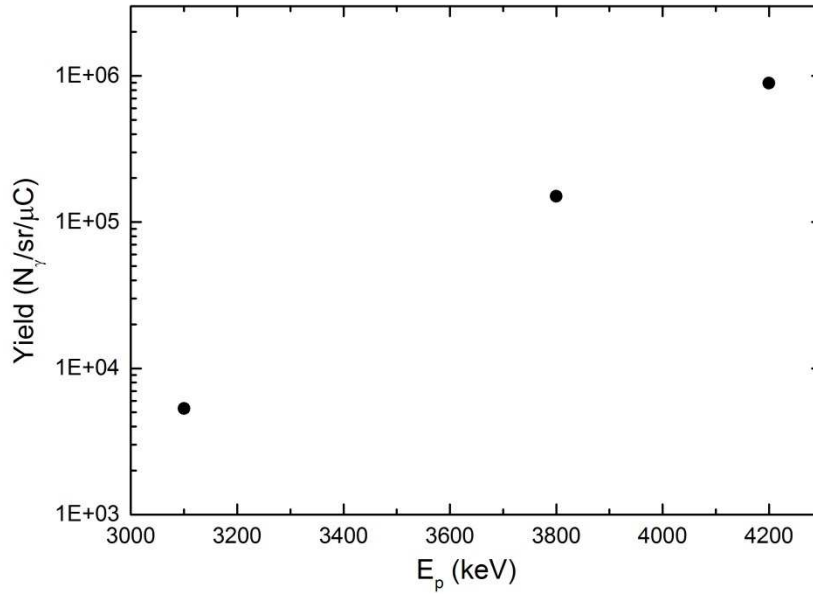


FIG. 4.92. Thick target yields of the 2130 keV γ -ray produced by the $^{32}\text{S}(p,p'\gamma)^{32}\text{S}$ reaction as a function of proton energy at 55° [4.2].

In Table 4.40, a compilation of the existing data regarding the resonances is presented.

TABLE 4.40. RESONANCE PARAMETERS OF THE $^{32}\text{S}(p,p'\gamma)^{32}\text{S}$ REACTION

| Reference | Resonance energy (keV) | | | Cross-section at 90° (mb.keV/sr) | | | Cross-section at 0° (mb.keV/s) | | |
|-----------|------------------------|-----------------|-----------------|---|-----------------|-----------------|---------------------------------------|-----------------|-----------------|
| | 1 st | 2 nd | 3 rd | 1 st | 2 nd | 3 rd | 1 st | 2 nd | 3 rd |
| | res. | res. | res. | res. | res. | res. | res. | res. | res. |
| [4.117] | 3089 | 3379 | 3717 | 8 | 30 | 35 | 18 ± 1 | 64 ± 3 | 70 ± 6 |
| [4.118] | 3095 | 3379 | 3716 | 10.88 | 41.84 | 48.10 | — | — | — |
| [4.119] | 3094 | 3379 | 3716 | | | | | | |
| [4.116] | 3094 | 3379 | 3714 | 6.2 ± 0.4 | 19.0 ± 1.1 | 20.5 ± 1.2 | 8.0 ± 0.5 | 27.5 ± 1.6 | 30.7 ± 1.8 |

From Table 4.40, it is clear that regarding the exact energies of the three resonances, only the position of the second one is common between the various authors. Moreover, the measured strength of the resonances varies in the literature: the strengths from Lagoyannis *et al.* [4.116] have the lowest values while those from Tsartsarakos *et al.* [4.118] have the highest values. The differences could be attributed to the angular acceptance of each experiment and to the strong angular dependence of the resonances. The experiment of Tsartsarakos *et al.* [4.118] was performed at an angle of $90^\circ \pm 30^\circ$, Rao *et al.* [4.116] at 0° and $90^\circ \pm 20^\circ$, and Lagoyannis *et al.* [4.116] at 0° and $90^\circ \pm 10^\circ$.

(c) Recommended data

Since only one thick-target yield dataset exists in the literature, it is not possible to make a recommendation for these cross-sections. In the case of the resonances that are important for depth profiling, only the energy of the second resonance can be recommended since all the available measurements agree. Finally, for the strength of the resonances, the values

suggested by Lagoyannis *et al.* [4.116] are recommended, since they were performed with a narrow angular divergence and thus are less sensitive to the angular distribution.

4.12.1.2. $^{32}\text{S}(p,\gamma_{1-0})^{33}\text{Cl}$, $^{32}\text{S}(p,\gamma_{6-1})^{33}\text{Cl}$, $^{34}\text{S}(p,\gamma_{1-0})^{35}\text{Cl}$ and $^{34}\text{S}(p,p\gamma_{1-0})^{34}\text{S}$: 811, 2035, 1219 and 2127 keV γ -rays, respectively

(a) Data in the literature and assessment

The 811 keV, 2035 keV and 1219 keV and 2127 keV γ -rays are emitted by the $^{32}\text{S}(p,\gamma_{1-0})^{33}\text{Cl}$, $^{32}\text{S}(p,\gamma_{6-1})^{33}\text{Cl}$, $^{34}\text{S}(p,\gamma_{1-0})^{35}\text{Cl}$ and $^{34}\text{S}(p,p\gamma_{1-0})^{34}\text{S}$ reactions, respectively. For these γ -rays, only thick-target yields exist in the literature, as measured by Kiss [4.2] and Anttila *et al.* [4.1]. Moreover, the data of Kiss *et al.* [4.2] have been normalized to those of Anttila *et al.* at $E_p = 2.4$ MeV, which means that these measurements are not independent. A compilation of the aforementioned data can be found in Fig. 4.93.

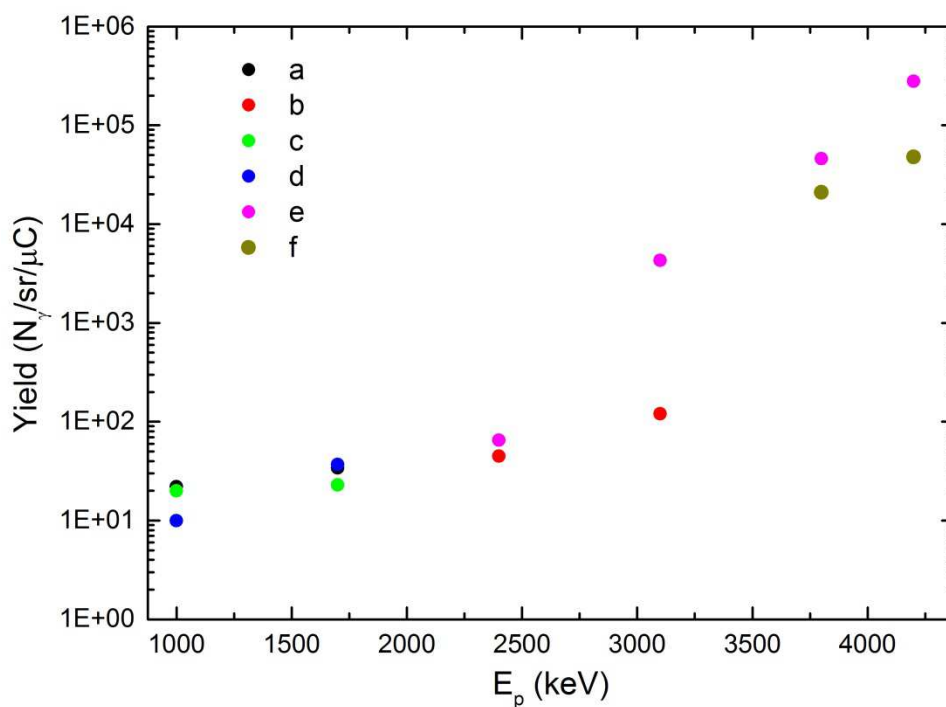


FIG. 4.93. Thick target yields measured by proton induced reactions from Sulphur at an angle of 55° as a function of proton energy. Data obtained from: (a) 811 keV [4.1], (b) 811 keV [4.2], (c) 2035 [4.1], (d) 1219 keV [4.1], (e) 1219 keV [4.2] and (f) 2127 [4.2].

(b) Recommended data

Since the two thick-target yield measurements are not independent, it is recommended that additional thick-target yield measurements be made.

4.12.2. Gamma-ray production cross-sections of sulphur from deuteron-induced nuclear reactions

4.12.2.1. $^{32}\text{S}(d,p\gamma_{1-0})^{33}\text{S}$: 841 γ -ray

As in the case of proton capture reactions on sulphur, there is only one measurement of thick-target yields in the literature, which was made by Elekes *et al.* [4.18]. The yield of the 841 keV γ -ray emitted by the $^{32}\text{S}(d,p\gamma_{1-0})^{33}\text{S}$ reaction is shown in Fig. 4.94.

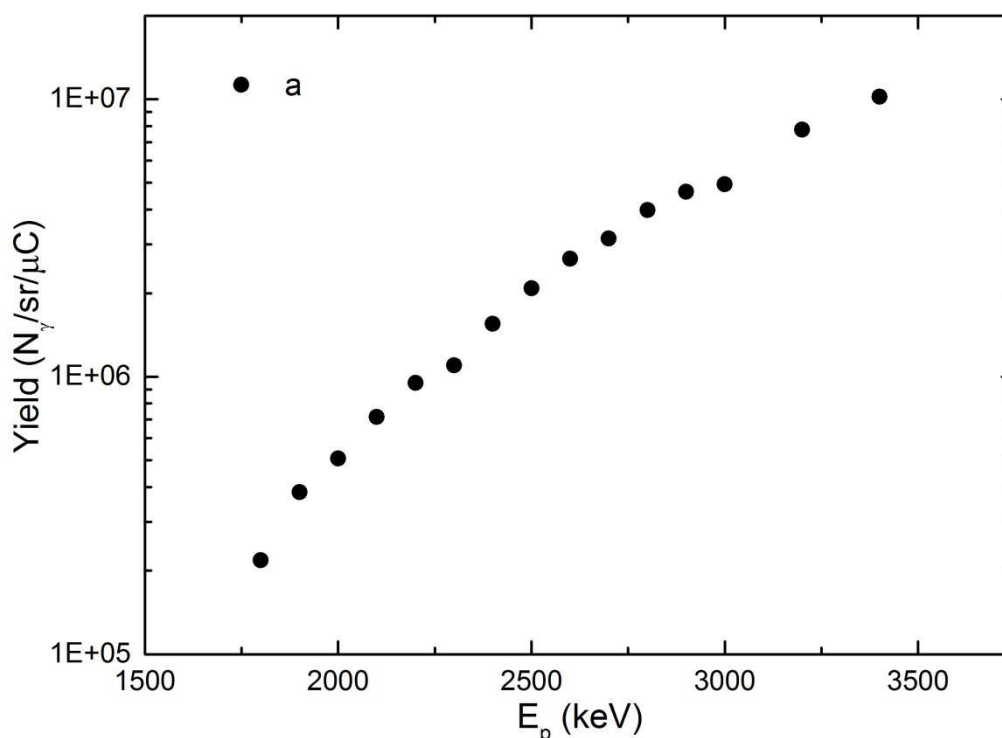


FIG. 4.94. Thick target yield of the 841 keV γ -ray produced from the $^{32}\text{S}(d,p\gamma_{1-0})^{33}\text{S}$ reaction at 135° as a function of proton energy [4.18].

(a) Recommended data

Since there is only one dataset available, no recommendation can be made. These measurements are of no interest for the analysis of sulfur, although they might be of interest for multi-elemental bulk analysis of material containing sulfur. Nevertheless, they are considered low priority.

4.13. TITANIUM

4.13.1. Gamma-ray production cross-sections of titanium from proton-induced nuclear reactions

4.13.1.1. $^{48}\text{Ti}(p,\gamma_{1-0})^{49}\text{V} + ^{49}\text{Ti}(p,n\gamma_{1-0})^{49}\text{V}$: 90.6 keV γ -ray

The 90.6 keV γ -ray from $^{48}\text{Ti}(p,\gamma)^{49}\text{V}$ and $^{49}\text{Ti}(p,n\gamma)^{49}\text{V}$ reactions have large yields and are therefore suitable for PIGE analysis [4.120]. The aim of the Ti work performed for the CRP

was to measure differential cross-sections for the production of 90.6 keV γ -rays from the $^{48}\text{Ti}(p,\gamma)^{49}\text{V}$ and $^{48}\text{Ti}(p,\gamma)^{49}\text{V} + ^{49}\text{Ti}(p,n\gamma)^{49}\text{V}$ reactions for proton energies ranging between 1.0 and 3 MeV at the laboratory angle of 90° using thin, isotopic, natural targets.

(a) New measurements

Measurements were carried out with the Van De Graff accelerator of Kharkov Institute of Physics and Technology (KIPT). The main parameters of the accelerator are the following: acceleration voltage 0.5–3.5 MeV, energy spread 0.07 %, ion beam current of the direct output 90 μA , ion beam current after the bending magnet 20 μA , accelerated ions H^+ and He^+ . The accelerator energy was calibrated by means of well-known resonances in the $^{27}\text{Al}(p,\gamma)^{28}\text{Si}$ reaction.

Thin TiN targets (natural Ti) on carbon backings were prepared by the ion beam assisted deposition (IBAD) technique. The isotopic target (^{48}Ti) on Ta backing was prepared by electrodeposition. The thickness (at/cm^2) of the targets were measured using back-scattering spectrometry with He and H ions at energies ranging from 1.6 to 1.8 MeV.

The measurements of the low-energy γ -rays were performed with a thin HPGe-detector. The calibration of the γ -ray detection system efficiency $\varepsilon(E\gamma)$ was carried out with the standard ^{133}Ba , ^{152}Eu , and ^{241}Am sources at the same geometry used for the cross-section measurements.

The excitation functions for the production of 90.6 keV γ -rays from the $^{48}\text{Ti}(p,\gamma)^{49}\text{V}$ and $^{48}\text{Ti}(p,\gamma)^{49}\text{V} + ^{49}\text{Ti}(p,n\gamma)^{49}\text{V}$ reactions for proton energies ranging between 1.0 and 3 MeV at the laboratory angle of 90° were measured with a variable energy step (ranging from 18 to 50 keV). The measured γ -ray production differential cross-sections are presented in Figs. 4.95 and 4.96.

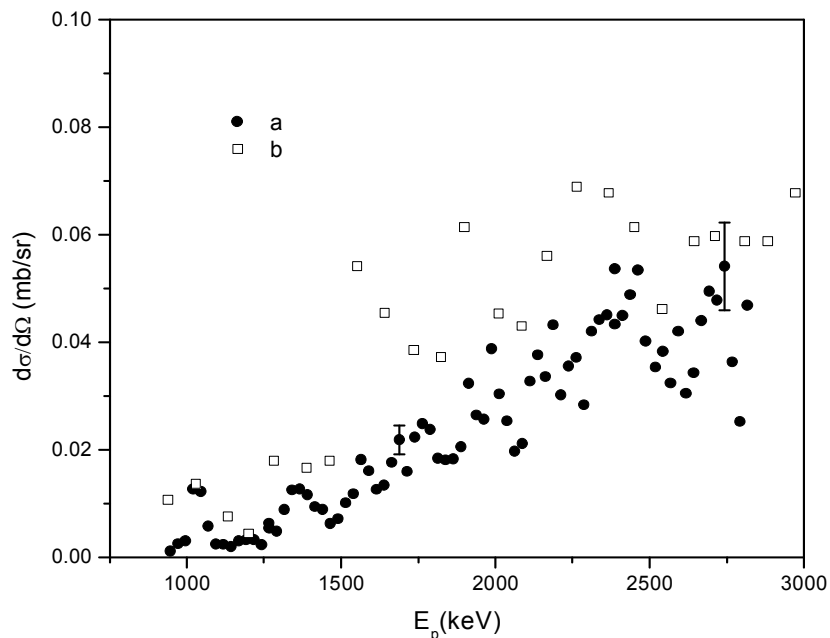


FIG. 4.95. a) The measured differential cross-section for production of the 90.6 keV γ -ray from the reaction $^{48}\text{Ti}(p,\gamma_{1-0})^{49}\text{V}$ as a function of proton energies ranging between 950 and 2820 keV at the laboratory angle of 90° , b) $\sigma_{\text{TOT}}/4\pi$ from the work of [4.121]. The target enrichment was equal 0.978 for ^{48}Ti .

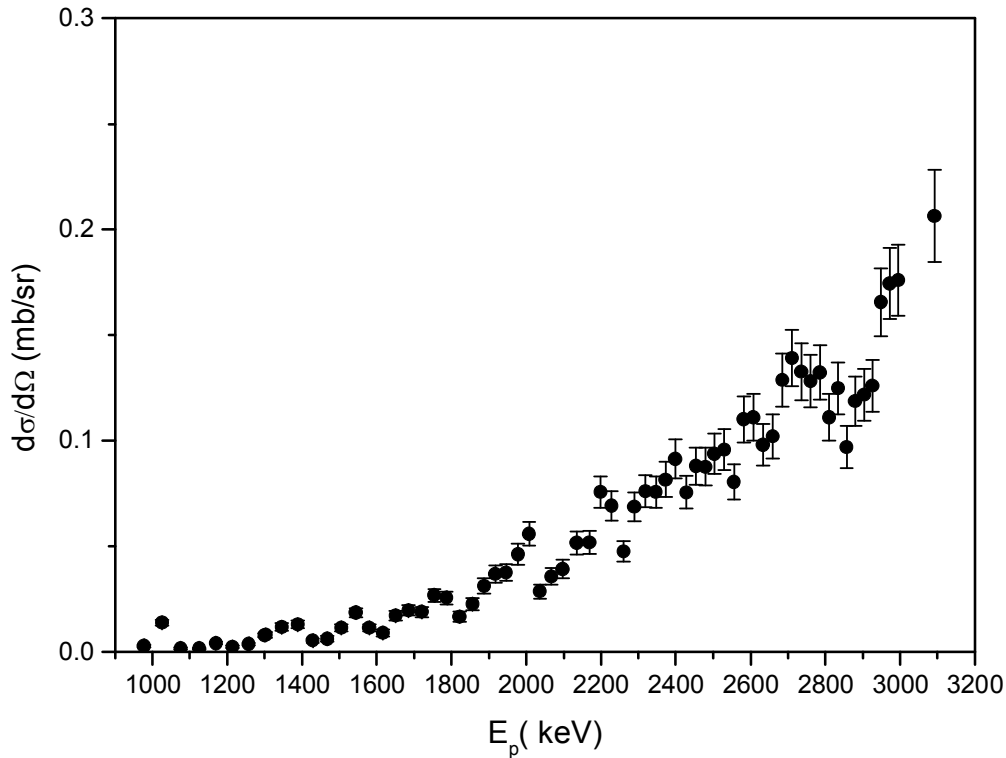


FIG. 4.96. The measured differential cross-section for production of the 90.6 keV γ -ray produced from the $^{48}\text{Ti}(p, \gamma_{1-0})^{49}\text{V}$ and $^{48}\text{Ti}(p, \gamma_{1-0})^{49}\text{V} + ^{49}\text{Ti}(p, n\gamma_{1-0})^{49}\text{V}$ reactions as a function of proton energies ranging between 900 and 3100 keV, at the laboratory angle of 90° .

The uncertainty budget is presented in Table 4.41.

TABLE 4.41. ESTIMATED UNCERTAINTY BUDGET FOR DIFFERENTIAL CROSS-SECTION MEASUREMENTS/PARAMETERS OF Ti REACTIONS

| Parameters | Uncertainty |
|-----------------------------------|-------------|
| γ -ray peak area | 3–14% |
| γ -ray detector efficiency | 6–7% |
| Target thickness | 5% |
| Integrated beam charges | 1% |
| Overall uncertainty | 9–17% |

(b) Data in the literature

The total cross-section of $^{48}\text{Ti}(p, \gamma)^{49}\text{V}$, for astrophysical purpose, was measured by Kennet *et al.* [4.121] and is compared with the new data in Fig. 4.95. The total cross-sections of [4.121] have been converted to differential cross-sections by dividing by a factor of 4π , assuming the γ -ray emission is isotropic. Gosset used two strong resonances of the $^{48}\text{Ti}(p, \gamma)^{49}\text{V}$ reaction at 1007 keV and 1013 keV for profiling Ti implanted in M50 steel [4.122].

4.13.1.2. Thick target yield: 90.6 keV γ -ray

Demortier *et al.* [4.120] has carried out thick-target yield measurements on natural titanium, as shown Fig. 4.97.

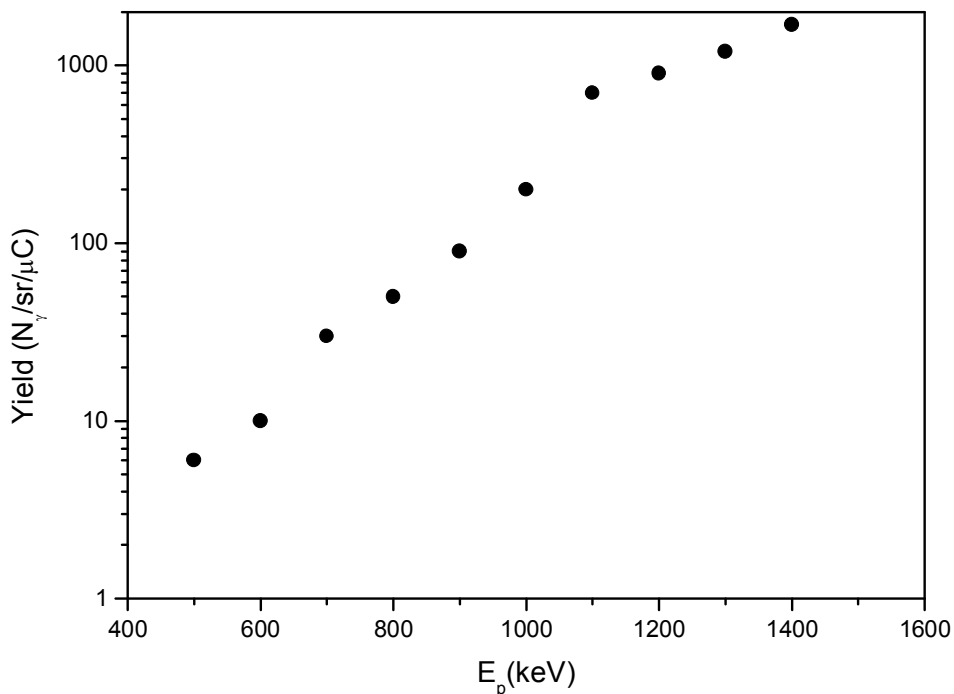


FIG. 4.97. Gamma-ray yield of the 90.6 keV γ -ray at 90° produced from natural titanium as a function of proton energy. Data from [4.120].

Thick-target yields were calculated from the new measured differential cross-sections. Since cross-sections were not measured at energies below 1000 keV, it is convenient to compare the difference of thick-target yields at the current proton beam energy and the thick-target yields at beam energy 1000 keV ($Y(E_p) - Y(1000 \text{ keV})$). The differences are shown in Fig. 4.98.

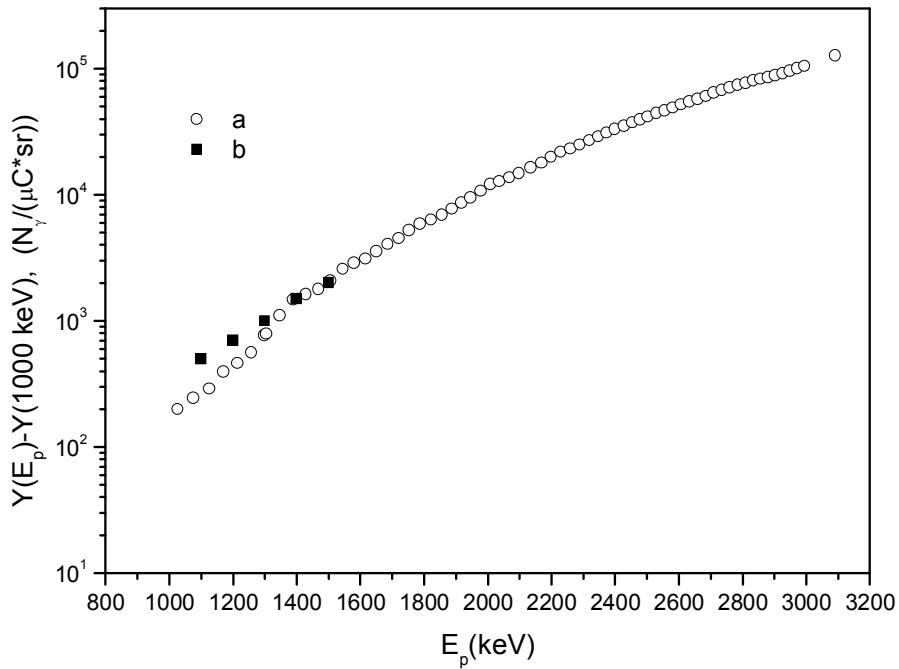


FIG. 4.98. The difference of thick target yields at current proton beam energy and thick target yields at the beam energy 1000 keV for 90.6 γ -ray produced from natural titanium at 90° as a function of proton energy. Data from: a) thick target yields calculated from the new measured differential cross-sections and b) measured thick-target yields [4.120].

(c) Recommended data

The excitation function for the 90.6 keV γ -ray produced by the $^{48}\text{Ti}(p,\gamma)^{49}\text{V}$ reaction shown in Fig. 4.95 can be used for analytical purposes only up to the energy of 1.5 MeV, since there is additional γ -ray yield from the $^{49}\text{Ti}(p,n\gamma)^{49}\text{V}$ reaction contributing at energies above 1.5 MeV. The excitation function for the production of the 90.6 keV γ -ray from the $^{48}\text{Ti}(p,\gamma)^{49}\text{V}$ and $^{48}\text{Ti}(p,\gamma)^{49}\text{V} + ^{49}\text{Ti}(p,n\gamma)^{49}\text{V}$ reactions, as shown in Fig. 4.96, can be used for analytical purposes in the whole energy range. All the new data have been uploaded in IBANDL.

4.13.1.3. $^{46}\text{Ti}(p,p\gamma_{1-0})^{46}\text{Ti}$: 889 keV γ -ray and $^{48}\text{Ti}(p,p\gamma_{1-0})^{48}\text{Ti}$: 983 keV γ -ray

For the analysis of titanium by PIGE, the differential cross-sections for the production of the 889 keV γ -ray from the $^{46}\text{Ti}(p,p'\gamma)^{46}\text{Ti}$ reaction and the 983 keV γ -ray from the $^{48}\text{Ti}(p,p'\gamma)^{48}\text{Ti}$ reaction can also be used. These cross-sections have been measured by Krivonosov *et al.* [4.123] and are presented in Fig. 4.99. However, the magnitude of these cross-sections is significantly smaller than that of the cross-section for production of the 90.6 keV γ -ray for proton energy up to 2.5 MeV, as shown in Figs. 4.95 and 4.96. Therefore, the latter are preferable for PIGE applications.

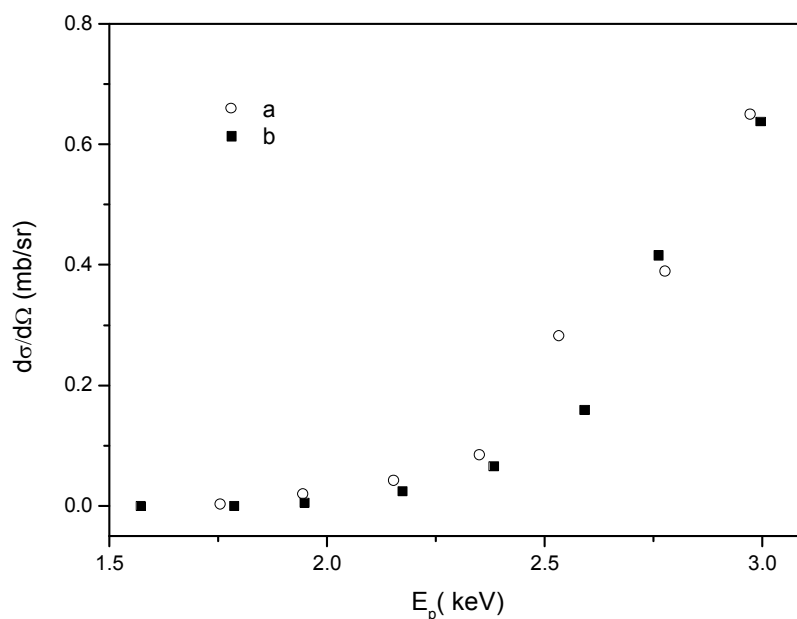


FIG. 4.99. Measured differential cross-sections as a function of proton energy for the a) 889 keV γ -ray from the $^{46}\text{Ti}(p,p\gamma_{1-0})^{46}\text{Ti}$ reaction, b) 983 keV γ -ray from the $^{48}\text{Ti}(p,p\gamma_{1-0})^{48}\text{Ti}$ reaction. Data from [4.123].

4.14. CHROMIUM

The 378 keV γ -ray produced from the $^{52}\text{Cr}(p,\gamma_{1-0})^{53}\text{Mn}$ and $^{53}\text{Cr}(p,n\gamma_{1-0})^{53}\text{Mn}$ reactions is suitable for analytical measurements according to [4.120] and [4.122]. The aim of the CRP was to measure differential cross-sections for the production of 378 keV γ -rays from the $^{52}\text{Cr}(p,\gamma)^{53}\text{Mn} + ^{53}\text{Cr}(p,n\gamma)^{53}\text{Mn}$ reactions for proton energies ranging between 1.0 and 3 MeV at the laboratory angle of 90° using thin natural targets. All the data have been uploaded in IBANDL.

4.14.1. Gamma-ray production cross-sections of chromium from proton-induced nuclear reactions

4.14.1.1. $^{52}\text{Cr}(p,\gamma_{1-0})^{53}\text{Mn} + ^{53}\text{Cr}(p,n\gamma_{1-0})^{53}\text{Mn}$: 378 keV γ -ray

(a) New measurements

Measurements were carried out with the Van De Graff accelerator of KIPT (see Section 4.13). The accelerator energy was calibrated by means of the well-known resonances produced by the $^{27}\text{Al}(p,\gamma)^{28}\text{Si}$ reaction.

Thin natural Cr targets on Ta backings were prepared by the vacuum deposition technique. The thickness (at/cm^2) of the targets were measured by using back-scattering spectrometry with He and H ions at energies ranging from 1.6 to 1.8 MeV.

The γ -ray measurement was performed using a co-axial Ge(Li)-detector. Calibration of the γ -ray detection system efficiency $\varepsilon(E\gamma)$ was carried out with the standard ^{133}Ba and ^{152}Eu sources with the same geometry used for the cross-section measurements.

The excitation functions for the production of the 378 keV γ -rays from the $^{52}\text{Cr}(p,\gamma)^{53}\text{Mn} + ^{53}\text{Cr}(p,n\gamma)^{53}\text{Mn}$ reactions for proton energies ranging between 1.0 and 3 MeV at the laboratory angle of 90° were measured with a variable energy step (ranging from 20 to 10 keV). The threshold of the second reaction for 378 keV γ -rays is at 1.79 MeV. The measured γ -ray production differential cross-sections are shown in Fig. 4.100.

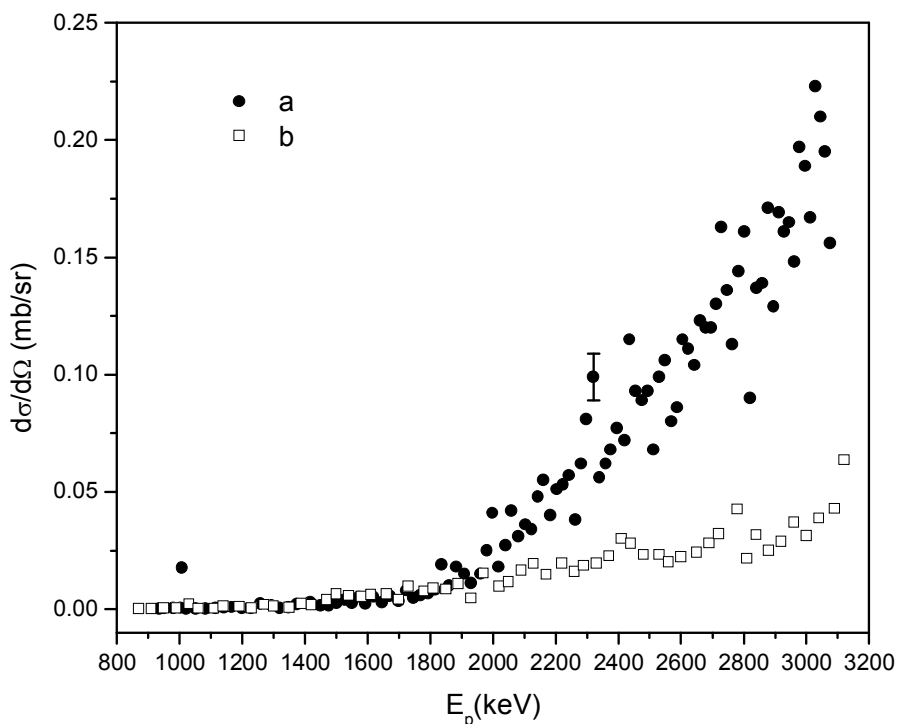


FIG. 4.100. a) measured differential cross-section for production of the 378 keV γ -ray from the $^{52}\text{Cr}(p,\gamma)^{53}\text{Mn} + ^{53}\text{Cr}(p,n\gamma)^{53}\text{Mn}$ reactions for proton energies ranging between 900 and 3100 keV at the laboratory angle of 90° , using ^{nat}Cr -target. b) $\sigma_{TOT}/4\pi$ for reaction $^{52}\text{Cr}(p,\gamma)^{53}\text{Mn}$ from the work of [4.124].

The uncertainty budget of the measurement is presented in Table 4.42.

TABLE 4.42. UNCERTAINTY BUDGET FOR THE CROSS-SECTION MEASUREMENTS OF PROTON-INDUCED Cr REACTIONS

| Parameter | Uncertainty |
|-----------------------------------|-------------|
| γ -ray peak area | 1–7% |
| γ -ray detector efficiency | 6% |
| Target thickness | 5% |
| Integrated beam charges | 1% |
| Overall uncertainty | 8–12% |

(b) Data in the literature

Total cross-sections of $^{52}\text{Cr}(p,\gamma)^{53}\text{Mn}$ have been measured by Kennet et.al. [4.124] for use in nuclear astrophysics applications. The data were compared with the new measurements in Fig. 4.100, after they had been converted to differential cross-sections by dividing by a factor of 4π . This simple conversion works under the assumption that the emitted γ -ray is isotropic. Gosset used the resonance of the $^{52}\text{Cr}(p,\gamma)^{53}\text{Mn}$ reaction at 1005 keV for profiling Cr that had been implanted in pure Fe [4.122].

4.14.1.2. Thick target yield on ^{nat}Cr : 378 keV γ -ray

Demortier *et al.* [4.120] has carried out thick-target yield measurements of the 378 keV γ -ray on natural chromium. The results are shown in Fig. 4.101.

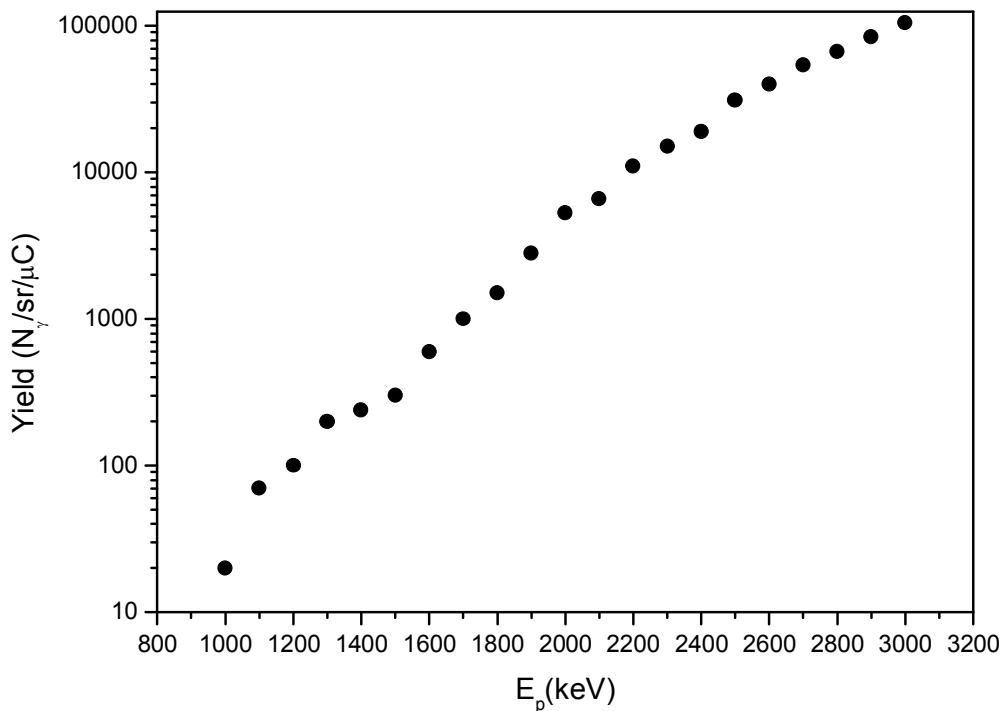


FIG. 4.101. Gamma-ray yield of the 378keV γ -ray as a function of proton energy for natural Chromium [4.120].

Thick-target yields were calculated from the new measured differential cross-sections. Since cross-sections at energies below 1000 keV were not measured, it is convenient to compare the difference of thick-target yields at the current proton beam energy and the thick-target yields at beam energy 1000 keV ($Y(E_p) - Y(1000 \text{ keV})$). The values of the difference are shown in Fig. 4.102.

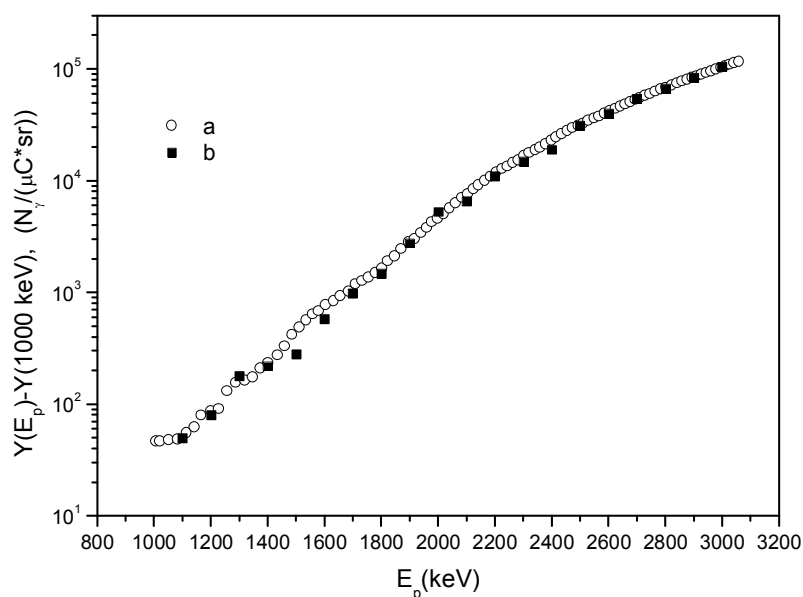


FIG. 4.102. The difference in thick target yields at the current proton beam energy and thick target yields at the beam energy of 1000 keV for the 378 γ -ray. a) thick target yields calculated from the new measured differential cross-sections at 90° . b) measured thick-target yields at 90° [4.120].

(c) Recommended data

The excitation function for the production of the 378 keV γ -ray produced by the $^{52}\text{Cr}(p,\gamma)^{53}\text{Mn}$ + $^{53}\text{Cr}(p, n\gamma)^{53}\text{Mn}$ reactions, as shown in Fig. 4.100, can be used for analytical purposes in the whole energy range.

REFERENCES TO SECTION 4

- [4.1] ANTTILA, A., HÄNNINEN, R., RAISÄNEN, J., Proton-induced thick-target gamma-ray yields for the elemental analysis of the $Z = 3-9, 11-21$ elements, *J. Radioanal. Nucl. Chem.* **62** (1981) 293.
- [4.2] KISS, Á., KOLTAY, E., NYAKÓ, B., SOMORJAI, E., ANTTILA, A., RÄISÄNEN, J., Measurements of relative thick target yields for PIGE analysis on light elements in the proton energy interval 2.4–4.2 MeV, *J. Radioanal. Nucl. Chem.* **89** (1985) 123.
- [4.3] RÄISÄNEN, J., WITTING, T., KEINONEN, J., Absolute thick-target γ -ray yields for elemental analysis by 7 and 9 MeV protons, *Nucl. Instrum. Methods Phys. Res. B* **28** (1987) 199.
- [4.4] RIO, S., MÉTRICH, N., MOSBAH, M., MASSIOT, P., Lithium, boron and beryllium in volcanic glasses and minerals studied by nuclear microprobe, *Nucl. Instrum. Methods Phys. Res. B* **100** (1995) 141.
- [4.5] BONI, C., CEREDA, E., BRAGA MARCASSAN, G.M., DE TOMASI, V., Prompt gamma emission excitation functions for PIGE analysis, *Nucl. Instrum. Methods Phys. Res. B* **35** (1988) 80–86.
- [4.6] CACIOLLI, A., CHIARI, M., CLIMENT-FONT, A., FERNÁNDEZ-JIMÉNEZ, M.T., GARCÍA-LÓPEZ, G., LUCARELLI, F., NAVA, S., ZUCCHIATTI, A., Measurement of γ -ray emission induced by protons on fluorine and lithium, *Nucl. Instrum. Methods Phys. Res. B* **249** (2006) 98–100.

- [4.7] ZIEGLER, JAMES F., ZIEGLER, M.D., BIRSACK, J.P., SRIM-the stopping and range of ions in matter (2010), Nucl. Instrum. Methods Phys. Res. B **268** (2010) 1818.
- [4.8] EXFOR database [<https://www-nds.iaea.org/exfor/exfor.htm>].
- [4.9] NEWSON, H.W., WILLIAMSON, R.M., JONES, K.W., GIBBONS, J.H., Marshak, H., $\text{Li}^7(p,n)$, $(p,p'\gamma)$, and (p, γ) reactions near neutron threshold, Phys. Rev. **108** (1957) 1294.
- [4.10] BACHILLER PAREA, D., CORVISIERO, P., JIMENEZ REY, D., JOCO, D., MAIRAL VIDAL, A., MUNOZ MARTIN, A., ZUCCHIATATTI, A., Measurement of gamma-ray production cross-sections in Li and F induced by protons from 810 to 3700 keV, Nucl. Instrum. Methods Phys. Res. B (2017) in press.
- [4.11] MATEUS, R., JESUS, A.P., BRAZINHA, B., CRUZ, J., PINTO, J.V., RIBEIRO, J.P., Proton-induced γ -ray analysis of lithium in thick samples, Nucl. Instrum. Methods Phys. Res. B **190** (2002) 117.
- [4.12] JESUS, A.P., *et al.*, private communication.
- [4.13] BROWN, A.B, SNYDER, C.W., FOWLER, W.A., LARITSEN, C.C., Excited States of the Mirror Nuclei, Li^7 and Be^7 , Phys. Rev. **82** (1951) 159.
- [4.14] PRESSER, G., BASS, R., Reactions ${}^7\text{Li} + n$, ${}^7\text{Li} + p$ and excited states of the $A = 8$ system, Nucl. Phys. A **182** (1972) 321.
- [4.15] GUZHOVSKIY, B.J., ABRAMOVICH, S.N., PROTOPOPOV, V.H., Izv. Akad. Nauk SSSR, Ser. Fiz.-Mat. **4** (1984) 24.
- [4.16] ASLAM, W.V., PRESTWICH, MCNEILL, F.E., Thin target ${}^7\text{Li}(p,p'\gamma)$ inelastic gamma-ray yield measurements, J. Radioanal. Nucl. Chem. **254** (2002) 533.
- [4.17] SAVIDOU, A., ASLANOGLAU, X., PARADELLIS, T., PILAKOUTA, M., Proton induced thick target γ -ray yields of light nuclei at the energy region $E_p = 1.0\text{--}4.1$ MeV, Nucl. Instrum. Methods Phys. Res. B **152** (1999) 12–18.
- [4.18] ELEKES, Z., KISS, Á.Z., BIRON, I., CALLIGARO, T., SALOMON, J., Thick target γ -ray yields for light elements measured in the deuteron energy interval of 0.7–3.4 MeV, Nucl. Instrum. Methods Phys. Res. B **168** (2000) 305.
- [4.19] SZIKI, G.Á., SIMON, A., SZIKSZAI, Z., KERTÉSZ, ZS., DOBOS, E., Gamma ray production cross-sections of deuteron induced nuclear reactions for light element analysis, Nucl. Instrum. Methods Phys. Res. B **251** (2006) 343.
- [4.20] SEPPÄLÄ, A., RÄISÄNEN, J., RAUHALA, E., SZÖKEFALVI-NAGY, Z., Absolute thick-target gamma-ray yields for the light elements induced by ${}^{12}\text{C}$, ${}^{14}\text{N}$ and ${}^{16}\text{O}$ ions, Nucl. Instrum. Methods Phys. Res. B **143** (1998) 233.
- [4.21] PERDIKAKIS, G., SPYROU, A., KOKKORIS, M., ZARKADAS, CH., KARYDAS, A.G., HARISSOPOULOS, S. KOSSIONIDES, S., On the determination of beryllium in light element matrices using PIGE and NRA, Nucl. Instrum. Methods Phys. Res. B **226** (2004) 622.
- [4.22] ZAHNOW, D., ANGULO, C., JUNKER, M., ROLFS, C., SCHMIDT, S., SCHULTE, W.H., SOMORJAI, E., Nucl. Phys. A **589** (1995) 95.
- [4.23] HORNYAK, W. F., LUDEMANN, C. A., ROUSH, M. L., Energy levels of B^{10} , Nucl. Phys. **50** (1964) 424.
- [4.24] FONSECA, M., JESUS, A.P., LUÍS, H., MATEU, R., CRUZ, J., GASQUES, L., GALAVIZ, D., RIBEIRO, J.P., PIGE analysis of magnesium and beryllium, Nucl. Instrum. Methods Res. B **268** (2010) 1806.
- [4.25] MEYERHOF, W.E., TANNER, N.W., HUDSON, C.M., Radiative capture of protons by Be^9 , Phys. Rev **115** (1959) 1227.
- [4.26] CALLIGARO, T., DRAN, J.-C., POIROT, J.-P., QUERRÉ, G., SALOMON, J., ZWAAN, J.C., PIXE/PIGE characterization of emeralds using an external micro-beam, Nucl. Inst. Meth. Phys. Res. B **161–163** (2000) 769.

- [4.27] MA XIN-PEI, MACARTHUR, J.D., ROEDER, P.L., MARIANO, A.N., Trace element fingerprinting of emeralds by PIXI/PIGE, *Nucl. Instrum. Methods Phys. Res. B* **75** (1993) 423.
- [4.28] STOTT, P.E., WOOTTON, A., GORINI, G., SINDORNI, E., BATANI, D., (Eds.) *Advanced Diagnostics for Magnetic and Inertial Fusion*, 1st edn, Springer US, New York (2002) p141.
- [4.29] BORDERIE, B., BARRANDON, J.N., New analytical developments in prompt gamma-ray spectrometry with low-energy tritons and alpha particles, *Nucl. Instrum. Methods* **156** (1978) 483–492.
- [4.30] LAPPALAINEN, R., ANTTILA, A., RÄISÄNEN, J., Absolute α -induced thick-target gamma-ray yields for the elemental analysis of light elements, *Nucl. Instrum. Methods Phys. Res.* **212** (1983) 441.
- [4.31] HEATON, P.K., LEE, H. W., ROBERTSON, B. C., NORMAN, E. B., LESKO, K. T., SUR, B., α -particle induced γ -ray transitions in light elements, *Phys. Rev. C* **56** (1997) 922.
- [4.32] SEGEL R.E., SINGH, P.P., HANNA, S.S., GRACE, M.A., Gamma rays from the $B^{10}+p$: decay schemes and excitation functions, *Phys. Rev.* **145** (1966) 736–745.
- [4.33] DAY, R.B., HUUS, T., Gamma radiation from B^{10} bombarded by protons, *Phys. Rev.* **95** (1954) 1003–1006.
- [4.34] LAGOYANNIS, A., PREKETES-SIGALA, K., AXIOTIS, M., FOTEINOU, V., HARISSOPULOS, S., KOKKORIS, M., MISAEELIDES, P., PANETA, V., PATRONIS, N., Study of the $^{10}B(p,\alpha\gamma)^7Be$ and $^{10}B(p,p'\gamma)^{10}B$ reactions for PIGE purposes, *Nucl. Instrum. Methods Phys. Res. B* **342** (2015) 271–276.
- [4.35] CHIARI, M., FERRACCIOLI, G., MELON, B., NANNINI, A., PEREGO, A., SALVESTRINI, L., LAGOYANNIS, A., PREKETES-SIGALAS, K., Measurement of proton induced thick target γ -ray yields on B, N, Na, Al and Si from 2.5 to 4.1 MeV, *Nucl. Instrum. Methods Phys. Res. B* **366** (2016) 77.
- [4.36] HUNT, S.E., POPE, R.A., EVANS, W.W., Investigation of the gamma radiation produced by irradiating B^{10} with protons in the energy range 0.7 to 3.0 MeV, *Phys. Rev.* **106** (1957) 1012–1015.
- [4.37] OPHEL, T.R., GLOVER, R.N., TITTERTON, E.W., Gamma ray yields from the proton bombardment of B^{10} , *Nucl. Phys.* **33** (1962) 198 – 201.
- [4.38] MATEUS, R., REIS, M.A., JESUS, A.P., RIBEIRO, J.P., Quantitative analysis of light elements in aerosol samples by PIGE, *Nucl. Instrum. Methods Phys. Res. B* **249** (2006) 784–788.
- [4.39] PREKETES-SIGALAS, K., LAGOYANNIS, A., AXIOTIS, M., HARISSOPULOS, S., KOKKORIS, M., MERTZIMEKIS, T.J., PANETA, V., PROVATAS, G., Study of the $^{11}B(p,p'\gamma)^{11}B$ reaction for PIGE applications, *Nucl. Instrum. Methods Phys. Res. B* **368** (2016) 71–74.
- [4.40] GURBICH, A. F., ISTOMIN, I. V., SEMENOV, A. V., A nuclear-physics method of composition analysis for the wall surface of a BN-600 steam generator, *Sov. J. Atom. Energy* **68** (1990), 236–239.
- [4.41] ZHANG WEICHENG, LEI XIANGGUO, Proton-induced gamma-ray emission for carbon tracer techniques, *Appl. Radiat. Isot.* **42** (1991) 1039.
- [4.42] ZHANG WEICHENG, ZHANG TIANMEI, LEI XIANGGUO, Determination of ^{13}C in breath sample by PIGE, *J. Radioanal. Nucl. Chem.* **151** (1991) 313.
- [4.43] ROLFS, C., AZUMA, R. E., Interference effects in $^{12}C(p,\gamma)^{13}N$ and direct capture to unbound states, *Nucl. Phys. A* **227** (1974) 291.
- [4.44] BURTEBAEV, N., IGAMOV, S.B., PETERSON, R.J., YARMUKHAMEDOV, R., ZAZULIN, D.M., New measurements of the astrophysical S factor for $^{12}C(p,\gamma)^{13}N$

reaction at low energies and the asymptotic normalization coefficient (nuclear vertex constant) for the $p + {}^{12}\text{C} \rightarrow {}^{13}\text{N}$ reaction, Phys. Rev. C **78** (2008) 035802.

- [4.45] GOERRES, J., private communication.
- [4.46] KING, J.D., AZUMA, R.E., VISE, J.B., Cross section and astrophysical S-factor for the ${}^{13}\text{C}(p,\gamma){}^{14}\text{N}$ reaction, Nucl. Phys A **567** (1994) 345.
- [4.47] BAKTIBAYEV, M.K., BURMINSKII, V.P., BURTEBAYEV, N., JAZAIROV-KAKHRAMONOV, V., KADYRZHANOV, K.K., SAGINDYKOV, SH.SH., ZARIFOV, R.A., ZAZULIN, D.M., Differential Cross Section Measurement of Radiative Capture of Protons by Nuclei ${}^{13}\text{C}$ (Proc. 3rd Eurasian Conf. Nucl. Sci. Appl. Uzbekistan, 2004) Vol. 38, INIS-UZ--123, Uzbekistan (2004) 375.
- [4.48] STANGEBY, P.C., *et al.*, C-Tracer Experiments in DIII-D Preliminary to Thermal Oxidation Experiments to Understand Tritium Recovery in DIII-D, JET, C-Mod, and MAST, (Proc. 33rd EPS Conf. on Plasma Phys. Rome, 2006) ECA Vol. 30I, European Physical Society, Mulhouse (2006) 5,145.
- [4.49] CABIOC'H, T., THUNE, E., JAOUEN, M., BODART, F., Resonant nuclear reaction analysis study of carbon phase formation during carbon ion-implantation into silver substrates, Nucl. Instrum. Methods Phys. Res. B **207** (2003) 409.
- [4.50] THEODOSSIU, W., BAUMANN, H., MARKWITZ, A., BETHGE, K., Characterisation of ${}^{13}\text{C}$ implantations in silicon by NRA [${}^{13}\text{C}(p,\gamma){}^{14}\text{N}$] and RBS, Fresenius' J. Anal. Chem. **353** (1995) 483.
- [4.51] KIENER, J., GROS, M., TATISCHEFF, V., ATTIE, D., BAILLY, I., BAUCHET, A., CHAPUIS, C., CORDIER, B., DELONCLE, I., PORQUET, M.G., SCHANNE, S., SEREVILLE, N., DE, TAUZIN, G., New determinations of gamma-ray line intensities of the $E_p + 550$ and 1747 keV resonances of the ${}^{13}\text{C}(p,\gamma){}^{14}\text{N}$ reaction, Nucl. Instrum. Methods Phys. Res. A **519** (2004) 623.
- [4.52] DYER, P., BODANSKY, D., SEAMSTER, A.G., NORMAN, E.B., MAXSON, D.R., Cross sections relevant to gamma-ray astronomy: proton induced reactions, Phys. Rev. C **23** (1981) 1865.
- [4.53] PIERCE, T.B., PECK, P.F., HENRY, W.M., Determination of carbon in steels by measurement of the prompt γ -radiation emitted during proton bombardment, Nature **4958** (1964) 571.
- [4.54] ENE, A., POPESCU, V., BADICA, T., Determination of carbon in steel using particle-induced gamma ray spectrometry, J. Optoelectron. Adv. M. **8**, (2006) 222–224.
- [4.55] LAPATTO, R., RÄISÄNEN, J., A rapid method for the quantification of C,N and O in biomedical samples by proton-induced gamma-ray emission analysis applied to human placental samples, Phys. Med. Biol. **33** (1988) 75.
- [4.56] BAIR, J.K., COHN, H.O., WILLARD, H.B., Level structure of N^{14} , Phys. Rev. **119** (1960) 2026.
- [4.57] BANERJEE, M., SRINIVASAN, N.B., ZHU, H., KIM, S.J., XU, K., WINTER, M., BECKER, H-W., ROGALLA, D., DE LOS ARCOS, T., BEKERMANN, D., BARRECAI, D., FISCHER, R.A., DEVI, A., Fabrication of ZrO_2 and ZrN films by metalorganic chemical vapor deposition employing new Zr precursors, Cryst. Growth Des. **12** (2012) 5079.
- [4.58] BEKERMANN, D., LUDWIG, A., TOADER, T., MACCATO, C., BARRECA, D., GASPAROTTO, A., BOCK, C., WIECK, A.D., KUNZE, U., TONDELLO, E., FISCHER, R.A., DEVI, A., MOCVD of ZnO films from Bis(ketoiminato) Zn(II) precursors: structure, morphology and optical properties, Chem. Vap. Deposition **17** (2011) 155.
- [4.59] CSEDREKI, L., UZONYI, I., SZÍKI, G.Á., SZIKSZAI, Z., GYÜRKY, GY., KISS, Á.Z., Measurements and assessment of ${}^{12}\text{C}(d,p\gamma){}^{13}\text{C}$ reaction cross sections in the

- deuteron energy range 740–2000 keV for analytical applications, Nucl. Instrum. Methods Phys. Res. B **328** (2014) 59.
- [4.60] TRYTI, S., HOLTEBEKK, T., REKSTAD, J., Angular distributions of protons near resonance for the reaction $^{12}\text{C}(d,p\gamma)^{13}\text{C}$ obtained by shape studies of γ -ray lines, Nucl. Phys. A **201** (1973) 135–144.
- [4.61] TRYTI, S., HOLTEBEKK, T., UGLETVEIT, F., Angular distributions of protons from the reaction $^{12}\text{C}(d,p\gamma)^{13}\text{C}$ obtained by shape studies of γ -ray lines, Nucl. Phys. A **251** (1975) 206–224.
- [4.62] PAPILLON, F., WALTER, P., Analytical use of the multiple gamma-rays from the $^{12}\text{C}(d,p\gamma)^{13}\text{C}^*$ nuclear reaction, Nucl. Instrum. Methods Phys. Res. B **132** (1997) 468–480.
- [4.63] MARCHAND, B., MIZOHATA, K., RÄISÄNEN, J., Proton induced gamma-ray production cross sections and thick-target yields for boron, nitrogen and silicon, Nucl. Instrum. Methods Phys. Res. B **378** (2016) 25–30.
- [4.64] AJZENBERG-SELOVE, F., Energy levels of light nuclei $A = 13$ – 15 , Nucl. Phys. A **523** (1991) 1–196.
- [4.65] RÄISÄNEN, J., TIKKANEN, P.O., Calibration of accelerator proton energy by the $^{14}\text{N}(p,p'\gamma)^{14}\text{N}$ reaction resonances, Nucl. Instrum. Methods Phys. Res. A **723** (2013) 5.
- [4.66] PHILLIPS, G.W., RICHARD, P., ELLIOT, D.O., HOPKINS, F.F., PORTER, A.C., Structure of mass 15: the $^{14}\text{N}(p,\gamma)^{15}\text{O}$ and $^{14}\text{N}(p,p'\gamma)$ reactions, Phys. Rev. C **5** (1972) 297.
- [4.67] BENHABILES-MEZHOUD, H., KIENER, J., THIBAUD, J.-P., TATISCHEFF, V., DELONCLE, I., COC, A., DUPRAT, J., HAMADACHE, C., LEFEBVRE-SCHUHL, DALOUZY, J.-C., DE GRACEY, F., DE OLIVEIRA, F., A., DAYRAS, DE SÉRÉVILLE, N., PELLEGRITI, M.-G., F., LAMIA, L., OUICHAOU, S., Measurements of nuclear γ -ray line emission in interactions of protons and α particles with N, O, Ne, and Si, Phys. Rev. C **83** (2011) 024603.
- [4.68] WEST, M.L., JONES, C.M., BAIR, J.K., WILLARD, H.B., Level structure in ^{15}O from the proton bombardment of ^{14}N , Phys. Rev. **179** (1969) 1047.
- [4.69] CHIARI, M., FERRACCIOLI, G., MELON, B., NANNINI, A., PEREGO, A., SALVESTRINI, L., LAGOYANNIS, A., PREKETES-SIGALAS, K., Measurement of proton induced thick target γ -ray yields on B, N, Na, Al and Si from 2.5 to 4.1 MeV, Nucl. Instrum. Methods Phys. Res. B **366** (2016) 77; Ion Beam Analysis Nuclear Data Library (IBANDL), <http://www-nds.iaea.org/ibandl/>
- [4.70] GORODETZKY, S., ADLOFF, J.C., BROCHARD, F., CHEVALLIER, P., DISPIER, D., GORODETZKY, PH., MODJTAHED-ZADEH, R., SCHEIBLING, F., Cascades γ - γ de quatre résonances de la réaction $^{15}\text{N}(p,\gamma)^{16}\text{O}$, Nucl. Phys. A **113** (1968) 221.
- [4.71] ROLFS, C., RODNEY, W.S., Proton capture by ^{15}N at stellar energies, Nucl. Phys. A **235** (1974) 450.
- [4.72] IMBRIANI, G., DEBOER, R. J., BEST, A., COUDER, M., GERVINO, G., GÖRRES, J., LEBLANC, P. J., LEISTE, H., LEMUT, A., STECH, E., STRIEDER, F., UBERSEDER, E., WIESCHER, M., Measurement of γ rays from $^{15}\text{N}(p,\gamma)^{16}\text{O}$ cascade and $^{15}\text{N}(p,\alpha_1\gamma)^{12}\text{C}$ reactions, Phys. Rev. C **85** (2012) 065810.
- [4.73] HÄNNINEN, R., RÄISÄNEN, J., Nitrogen determination with external beam proton induced gamma-ray emission analysis, Nucl. Instrum. Methods Phys. Res. B **5** (1984) 34–38.

- [4.74] VAN BEBBER, H., BORUCKI, L., FARZIN, K., KISS, Á.Z., SCHULTE, W.H., Total cross section of the $^{14}\text{N}(\text{d},\text{p}\gamma)^{15}\text{N}$ nuclear reaction for analytical applications, *Nucl. Instrum. Methods Phys. Res. B* **136–138** (1998) 72.
- [4.75] CSEDREKI, L., UZONYI, I., SZIKSZAI, Z., GYÜRKY, GY., SZÍKI, G.Á., KISS, Á.Z., Measurement of gamm-ray production cross section for nuclear reactions $^{14}\text{N}(\text{d},\text{p}\gamma)^{15}\text{N}$ and $^{28}\text{Si}(\text{d},\text{p}\gamma)^{29}\text{Si}$, *Nucl. Instrum. Methods Phys. Res. B* **328** (2014) 20–26.
- [4.76] CSEDREKI, L., Experimental conditions for cross-section measurements for analytical purposes, *Acta Phys. Debrecina* **46** (2012) 25–35.
- [4.77] CSEDREKI, L., HALÁSZ, Z., KISS, Á.Z., Assessment of experimental d-PIGE γ -ray production cross-sections for ^{12}C , ^{14}N and ^{16}O and comparison with absolute thick target yields, *Nucl. Instrum. Methods Phys. Res. B* **380** (2016) 1–10.
- [4.78] Unpublished data found on IBANDL [<https://www-nds.iaea.org/exfor/ibandl.htm>].
- [4.79] ZAMBONI, I., SIKETIĆ, Z., JAKŠIĆ, M., BOGDANOVIĆ RADOVIĆ, I., Measurement of proton induced γ -ray emission cross-sections on MgF_2 target in the energy range 1.95–3.05 MeV, *Nucl. Instrum. Methods Phys. Res. B* **342** (2015) 266–270.
- [4.80] ALLEGRO, P.R.P., DE ALMEIDA RIZZUTTO, M., MEDINA, N.H., Improvements in the PIGE technique via gamma-ray angular distribution, *Microchem. J.* **126** (2016) 287–295.
- [4.81] CHAUDRI, M. A., The absolute total cross-section and thick target yields of the $^{19}\text{F}(\text{p},\text{p}'\gamma)^{19}\text{F}$ reaction from 0.4 to 4.3 MeV, *Radiat. Eff. Defect. S.* **94** (1986) 145–150.
- [4.82] JESUS, A.P., BRAZINHA, B., RIBEIRO, J.P., Excitation function and cross-section of the reaction $^{19}\text{F}(\text{p},\text{p}'\gamma)^{19}\text{F}$, *Nucl. Instrum. Methods Phys. Res. B* **161–163** (2000) 186–190.
- [4.83] GRAMBOLE, D., BAUER, C., GIPPNER, P., PHEISER, C., RUDOLPH, W., THOMAS, H.J., Fluorine determination in the near-surface region of solids using the $^{19}\text{F}(\text{p},\text{p}'\gamma)^{19}\text{F}$ resonance reaction, *J. Radioanal. Nucl. Chem.* **83** (1984) 107.
- [4.84] RANKEN, W.A., BONNER, T.W., MCCRARY, J.H., Energy dependence of $\text{F}^{19} + p$ reactions, *Phys. Rev.* **109** (1958) 1646–1651.
- [4.85] LAGOYANNIS, A., private communication.
- [4.86] KENNY, M.J., Thick target gamma yields from fluorine, *Austr. J. Phys.* **34** (1981) 35–42.
- [4.87] MATEUS, R., JESUS, A.P., RIBEIRO, J.P., Quantitative analysis of light elements in thick samples by PIGE, *Nucl. Instrum. Methods Phys. Res. B* **219–220** (2004) 519–523.
- [4.88] CHIARI, M., ALVES, E. BOGDANOVIĆ RADOVIĆ, I., CRUZ, J., CSEDREKI, L. FONSECA, M., GALAVIZ, D., HENRIQUES, A., JAKŠIĆ, M., JESUS, A.P., KAKUEE, O., KISS, Á.Z., LAGOYANNIS, A., LOURENÇO, F., LUÍS, H., MACHADO, J., MELON, B., NUVIADENU, C.K., SALVESTRINI, L., SHARIFZEDEH, N., SIKETIĆ, Z., SZÍKI, G.Á., SZIKSZAI, Z., TEUBIG, P., VELHO, P., ZAMBONI, I., ZARZA, M., Measurement of proton induced γ -ray emission cross-sections on Na from 1.0 to 4.1 MeV, *Nucl. Instrum. Methods Phys. Res. B* (2017) available online.
- [4.89] CACIOLLI, A., CALZOLAI, G., CHIARI, M., CLIMENT-FONT, A., GARCIA, G., LUCARELLI, F., NAVA, S., Proton elastic scattering and proton induced γ -ray emission cross-sections on Na from 2 to 5 MeV, *Nucl. Instrum. Methods Phys. Res. B* **266** (2008) 1392.

- [4.90] MATEUS, R., JESUS, A.P., CRUZ, J., RIBEIRO, J.P., Measurement of the inelastic scattering of protons by ^{23}Na in the energy range 1.25–2.40 MeV, *Nucl. Instrum. Methods Phys. Res. B* **219–220** (2004) 307.
- [4.91] TROCELLIER, P., ENGELMANN, CH., Fonctions d'excitation des reaction snucleaires: $^{23}\text{Na}(p,p'\gamma)^{23}\text{Na}$, $^{23}\text{Na}(p,\alpha\gamma)^{20}\text{Ne}$ et $^{23}\text{Na}(p,\alpha_0)^{20}\text{Ne}$ entre 500 et 1700 keV, *J. Radioanal. Nucl. Chem.* **67** (1981) 135–142.
- [4.92] CALZOLAI, G., CHIARI, M., LUCARELLI, F., NAVA, S., PORTARENA, S., Proton induced γ -ray emission yields for the analysis of light elements in aerosol samples in an external beam set-up, *Nucl. Instrum. Methods Phys Res. B* **268** (2010) 1540.
- [4.93] STELSON, P.H., PRESTON, W.M., Resonant states of Mg^{24} excited by protons on sodium, *Phys. Rev.* **95** (1954) 974.
- [4.94] HIRATATE, Y., TAKEUCHI, Y., YAMAYA, T., MORITA, S., Some studies of the $^{23}\text{Na} + p$ reaction at $E_p = 2.2\text{--}4.5$ MeV, *J. Phys. Soc. Jpn.* **24** (1968) 690.
- [4.95] ASKING, L., SWIETLICKI, E., GARG, M.L., PIGE analysis of sodium in thin aerosol samples, *Nucl. Instrum. Methods Phys. Res. B* **22** (1987) 368.
- [4.96] BODART, F., DECONNINCK, G., DEMORTIER, G., Quantitative analysis of sodium by (p,γ) reactions, *J. Radioanal. Nucl. Chem.* **35** (1977) 95.
- [4.97] GURBICH, A.F., Evaluation of cross-sections for particle induced gamma-ray emission (PIGE) spectroscopy, *Nucl. Instrum. Methods Phys. Res. B* **331** (2014) 31.
- [4.98] SALAH, H., TOUCHRIFT, B., Multielemental analysis of zeolites using prompt nuclear reactions gamma rays, *Nucl. Instrum. Methods Phys. Res. B* **129** (1997) 261–265.
- [4.99] SMIT, Z., JEZERŠEK, D., KNIFIC, T., ISTENIĆ, J., PIXE-PIGE analysis of Carolingian period glass from Slovenia, *Nucl. Instrum. Methods Phys. Res. B.* **267** (2009) 121–124.
- [4.100] SHARIFZADEH, N., KAKUEE, O., MOHAMMADI, S., Measurements of proton induced γ -ray emission cross-sections on Mg from 1.0 to 3.0 MeV, *Nucl. Instrum. Methods Phys. Res. B* **372** (2016) 109–113.
- [4.101] CHIARI, M., MELON, B., SALVESTRINI, L., FONSECA, M., ALVES, E., JESUS, A.P., Measurement of proton induced γ -ray emission cross-sections on Al from 2.5 to 4.1 MeV, *Nucl. Instrum. Methods Phys. Res. B* **332** (2014) 355–358.
- [4.102] JOKAR, A., KAKUEE, O., LAMEHI-RACHTI, M., SHARIFZADEH, N., FATHOLLAHI, V., Differential cross-section measurements of $^{27}\text{Al}(p,p'\gamma)^{27}\text{Al}$ and $^{27}\text{Al}(p,\alpha\gamma)^{24}\text{Mg}$ reactions in the energy range of 1.6–3.0 MeV, *Nucl. Instrum. Methods Phys. Res. B* **362** (2015) 138–141.
- [4.103] JOKAR, A., KAKUEE, O., LAMEHI-RACHTI, M., FATHOLLAHI, V., Thick target yields of proton induced gamma-ray emission from Al, Si and P, *Nucl. Instr. Phys. Meth. Res. B* **394** (2017) 28–32.
- [4.104] WARSH, K.L., TEMMER, G.M., BLIEDEN, H.R., The $\text{Al}^{27}(p,\alpha)\text{Mg}^{24}$ reaction with 3 to 12 MeV protons, *Nucl. Phys.* **44** (1963) 329–337.
- [4.105] HARISSOPULOS, S., CHRONIDOU, C., SPYROU, K., PARADELLIS, T., ROLFS, C., SCHULTE, W.H., BECKER, H.W., The $^{27}\text{Al}(p,\gamma)^{28}\text{Si}$ reaction: direct capture cross-section and resonance strengths at $E_p = 0.2\text{--}1.12$ MeV, *Eur. Phys. J. A* **9** (2000) 479.
- [4.106] WANG, Y., NASTASI, M., (eds), *Handbook of Modern Ion Beam Materials Analysis*, 2nd edn, Materials Research Society, Warrendale, Pennsylvania (2010).
- [4.107] DECONNINCK, G., DEMORTIER, G., Quantitative analysis of aluminum by prompt nuclear reactions, *J. Radioanal. Nucl. Chem.* **12** (1972) 189–208.

- [4.108] JOKAR, A., KAKUEE, O., LAMEHI-RACHTI, M., Differential cross-sections measurement of $^{28}\text{Si}(p, p'\gamma)^{28}\text{Si}$ and $^{29}\text{Si}(p, p'\gamma)^{29}\text{Si}$ reactions for PIGE applications, Nucl. Instrum. Methods Phys. Res. B **371** (2016) 37–40.
- [4.109] RÄISÄNEN, J., HIRVONEN, J., ANTTILA, A., The diffusion of silicon in germanium, Solid-State Electron. **24** (1981) 333–336.
- [4.110] RÄISÄNEN, J., KEINONEN, J., Annealing behaviour of Si in ion-implanted α -Ti, Appl. Phys. Lett. **49** 13 (1986) 773–775.
- [4.111] AHLGREN, T., LIKONEN, J., SLOTTE, J., RÄISÄNEN, J., RAJATORA, M., KEINONEN, J., Concentration dependent and independent Si diffusion in ion-implanted GaAs, Phys. Rev. B **56** (1997) 4597–4603.
- [4.112] CHIARI, M., FERRACCIOLI, G., MELON, B., NANNINI, A., PEREGO, A., SALVESTRINI, L., LAGOYANNIS, A., PREKETES-SIGALAS, K., Measurement of proton induced thick target γ -ray yields on B, N, Na, Al and Si from 2.5 to 4.1 MeV, Nucl. Instrum. Methods Phys. Res. B **366** (2016) 77–82.
- [4.113] CSEDREKI, L., UZONYI, I., SZIKSZAI, Z., GYÜRKY, GY., SZÍKI, G.Á., KISS, Á.Z., Measurement of gamma-ray production cross-sections for nuclear reactions $^{14}\text{N}(d, p\gamma)^{15}\text{N}$ and $^{28}\text{Si}(d, p\gamma)^{29}\text{Si}$, Nucl. Instrum. Methods Phys. Res. B **328** (2014) 20–26.
- [4.114] JOKAR, A. KAKUEE, O., LAMEHI-RACHTI, M., Differential cross-section measurement of $^{31}\text{P}(p, p\gamma_1)^{31}\text{P}$ reaction for PIGE applications, Nucl. Instrum. Methods Phys. Res. B **383** (2016) 152–155.
- [4.115] DEMORTIER, G., BODART, F., Quantitative analysis of phosphorus by (p, γ) reactions, J. Radioanal. Nucl. Chem. **12** (1972) 209–219.
- [4.116] LAGOYANNIS, A., *et al.*, private communication.
- [4.117] RAO, P., KUMAR, S., VIKRAMKUMAR, S., RAJU, V.S., Measurement of differential cross-sections and widths of resonances in $^{32}\text{S}(p, p'\gamma)^{32}\text{S}$ reaction in the 3.0–4.0 MeV region, Nucl. Instrum. Methods Phys. Res. B **269** (2011) 2557
- [4.118] TSARTSARAKOS, C., MISAEILIDES, P., KATSANOS, A., Cross-sections for the $^{32}\text{S}(p, p'\gamma)^{32}\text{S}$ nuclear reaction used for the profiling of sulphur on materials surfaces, Nucl. Instrum. Methods Phys. Res. B **45** (1990) 33–35.
- [4.119] OLNESS, J. W., HAEBERLI, W., LEWIS, H.W., Levels of Cl33 from $\text{S}^{32}(p, p)\text{S}^{32}$ and $\text{S}^{32}(p, p'\gamma)\text{S}^{32}$, Phys. Rev. **112** (1958) 1702.
- [4.120] DEMORTIER, G., Prompt gamma-ray yields from proton bombardment of transition elements (Ti to Zn), J. Radioanal. Nucl. Chem. **45** (1978) 459–496.
- [4.121] KENNET, S.R., MITCHELL, L.W., ANDERSEN, M.R., SARGOOD, D.G., Cross-section measurements and thermonuclear reaction rates for $^{46}\text{Ti}(p, \gamma)^{47}\text{V}$, $^{47}\text{Ti}(p, \gamma)^{48}\text{V}$, $^{47}\text{Ti}(p, n)^{47}\text{V}$ and $^{48}\text{Ti}(p, \gamma)^{49}\text{V}$, Nucl. Phys. A **368** (1981) 337–351.
- [4.122] GOSSETT, C.R., A method for determining depth profiles of transition elements in steels, Nucl. Instrum. Methods **168** (1980) 217–221.
- [4.123] KRIVONOSOV, G.A., NEMASHKALO, B.A., STORIZHKO, V.E., KLYUCHAREV, A.P., EKHCHEV, O.I., CHIRT, V.K., Inelastic scattering of protons by medium-weight nuclei at low energies, Yad. Fiz. **24** (1976) 461.
- [4.124] KENNET, S.R., MITCHELL, L.W., ANDERSON, M.R., SARGOOD, D.G., Cross-section measurements and thermonuclear reaction rates for $^{52}\text{Cr}(p, \gamma)^{53}\text{Mn}$ and $^{54}\text{Fe}(p, \gamma)^{55}\text{Co}$, Nucl. Phys. A **363** (1981) 233.

5. THE EMITTED RADIATION YIELD ANALYSIS (ERYA) CODE FOR PIGE ANALYSIS

5.1. INTRODUCTION

Emitted Radiation Yield Analysis (ERYA) [5.1] is a code developed for PIGE analysis. It uses relevant quantities and experimental parameters to calculate the concentrations of elements/isotopes, given their gamma-ray yield (and vice-versa). At the onset, ERYA was programmed only for in-depth homogeneous samples, i.e. bulk analysis. In order to deal with depth-dependent concentrations, ERYA-profiling was developed, which is a code based on ERYA. Both codes are discussed in more detail in the following sections.

5.2. ERYA

5.2.1. ERYA-bulk

Section 2.1 provides the basis of the calculations made by ERYA [5.2]. Eq. 5.1 calculates the yield of gamma-rays for an in-depth homogeneous sample, with energy E_γ detected at a given ion beam energy E_0 . The yield is assumed to be isotropic.

$$Y(E) = \varepsilon_{\text{abs}}(E_\gamma) \cdot \left(\frac{Q}{e} \right) \cdot f_m \cdot f_i \cdot N_{\text{av}} \cdot A^{-1} \cdot \int_0^{E_0} \sigma(E) / S_m(E) dE, \quad (5.1)$$

where Q/e is the number of bombarding ions, Q is the collected charge, e is the electric charge of the ion beam, σ is the relevant nuclear reaction cross-section, ε_{abs} is the absolute efficiency of detection, f_i is the isotopic abundance, N_{av} is the Avogadro number, A is the atomic mass of the relevant element and $S_m(E)$ is the mass stopping power, expressed in energy per areal mass units.

In order to perform the calculation, specifically the integration, ERYA divides the sample into n sublayers that are perpendicular to the incident beam, i.e. the energy range of the incident ions is divided into several energy intervals. The magnitude of each interval is such that, within each interval, the stopping power cross-section can be assumed to be constant. The energy intervals may be set equal to the energy steps that are necessary to accurately define the employed excitation function. This means that the energy steps are small enough to assume that, in between any two consecutive values of the energy, the excitation function has a linear dependence on the energy. Taking the above considerations into account, the integral may be approximated by the following sum:

$$\int_0^{E_0} \sigma(E) / \varepsilon(E) dE = \sum_k \left[(1/S_{mk}) \cdot \int_{E_k}^{E_{k+1}} \sigma(E) dE \right] = \sum_k \left[(1/S_{mk}) \cdot \sigma(E_{k,k+1}) \cdot (E_{k+1} - E_k) \right] \quad (5.2)$$

where the cross-section for each layer k is the mean between σ_k and σ_{k+1} , i.e. the measured cross-sections at energies E_k and E_{k+1} . The integrated cross-section increases rapidly with the proton energy until the minimum energy in the cross-section data file E_{min} is reached, which replaces zero, in this case, as the end point of integration.

The code was developed in a Labview-based interface in order to be user-friendly. The main interface is shown in Fig. 5.1. The eight inputs listed below were introduced via this interface and are necessary to perform the proper calculations.

- (i) **Efficiency of the gamma-ray detector** — accessible through the “database” button on the main interface (Fig. 5.1). Users can also upload a text file to the code folder, with a table of efficiency values for a given energy range or function of the gamma energy. A specific function or number for a particular gamma-ray may be entered via the main interface (Fig. 5.1). Number of elements and choice of elements may also be entered via the main interface (Fig. 5.1) and includes the elements/isotopes to be quantified by PIGE, which may be minor or trace components of the sample, and the elements which are major components of the sample composition. This information is important for calculation of the stopping power. There is a database associated with ERYA that contains the atomic number and masses of some elements and respective isotopic abundances (Fig. 5.2). This information will be automatically uploaded when the user chooses an element, but the user may also access the database through a button on the main interface and modify or add information as needed (Fig. 5.2).
- (ii) **Cross-Section of the gamma-producing reaction used to quantify the corresponding isotope** — accessible through the “database” button on the main interface (Fig. 5.1). There is a database of excitation functions, which were measured or adopted by the Lisbon group and that is connected with ERYA. This database reduces input from individual users since the appropriate isotope can just be selected via the interface. If more than one gamma-ray is associated with the isotope, the user must choose the gamma-ray as well. The user may also replace the existing excitation functions through the same menu as referred to in #2. Direct input from IBANDL database is also possible.
- (iii) **Stopping power** — accessible through the “database” button on the main interface (Fig. 5.1). The user will find a table of Ziegler parameters (see the respective window, in an inset over the graph in Fig. 5.1) for the semi-empirical calculation of the stopping power. The user can modify these parameters as needed.
- (iv) **First guess of the sample composition** — atomic fractions of the sample components, which must sum up to 1, are entered in the “%” column (Fig. 5.1).
- (v) **Gamma-ray experimental yields** — entered in the column marked “YoExp” (Fig. 5.1). These must correspond to 1 μC of collected charge, which is the default value. If not, the user must enter the charge in the respective field on the main interface (Fig. 5.1).
- (vi) **Target thickness** — entered in the “thick” field (Fig. 5.1). A value only needs to be added for a thin or semi-thick sample.
- (vii) **Proton energy of analysis** — entered in the “energy max” field on the main interface (Fig. 5.1). The sum in Eq. 5.2 will start from this ‘maximum’ energy and will proceed by summing terms in well-defined energy steps until the minimum energy in the cross-section data file E_{\min} is reached. A different step than the experimental step used in the measurement may be chosen from the “step size” field on the main interface (Fig. 5.1). The default value is 1 keV.

- (viii) **Calibration parameter** — entered in the “CP” column on the main interface (Fig. 5.1). The calibration parameter (see Section 2.1) may be inserted in order to take into consideration the experimental system of the user.

After (i–viii) have been entered, the ERYA main interface will display the resulting yields that correspond to the inserted atomic fractions in the column marked “YoSimul”. Users can then compare “YoSimul” with “YoExp” and modify the introduced atomic fractions until “YoSimul” agrees with “YoExp”.

The ERYA code can also perform a fitting operation, which employs a non-linear Levenberg-Marquar algorithm [5.3, 5.4] and provides the optimal sample composition by simultaneously fitting the gamma-ray yields of all the elements in the sample to be quantified. The user can choose either of the following options:

- (a) Set the initial guess for some of the elements and allow the fit to modify the others (see the corresponding column on the main interface and the example in Fig. 5.1);
- (b) Group the elements in order to keep their atomic ratio constant and allow the fit to modify the specific amounts of each element (fitting mode field on the main interface in Fig. 5.1).

The information provided for the major component of the sample composition usually has two sources: (i) other analytical sources, e.g. from PIXE analysis and (ii) the chemical content. This results in the following situations, which explain the corresponding two options above:

- (a) From PIXE analyses one obtains concentrations of elements heavier than Na, in the case of thin window detectors, and heavier than Mg, in all other cases. In order to reach a concentration sum of 100%, the undetected lighter elements are usually assumed to be oxygen, which is the main light element of most samples. In this case, the ERYA fit should use the PIXE data as a first guess and the fit should be performed on the elemental concentrations of the elements seen by PIGE (even if also detected by PIXE) and the oxygen concentration. The concentrations of the other elements, which are only detected by PIXE, should remain fixed;
- (b) If the major chemical composition of the sample is known, assuming that the elements to be quantified by PIGE are only minor or trace elements of the sample, the major chemical composition may be given as the first guess. The fit should be performed with the corresponding major elements grouped so that the ratios will stay constant while the sum of the concentrations is allowed to vary.

In the example given in Fig. 5.1, given option (b), Ag would be included in the fitting procedure, and Li and F would be grouped to keep the LiF stoichiometry. As a result, a better fit would be achieved.

To conclude this section on ERYA-bulk, the flow chart of the main code is illustrated in Fig. 5.3.

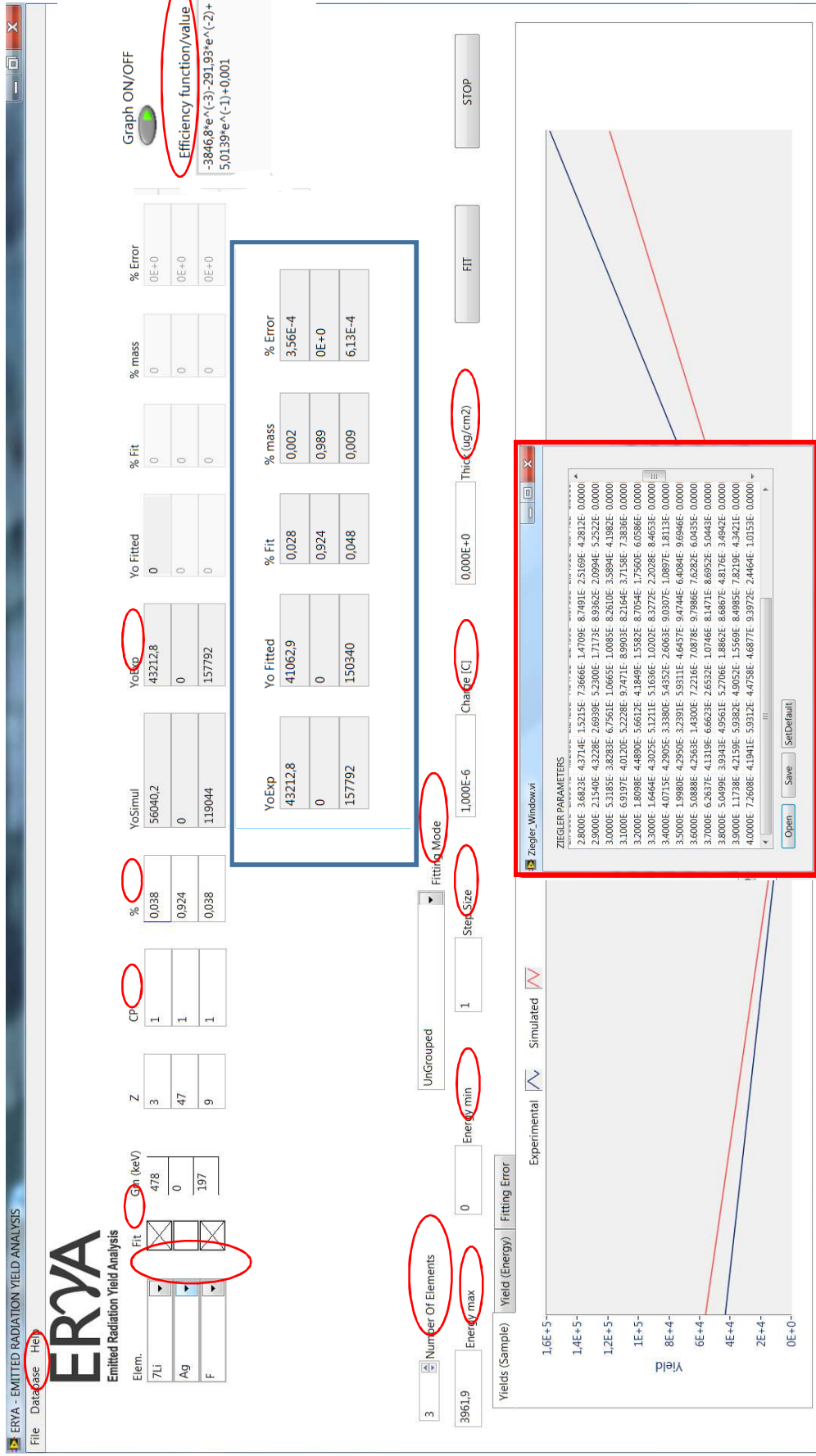


FIG. 5.1. Main interface of ERYA. The meaning of each different field is explained in the text. In this case, a mixture of Ag powder with LiF is displayed before the fitting procedure. The first guess of the atomic fraction was entered under the “%” column. In the inset (blue square), results are shown from after the fitting, where “% fit” and “% mass” give the atomic fractions and the mass fractions respectively.

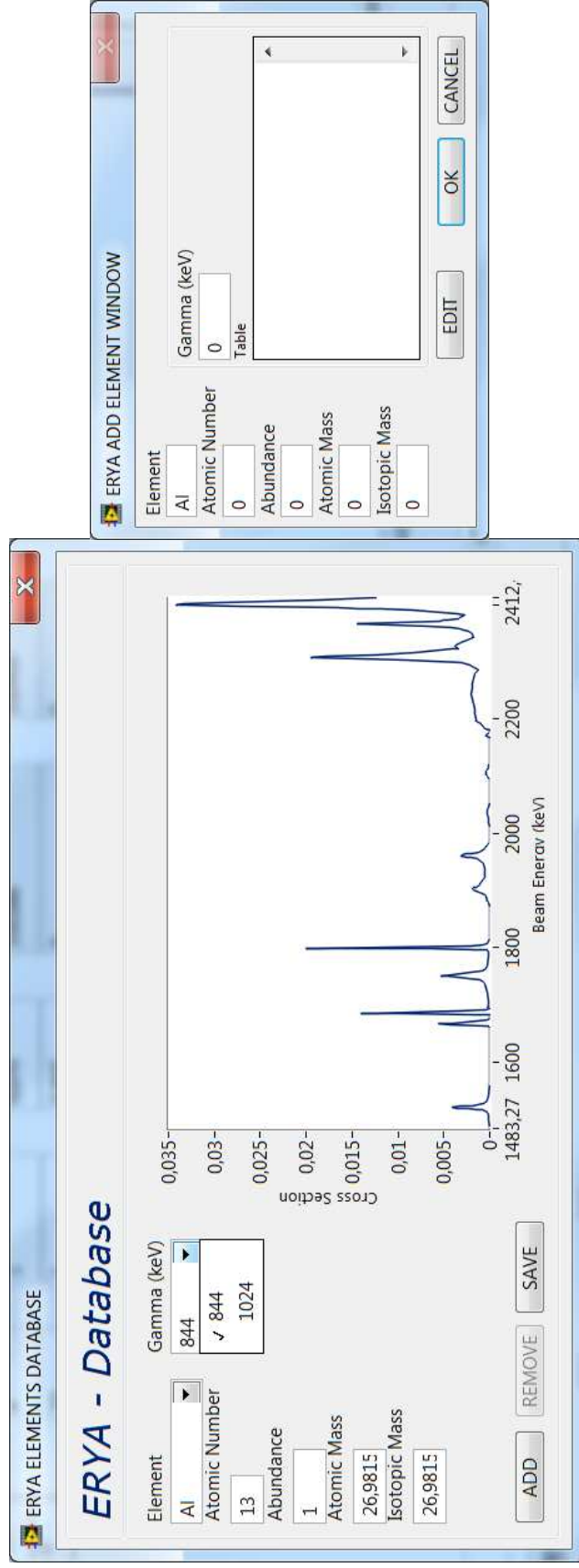


FIG. 5.2. The database associated with ERYA. The scale of the graph may be modified in order to zoom into a specific energy range. Information about new elements/isotopes, including different excitation functions, can be inserted through the "add element" window.

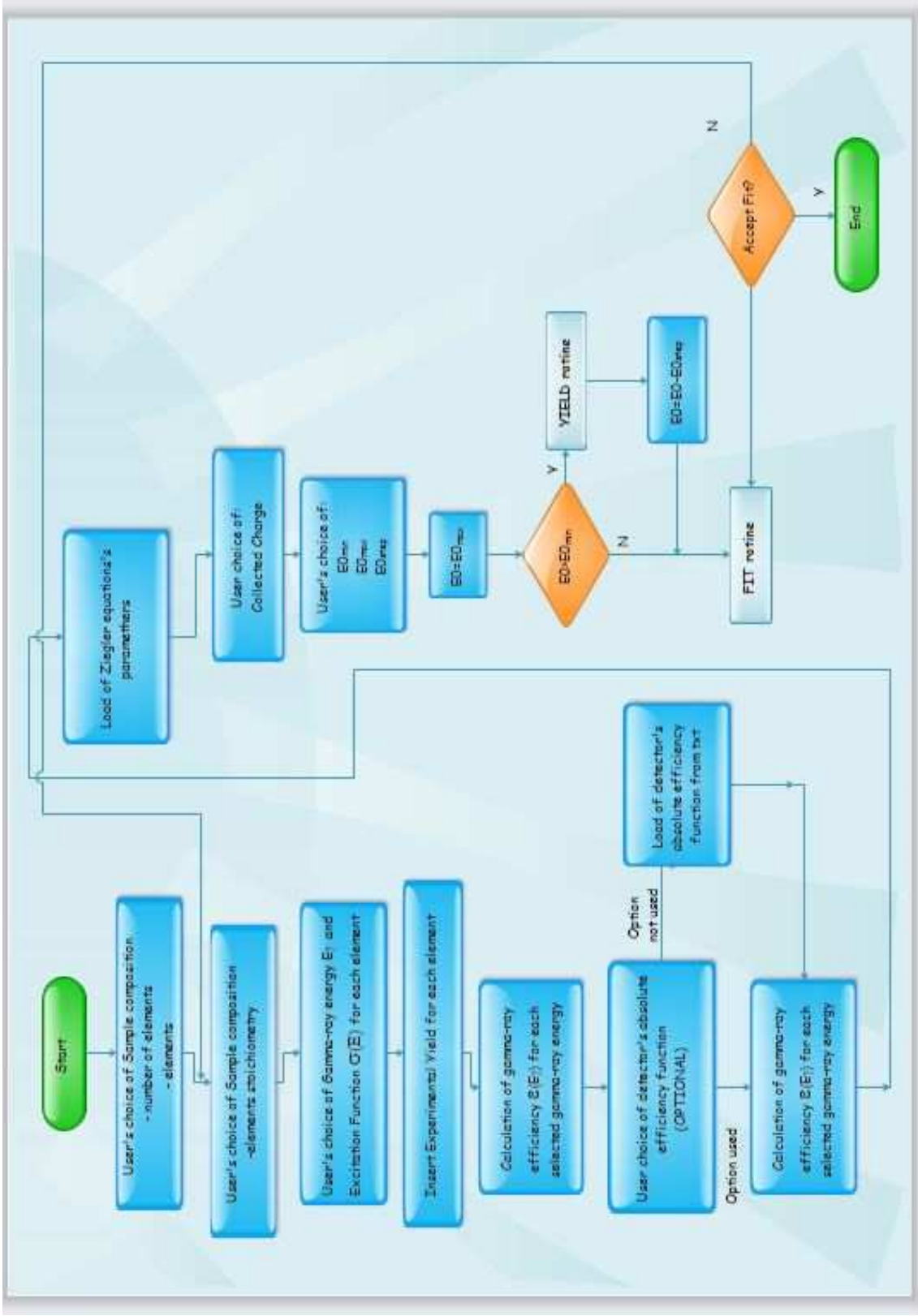


FIG. 5.3. Flow chart of the main code, highlighting the choices and parameters to be introduced by the user.

5.2.2. ERYA-profiling

Resonant nuclear reaction depth profiling (see Section 2.2) is based on the following assumption: if a proton beam with energy equal to E_R , where E_R is the energy of a resonance of the nucleus in the sample, bombards a sample, only the nuclei at the surface contribute to the gamma-ray yield. Since the nuclei contributing to the gamma-ray yield are the ones corresponding to energy E_R , increasing the incident energy moves the resonance inside the sample. The incoming protons shed part of their incident energy at a certain depth, which depends on the incident energy and the stopping power of protons in the sample material. Therefore, by increasing the energy above E_R , gamma-ray yield can be measured as a function of the incident energy, which, for thin isolated resonances, gives the concentration of the given element/isotope of the sample with respect to the depth in the sample.

In reality, the obtained profile is influenced by the energy resolution of the proton beam and the energy straggling of the proton beam along the depth of the sample. Also, if more than one resonance contributes to the yield, certain calculations need to be performed in order to obtain the correct depth profile of the sample. ERYA-profiling is a code that has been developed to perform these calculations by using a database of excitation functions in numeric form (the same as for ERYA-bulk) and taking into consideration the energy resolution of the proton beam and the energy straggling of the proton beam along the depth of the sample.

Regarding energy straggling, different approximations are implemented, i.e. the approximations of Landau, Vavilov and Gaussian [5.5–5.7]. These three approximations are considered to be valid for the amount of energy lost in the samples. To this date, this is the first code to implement energy straggling to such a high degree of accuracy. For in-depth homogeneous samples, the gamma-ray yield is given by:

$$Y(E) = \varepsilon_{\text{abs}}(E_\gamma) \cdot \left(\frac{Q}{e}\right) \cdot f_m \cdot f_i \cdot N_{\text{av}} \cdot A^{-1} \cdot \int_0^{E_0} \sigma(E) / S_m(E) \, dE \quad (5.3)$$

For in-depth heterogeneous samples, i.e. with mass fraction dependent on depth, which is equivalent to being dependent on energy, Eq. 5.3 can be modified to Eq. 5.4:

$$Y(E) = \varepsilon_{\text{abs}}(E_\gamma) \cdot \left(\frac{Q}{e}\right) \cdot f_i \cdot N_{\text{av}} \cdot A^{-1} \cdot \int_0^{E_0} f_m(E) \cdot \sigma(E) / S_m(E) \, dE \quad (5.4)$$

If, for each layer contributing to the integral, the protons do not have the same energy, but rather follow an energy distribution $F_{\bar{E}}(E)$ with mean proton energy \bar{E} , the equation above can be transformed into:

$$Y(E) = \varepsilon_{\text{abs}}(E_\gamma) \cdot \left(\frac{Q}{e}\right) \cdot f_i \cdot N_{\text{av}} \cdot A^{-1} \cdot \int_0^{E_0} \frac{f_m(\bar{E})}{S_m(\bar{E})} \cdot \left[\int_0^\infty F_{\bar{E}}(E) \cdot \sigma(E) \cdot dE \right] \cdot d\bar{E} \quad (5.5)$$

If the sample is divided into n layers thin enough so that the variations of the mean energy of the stopping power and of the mass fraction are negligible, the yield can be given by:

$$Y(E) = \varepsilon_{\text{abs}}(E_\gamma) \cdot \left(\frac{Q}{e}\right) \cdot f_i \cdot N_{\text{av}} \cdot A^{-1} \cdot \sum_{k=1}^{k=n} \frac{f_m(\bar{E}_k)}{S_m(\bar{E}_k)} \cdot \left[\int_0^\infty F_{\bar{E}}(E) \cdot \sigma(E) \cdot dE \right] \cdot \Delta\bar{E}_k \quad (5.6)$$

where the integral within brackets can also be calculated as a sum of a finite small number of energy values.

ERYA-profiling uses the same database as ERYA-bulk for excitation functions $\sigma(E)$ and stopping powers $S_m(E)$. Therefore, it was a natural choice to implement the code in the same Labview platform. The computer program C was used for the more involved distribution calculations.

The implemented Labview interface is user-friendly, with several fields for entering information, including (Fig. 5.4):

- (a) Number of elements necessary for profiling or calculating stopping power (major composition of the sample)
- (b) Type of elements
- (c) Gamma-ray chosen for profiling
- (d) Collected beam charge (default is 1 μC)
- (e) Minimum incident energy
- (f) Maximum incident energy
- (g) Concentration of elements versus depth (atoms per surface unit). Alternatively, the user can specify the density, linear thickness and composition (stoichiometry) of each layer.
- (h) Beam energy resolution
- (i) Sample temperature (a Doppler broadening distribution is also implemented in the code)

This code applies a non-automatic, user-based, iterative approach to obtain the concentration of the element versus depth. Users enter an initial guess of the concentration and compare the experimental yields obtained with the calculated ones. Next, they modify the guess in order to improve the match between measured and calculated yields.

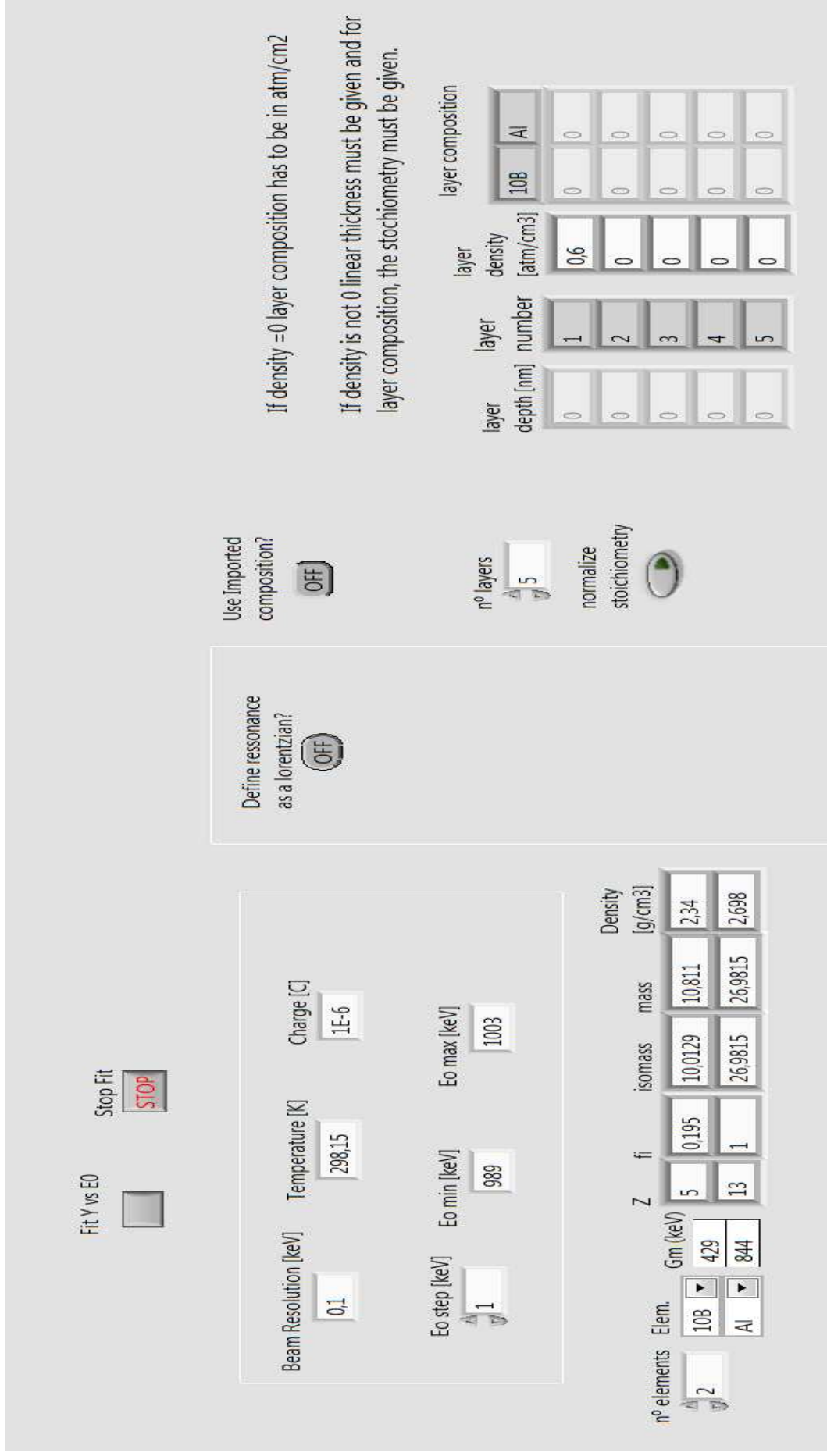


FIG. 5.4. ERYA-profiling main interface. The meaning and purpose of all buttons and fields are described in the text.

The interface has a window to upload the experimental yield versus incident energy data. The calculated yield appears in the same window, after the calculation is complete (Fig. 5.5).

Several options are available to specify the concentration of the desired element at various depths: (a) directly through the interface or (b) uploading a text file with either number of atoms of the element versus number of atoms per area of the sample, or with number of atoms per area of the element versus beam energy.

In order to more accurately define the resonance to be used for analysis, the user may choose to use a Breit-Wigner function between E_{\min} and E_{\max} , as long as the resonance energy E_R , the width of the resonance Γ_R , and the maximum cross-section value are known. The values of E_{\min} and E_{\max} may be chosen by the user. Default values used by the code correspond to $E_R \pm 5\Gamma_R$.

Figure 5.6 and 5.7 show flowcharts corresponding to the main routines.

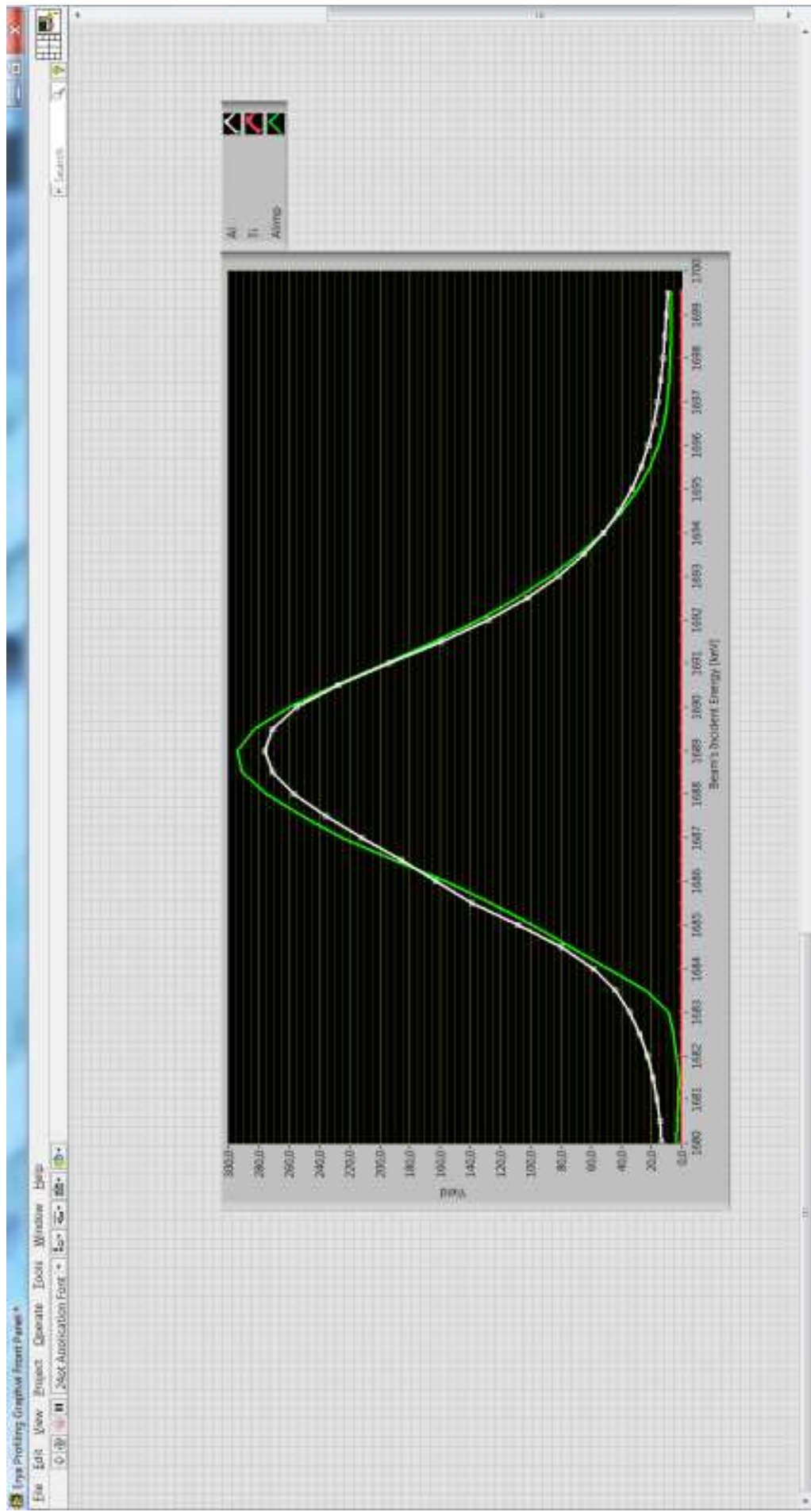


FIG. 5.5. Interface page for the comparison between experimental and calculated yields as a function of incident energy.

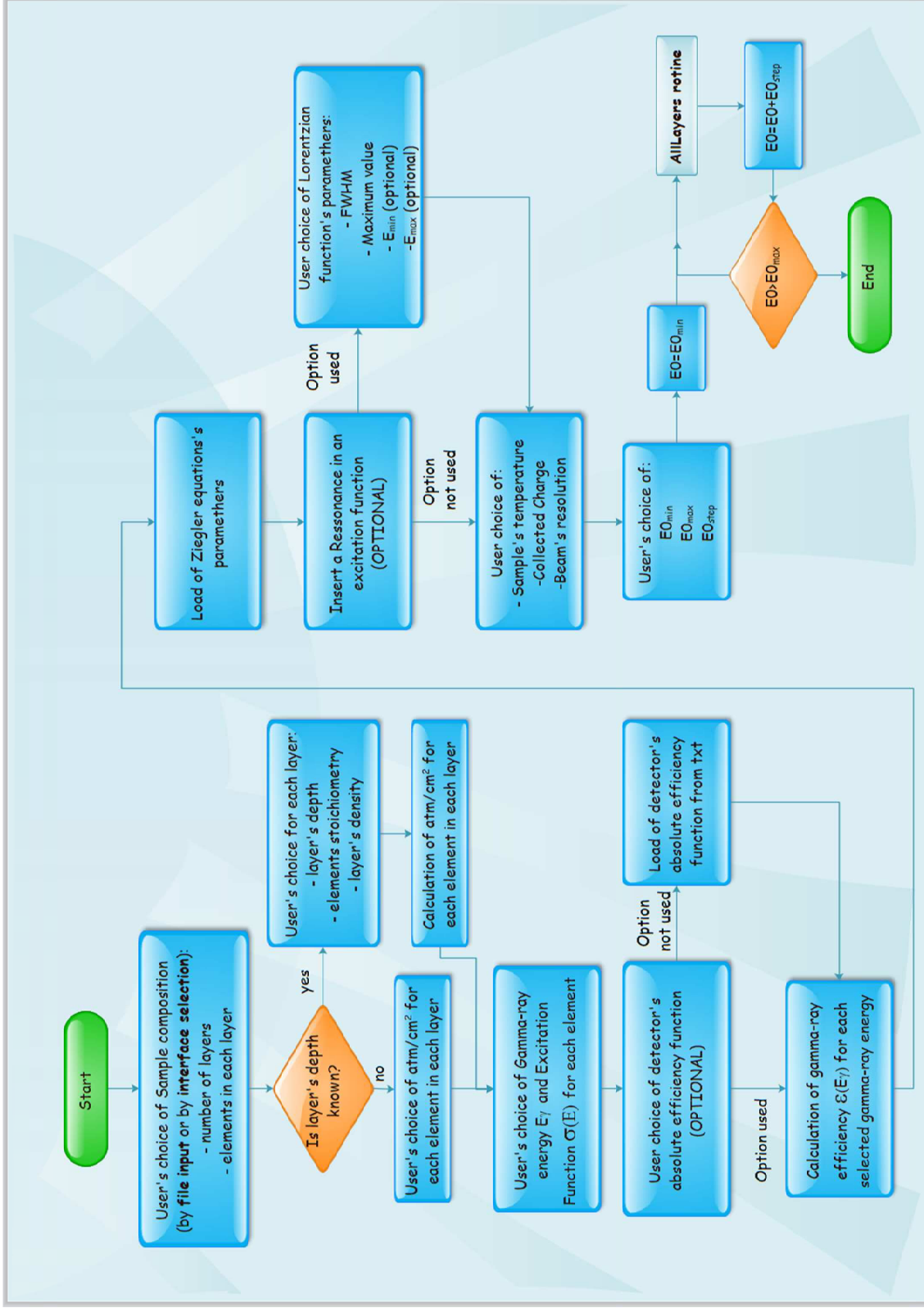


FIG. 5.6. Flowchart of ERYA-profiling main routine, highlighting the choices and parameters to be introduced by the user.

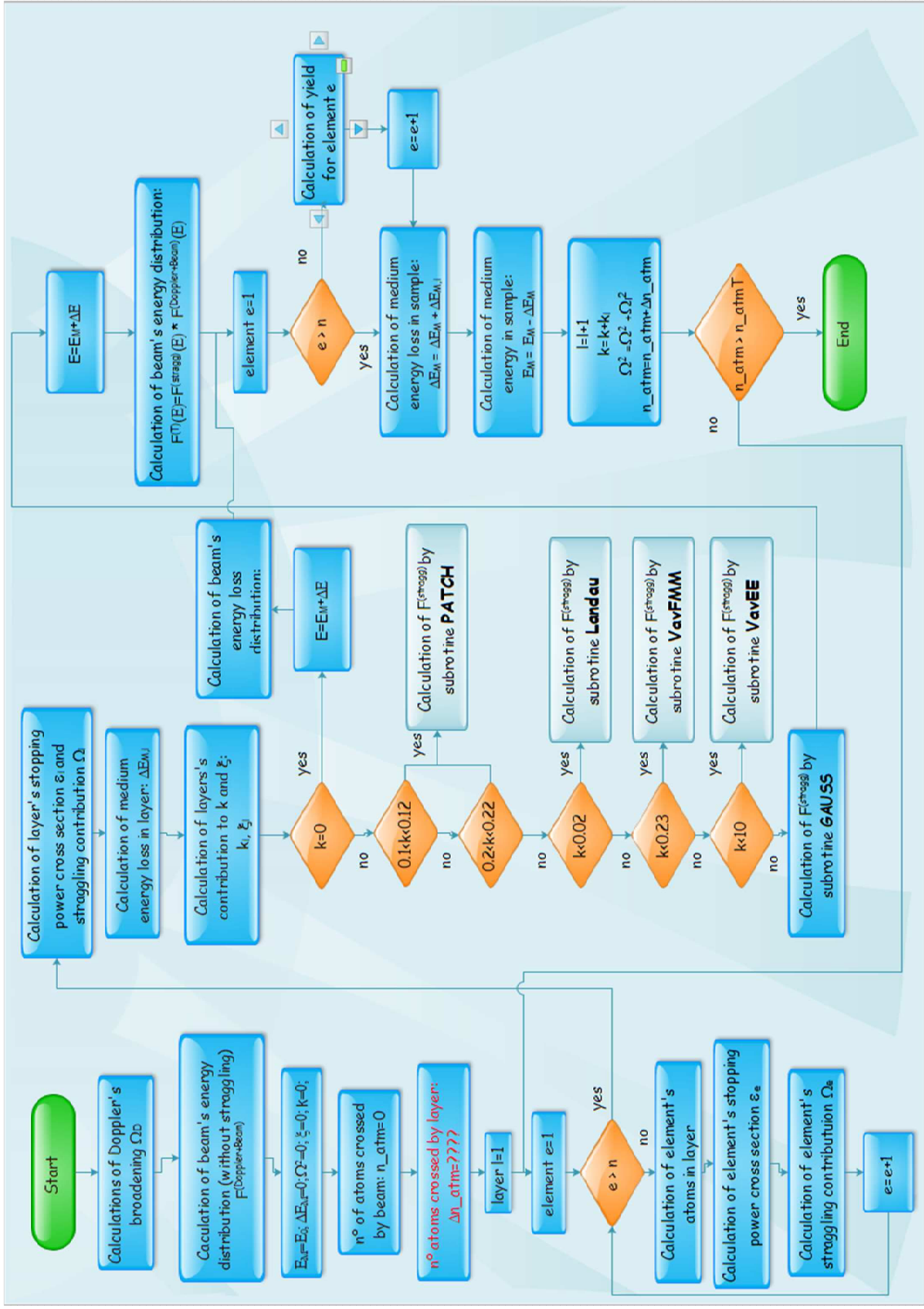


FIG. 5.7. Flowchart of the AllLayers routine, which is visible in the lower right corner of the flowchart of Fig. 5.6.

5.3. USER FEEDBACK AND FUTURE DEVELOPMENTS

Since 2013, the ERYA-bulk code has been available to be downloaded from the following webpage: http://www.ctn.tecnico.ulisboa.pt/sec/fis/rn/uk_rn_erya.htm (Fig. 5.8), where a comprehensive user's manual is also available.

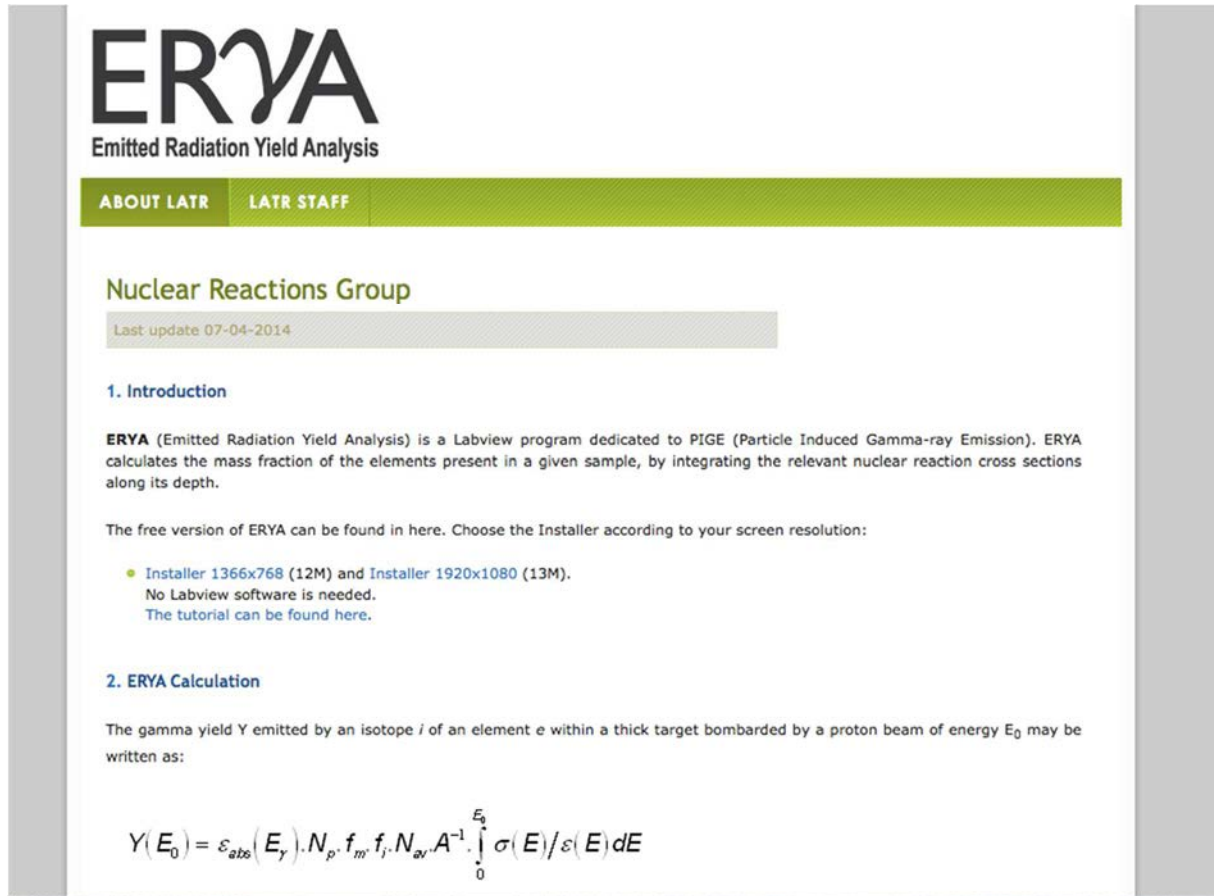


FIG. 5.8. Screenshot of the ERYA webpage.

Feedback from users has generally been positive, with the main complaints/problems falling into the following categories:

- Installation difficulties on some computers;
- Unavailability of a 32-bit version;
- Problems with screen resolution that causes the interface and corresponding fields to appear unformatted;
- User error, due to not reading the manual;
- Initially a bug prevented the introduction of a new excitation function. This problem has since been resolved;
- Some users found the graph in the main interface (Fig. 5.1) not useful and thought that it occupied too much space. The graph is now optional.

The ERYA-profiling code will be available to the public on the same webpage as the ERYA-bulk code, starting mid-April 2016. The page will also include a manual for the code.

Although not yet assessed by users, other tests have already been made, which were presented at the 22nd International Conference on Ion Beam Analysis, June 14–19, 2015 - Opatija, Croatia [5.8].

Taking into consideration the problems mentioned above, an effort is being made to implement ERYA-bulk and ERYA-profiling in a different programming language and platform interface, which will make it more suitable for the majority of users. Some improvements, such as the possibility to use resonance strengths instead of cross-sections for profiling, will be implemented.

REFERENCES TO SECTION 5

- [5.1] FONSECA, M., JESUS, A.P., LUÍS, H., MATEUS, R., CRUZ, J., GASQUES, L., GALAVIZ, D., RIBEIRO, J.P., PIGE analysis of magnesium and beryllium, *Nucl. Instrum. Methods Phys. Res. B* **268** (2010) 1806–1908.
- [5.2] MATEUS, R., JESUS, A.P., RIBEIRO, J.P., A code for quantitative analysis of light elements in thick samples by PIGE, *Nucl. Instrum. Methods Phys. Res. B* **229** (2005) 302–308.
- [5.3] LEVENBERG, K., A method for the solution of certain non-linear problems in least squares, *Quart. Appl. Math.* **2** (1944) 164–168.
- [5.4] MARQUARDT, D.W., An algorithm for least-squares estimation of nonlinear parameters, *J. Soc. Indust. Appl. Math.* **11** (1963) 431–441.
- [5.5] WANG, Y., NASTASI, M., (eds), *Handbook of Modern Ion Beam Materials Analysis*, 2nd edn, Materials Research Society, Warrendale, Pennsylvania (2010).
- [5.6] ROTONDI, A. AND MONTAGNA, P., Fast calculation of vavilov distribution, *Nucl. Instrum. Methods Phys. Res. B* **47** (1990) 215–223.
- [5.7] WILKINSON, D.H., Ionization energy loss by charged particles part I. The Landau distribution, *Nucl. Instrum. Methods Phys. Res. A* **383** (1996) 513–515.
- [5.8] BOGDANOVIĆ RADOVIĆ, I., JAKŠIĆ, M., KARLUŠIĆ, M., VIDOŠ, A., (Eds) *Book of Abstracts: 22nd International Conference on Ion Beam Analysis*, Ruder Boskovic Institute, Zagreb (2015).

6. CONCLUSIONS

Particle Induced Gamma Ray Emission (PIGE) is a well-established method of ion beam analysis that is predominantly used for measurements performed relative to a well-known standard sample. Due to the previous lack of many cross-section data, the full potential of this technique could not be reached. The purpose of this CRP was to address the lack of a comprehensive, up-to-date compilation of available PIGE cross-sections and yields for IBA purposes, i.e. inelastic scattering and nuclear reactions, and the scarcity of pre-existing PIGE data. The ultimate goal is to address the long-standing needs of the IBA community in implementing a fully developed standardless PIGE analysis technique and the CRP was a major step towards achieving this vision.

To meet these goals, a large number of new measurements needed to be performed, plus all pre-existing data needed to be compiled and evaluated. In the end, these goals were accomplished, which lead to an unprecedented amount of new data, plus an exhaustive compilation of previous data, being uploaded to the Ion Beam Analysis Nuclear Data Library (IBANDL).

Currently there are over 700 compiled data sets of gamma-producing reactions in IBANDL, which is a huge increase from the approximately 70 sets before the CRP. IBANDL is now fairly complete for most of the isotopes that are considered to be significant for PIGE analysis of light projectiles. In order to successfully incorporate the new PIGE data into IBANDL, it was necessary to modify the database. As part of the modification, it is now possible for anyone to compare total isotropic cross-sections and differential cross-sections.

Since the new PIGE measurements were performed in ten different laboratories, it was necessary to establish a common methodology for measuring differential cross-sections and thick-target yields and to ensure consistent treatment of uncertainties. With the aid of a well-defined inter-laboratory exercise, it was possible to identify the limitations and (lack of) accuracy of the techniques. With this information, it could be decided which improvements needed to be made in the measurement techniques and laboratory practices for a completely standardless and accurate PIGE measurement.

Evaluated cross-section data are indispensable for a reliable and accurate implementation of the standardless PIGE technique. During this CRP, theoretical evaluations of cross-sections from gamma-ray producing reactions were performed, using an approach based on R-matrix theory. Some of the recommended cross-sections have also become available to PIGE practitioners.

In the absence of a complete set of evaluated cross-section data for PIGE analysis, alternative ways of verifying and validating the measured cross-sections had to be employed. In this CRP, special emphasis was placed on the comparison of measured cross-sections and thick-target yields. Agreement between yields calculated from the measured cross-sections and measured thick-target yields indicate a good understanding of the reaction and allows the reliable analysis of samples of different thicknesses, without the use of individual standards. This comparison technique was applied to all the data of gamma-ray producing reactions that were measured and collected from the literature, i.e. reactions involving Li, Be, B, C, N, F, Na, Mg, Al, Si, P, S, Ti and Cr. Although this project was extensive, additional measurements of cross-sections and thick-target yields are needed for the following reactions in order to properly validate all results:

- ^{14}N , ^{28}Si , ^{29}Si , P, Cr, Ti, and deuteron-induced reactions in general, due to scarcity of the existing data
- ^7Li , ^{19}F and ^{25}Mg , due to discrepancies among the existing data.

In addition, for the needs of high-resolution depth profiling, which is one of the most developed and advanced PIGE analysis techniques, IBANDL will need to be modified to accommodate the energies, widths and strengths of narrow resonances.

Finally, a simulation code was developed and tested that combines cross-section and stopping power data, over a given sample depth, to produce desired yields. This code was implemented during the CRP. The ERYA code has been made available to the user community free of charge in order to enhance the implementation of standardless PIGE analysis and enable its comparative advantages in the analysis of in-depth homogeneous samples. The future release of a simulation and analysis code for PIGE depth-profiling is expected to further promote the use of standardless PIGE depth profiling, which would have significant benefits for the user community at large.

Appendix

TABLE A.1. LIST OF REACTION CROSS-SECTIONS MEASURED DURING THE CRP (2011–2015)

| Isotope | Reaction | γ -ray Energy [keV] | Incident Energy Range [MeV] | Detection Angle | Type of Data |
|-------------------|---------------------------|----------------------------|-----------------------------|-------------------------|-------------------------|
| ${}^7\text{Li}$ | (p,p' γ) | 478 | 2–4, 2–10 | 130, 135 | cross-sections + yields |
| ${}^7\text{Li}$ | (p,n' γ) | 429 | 2–10 | 135 | cross-sections + yields |
| ${}^9\text{Be}$ | (p, γ) | 718 | 0.5–1.7 | 135 | cross-sections + yields |
| ${}^{10}\text{B}$ | (p,p' γ) | 718 | 1–3, 3–4, 3–5 | 0, 45, 55, 90, 165 | cross-sections + yields |
| ${}^{10}\text{B}$ | (p, α ' γ) | 429 | 1–3, 2–4, 3–4, 1–3.8 | 0, 45, 55, 90, 130, 165 | yields |
| ${}^{11}\text{B}$ | (p,p' γ) | 2124 | 1–3, 3–4, 2.8–3.8 | 0, 45, 55, 90, 165 | cross-sections + yields |
| ${}^{12}\text{C}$ | (p, γ) | | 1.1–2.6 | 0, 55 | cross-sections |
| ${}^{12}\text{C}$ | (d, p' γ) | 3089 | 0.6–2 | 55 | cross-sections |
| ${}^{14}\text{N}$ | (p, p' γ) | 2313 | 4–7, 3.5–4 | 45, 55 | cross-sections + yields |

TABLE A.1. LIST OF REACTION CROSS-SECTIONS MEASURED DURING THE CRP (2011–2015) (cont.)

| Isotope | Reaction | γ -ray Energy [keV] | Incident Energy Range [MeV] | Detection Angle | Type of Data |
|------------------|--------------------------|----------------------------|------------------------------|-------------------------|-------------------------|
| ^{14}N | (d, p' γ) | 1885 | 0.6–2 | 55, 90 | cross-sections + yields |
| ^{14}N | (d, p' γ) | 2297 | 0.6–2 | 55, 90 | cross-sections + yields |
| ^{14}N | (d, p' γ) | 8310 | 0.6–2 | 55, 90 | cross-sections + yields |
| ^{19}F | (p, p' γ) | 110 | 2–4, 2–6 | 130, 135 | cross-sections + yields |
| ^{19}F | (p, p' γ) | 197 | 2–4, 2–6 | 130, 135 | cross-sections + yields |
| ^{19}F | (p, α' γ) | 6000–7000 | 0.8–4, 2–6 | 130, 135 | cross-sections + yields |
| ^{23}Na | (p, p' γ) | 440 | 2–4, 1.8–3, 3–4, 2–3, 1–2.9, | 0, 55, 90, 130, 135 | cross-sections + yields |
| ^{23}Na | (p, p' γ) | 1636 | 2–4, 1.8–3, 3–4, 2–3, 1–2.9, | 0, 55, 90, 130, 135 | cross-sections + yields |
| ^{24}Mg | (p, p' γ) | 1369 | 1.9–3, 1–3, 2–6 | 0, 15, 55, 90, 135 | cross-sections |
| ^{25}Mg | (p, p' γ) | 390 | 1.9–3, 1.5–2.4, 1–3, 2–6 | 0, 15, 55, 90, 135, 130 | cross-sections + yields |
| ^{25}Mg | (p, p' γ) | 585 | 1.9–3, 1.5–2.4, 1–3, 2–6 | 0, 15, 55, 90, 135, 130 | cross-sections + yields |
| ^{25}Mg | (p, p' γ) | 974 | 1.5–2.4, 1–3 | 90, 130 | cross-sections + yields |

TABLE A.1. LIST OF REACTION CROSS-SECTIONS MEASURED DURING THE CRP (2011–2015) (cont.)

| Isotope | Reaction | γ -ray Energy [keV] | Incident Energy Range [MeV] | Detection Angle | Type of Data |
|--------------------------|--------------------------|----------------------------|---|------------------------------|-------------------------|
| ^{26}Mg | (p, γ) | 1014 | 1–3 | 90 | cross-sections |
| ^{27}Al | (p,p' γ) | 844 | 1.5–3, 1–3, 2.5–5, 2.5–4, 2.5–3, 1.8–3, 1.5–3.8 | 0, 45, 55, 90, 135, 130, 165 | cross-sections + yields |
| ^{27}Al | (p,p' γ) | 1014 | 1.5–3, 1–3, 2.5–5, 2.5–4, 2.5–3, 1.8–3, 1.5–3.8 | 0, 45, 55, 90, 135, 130, 165 | cross-sections + yields |
| ^{27}Al | (p, γ) | 1779 | 1.5–4, 1–3, 2.5–5, 2–6, 2.5–3, 1.5–3.8 | 0, 45, 55, 90, 135, 130, 165 | cross-sections + yields |
| ^{27}Al | (p, α' γ) | 1369 | 1.5–4, 1–3, 2.5–5, 2–6, 1.5–3.8, 2.5–3 | 0, 45, 55, 90, 135, 130, 165 | cross-sections + yields |
| ^{28}Si | (p,p' γ) | 1779 | 1–3, 4–7, 2.5–5 | 55, 90, 45 | cross-sections + yields |
| ^{28}Si | (d, p' γ) | 1273 | 0.6–2 | 55 | cross-sections |
| ^{28}Si | (d, p' γ) | 2028 | 0.6–2 | 55 | cross-sections |
| ^{29}Si | (p,p' γ) | 1274 | 1–3, 4–7, 2.5–5 | 55, 90, 45 | cross-sections + yields |
| $^{\text{nat}}\text{Si}$ | (p,p' γ) | 1274 | 2.5–4 | 45 | yields |

TABLE A.1. LIST OF REACTION CROSS-SECTIONS MEASURED DURING THE CRP (2011–2015) (cont.)

| Isotope | Reaction | γ -ray Energy [keV] | Incident Energy Range [MeV] | Detection Angle | Type of Data |
|-------------------|-------------------|----------------------------|-----------------------------|-----------------|-------------------------|
| ^{nat} Si | (p, p' γ) | 1779 | 2.5–4 | 45 | yields |
| ³¹ P | (p, p' γ) | 1266 | 1–3, 2–4 | 90, 130 | cross-sections + yields |
| ³² S | (p, p' γ) | 2230 | 3–6 | 0, 15, 55, 90 | cross-sections |
| ³² S | (d, p' γ) | 841 | 1–2 | 90 | cross-sections + yields |
| ⁴⁸ Ti | (p, γ) | 62.3/90.6 | 1–3 | 90 | cross-sections |
| ^{nat} Ti | (p, γ) | 62.3/90.6 | 1–3 | 90 | cross-sections |
| ^{nat} Ti | (p, n γ) | 62.3/90.6 | 1.5–3 | 90 | cross-sections |
| ⁵³ Cr | (p, γ) | 62.3/90.6 | 1–3 | 90 | cross-sections |
| ⁵⁴ Cr | (p, n γ) | 62.3/90.6 | 1–3 | 90 | cross-sections |

LIST OF ABBREVIATIONS

| | |
|------------|--|
| ATOMKI | ATOMKI Institute for Nuclear Research of the Hungarian Academy of Sciences |
| CMAM-UAM | Centro de Micro Análisis de Materiales, Universidad Autónoma de Madrid |
| CPSSR | Coulomb-Repulsion Perturbed-Stationary State Relativistic Theory |
| CRP | Coordinated Research Project |
| CTN/IST | Campus Tecnológico Nuclear/Institut Superior Tecnico |
| DE | Double Escape |
| EBS | Elastic backscattering |
| ERDA | Elastic Recoil Detection Analysis |
| ERYA | Emitted Radiation Yield Analysis |
| FC | Faraday Cup |
| FE | Full Escape |
| FWHM | Full width at half-maximum |
| Ge(HP) | High Purity Germanium semiconductor detector |
| Ge(Li) | Germanium semiconductor detector with Lithium doped crystals |
| GVM | Generating VoltMeter |
| HVEE | |
| IAEA | International Atomic Energy Agency |
| IBA | Ion beam analysis |
| IBANDL | Ion Beam Analysis Data Library |
| KIPT | Kharkov Institute of Physics and Technology |
| LABEC-INFN | Laboratorio di Technice Nucleari per I Beni Culturali, Istituto Nazionale di Fizica Nuclear, Firenze |
| LaBr | Lanthanum Bromide scintillation radiation detector |
| MDL | Minimum detection limit |
| MOCVD | Metal-organic chemical vapor deposition |
| NaI | Sodium Iodine detector |
| NDF | General purpose code for analysis of Ion Beam Analysis Data |
| NDS | Nuclear Data Section |
| NMR | Nuclear Magnetic Resonance |
| NRA | Nuclear reaction analysis |
| NSTRI | Nuclear Science and Technology Research Institute |
| PIGE | Particle-induced gamma-ray emission spectroscopy |
| PIPS | Passivated Implanted Planar Silicon detector |
| PIXE | Particle-induced X-ray emission spectroscopy |
| RBI | Ruder Boskovic Institute |
| RBS | Rutherford backscattering |
| RCM | Research Coordination Meeting |
| REGe | Reverse electrode coaxial Germanium detector |
| SDD | Silicon drift detector |
| SIMNRA | Microsoft Windows program for the simulation of backscattering spectra for ion beam analysis with MeV ions |
| SSB | Silicon Surface Barrier |

LIST OF CONTRIBUTORS TO DRAFTING AND REVIEW

| | |
|------------------------|--|
| Becker, H-W. | Ruhr Universität Bochum, Germany |
| Bogdanović Radović, I. | Ruder Boskovic Institute, Croatia |
| Chiari, M. | Istituto Nazionale di Fisica Nucleare, Italy |
| Goncharov, A. | Kharkov Institute of Physics and Technology – National Science Center Kharkov Institute of Physics & Technology, Ukraine |
| Kakuee, O. | Nuclear Science & Technology Research Institute, Iran |
| Kiss, A.Z. | Institute for Nuclear Research (ATOMKI) of the Hungarian Academy of Sciences, Hungary |
| Lagoyannis, A. | National Center of Scientific Research “Demokritos”, Greece |
| Pedro de Jesus, A. | Centro de Fisica Nuclear, Portugal |
| Raisanen, J. | University of Helsinki, Finland |
| Zucchiatti, A. | Centro de Micro-Analisis de Materiales Universidad Autónoma de Madrid, Spain |
| Dimitriou, P. | Scientific Secretary |
| Abriola, D. | Scientific Secretary |

Research Coordination Meetings

Vienna, Austria: 16-20 May 2011

Vienna, Austria: 8-12 October 2012

Vienna, Austria: 7-11 April 2014



IAEA

International Atomic Energy Agency

No. 25

ORDERING LOCALLY

In the following countries, IAEA priced publications may be purchased from the sources listed below or from major local booksellers.

Orders for unpriced publications should be made directly to the IAEA. The contact details are given at the end of this list.

CANADA

Renouf Publishing Co. Ltd

22-1010 Polytek Street, Ottawa, ON K1J 9J1, CANADA

Telephone: +1 613 745 2665 • Fax: +1 643 745 7660

Email: order@renoufbooks.com • Web site: www.renoufbooks.com

Bernan / Rowman & Littlefield

15200 NBN Way, Blue Ridge Summit, PA 17214, USA

Tel: +1 800 462 6420 • Fax: +1 800 338 4550

Email: orders@rowman.com Web site: www.rowman.com/bernan

CZECH REPUBLIC

Suweco CZ, s.r.o.

Sestupná 153/11, 162 00 Prague 6, CZECH REPUBLIC

Telephone: +420 242 459 205 • Fax: +420 284 821 646

Email: nakup@suweco.cz • Web site: www.suweco.cz

FRANCE

Form-Edit

5 rue Janssen, PO Box 25, 75921 Paris CEDEX, FRANCE

Telephone: +33 1 42 01 49 49 • Fax: +33 1 42 01 90 90

Email: formedit@formedit.fr • Web site: www.form-edit.com

GERMANY

Goethe Buchhandlung Teubig GmbH

Schweitzer Fachinformationen

Willstätterstrasse 15, 40549 Düsseldorf, GERMANY

Telephone: +49 (0) 211 49 874 015 • Fax: +49 (0) 211 49 874 28

Email: kundenbetreuung.goethe@schweitzer-online.de • Web site: www.goethebuch.de

INDIA

Allied Publishers

1st Floor, Dubash House, 15, J.N. Heredi Marg, Ballard Estate, Mumbai 400001, INDIA

Telephone: +91 22 4212 6930/31/69 • Fax: +91 22 2261 7928

Email: alliedpl@vsnl.com • Web site: www.alliedpublishers.com

Bookwell

3/79 Nirankari, Delhi 110009, INDIA

Telephone: +91 11 2760 1283/4536

Email: bkwell@nde.vsnl.net.in • Web site: www.bookwellindia.com

ITALY

Libreria Scientifica "AEIOU"

Via Vincenzo Maria Coronelli 6, 20146 Milan, ITALY
Telephone: +39 02 48 95 45 52 • Fax: +39 02 48 95 45 48
Email: info@libreriaaeiou.eu • Web site: www.libreriaaeiou.eu

JAPAN

Maruzen-Yushodo Co., Ltd

10-10 Yotsuyasakamachi, Shinjuku-ku, Tokyo 160-0002, JAPAN
Telephone: +81 3 4335 9312 • Fax: +81 3 4335 9364
Email: bookimport@maruzen.co.jp • Web site: www.maruzen.co.jp

RUSSIAN FEDERATION

Scientific and Engineering Centre for Nuclear and Radiation Safety

107140, Moscow, Malaya Krasnoselskaya st. 2/8, bld. 5, RUSSIAN FEDERATION
Telephone: +7 499 264 00 03 • Fax: +7 499 264 28 59
Email: secnrs@secnrs.ru • Web site: www.secnrs.ru

UNITED STATES OF AMERICA

Bernan / Rowman & Littlefield

15200 NBN Way, Blue Ridge Summit, PA 17214, USA
Tel: +1 800 462 6420 • Fax: +1 800 338 4550
Email: orders@rowman.com • Web site: www.rowman.com/bernan

Renouf Publishing Co. Ltd

812 Proctor Avenue, Ogdensburg, NY 13669-2205, USA
Telephone: +1 888 551 7470 • Fax: +1 888 551 7471
Email: orders@renoufbooks.com • Web site: www.renoufbooks.com

Orders for both priced and unpriced publications may be addressed directly to:

Marketing and Sales Unit
International Atomic Energy Agency
Vienna International Centre, PO Box 100, 1400 Vienna, Austria
Telephone: +43 1 2600 22529 or 22530 • Fax: +43 1 2600 29302 or +43 1 26007 22529
Email: sales.publications@iaea.org • Web site: www.iaea.org/books

International Atomic Energy Agency
Vienna
ISBN 978-92-0-106317-5
ISSN 1011-4289